

**Project Report
ASAP-8**

Volume 1

Proceedings of the Adaptive Sensor Array Processing (ASAP) Workshop 14–15 March 2000

**J. O'Brien
Editor**

5 September 2000

Lincoln Laboratory
MASSACHUSETTS INSTITUTE OF TECHNOLOGY
LEXINGTON, MASSACHUSETTS



Prepared for the Defense Advanced Research Projects Agency and the Department of the Navy
under Air Force Contract F19628-00-C-0002.

Approved for public release; distribution is unlimited.

DTIC QUALITY INSPECTION

20001010 047

This report is based on studies performed at Lincoln Laboratory, a center for research operated by Massachusetts Institute of Technology. The work was sponsored in part by the Defense Advanced Research Projects Agency and in part by the Department of the Navy under Air Force Contract F19628-00-C-0002.

This report may be reproduced to satisfy needs of U.S. Government agencies.

The ESC Public Affairs Office has reviewed this report, and it is releasable to the National Technical Information Service, where it will be available to the general public, including foreign nationals.

This technical report has been reviewed and is approved for publication.

FOR THE COMMANDER



Gary Tutungian
Administrative Contracting Officer
Plans and Programs Directorate
Contracted Support Management

Non-Lincoln Recipients

PLEASE DO NOT RETURN

Permission is given to destroy this document
when it is no longer needed.

MASSACHUSETTS INSTITUTE OF TECHNOLOGY
LINCOLN LABORATORY

**PROCEEDINGS OF THE ADAPTIVE SENSOR ARRAY
PROCESSING (ASAP) WORKSHOP
14-15 MARCH 2000**

J. O'BRIEN
EDITOR
Division 10

PROJECT REPORT ASAP-8, VOLUME 1

5 SEPTEMBER 2000

Approved for public release; distribution is unlimited.

ASAP 2000 Workshop Theme

This year marks the eighth annual Adaptive Sensor Array Processing workshop, which is sponsored jointly by the DARPA Advanced Technology and Tactical Technology Offices, the Navy AEGIS and E2C Program Offices, the Office of Naval Research, and the NAVSEA Advanced Systems Technology Office. This year, the first IEEE Sensor Array and Multichannel (SAM) Signal Processing Workshop to be held in nearby Cambridge, Massachusetts, will follow ASAP on 16-17 March 2000. This unique pairing of ASAP with SAM will provide an unparalleled opportunity for the adaptive sensor array processing community, combining ASAP's focus on state-of-the-art signal processing advances for military systems with the broader international scope and strong academic participation of the IEEE SAM workshop.

As the ASAP workshop has evolved over its eight-year history, a common theme has been to highlight the similarity of adaptive sensor array processing techniques for various disciplines. The ASAP forum has provided researchers from academia, government, and industry the opportunity to discuss common problems, developing ideas, and solutions related to how these diverse technologies can be applied to national defense interests. This year will continue to stress the strong coupling between government, industry and academia. A key theme will be the cross-fertilization of ideas between the ASAP and SAM participants to provide new areas of exploration and accelerate technological advances.

We welcome your participation in the eighth annual ASAP Workshop.



CAPT John Geary
US Navy PMS-400



Dr. John Tague
ONR



Mr. Fred Lee
US Navy/PMA-231 AD



CAPT John Polcari
DARPA/ATO

Mr. James Thompson
PEO (USW) ASTO

Dr. Allan Steinhardt
DARPA/TTO



Workshop Chairman, Edward Baranoski
Technical Program Coordinator, Nicholas Pulsone
Workshop Administrator, Kathleen Ballos

Technical Committee

Arthur Baggeroer / MIT
Lloyd Griffiths / George Mason University
Peter Mikhalevsky / SAIC
Tom Miller / Raytheon

Lee Swindlehurst / Brigham Young University
Donald Tufts / University of Rhode Island
James Ward / MIT Lincoln Laboratory
Michael Zatman / MIT Lincoln Laboratory

TABLE OF CONTENTS

	Page
Bistatic STAP for Airborne Radar Systems S. Kogon and M. Zatman	1
Parametric Clutter Rejection for Space-Time Adaptive Processing L. Swindlehurst and P. Parker	7
Multistage Adaptation for Large Digital Arrays D. Rabideau	13
Space-Time Adaptive Detection of Distributed Targets in Homogeneous Environment E. Conte, A. DeMaio, and G. Ricci	19
Evaluation of Reduced-Rank Adaptive Matched Field Processing For Shallow-Water Target Detection N. Lee, L. Zurk, and J. Ward	25
Radar Imaging Using a Wideband Adaptive Array M. Curry and Y. Kuga	31
Novel Impact Echo Imaging Technique Using Multiresolution Enhancements in Temporal and Spatial Domains A. Al-Fahoum and A. Reza	37
Adaptive Beampattern Control Using Quadratic Constraints for Circular Array STAP K. Bell, H. Van Trees, and L. Griffiths	43
PARAFAC-STAP for the UESA Radar T. Li, N. Sidiropoulos, and G. Giannakis	49
Adaptive Processing of Element-Digitised Airborne-Intercept Phased Array Radar J. Mather, H. Rees, M. Cook and J. Wood	55

TABLE OF CONTENTS (Continued)

	Page
Adaptive Beamformer Orthogonal Rejection Test (ABORT) N. Pulsone and C. Radar	61
Cramér-Rao Bounds: The Adaptive Array Story C. Richmond	67
Simultaneous DOA Estimation of Fully Correlated and Uncorrelated Gaussian Sources in Nonuniform Linear Antenna Arrays Y. Abramovich and N. Spencer	73
Array Calibration for Circular-Array STAP Using Clutter Scattering and Projection Matrix Fitting D. Furhrmann and D. Rieken	79
Theory and Application of Adaptive Transmitter Radar J. Guerci and S. Pillai	85
Distributed Processing for 3-D Localization Using Acoustic Vector Sensors on the Seabed or Battlefield M. Hawkes and A. Nehorai	91
Space-Time Matched-Field Depth Estimation With Active Sonar G. Hickman and J. Krolik	97
Adaptive Matched Field Processing for a Moving Target in a Noisy Shallow Water Channel L. Zurk, N. Lee, J. Ward, and A. Gronosky	103
Adaptive Self-Noise Suppression for Passive Sonar Towed Arrays V. Premus	109
A Unified Method for Passive Measurement and Tracking of Contacts From an Array of Sensors R. Zarnich, K. Bell, and H. Van Trees	115

BISTATIC STAP FOR AIRBORNE RADAR SYSTEMS

Stephen M. Kogon and Michael A. Zatman

MIT Lincoln Laboratory
244 Wood Street
Lexington, MA 02420-9108
kogon@ll.mit.edu, zatman@ll.mit.edu

ABSTRACT

One of the major challenges to an airborne bistatic radar system is the mitigation of ground clutter returns using space-time adaptive processing (STAP) to enable the detection of moving targets. Unlike the monostatic case, the relationship between Doppler frequency and cone angle of clutter is very complicated in an airborne bistatic radar due to the independent motions of the transmitter and receiver. This complex relationship leads to clutter that is non-stationary in range and not always easily compensated for as is possible in monostatic systems. Effective implementation of STAP relies on the availability of sufficient homogeneous training data to estimate the adaptive weights. A fundamental issue for bistatic STAP is the non-stationary nature in range of bistatic clutter and its impact on adaptive weight training. In this paper, we look at two different approaches to bistatic STAP, Doppler warping and derivative-based updating, that attempt to account for the non-stationary nature of bistatic clutter. The performance of these methods is contrasted for a bistatic scenario and limitations on the ability of STAP to cancel clutter are quantified.

1. INTRODUCTION

Space-time adaptive processing (STAP) for an airborne radar uses a series of pulses along with an array of sensors to mitigate ground clutter returns. Through an extensive research effort, STAP has evolved from initial theoretical studies to a fairly mature field that can be implemented in real-time systems [1, 2, 3]. The realization of STAP into actual military systems is made possible not only by advances in processor technology but also by the development of efficient algorithms and effective training strategies to compute the adaptive STAP weights. In this context, a series of non-adaptive processing steps lead to an elegant STAP solution that computes a single set of adaptive weights that are applied to radar returns from all range gates. To date, STAP research has focused on monostatic systems for which the transmitter and receiver have a common platform. Many future systems, however, are considering bistatic operation [4, 5, 6]. A major obstacle for these bistatic systems is the cancellation of bistatic clutter.

Bistatic radars, ones in which the transmitter and receiver are not co-located, have been considered since the first deployments of radar systems [7]. These systems offer several advantages over

their monostatic counterparts, including an extended detection range achieved by placing the receive platform in close proximity to an area of interest without having to risk easy detection since the receiver is passive. However, the complicated nature of bistatic clutter discourages the use of a bistatic radar in airborne systems for moving target indication (MTI). In particular, the separate motion of the transmitter and receiver creates two sources of Doppler for bistatic clutter. The resulting iso-Doppler relationship is non-stationary in range and difficult to compensate for with monostatic STAP techniques [8]. Since the characteristics of bistatic clutter are strongly dependent on the geometry between the transmitter and receiver, it is important to develop robust clutter cancellation techniques and to understand and quantify favorable transmitter/receiver configurations.

The adaptive weights used by STAP must be computed using a clutter-plus-noise sample covariance matrix estimated from data samples collected over range. The ability to obtain an accurate estimate of the covariance matrix relies on the availability of sufficient training data with the same characteristics. Though the clutter power may be nonhomogeneous in range, the crucial requirement is that the angle/Doppler relationship be approximately constant over range. This requirement means that the locus of clutter energy in angle/Doppler space, known as the clutter ridge, be constant over range. For a monostatic airborne radar, clutter is stationary in range when the velocity of the platform is aligned with the array. For cases when this condition is violated, a technique known as Doppler warping can be employed to realign the clutter ridge and make it approximately stationary in range for a uniform linear array [8]. This compensation is made possible by the fact that clutter Doppler and cone angle have a common reference point, the transmitter/receiver platform. In the case of bistatic systems, clutter has two independent sources of Doppler due to the separate motion of the transmitter and receiver. The cone angles of clutter, however, are measured with respect to the array on the receiver platform. The result of the independent transmitter Doppler produced by another platform is rapid variation of clutter in range that is not so easily compensated for.

Bistatic STAP requires that either compensation prior to STAP be performed or the adaptive weights vary with range in order to effectively mitigate the non-stationary clutter. As we will see, the variation of bistatic clutter is so rapid that both approaches are limited to smaller range extents, thus, limiting the amount of training data available. This paper begins with a characterization of bistatic clutter in Section 2. Here, we describe the angle/Doppler relationships of a specific scenario and demonstrate the rapid variation of bistatic clutter in range as contrasted with monostatic clutter. Next, in Section 3, we study the performance of STAP when train-

This work was supported by DARPA under Air Force Contract #F19628-95-C-0002. Opinions, interpretations, conclusions and recommendations are those of the authors and are not necessarily endorsed by the United States Air Force.

ing is done ignoring the non-stationarity and also when Doppler warping is employed. Section 4 describes range-varying STAP weights adapted using a technique known as derivative-based updating. The performance of derivative-based updating is compared with the methods from Section 3. All results are theoretical using ideal covariance matrices averaged across the training interval.

2. BISTATIC CLUTTER

Bistatic clutter refers to the ground reflections of the transmitted waveform as seen by the receiver in a bistatic system. In order to better understand the performance of STAP, it is useful to study the characteristics of bistatic clutter. We start by reviewing clutter in a monostatic system and the characteristics that allow it to be effectively cancelled using STAP. The monostatic scenario is contrasted with two bistatic scenarios, one with a stationary transmitter and one with a moving transmitter. The characteristics of the resulting bistatic clutter are then studied, particularly those that are crucial to STAP. Throughout this discussion, we focus on a uniform linear array (ULA) with a radar operating frequency of $f = 435$ MHz, a frequency used for previous STAP analyses [1]. Altitudes of the airborne radar platforms are 10 km.

In the case of a monostatic airborne radar, the clutter Doppler is related to the cone angle between the clutter on the ground and the receiver/transmitter ϕ_{rt} and is given by

$$f_d = \frac{2v_{rt}}{\lambda} \cos \phi_{rt} \quad (1)$$

where v_{rt} is the radar platform velocity and λ is the radar wavelength. Likewise, the spatial frequency for the ULA is determined by the cone angle of the clutter patch with respect to the array ϕ_a and is given by

$$u = \frac{d}{\lambda} \cos \phi_a \quad (2)$$

where d is the inter-element spacing of the ULA. Since both the ULA and the platform velocity have the same point of reference, i.e., the receiver/transmitter, the two cone angles are related by

$$\phi_{rt} = \phi_a + \phi_{mis} \quad (3)$$

where ϕ_{mis} is the misalignment angle between the array and the platform velocity, which can be caused by crab in the case of the aircraft heading altered by strong winds or by a rotating array. A plot of the Doppler frequencies of an area on the ground is shown in Fig. 1. The black lines correspond to contours of constant array cone angle and the gray lines correspond to contours of constant range. In this example, the platform velocity of the receiver/transmitter platform is $v_{rt} = 100$ m/sec, its location is (0 km, 0 km) and the array is aligned with the platform velocity vector ($\phi_{mis} = 0^\circ$). As we can see from Fig. 1, each iso-cone angle contour of the array perfectly aligns with a constant Doppler frequency, known as an iso-Doppler contour.

The clutter ridge for each range can be constructed by plotting the clutter Doppler frequency as a function of cone angle. A plot of clutter ridges at ranges of 25 km, 50 km and 100 km is shown in Fig. 2. All of these clutter ridges lie on the same locus in angle/Doppler space, independent of range. Thus, clutter is stationary in range. As a result, STAP can use a common set of weights for all range cells. Not only is the use of a common weight across all range cells desirable from a computational point of view since a different set of weights does not need to be computed for

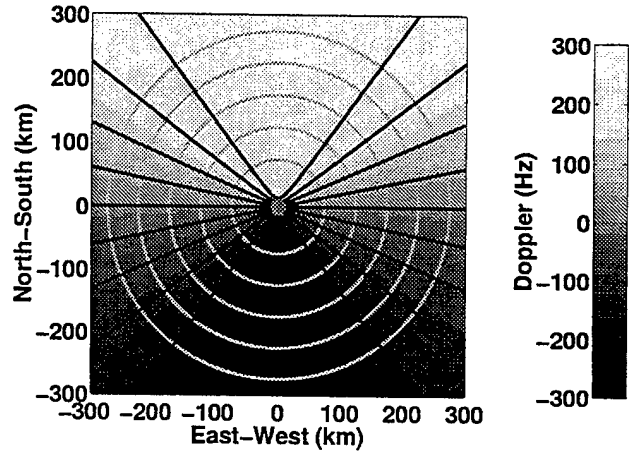


Figure 1: Clutter Doppler frequency of a monostatic airborne radar located at (0 km, 0 km) moving north at $v_{rt} = 100$ m/sec with iso-cone angle (black) and iso-range contours (gray).

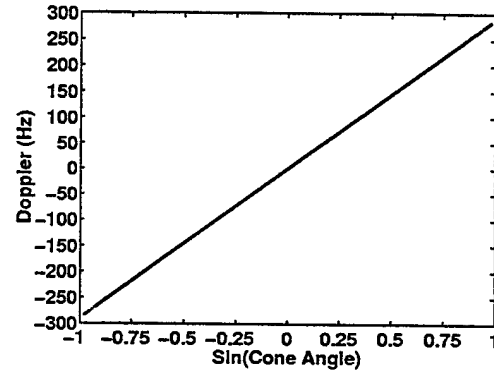


Figure 2: Monostatic clutter ridges for the scenario from Fig. 1 at two-way ranges of 25 km (solid), 50 km (dash-dot) and 100 km (dashed). All three clutter ridges overlap each other.

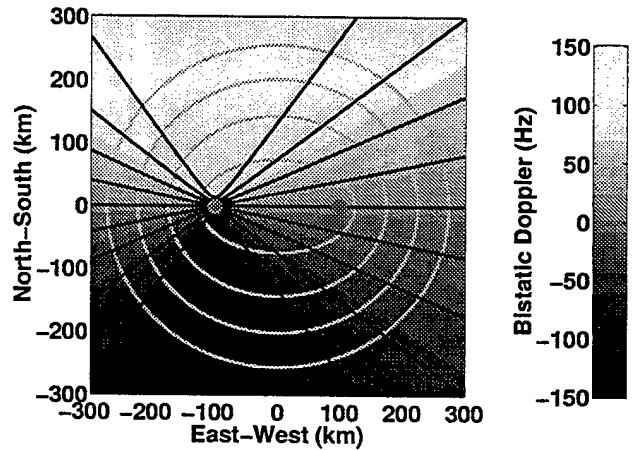


Figure 3: Bistatic clutter Doppler frequency with a stationary (ground-based) transmitter at (100 km, 0 km) and a receiver at (-100 km, 0 km) moving north at $v_r = 100$ m/sec, with iso-cone angle (black) and iso-range contours (gray).

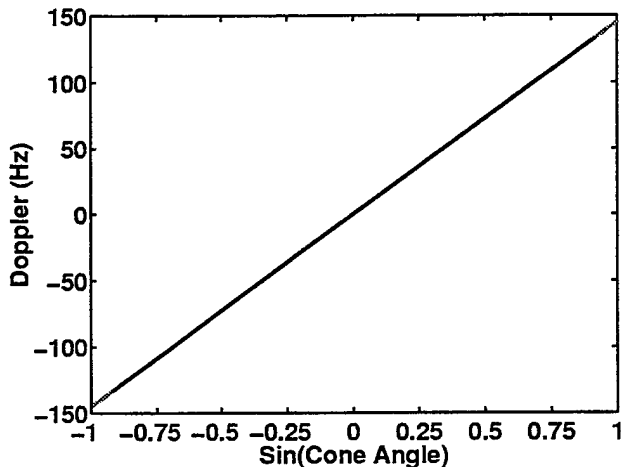


Figure 4: Bistatic clutter ridges for the scenario from Fig. 3 with a stationary transmitter at bistatic ranges of 225 km (solid), 250 km (dash-dot), and 300 km (dashed). All three clutter ridges overlap each other.

every range cell, but also the STAP algorithm has an abundance of training cells to compute the adaptive weights. Since all range cells share the same clutter locus, all range cells can be used for STAP weight training. In the case of an array that is misaligned with the velocity vector ($\phi_{\text{mis}} \neq 0^\circ$), iso-Dopplers will not align with iso-cone angles, particularly at short ranges. However, an efficient very effective transformation exists, known as Doppler warping [8], that produces a range-dependent Doppler shift to align the clutter in angle/Doppler space for a ULA. Doppler warping will be discussed in more detail in Section 3.

Bistatic clutter is somewhat more complicated due to the independent motion of both the transmitter and receiver. Bistatic Doppler is given by

$$f_d = \frac{v_t}{\lambda} \cos \phi_t + \frac{v_r}{\lambda} \cos \phi_r \quad (4)$$

where v_t and v_r are the transmitter and receiver velocities, respectively. ϕ_t and ϕ_r are the cone angles of the clutter patch with respect to the transmitter and receiver headings. Note that in the case of a stationary transmitter ($v_t = 0$), bistatic Doppler has exactly the same form as monostatic clutter except that the factor of two is gone since the only motion is due to the receiver and not both the receiver and transmitter as is the monostatic case.

An example of bistatic Doppler with a stationary, ground-based transmitter at the point (100 km, 0 km) and a receiver at (-100 km, 0 km) with its array aligned with the platform velocity vector ($\phi_{\text{mis}} = 0^\circ$) is shown in Fig. 3. In this case, as in the monostatic case, all of the Doppler is due to the motion of one platform. The similarity to the monostatic case is evident as we can see that each iso-cone angle of the ULA has a constant Doppler for all range and thus aligns with an iso-Doppler contour. The bistatic clutter ridges are stationary in range as can be seen in Fig. 4 for the clutter ridges at bistatic ranges of 225 km, 250 km and 300 km. Note that the minimum bistatic range is approximately 201 km. In this case, STAP clutter mitigation simply reverts to a "monostatic-like" problem for which all of the methods that have been successfully demonstrated for monostatic STAP [2, 3] can also be applied.

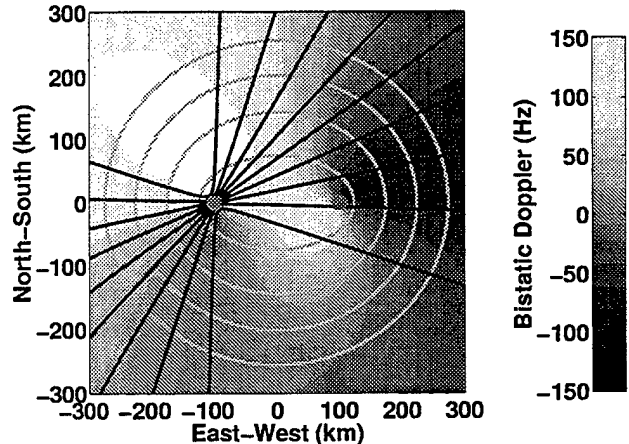


Figure 5: Bistatic clutter Doppler frequency with a transmitter at (100 km, 0 km) moving southeast at $v_t = 100$ m/sec and a receiver at (-100 km, 0 km) moving north at $v_r = 100$ m/sec with the array misaligned with the platform velocity vector by $\phi_{\text{mis}} = 35^\circ$. Iso-cone angle contours are indicated in black and iso-range contours in gray.

The nature of bistatic clutter, however, changes dramatically when the transmitter is in motion. In this case, bistatic Doppler has two, independent sources: the transmitter motion and the receiver motion. An example of bistatic Doppler is shown in Fig. 5 in which the receiver at (-100 km, 0 km) is heading north and the transmitter at (100 km, 0 km) is heading southwest, both with a velocity of 100 m/sec. Though the Doppler exhibits the expected characteristics of large, positive values in front of both the receiver and transmitter and negative values behind the headings of the platforms, the characteristics of the bistatic clutter are quite complicated. As can be seen by the overlaying iso-range contours (gray lines) and iso-cone angle contours (black lines), the bistatic Doppler along an iso-cone angle contour changes dramatically with range. When we examine the resulting clutter ridges in Fig. 6 at bistatic ranges of 225 km, 250 km and 300 km, we see a very complicated structure. Unlike the cases of a monostatic radar or bistatic radar with a stationary transmitter, the independent motion of the transmitter is produced from a different reference point than the array cone angles. Thus, the resulting bistatic Doppler cannot be easily aligned with the iso-cone angles of the array on the receiver platform. Examining Fig. 6, we see that the clutter ridges actually intersect and vary dramatically even over a very short range. This rapid variation with range has implications in terms of STAP training as will be discussed in the next section.

3. PERFORMANCE OF BISTATIC STAP

Bistatic clutter presents a very challenging problem to STAP due to its complex, non-stationarity in range. Two approaches can be adopted to attempt to cope with the variation in range: a priori transformation prior to STAP or range-varying STAP weights. Range-varying STAP weights raise several issues, including the availability of sufficient training data as well as computational complexity. A method that incorporates range-varying STAP weights will be discussed in Section 4. In this section, we examine the performance of STAP for which a STAP weight is computed by

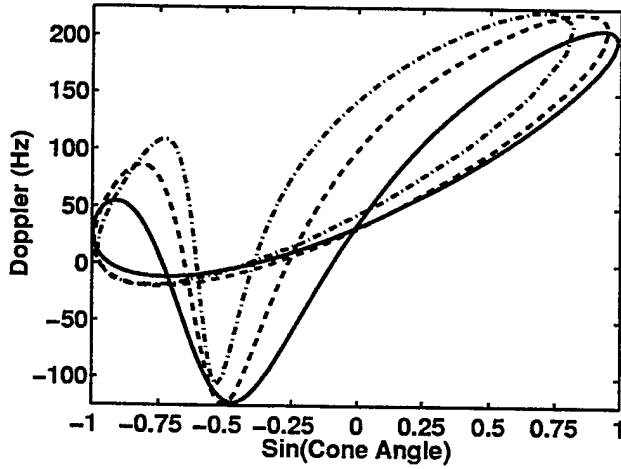


Figure 6: Bistatic clutter ridges for the scenario from Fig. 3 at bistatic ranges of 225 (solid), 250 (dash-dot), and 300 km (dashed).

averaging over a range interval with and without an a priori transformation.

The optimum STAP weight vector emphasizes target signals from an angle ϕ_t and Doppler frequency f_t while rejecting all other significant energy. The optimum STAP weights for range cell n are given by

$$\mathbf{w}_{\text{opt}}(n) = \mathbf{R}(n)^{-1} \mathbf{v}_t \quad (5)$$

where $\mathbf{R}(n) = E\{\mathbf{x}(n)\mathbf{x}^H(n)\}$ is the clutter-plus-noise covariance matrix at range cell n . The space-time steering vector \mathbf{v}_t is the Kronecker product of the spatial steering vector $\mathbf{a}(\phi_t)$ and the Doppler steering vector $\mathbf{b}(f_t)$

$$\mathbf{v}_t = \mathbf{v}(\phi_t, f_t) = \mathbf{b}(f_t) \otimes \mathbf{a}(\phi_t) \quad (6)$$

where both \mathbf{a} and \mathbf{b} are Vandermonde steering vectors [1] and ϕ_t is the presumed target angle with respect to the ULA that determines the spatial frequency as in (2) and f_t is the presumed target Doppler. Of course, this optimum STAP weight vector presumes knowledge of $\mathbf{R}(n)$ and, therefore, serves as an upper bound on the performance for any STAP weight that is obtained by estimating the clutter statistics from the data.

A common performance metric for STAP is the loss incurred due to the presence of interference, known as signal-to-interference-plus-noise ratio (SINR) loss. In the context of clutter mitigation, this quantity is a measure of the loss due to the presence of clutter and is typically evaluated for a single angle for all unambiguous target velocities. The resulting SINR loss curve then gives an indication of the performance in terms of minimum detectable velocity (MDV) for a specified, maximum tolerable SINR loss. For an arbitrary STAP weight vector \mathbf{w} , SINR loss is given by

$$\begin{aligned} L_{\text{SINR}} &= \frac{\text{SINR}}{\text{SINR}_0} \\ &= \frac{|\mathbf{w}^H \mathbf{v}_t|^2}{[\mathbf{w}^H \mathbf{R}(n) \mathbf{w}] \cdot [\mathbf{v}_t^H \mathbf{v}_t]} \end{aligned} \quad (7)$$

where $\mathbf{R}(n)$ is the true covariance matrix at range cell n . SINR loss has a maximum value of unity, which indicates that performance is not impacted by clutter, and a minimum value equal to

the clutter-to-noise ratio for zero velocity targets. Theoretically, optimum or ideal performance is obtained when the STAP weight vector is equal to the optimum weights from (5).

In practice, the STAP weights are obtained by estimating the clutter-plus-noise covariance matrix from space-time data snapshots. The sample covariance matrix is given by

$$\hat{\mathbf{R}}(n) = \frac{1}{K} \sum_{k=1}^K \mathbf{x}(n_k) \mathbf{x}^H(n_k) \quad (8)$$

where the indices n_k define the K range gates that comprise the STAP training set. Note that we have not placed any presumptions on how these range gates are chosen. In this analysis, we consider strategies that compute the sample covariance matrix using K snapshots centered about, but excluding, the range cell n . The range cell of interest n is typically not included in training to prevent target cancellation or self-nulling. To model this covariance matrix computed from data snapshots over the range interval centered about range n , we can average the true covariances at each range gate over this range interval

$$\bar{\mathbf{R}}(n) = \frac{1}{K} \sum_k \mathbf{R}(k) \quad (9)$$

for $n - \frac{K-1}{2} \leq k \leq n + \frac{K-1}{2}$ for $k \neq n$.

Clutter that is non-stationary in range has a clutter ridge that varies its location in angle/Doppler over range. One can attempt to align the clutter ridges using a range-dependent transformation to the data prior to STAP. One such method is known as Doppler warping [8]. This method takes each range and applies a Doppler shift to align the clutter ridge at a common Doppler frequency for a given angle, e.g., array broadside. If the clutter ridge has a similar shape but is only displaced in Doppler over range, then this Doppler shift will realign the clutter ridge for all ranges. Though this will perfectly align the clutter ridge at one angle, for other angles the alignment is only approximate. For more details, see [8]. Doppler warping incorporates a Doppler shift by producing a phase ramp across pulses which can be formulated using the transformation matrix

$$\mathbf{T}_w = [1 \ e^{j2\pi f_w(n)} \ \dots \ e^{j2\pi(L-1)f_w(n)}] \otimes \mathbf{I} \quad (10)$$

where $f_w(n)$ is the Doppler shift for range gate n and L is the total number of pulses in the CPI. The $M \times M$ identity matrix in (10) simply means that the same transformation is applied to all M elements of the ULA. The transformation or Doppler warping matrix \mathbf{T}_w simply applies a phase ramp across pulses to Doppler shift the entire data snapshot for range gate n . The resulting Doppler warped output at range gate n is

$$\mathbf{x}_w(n) = \mathbf{T}_w^H(n) \mathbf{x}(n). \quad (11)$$

Likewise, the covariance matrix for range gate n following Doppler warping is given by

$$\mathbf{R}_w(n) = \mathbf{T}_w^H(n) \mathbf{R}(n) \mathbf{T}_w(n). \quad (12)$$

The performance of STAP obtained while training over a specified range extent is contrasted for the cases of with and without Doppler warping. We consider the same scenario from Figs. 5 and 6 with a receiver platform heading north at $v_r = 100$ m/sec and a transmitter traveling southwest at $v_t = 100$ m/sec, with both platforms at an altitude of 10 km. The radar frequency is 435 MHz,

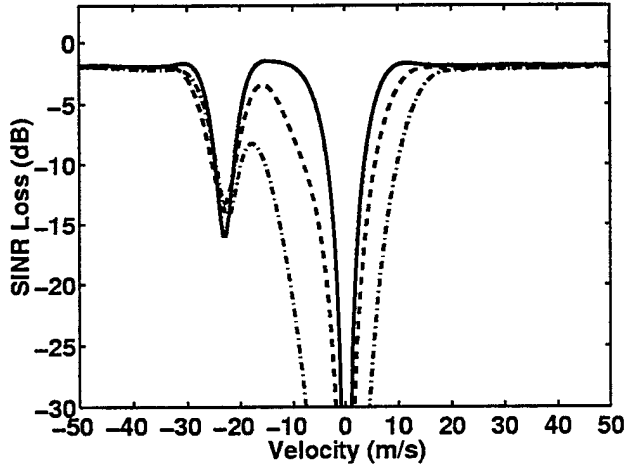


Figure 7: SINR loss vs. target velocity for the bistatic clutter scenario in Fig. 5 for training over a 12 km training region without any compensation (dash-dot) and with Doppler warping (dashed) compared to ideal STAP performance (solid).

the bandwidth is 5 MHz, the ULA has $M = 18$ elements with $\lambda/2$ spacing, the PRF is 300 Hz, and the CPI length is 18 pulses. Note that these parameters are the same ones used in the STAP analysis in [1] and are also very similar to those used in the Mountaintop experiment [9]. The SINR loss of STAP with and without Doppler warping is shown in Fig. 7 for a range training interval of 12 km. Although, Doppler warping improves STAP performance significantly, the SINR loss with Doppler warping is still considerably worse than in the ideal case. Clearly, the width of the null at zero velocity widens appreciably indicating an increase in the minimum detectable velocity (MDV). Examining the clutter ridges for this scenario in Fig. 6, we see that for the different ranges not only do the clutter ridges vary in range but their shape changes as well. Thus, Doppler warping, which correctly focuses to one point on the clutter ridge, can only properly correct this point. The other portions of the clutter ridge are still misaligned and cause the increase in MDV in the SINR loss.

4. DERIVATIVE-BASED UPDATING FOR BISTATIC STAP

Another approach that addresses the non-stationary clutter found in an airborne bistatic radar is to compute updated STAP weights for each range gate. A variety of criterion can be used to estimate the varying STAP weights including dynamic adaptive techniques such as least mean-square (LMS) or recursive least squares (RLS) adaptive weights that are updated for every sample. Another approach is to use an entire interval of $K + 1$ range gates centered at range gate n to compute a range-varying STAP weight across the interval. The range-varying STAP weights can be rewritten as a Taylor series expansion. This expansion can be approximated using only the first-order derivative provided the higher order terms are negligible. The result, known as *derivative-based updating* (DBU), can be written as a linearly range-varying weight vector [10]

$$\mathbf{w}(k) = \mathbf{w}_0 + k\dot{\mathbf{w}}_0 \quad (13)$$

where $\mathbf{w}_0 = \mathbf{w}(n)$ and $\dot{\mathbf{w}}_0 = \dot{\mathbf{w}}(n)$ are the weight vector and derivative of the STAP weight vector at $k = n$, i.e., the center of the training interval. A brief sketch of the computation of DBU-STAP weights is given below followed by the results of the application of DBU-STAP to the bistatic clutter mitigation example examined in the previous section.

The output of DBU-STAP is obtained by applying the range-varying weight vector from (13) to the n th STAP data snapshot (training range gate)

$$\begin{aligned} y(k) &= \mathbf{w}^H(k) \mathbf{x}(k) \\ &= \mathbf{w}_0^H \mathbf{x}(k) + k\dot{\mathbf{w}}_0^H \mathbf{x}(k) \\ &= \begin{bmatrix} \mathbf{w}_0 \\ \dot{\mathbf{w}}_0 \end{bmatrix}^H \begin{bmatrix} \mathbf{x}(k) \\ k\mathbf{x}(k) \end{bmatrix} \\ &= \tilde{\mathbf{w}}^H \tilde{\mathbf{x}}(k) \end{aligned} \quad (14)$$

where $\tilde{\mathbf{x}}(k)$ is the augmented data vector and $\tilde{\mathbf{w}}$ is the augmented STAP weight vector. Note that $\tilde{\mathbf{w}}$ is constant for all k . Rather than the augmented data vector absorbs the varying component. The sample covariance matrix of the augmented data vector is computed by substituting $\tilde{\mathbf{x}}(k)$ into the sample covariance computation in (8) where the training indices correspond to the interval $n - \frac{K-1}{2} \leq k \leq n + \frac{K-1}{2}$ for $k \neq n$. This sample covariance matrix can be modeled by substituting the true range-varying covariance matrix at each range gate

$$\tilde{\mathbf{R}} = \frac{1}{K} \sum_k \begin{bmatrix} \mathbf{R}(k) & k\mathbf{R}(k) \\ k\mathbf{R}(k) & k^2\mathbf{R}(k) \end{bmatrix}. \quad (15)$$

The resulting DBU-STAP weight vector is then found to be

$$\tilde{\mathbf{w}} = \begin{bmatrix} \mathbf{w}_0 \\ \dot{\mathbf{w}}_0 \end{bmatrix} = \tilde{\mathbf{R}}^{-1} \begin{bmatrix} \mathbf{v}(\phi_t, f_t) \\ 0 \end{bmatrix}. \quad (16)$$

Note that the degrees of freedom for the DBU-STAP weights is now twice that of the other STAP methods considered, since both the weights and their first-order derivative have to be computed at range n . For more details see [10, 11]. A performance analysis of the DBU algorithm is given in [11].

The DBU-STAP weights are applied to the bistatic clutter scenario presented in Section 3. Again, the STAP training region is 12 km. The DBU-STAP performance is compared to a constant STAP weight with Doppler warping, as well as the ideal performance for the case in which the bistatic clutter covariance matrix is known. The results are shown in Fig. 8. The DBU-STAP performance almost perfectly matches the ideal STAP performance had the covariance matrix been known. Thus, the first-order approximation in the DBU algorithm holds over this 12 km training region for the given scenario. Next, we look to extend the training region to see over how large a region the DBU-STAP weight approximation is valid. These results are shown in Fig. 9 for training regions of 20 km, 60 km, and 90 km which are also compared to the ideal STAP performance. For training regions up to 60 km, the DBU-STAP performance is very close to ideal though the width of the SINR loss notch grows as the training region is increased due to the first-order approximation of the DBU-STAP weights. Once the training region is extended to 90 km, however, a significant degradation is seen in the form of an additional notch in the SINR loss. Although all of these results are very much geometry dependent, the notion of a range-varying STAP weight shows significant promise and for the scenario considered here provides a significant performance gain.

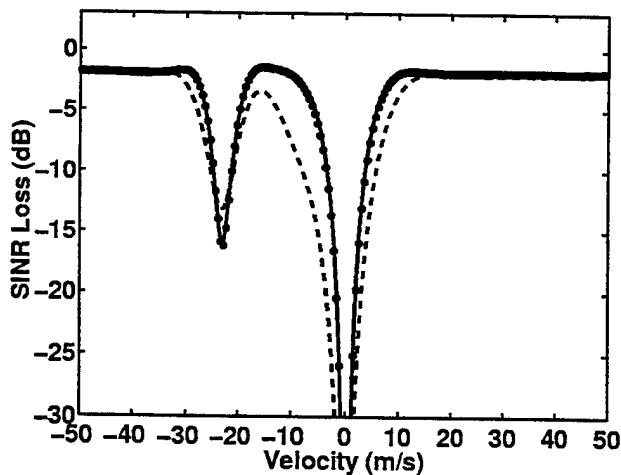


Figure 8: Bistatic STAP performance in terms of SINR loss vs. target velocity for scenario in Fig. 5 using a 12 km training interval comparing derivative-based updating (dots) to Doppler warping (dashed), and the ideal performance (solid).

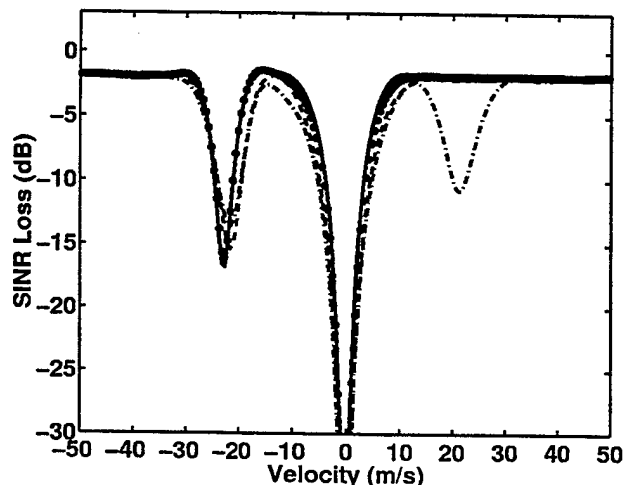


Figure 9: Bistatic STAP performance of derivative-based updating as a function of range training interval size in terms of SINR loss vs. target velocity. The STAP training intervals used are 20 km (dots), 60 km (dashed) and 90 km (dash-dot). Performance is compared to ideal STAP (solid).

5. SUMMARY

The mitigation of bistatic clutter presents a new and challenging problem to the STAP community. The angle/Doppler relationship of bistatic clutter can be very complex and non-stationary in range for an airborne transmitter. This complex relationship arises from the fact that the transmitter introduces a second source of Doppler that is independent of the receiver platform from which the array cone angles are measured. In the absence of transmitter motion, e.g., a ground-based transmitter, successful mitigation of bistatic clutter can be accomplished using traditional STAP approaches developed for monostatic radar. For a moving transmitter, however, bistatic STAP must be able to cope with the rapid variation in range of clutter. Doppler warping, though it improved STAP performance, cannot restore ideal performance. Derivative-based updating shows promise in terms of achieving near ideal performance over a larger range extent at the expense of increasing the adaptive degrees of freedom by a factor of two.

6. REFERENCES

- [1] J. Ward, *Space-Time Adaptive Processing for Airborne Radar*, MIT Lincoln Laboratory Technical Report, TR-1015, 1994.
- [2] J. Ward, "Space-time adaptive processing for airborne radar," *Proc. of IEEE Int. Conf. on Acoustics, Speech, and Signal Processing*, 1995, pp. 2809-2812.
- [3] R. Klemm, *Space-Time Adaptive Processing*, IEE, London, England, 1999.
- [4] R. L. Fante, "Ground and airborne target detection with bistatic adaptive space-based radar," *Proc. IEEE Radar Conference*, 1999, pp. 7-11.
- [5] R. Klemm, "Prospectives in STAP Research," to appear in *Proc. of IEEE Sensor Array and Multichannel Signal Processing Workshop*, 2000.
- [6] B. Himed, J. H. Michels, and Y. Zhang, "STAP performance for bistatic phased array radar applications," to appear in *Proc. IEEE Southeastern Sym. on System Theory*, 2000.
- [7] N. J. Willis, *Bistatic Radar*, 2nd edition, Artech House, Boston, MA.
- [8] G. K. Borsari "Mitigating effects on STAP processing caused by an inclined array," *Proc. IEEE Radar Conference*, 1998, pp. 135-40.
- [9] G. W. Titi and D. F. Marshall, "The ARPA/Navy Mountaintop Program: adaptive signal processing for airborne early warning radar," *Proc. of IEEE Int. Conf. on Acoustics, Speech, and Signal Processing*, 1996, pp.1165-1168.
- [10] S. D. Hayward, "Adaptive beamforming for rapidly moving arrays," *Proc. Int. Conf. on Radar*, 1996, pp. 546-549.
- [11] M. A. Zatman, "The properties of adaptive algorithms with time varying weights", to appear in *Proc. of IEEE Sensor Array and Multichannel Signal Processing Workshop*, 2000.

PARAMETRIC CLUTTER REJECTION FOR SPACE-TIME ADAPTIVE PROCESSING

A. Lee Swindlehurst and Peter Parker

Dept. of Electrical & Computer Engineering
Brigham Young University
Provo, UT 84602
{swindle, parkerp}@ee.byu.edu

ABSTRACT

Practical STAP implementations rely on reduced-dimension processing, using techniques such as principle components or partially adaptive filters. The dimension reduction not only decreases the computational load, it also reduces the sample support required for estimating the interference statistics. This results because the clutter covariance is implicitly assumed to possess a certain (non-parametric) structure. In this paper, we demonstrate how imposing a parametric structure on the clutter and jamming can lead to a further reduction in both computation and secondary sample support. Our approach, referred to as Space-Time AutoRegressive (STAR) filtering, is applied in two steps: First, a structured subspace orthogonal to that in which the clutter and interference reside is found; Second, a detector matched to this subspace is used to determine whether or not a target is present. Using a realistic simulated data set for circular array STAP, we demonstrate that this approach achieves significantly lower SINR loss with a computational load that is less than that required by the reduced-dimension PRI-staggered STAP method. The STAR algorithm also yields excellent performance with very small secondary sample support, a feature that is particularly attractive for circular array STAP where the clutter statistics are range dependent.

1. INTRODUCTION

The use of fully adaptive space-time adaptive processing (STAP) [1, 2] is prohibitive in most radar applications due to the computational cost and the large number of secondary data vectors required to accumulate the second-order statistics of the clutter and interference. The latter is particularly a problem when using a circular array, since the clutter statistics are non-stationary at close range [3]. One approach to mitigating this problem is to use so-called "partially adaptive" STAP filters [1, 2], which, for example, employ beamspace techniques or pre-Doppler filtering to reduce the number of degrees of freedom available for adaptation. The dimension reduction serves not only to reduce computation, it also reduces the sample support required for estimating the clutter and interference statistics.

In this paper, we present an alternative approach to clutter and interference suppression that relies on the use of vector autoregressive (AR) modeling. The use of vector AR models for radar clutter has been previously proposed in [4]. These models have been

employed in developing generalized likelihood ratio and matched-filter based detectors for both Gaussian and non-Gaussian interference [5, 6, 7, 8]. In the algorithm presented here, we use a vector AR model estimated from the secondary data to construct a structured subspace that is as orthogonal to the clutter and interference subspace as possible. Instead of using the inverse of the clutter covariance matrix to whiten the primary data vector as in the fully adaptive STAP method, we project out the estimated interference subspace prior to beamforming and Doppler filtering. This approach, which we refer to as Space-Time AutoRegressive (STAR) filtering, can be thought of as an adaptive implementation of the matched subspace detector described in [9]. As we will see, there are two important advantages to the STAR method:

1. The computation involved in calculating the vector AR model, forming the projection matrix, and applying the projection to the primary data vector is significantly less than the corresponding steps not only for fully adaptive STAP, but for the partially adaptive methods as well.
2. The amount of secondary data required to reliably estimate the STAR model is considerably less than that required for estimating the covariance matrices used in either the fully adaptive or partially adaptive algorithms. This not only helps reduce computation, but it reduces the secondary data interval over which we require stationarity.

The advantages listed above will be illustrated by means of a synthetic data set generated by MIT Lincoln Laboratories that simulates the output of a 20 element antenna array whose elements lie along a circular arc of 120° [3]. Circular array geometries are currently being considered for use in airborne surveillance radars since they can electronically scan the full 360° surroundings in much less time than a mechanically steered array. An experimental circular array is currently being developed by Raytheon as part of the UHF Electronically Scanned Array (UESA) program sponsored by the Office of Naval Research. The array is composed of 60 directional elements evenly spaced around the edge of the circular aperture, but nominally only 20 are used at any given time for transmit and receive. The use of this type of array geometry is especially revealing for the topic of this paper, since the locus of the clutter ridge in the cone angle/Doppler space is non-stationary, especially at close range. This effect tends to increase the rank of the clutter covariance matrix, which in turn means that more secondary data vectors are required to estimate the clutter statistics. The non-stationarity of the clutter makes this very difficult to achieve. The ability of the STAR method to obtain a solution with minimal secondary sample

This work was supported by the Office of Naval Research under contract N00014-99-1-0692.

support makes it extremely attractive for the circular array STAP problem. Similar improvements in performance are also seen in the more easily handled case involving a linear array.

In the next section, we present the standard data model assumed for STAP problems and develop the notation we will use throughout the paper. The STAR filtering technique is outlined in Section 3, along with a detailed computational count and a description of how the model order is selected. The results of a series of numerical experiments comparing the STAR approach to standard STAP algorithms are presented in Section 4.

2. MATHEMATICAL MODEL

A target present in a particular range bin during some CPI (coherent processing interval) may be modeled as producing the following baseband vector signal (after pulse compression and demodulation) [1]:

$$\mathbf{x}(t) = b\mathbf{a}(\theta)e^{j\omega t} + \mathbf{n}(t) \in \mathcal{C}^m, \quad t = 1, \dots, N, \quad (1)$$

where b is the complex amplitude of the signal, ω is the Doppler shift due to the relative motion between the array platform and the target, $\mathbf{a}(\theta)$ is the response of the array to a unit amplitude plane wave arriving from direction θ (azimuth and elevation angles), and $\mathbf{n}(t)$ contains contributions from clutter, jamming, and thermal noise. In (1), we are assuming an array of m elements and a total of N transmitted pulses.

If we stack the N array outputs into a single $mN \times 1$ space-time snapshot, we may re-write (1) as

$$\mathbf{x} \stackrel{\text{def}}{=} \begin{bmatrix} \mathbf{x}(1) \\ \vdots \\ \mathbf{x}(N) \end{bmatrix} = b\mathbf{v}(\theta, \omega) + \boldsymbol{\eta}, \quad (2)$$

where

$$\begin{aligned} \mathbf{s}(\theta, \omega) &= \mathbf{v}(\omega) \otimes \mathbf{a}(\theta) \\ \mathbf{v}(\omega) &= [1 \ e^{j\omega} \ \dots \ e^{j(N-1)\omega}]^T \end{aligned}$$

and \otimes represents the Kronecker product. The vector $\boldsymbol{\eta}$ contains the stacked vector samples of the clutter and interference, and has an unknown covariance matrix denoted by

$$\mathcal{E}\{\boldsymbol{\eta}\boldsymbol{\eta}^*\} = \mathbf{R}.$$

The clutter is neither temporally nor spatially white; in fact, the rank of \mathbf{R} is typically much less than mN . According to Brennan's rule [10], the rank (ρ) of \mathbf{R} for a uniform linear array is $m + (N - 1)\beta$, where β is a factor that depends on the speed of the array platform and the pulse repetition frequency (PRF), and is usually between 0.5 and 1.5. No corresponding expression exists for a circular arc array like the one described above, but ρ has been observed to be typically about a factor of two greater than that predicted by Brennan's rule. The rank of \mathbf{R} is important because it determines how many secondary data samples are required to accurately estimate it when it is unknown. According to [11], the number of required samples is on the order of 2ρ to 5ρ .

The term STAP is used to refer to the "adaptive" (i.e., data dependent) calculation of a space-time weight vector or beamformer $\mathbf{w}(\theta, \omega)$ that is applied to \mathbf{x} to create a two-dimensional angle-Doppler spectrum:

$$P(\theta, \omega) = |\mathbf{w}^*(\theta, \omega)\mathbf{x}|^2.$$

In fully adaptive STAP, the weight vector is chosen to maximize the signal-to-interference plus noise ratio (SINR), which yields the well known solution

$$\mathbf{w}_{FA}(\theta, \omega) = \mathbf{R}^{-1}\mathbf{s}(\theta, \omega). \quad (3)$$

Since \mathbf{R} is not known *a priori*, it is replaced by a sample average $\hat{\mathbf{R}}$:

$$\hat{\mathbf{R}} = \sum_{k=1}^P \mathbf{x}_k \mathbf{x}_k^*, \quad (4)$$

where \mathbf{x}_k is a secondary data vector from a different (target-free) range bin. As mentioned above, $P > 2\rho$ is desired, but a larger value for P means that the clutter must be considered to be stationary over a longer interval.

The size and ill-conditioning of \mathbf{R} (or $\hat{\mathbf{R}}$) make calculation of the inverse in (3) prohibitive, and thus the fully adaptive method is rarely implemented directly. Diagonal loading or principle components are often used to eliminate numerical problems in calculating the optimal weight vector. Also popular are partially adaptive STAP methods that use pre-processing to reduce the dimension of the data. The dimension reduction not only improves the numerical conditioning, but it reduces the required secondary sample support and decreases the computational load as well. In essence, these techniques impose certain structural constraints on \mathbf{R} to reduce the number of degrees of freedom that must be estimated from the data to perform the required space-time filtering. In the next section, we present an alternative way to impose structure on the subspace spanned by the clutter and interference. We will see that the proposed technique enjoys significant advantages over standard STAP algorithms.

3. SPACE-TIME AUTOREGRESSIVE FILTERING

In the approach presented here, we postulate the existence of a set of L matrices $\mathbf{H}_0, \mathbf{H}_1, \dots, \mathbf{H}_{L-1}$ of dimension $m' \times m$ that satisfy

$$\sum_{i=0}^{L-1} \mathbf{H}_i \mathbf{n}(t+i) = 0, \quad t = 1, \dots, N-L+1, \quad (5)$$

for the interference and clutter in the primary range bin¹. We may also write (5) in the following two different ways:

$$\underbrace{[\mathbf{H}_0 \ \dots \ \mathbf{H}_{L-1}]}_{\mathbf{H}^*} \underbrace{\begin{bmatrix} \mathbf{n}(1) & \dots & \mathbf{n}(N-L+1) \\ \vdots & & \vdots \\ \mathbf{n}(L) & \dots & \mathbf{n}(N) \end{bmatrix}}_{\mathbf{N}} = 0 \quad (6)$$

or

$$\mathbf{H}^* \boldsymbol{\eta} = 0, \quad (7)$$

where

$$\mathbf{H}^* = \begin{bmatrix} \mathbf{H}_0 & \dots & \mathbf{H}_{L-1} & & \\ & \mathbf{H}_0 & \dots & \mathbf{H}_{L-1} & \\ & & \ddots & \ddots & \\ & & & \mathbf{H}_0 & \dots & \mathbf{H}_{L-1} \end{bmatrix}. \quad (8)$$

¹Note that we do not require one of the matrix taps to be the identity since the clutter is not spatially white, and we have observed much better performance without this constraint.

We assume that equations (6) and (7) also hold for the secondary data as well:

$$\mathbf{H}^* \mathbf{N}_k = 0 \quad (9)$$

$$\mathcal{H}^* \boldsymbol{\eta}_k = 0, \quad (10)$$

for $k = 1, \dots, P$, where \mathbf{N}_k is formed from $\boldsymbol{\eta}_k$ as in (6).

The matrix \mathcal{H} is $mN \times m'(N - L + 1)$. If (5) holds and m' and L are chosen so that $m'(N - L + 1)$ is large enough, the columns of \mathcal{H} form a basis for the space orthogonal to the clutter and interference subspace. This suggests the use of the following space-time filter as an alternative to (3):

$$\mathbf{w}_{AR}(\theta, \omega) = \mathbf{P}_{\mathcal{H}} \mathbf{s}(\theta, \omega), \quad (11)$$

where $\mathbf{P}_{\mathcal{H}}$ is the projection onto the columns of \mathcal{H} :

$$\mathbf{P}_{\mathcal{H}} = \mathcal{H}(\mathcal{H}^* \mathcal{H})^{-1} \mathcal{H}^*. \quad (12)$$

We refer to the implementation of STAP with the weight vector of (11) as Space-Time AutoRegressive (STAR) filtering. The STAR filter weights are still "adaptive" in the sense that \mathcal{H} must be estimated from the secondary data prior to computation of \mathbf{w}_{AR} . A procedure for calculating \mathcal{H} is outlined below.

3.1. Algorithm Implementation

The $mL \times m'$ matrix of coefficients \mathbf{H} completely specifies \mathcal{H} . If (5) holds, then using (10) we see that \mathbf{H} could be found as the left nullspace of the $mL \times P(N - L + 1)$ matrix

$$\mathcal{N} = [\mathbf{N}_1 \dots \mathbf{N}_P], \quad (13)$$

provided that

$$P \geq \frac{mL}{N - L + 1}.$$

Since (5) will not hold exactly in practice (due, for example, to the presence of thermal white noise), \mathcal{N} is generically full rank. Consequently, we choose \mathbf{H} as the m' left singular vectors of \mathcal{N} with the smallest singular values. The computation involved in this step is $O(m^2 L^2 P(N - L + 1))$ flops.

Once \mathbf{H} is found, we proceed to the calculation of $\mathbf{P}_{\mathcal{H}} \boldsymbol{\chi}$, which is used in forming the 2-D STAR spectrum:

$$P_{AR}(\theta, \omega) = |\mathbf{s}^*(\theta, \omega) \mathbf{P}_{\mathcal{H}} \boldsymbol{\chi}|^2. \quad (14)$$

A statistic of the form (14) is referred to as a matched subspace detector, following the development of [9]. Implementation of (14) is considerably simplified by the block Toeplitz structure of \mathcal{H} . In particular, the inverse $(\mathcal{H} \mathcal{H}^*)^{-1}$ required for $\mathbf{P}_{\mathcal{H}}$ is much less costly to implement than its dimension would suggest due to the fact that, for typical values of m' and L , $\mathcal{H} \mathcal{H}^*$ is a sparse banded block Toeplitz matrix. Taking this and the structure involved in the matrix product $\mathcal{H} \boldsymbol{\chi}$ into account, calculation of $\mathbf{P}_{\mathcal{H}} \boldsymbol{\chi}$ requires $O(m' m^2 L^2 (N - L + 1))$ flops. With $\mathbf{P}_{\mathcal{H}} \boldsymbol{\chi}$ in hand, the calculation of $P_{AR}(\theta, \omega)$ has negligible cost compared with the first two steps, especially since the FFT can be used for at least the ω dimension (and the θ dimension as well if the array is uniform and linear).

For the following typical parameter values encountered when implementing the algorithm for the circular array data: $m = 20$, $N = 18$, $L = 3$, and $m' = 15$, the computational order of the STAR filtering algorithm is

$$\text{STAR} = O(5.8 \times 10^4 N_s) + O(8.6 \times 10^5).$$

Compare this with the cost of fully adaptive STAP (using a principle components implementation):

$$\begin{aligned} \text{Fully Adaptive} &= O(m^2 N^2 N_s) + O(\rho m^2 N^2) \\ &= O(1.3 \times 10^5 N_s) + O(9.7 \times 10^6), \end{aligned}$$

where we have assumed a nominal clutter rank of $\rho = 75$ (corresponding to roughly twice Brennan's rule). As an example of a partially adaptive method, the PRI-staggered post-Doppler STAP algorithm [10] has a computational cost of

$$\begin{aligned} \text{PRI Staggered} &= O(m^2 N^2 K^2 N_s) + O(\rho_K m^2 K^2 N^2) \\ &= O(6.5 \times 10^4 N_s) + O(2.9 \times 10^6), \end{aligned}$$

where K is the number of sub-CPIs (assumed to be three for the numerical values) and ρ_K is the rank of the sub-CPI covariance matrix (assumed to be nominally equal to 45). When all algorithms use the same number of secondary vectors, the computational savings of the STAR approach over the other algorithms is clear. But what is remarkable is that, to achieve the same level of performance as fully adaptive or PRI-staggered STAP, the STAR algorithm requires a value of N_s that is several times smaller than for the other algorithms.

3.2. Model Order Selection

The biggest difficulty associated with the use of AR methods for this (or any other) application is the choice of the model order. Here the problem is complicated by the fact that there are two parameters to be chosen: m' and L . A standard prediction error approach would be to calculate the residual

$$\epsilon(m', L) = \|\mathbf{H}^* \mathcal{N}\|^2 \quad (15)$$

for values of m' and L on a grid, add a penalty term to account for the number of free parameters in the model (as in Akaike's criterion [12] or the minimum description length (MDL) approach [13]), and then minimize the resulting expression. Such an approach is taken in [14] for 2-D AR models. However, the number of required prediction error evaluations is quite large for this approach, and a simpler solution is desirable. To find such a solution, we observe the following:

1. We expect L to be fairly small, less than five in most applications.
2. Our experience with simulated data suggests that performance does not vary dramatically with small changes in m' .
3. If (5) holds for some L , then the proper choice for m' would be the value that matches the rank of \mathcal{H} with that of \mathbf{R} :

$$\text{rank}(\mathbf{R}) = \rho = \text{rank}(\mathcal{H}) = mN - m'(N - L + 1). \quad (16)$$

4. Assuming $m = 20$, $N = 18$, and a nominal value of $\rho = 75$ for the UESA circular array scenario, solving (16) for values of L between 2-5 yields m' between 17-22.

Based on the above, we propose fixing m' at a value in the range suggested by the predicted rank of \mathbf{R} and typical values of L , and then using a 1-D prediction-error based model-order selection scheme to choose L . For the results presented in the next section, we used the MDL-like criterion below:

$$\hat{L} = \arg \min_q \epsilon(m', q) + \log_2 \left(\frac{m' m q - m'(m' + 1)/2}{m N P} \right), \quad (17)$$

where the penalty term takes into account the fact that the columns of \mathbf{H} are constrained to be orthonormal by the STAR filter computation. Results are given below for both $m' = 15$ and $m' = 20$ to validate our assumptions. We note that an alternative method based on "prediction error power" has recently been proposed for vector AR models in [15].

4. NUMERICAL RESULTS

Since the prototype UESA circular array has yet to be field tested, a data package has been created by MIT Lincoln Laboratories to simulate the output of the array due to clutter in a standard operating scenario. Instead of 60 elements, the simulated data assumes an array of 54 elements uniformly spaced around a circle of 5.93m diameter. Only $m = 20$ of the elements are assumed to be used for transmit and receive during one CPI. The antenna elements are assumed to have a cosine-shaped response with a -30 dB back-lobe for both the azimuth and elevation dimensions. The airborne platform is moving with a velocity of 100 m/s above a 4/3 earth model at an altitude of 9000 m. The operating frequency of the radar is taken to be 435 Mhz, the radar bandwidth and sampling frequency are 3.75 Mhz, the pulse-repetition frequency is 300 Hz, and $N = 18$ pulses are assumed to be transmitted during one CPI. Data are generated for 9325 range gates between 20-400 km with a clutter-to-white-noise power ratio of 45 dB. A jammer signal can be injected at range gate k by adding a term of the form

$$b_j \mathbf{v}_k \otimes \mathbf{a}(\theta_j),$$

where b_j and θ_j are the amplitude and direction of arrival of the jammer, respectively, and \mathbf{v}_k is a unit variance Gaussian noise sequence that is white in both slow-time (the elements of \mathbf{v}_k are uncorrelated) and fast-time (\mathbf{v}_k and \mathbf{v}_i are uncorrelated when $i \neq k$). When present, the jammer-to-clutter power ratio is assumed to be 10 dB. When secondary data are used to estimate the clutter covariance or STAR filter parameters, equal amounts of data from range gates on either side of the target range gate are used.

The true clutter covariance matrix used to generate the data is known for 20 of the 9325 range bins, and thus the maximum achievable SINR can be calculated at these ranges. Figure 1 shows a sample plot of SINR achieved using $N_s = 30$ secondary data vectors as training by the STAR, fully adaptive, and PRI-staggered partially adaptive algorithms compared with the best possible SINR for a target at 50 km. The fully adaptive algorithm was implemented with diagonal loading in order to compute the inverse of $\hat{\mathbf{R}}$, and the PRI-staggered algorithm was implemented with $K = 3$ sub-CPIs. Both the diagonal loading factor and K were chosen to yield the best performance for these two algorithms. For the STAR method, m' was set to 15 and (17) was used to choose a value of $L = 4$. The STAR algorithm shows substantially better performance than the other two algorithms, up to 10 dB better than the PRI-staggered method, and 25 dB better than the fully adaptive implementation. Of course, this is primarily due to the small secondary sample size – both of the other algorithms can achieve a higher level of performance, but with nearly an order of magnitude more secondary data. More examples illustrating this point will be shown below. In subsequent plots, we will show "average" SINR loss for each algorithm, which is defined to be the area between the algorithm's SINR curve and that achievable assuming \mathbf{R} is perfectly known. A graphical depiction is given in Figure 2.

Figures 3 and 4 show the average SINR loss for the STAR algorithm as a function of L at two different ranges and for various

values of m' . No jammer is present in this data. These figures show that, as long as m' is not chosen to be too small (less than 15), the performance of the algorithm at the best value of L is not a strong function of m' . The best SINR loss for each m' is within 1-2 dB of the others. Note that larger model orders ($L = 4 - 6$) are needed for the short range case compared with those at the longer range ($L = 2 - 3$). At short ranges, the STAR filter attempts to compensate for the non-stationary clutter by increasing the model order.

Figures 5 and 6 show algorithm performance when a jammer is present as a function of range, assuming $N_s = 30$ and $N_s = 100$, respectively. The STAR algorithm is implemented with $m' = 15$ and $m' = 20$, and both give roughly identical SINR loss. Performance improves with range as the clutter becomes more and more stationary, particularly for the fully and partially adaptive algorithms. Still, the performance of the STAR algorithm is clearly superior at nearly all ranges. The slight degradation in performance for the STAR algorithm between 100-150 km is due to the model-order selection algorithm in (17) switching too early from $L = 4$ to $L = 3$. Figure 7 shows the performance of the algorithms versus N_s at 300 km with a jammer present. The STAR method is able to reach its best SINR with only 10 secondary samples, while the PRI-staggered algorithm requires about $N_s = 30$ for 2 dB worse performance, and the fully adaptive method needs 100 samples for a similar SINR loss. Figure 8 shows similar results for 50 km without a jammer present.

5. CONCLUSIONS

We have presented a new technique for space-time adaptive processing (STAP) based on vector autoregressive (AR) modeling. The algorithm uses the AR model to generate a structured subspace that is as orthogonal as possible to the clutter, and then uses this subspace to project out the clutter prior to space-time filtering. The parametric structure imposed by the algorithm results in a significant computational savings over both fully adaptive and partially STAP algorithms. It is able to provide excellent performance with minimal secondary sample support, an advantage that makes it ideally suited for applications involving non-stationary clutter (e.g., as encountered in the circular array STAP problem). Using synthetic circular array data provided by MIT Lincoln Laboratories, we have shown numerous experimental results that demonstrate the superior performance of the STAR approach.

6. REFERENCES

- [1] J. Ward, "Space-Time Adaptive Processing for Airborne Radar", Technical Report TR-1015, MIT Lincoln Labs, Dec. 1994.
- [2] R. Klemm, editor, *Space-Time Adaptive Processing: Principles and Applications*, The Institution of Electrical Engineers, London, UK, 1998.
- [3] M. Zatman, "Circular Array STAP", In *Proc. 7th Annual Workshop on Adaptive Sensor Array Processing*, MIT Lincoln Labs, March 1999.
- [4] J. Román, D. Davis, and J. Michels, "Multichannel Parametric Models for Airborne Phased Array Clutter", In *Proc. IEEE Radar Conf.*, volume 1, pages 72-77, Syracuse, NY, 1997.

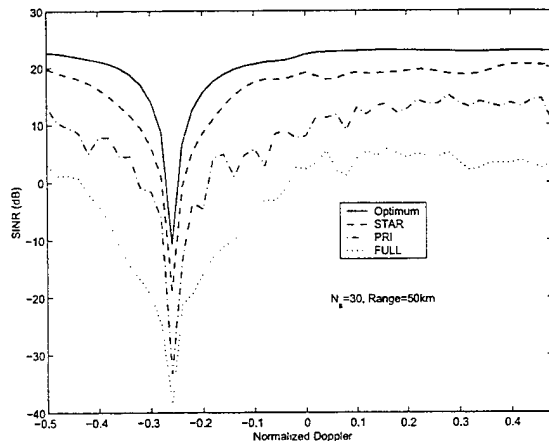


Figure 1: SINR curves compared with optimum for $N_s = 30$ at 50 km, no jammer present

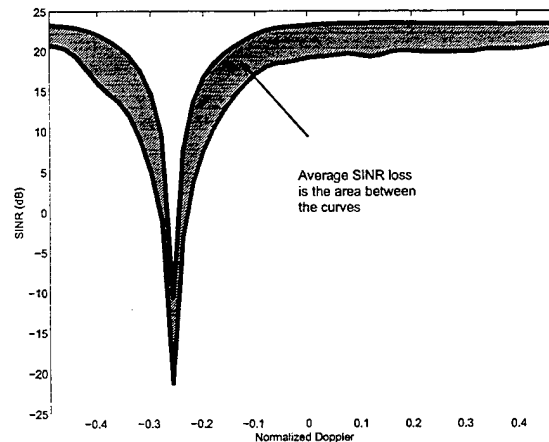


Figure 2: Definition of average SINR loss for a particular algorithm.

- [5] M. Rangaswamy, J. Michels, and D. Weiner, "Multichannel Detection for Correlated Non-Gaussian Random Processes Based on Innovations", *IEEE Trans. on Sig. Proc.*, 43(8):1915–1922, August 1995.
- [6] J. Michels, P. Varshney, and D. Weiner, "Multichannel Signal Detection Involving Temporal and Cross-Channel Correlation", *IEEE Trans. on Aero. and Elec. Sys.*, AES-31(3):866–879, July 1995.
- [7] M. Rangaswamy and J. Michels, "A Parametric Multichannel Detection Algorithm for Correlated Non-Gaussian Random Processes", In *Proc. IEEE Radar Conf.*, Syracuse, NY, 1997.
- [8] J. Michels, T. Tsao, B. Himed, and M. Rangaswamy, "Space-Time Adaptive Processing (STAP) in Airborne Radar Applications", In *Proc. IASTED Int'l Conf. on Sig. Proc. and Commun.*, Canary Islands, Spain, 1998.
- [9] L. Scharf and B. Friedlander, "Matched Subspace Detectors", *IEEE Trans. on Sig. Proc.*, 42(8):2146–2157, August 1994.
- [10] L. Brennan and F. Staudaher, "Subclutter Visibility Demonstration", Technical Report RL-TR-92-21, Adaptive Sensors, Inc., 1992.
- [11] I. S. Reed, J. D. Mallett, and L. E. Brennan, "Rapid Convergence Rate in Adaptive Arrays", *IEEE Trans. on Aero. and Elec. Sys.*, AES-10:853–862, Nov. 1974.
- [12] H. Akaike, "Fitting Autoregressive Models for Prediction", *Ann. Inst. Stat. Math.*, 21:243–347, 1969.
- [13] J. Rissanen, "Modeling by Shortest Data Description", *Automatica*, 14:465–471, 1978.
- [14] B. Aksasse and L. Radouane, "Two-Dimensional Autoregressive (2-D AR) Model Order Estimation", *IEEE Trans. on Sig. Proc.*, 47(7):2072–2077, July 1999.
- [15] J. Castro and J. LeBlanc, "Model Order Selection for Multidimensional Innovations Based Detection in Airborne Radar", In *Proc. IEEE Radar Conf.*, 1998.

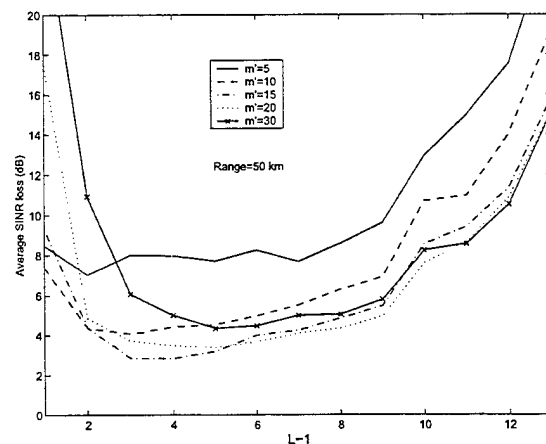


Figure 3: STAR performance as a function of L for various m' at 50 km, no jammer present.

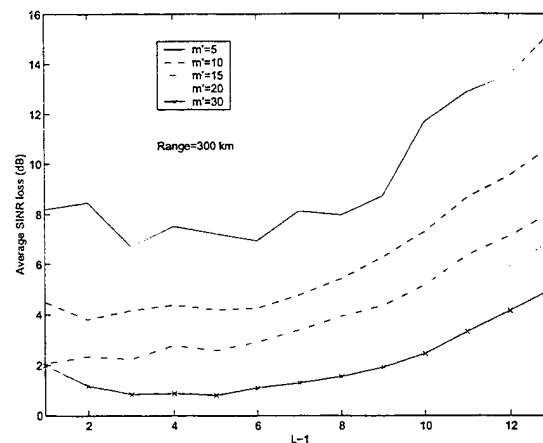


Figure 4: STAR performance as a function of L for various m' at 300 km, no jammer present

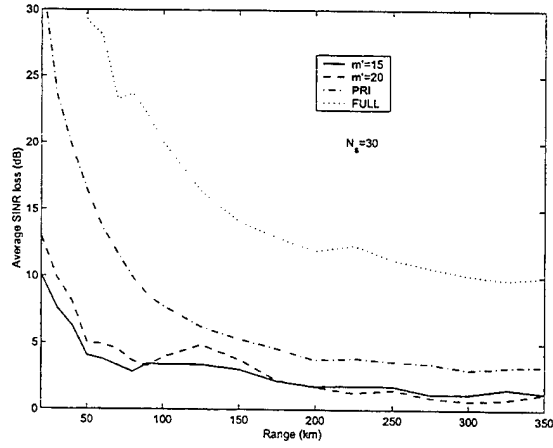


Figure 5: SINR loss as a function of range for $N_s = 30$ with jammer present.

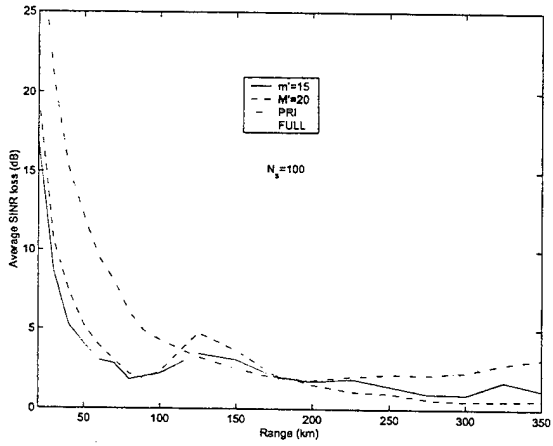


Figure 6: SINR loss as a function of range for $N_s = 100$ with jammer present.

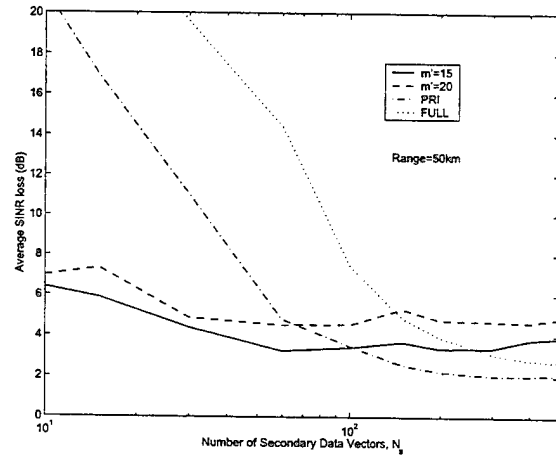


Figure 8: SINR loss as a function of N_s at 50 km, no jammer present

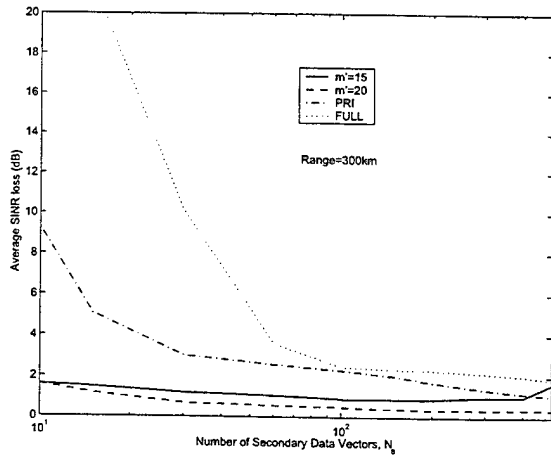


Figure 7: SINR loss as a function of N_s at 300 km with jammer present.

Multistage Adaptation for Large Digital Arrays

Daniel J. Rabideau

MIT Lincoln Laboratory, 244 Wood Street, Lexington, MA 02420-9108

Abstract

This work is concerned with efficient techniques for adaptive interference cancellation, and their application to very large digital arrays. Such arrays provide many Degrees of Freedom (DOFs) that can be used for filtering. However, the processing hardware required to fully utilize these DOFs (i.e., in a simultaneous, data-adaptive fashion) is prohibitive. To address this problem, we suggest two adaptive beamforming frameworks: feed-forward multistage adaptation, and closed-loop multistage adaptation. We demonstrate the capabilities of these new signal processing architectures. In typical applications, multistage adaptive beamforming is shown to potentially result in one of the following desirable results: (1) a large reduction in both hardware and processing for a given performance level. (2) a large improvement in interference rejection for a given number of instantaneously adaptive DOFs.

1. Introduction

As radar enters the new millennium, requirements on dynamic range and system sensitivity are surpassing the abilities of conventional active array technologies. Fortunately for us, extraordinary advances are being made in the areas of communications, computers and networks. By exploiting these technologies through increasing levels of array digitization, it should be possible to meet forecasted requirements.

Of course, increasing levels of array digitization will introduce fundamental shifts in the way we look at adaptive arrays. For example, "Degrees of Freedom" (DOFs) will be abundant, but how will we tap into them? The processing and hardware required to fully utilize these DOFs (i.e., in a simultaneous, data adaptive fashion) is prohibitive.

To address this problem, we decompose the adaptive DOFs into multiple stages. Two adaptive beamforming (ABF) architectures are proposed: feed-forward multistage ABF, and closed-loop multistage ABF. After briefly summarizing the forces that are driving us to digital array technology, we will describe these architectures and evaluate their performance.

2. Digital vs. Analog Array Technology

In the author's opinion, there are several compelling reasons for why digital array technology (Figure 1b) will eventually supplant the competing active analog array technology (Figure 1a) that is so prevalent today.

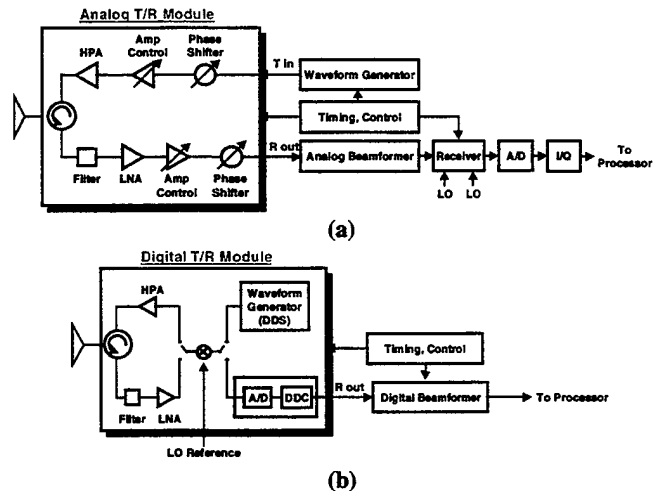


Figure 1. Analog and digital array technologies

First, consider the distribution of signals. Analog arrays distribute signals via lossy methods. Furthermore, good performance necessitates that the signal paths be carefully matched. Digital arrays, on the other hand, distribute signals using more robust digital methods. On transmit, digital control words command each module to create its own piece of the transmitted waveform (a process known as direct digital synthesis, DDS). On receive, signals are sampled within each module, followed by digital down conversion (DDC). In many cases we may choose digital components (i.e., DDS, DDC, A/D, etc.) that are also used in commercial wireless communications systems, resulting in low costs due to both competition and high volume manufacturing.

Next, consider dynamic range. To cancel interference down to the noise level, the receiver's dynamic range must be at least as great as the dynamic range of the interference. This figure can be quite high, for example, in littoral clutter environments. In an active analog array, the receiver device that typically limits the achievable dynamic range is the analog to digital converter (A/D). The dynamic range of current A/D converter technology, however, is typically 15 to 20 dB below the requirement for littoral clutter. Moreover, A/D converter technology is improving at a very slow rate. Fortunately, by moving the A/D into the module, digital arrays can increase their dynamic range through array integration (i.e., beamforming).

Finally, consider the beamformer itself. The beamformer creates a small number of beams that are subsequently combined by the adaptive processor. Flexible beam selection is a critical factor in determining array performance in an interference rich environment. Analog beamforming methods, however, are not easily adjusted to accommodate changing interference

This work was sponsored by U.S. Navy under Air Force Contract F19628-95-C-0002. Opinions, interpretations, conclusions and recommendations are those of the author and are not necessarily endorsed by the United States Air Force.

environments and (in the case of multifunction radar) operating modes. Digital beamforming offers much more flexibility.

3. Beamforming for Large Arrays

Consider an array consisting of N digitized channels. Let \mathbf{x}_k be the $N \times 1$ vector of samples present at time instant k . This snapshot contains energy from J nonstationary interference sources (hereafter referred to as jammers) and noise. Our task is to build a filter capable of suppressing this interference while receiving signals from direction Θ .

There are two conventional approaches to solving this problem. The first approach, "fully adaptive beamforming," simultaneously adapts on all N DOFs. This approach is unattractive, however, because of the large quantity of resources required (e.g., processing complexity, training data, etc.). Instead, we seek a more efficient beamforming technique.

The second conventional approach, "beamspace ABF," involves mapping the N channels into M beams prior to adaptive interference rejection (see Figure 2). When M is much less than N , this yields a substantial reduction in required resources.

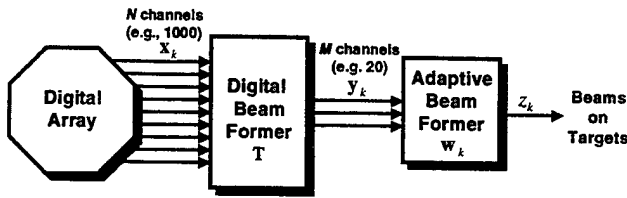


Figure 2. Conventional Beamspace Adaptation

Conceptually, we can think of this mapping as being performed by an $N \times M$ linear transformation matrix, \mathbf{T} (e.g., the columns of \mathbf{T} may define a set of beams, subarrays, and/or sidelobe cancellers). The $M \times 1$ beamspace data vector at the output of this transformation is given by $\mathbf{y}_k = \mathbf{T}^H \mathbf{x}_k$.

The beamspace snapshot, \mathbf{y}_k , contains J jammers that interfere with target reception. An adaptive filter, $\mathbf{z}_k = \mathbf{w}_k^H \mathbf{y}_k$, is used to suppress this interference. In a radar context, the optimal filter for rejecting the interference in \mathbf{y}_k is the Wiener filter:

$$\mathbf{w}_k = \mathbf{R}_k^{-1} (\mathbf{T}^H \mathbf{d}) \quad (1)$$

where $\mathbf{R}_k = E\{\mathbf{y}_k \mathbf{y}_k^H\}$ and \mathbf{d} is a vector containing the array's response to a target signal of interest.

It is known that beamspace ABF gives nearly optimal performance as long as $M > J$ and \mathbf{T} is chosen appropriately. However, if $M \leq J$ we cannot suppress the interference by merely combining elements of \mathbf{y}_k . The apparent implications of this statement is ominous:

1. At most, only $M-1$ jammers can be cancelled. In practice, however, the actual number of jammers will vary with time and are not under our control (to state the obvious). As a result, the real-time processing hardware must be in-place to support the maximum number of jammers anticipated.
2. Proper selection of \mathbf{T} is essential and can be costly.

This paper focuses on creating ABF architectures that address these problems. Before we begin, let us note some relevant prior work relating to item 2. Generally speaking it is known that the best beamspace, \mathbf{T} , contains a set of beams spanning the interference subspace [1]. This implies prior knowledge about the jamming which, in turn, can be gained by open-loop spectral estimation applied to the raw channel data [1,2]. However, these techniques can be costly.

As for item 1, the question of how to reduce the number of instantaneously adaptive DOFs, M , beyond $J+1$ has received considerably less attention. As we shall see, the solution to this problem lies in separating the notions of "adaptive DOFs" and "instantaneously adaptive DOFs".

4. Closed-Loop Multistage Adaptive Processing

This paper describes two new approaches to adaptive beamforming with large digital arrays. The first of these, Closed-Loop Multistage (CLM) processing, is described in this section.

Compared with conventional beamspace adaptation, CLM-ABF amounts to a relatively simple hardware modification combined with a creative combination of spectral estimation, subspace tracking, and beamforming. CLM-ABF is capable of canceling up to $N-1$ jammers using only M instantaneously adaptive DOFs. Each jammer can be moving, stationary, or some combination thereof. This is accomplished at a fraction of the hardware cost of fully adaptive beamforming.

Of course, there is no free lunch. In our case, the "catch" is that we must distinguish between the traditional notion of adaptive DOFs, and something we call "instantaneously adaptive DOFs". Let us explain. Our interference canceller is composed of three core elements, interconnected as shown in Figure 3:

1. A programmable digital transformation device that reduces the number of DOFs by producing a mainbeam (in which desired signals are sought) and a small number of other channels.
2. An adaptive processor that operates only on the outputs of the digital transformation device. It uses these outputs for two purposes: (a) rejection of interference and (b) control processing.
3. A control link to feed filter weights from the adaptive processor back to the digital transformation device.

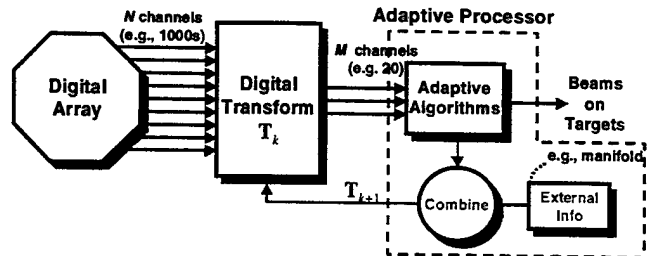


Figure 3. Closed-Loop Multistage ABF

As in conventional beamspace ABF, the digital transformation device simply transforms the N -dimensional channel-space data into M -dimensional beamspace data via $\mathbf{y}_k = \mathbf{T}_k^H \mathbf{x}_k$.

The subsequent adaptive processor operates only on the outputs of this device. It performs two tasks: interference

rejection and control processing. The two tasks are not independent! One can view the combined processor as a single adaptive filter, $\mathbf{z}_k = \tilde{\mathbf{w}}_k^H \mathbf{x}_k$ where the adaptive weights, $\tilde{\mathbf{w}}_k$, are simply factored into two components

$$\tilde{\mathbf{w}}_k = \mathbf{T}_k \mathbf{w}_k. \quad (2)$$

The adaptive processor must choose both components. To accomplish this, it uses the following control rules:

1. Compute weights, \mathbf{w}_k , that have the desired directivity while simultaneously rejecting the interference present in \mathbf{y}_k .
2. Create a transformation \mathbf{T}_{k+1} such that (a) many of the instantaneously adaptive DOFs that were allocated to rejecting interference during the formation of \mathbf{w}_k will be released for other uses when forming $\mathbf{w}_{k+\epsilon}$ (where ϵ is some small integer). (b) nulls on previously acquired jammers are periodically updated.

The first item (illustrated by the upper path in Figure 4) is accomplished by using traditional beamspace ABF techniques, e.g., see [3, sect. IV-VI]. Items 2a and 2b are termed "acquisition" and "updating," respectively (see lower path of Figure 4). An implementation of these functions is described in the following sections.

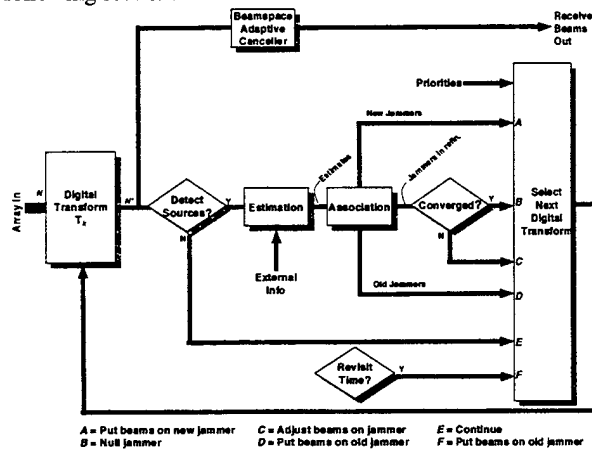


Figure 4. Flow diagram for typical closed-loop multistage adaptive beamformer

4.1 Acquisition

The acquisition of new jammers is performed in three phases: detection, initial estimation, and refinement. Each of these operations is performed using the beamspace data. The beams consist of n' main beams and m' other beams. Together, $M = n' + m'$. The n' main beams integrate target energy with the goal of enhancing detection and estimation. Additionally, each main beam contains nulls in the directions of previously acquired jammers.

The m' other beams are composed of r refinement beams and a auxiliary beams. The auxiliary beams are designed to cover the broad region corresponding to potential interference. The refinement beams are chosen to have directional responses as discussed below (for simplicity, initially assume $r = 0$). In both cases, these beams will have nulls steered toward previously acquired jammer subspaces.

Detection: The purpose of jammer detection is to identify the presence of (1) new jammers or (2) old jammers that, for one reason or another, are inadequately nulled*. Jammer detection has been studied in the literature, and a suitable method can be adapted to our purpose. For example, at time k we first construct a matrix of recent beamspace snapshots, \mathbf{Y}_k . Then, its singular value decomposition is computed, $\mathbf{Y}_k = \mathbf{U}_k \mathbf{S}_k \mathbf{V}_k^H$. Finally, the singular values are compared to a threshold, telling us if jammers are present and how many. A method for determining the threshold is described in [4].

Initial Estimation: After a jammer detection occurs, we form an initial estimate of its subspace. Direct estimation of the jammer subspace from the beamspace data is undesirable, as discussed in [5]. Instead, we need to use external information (i.e., information not contained within the data snapshots produced by transformation \mathbf{T}_k).

A suitable initial estimate can be generated by first performing parameter estimation (using the beamspace data), then substituting these parameters into a model for the array's response (as a function of those parameters). The literature describes many techniques that can be used for the parameter estimation stage†. For example, beamspace MUSIC computes the spectrum:

$$S(\theta) = \frac{1}{\mathbf{s}^H(\theta) \mathbf{U}_N \mathbf{U}_N^H \mathbf{s}(\theta)}$$

where $\mathbf{s}(\theta)$ is an estimate of the beamspace array response to a signal from θ , and \mathbf{U}_N is a matrix containing the left singular vectors of \mathbf{Y}_k corresponding to the $M - J'$ smallest singular values. The J' peaks of $S(\theta)$ are then used to initially estimate the θ 's corresponding to the J' jammers in acquisition.

Once the peaks have been identified, the associated parameters are substituted into a model for the array's response (often called the manifold), resulting in a suitable initial jammer subspace estimate. Due to the extremely small number of DOFs that are used during the parameter estimation stage, the initial subspace estimate is likely to contain errors. It is for this reason that initial estimation is followed by refinement.

Refinement: In the refinement phase, we use previously computed estimates of the jammer subspace to select a new digital transformation, \mathbf{T}_{k+1} . Our objective is to choose \mathbf{T}_{k+1} so that subsequent jammer estimates will have reduced errors. We accomplish this by pointing refinement beams toward the estimated jammer subspaces.

After adjusting \mathbf{T}_{k+1} and forming \mathbf{y}_{k+1} , we then re-estimate the jammer subspace. This new estimate will have smaller errors (e.g., see [6]). The adjusted beamspace also improves cancellation of jamming by the beamspace adaptive canceller (e.g., see [1]).

The refinement procedure is repeated until the jammer subspace converges, at which time a final estimate of the jammer subspace is made. If the array manifold is known to a high

* For example, a jammer may have moved since its subspace was last acquired and used to steer nulls. Alternatively, there may be residual jamming due to errors in prior jammer subspace estimates.

† Relevant techniques which can be easily adapted to our purpose include MUSIC, ESPRIT and Maximum Likelihood estimation.

degree of precision, the final jammer subspace estimate can be made in the same manner as the initial estimate above. When the array manifold is not known to a high degree of precision, the final estimate can be made from the dominant singular vectors of the beamspace data matrix (after transformation back into N dimensional space). See [5] for some details on this procedure.

4.2 Formation of Nulling Transformations

Given a final estimate (at time k) of the jammer subspace $\mathbf{E}_J = [\mathbf{e}_1 \cdots \mathbf{e}_J]$ corresponding to the jammers present at the input of the adaptive processor, the next digital transformation should be modified to null it. This can be accomplished via:

$$\mathbf{T}_{k+1} = \mathbf{P}_k \mathbf{T}_k = \mathbf{P}_k \mathbf{P}_{k-1} \cdots \mathbf{P}_1 \mathbf{T}_1. \quad (3)$$

The matrix \mathbf{P}_k removes the jamming present in \mathbf{y}_k . For example, \mathbf{P}_k may be a projection matrix, $\mathbf{P}_k = \mathbf{I} - \mathbf{E}_J (\mathbf{E}_J^H \mathbf{E}_J)^{-1} \mathbf{E}_J^H$. (Alternately, the square-root conjugate transpose of jammer covariance estimates may be used, see [5]).

4.3 Updating

If the jammer subspace changes after acquisition (as, for example, due to jammer motion), system performance may degrade. Therefore, it is desirable to update the jammer subspace from time to time. This is accomplished by scheduling a future digital transformation, $\mathbf{T}_{k+\tau}$, to pass the jammer(s) (instead of nulling them) and to include beams pointed at the jammer(s). After collecting data with such a transformation, the jammer subspace re-enters the refinement phase as described in Section 4.1.

The revisit time, τ , required for a specific jammer subspace is determined by the shape of the jammer null and the worst-case predicted motion. To lengthen the revisit time, we can intentionally widen the interference notches. This can be done through conventional techniques (e.g., the design of stopband beamformers) or via newer techniques such as the introduction of array troughs [7].

Note that our framework is robust to incorrect choices in τ . If a jammer's subspace changes before its scheduled revisit time, the residual jamming will be cancelled in the subsequent beamspace adaptive canceller (assuming enough DOFs exist). At the same time, this should automatically initiate a new acquisition cycle for the jammer. By comparing the newly estimated jammer subspace to the set of previously acquired subspaces, near matches can be identified as possible jammer motion. When this happens, the relevant (previously acquired) jammer subspace also directly enters the refinement phase.

5. Feed-Forward Multistage Processing

Next we consider a second approach to adaptive beamforming. Feed-forward multistage processing borrows and modifies an idea first exploited by Eilts and Compton [8]. They were faced with analog beamforming technology of limited dynamic range. They showed that a cascade of adaptive processors could be used to enhance dynamic range by adjusting the first stage to null only large signals, and the second stage to null the smaller signals. Later, Liu [9] showed that LCMV adaptive beamformers could, in general, be expressed in a

factored form. At each stage, the adaptive processor is permitted to use only a subset of DOFs. Data dimensionality was maintained throughout the stages. Later, Niezgoda [10] experimented with the idea of updating the filtering stages at different rates.

Our feed-forward multistage processor departs from the others principally in its objective. We wish to minimize implementation cost and training requirements. In doing so, we decompose our beamformer into multiples stages as shown in Figure 5 (for the special case of 2 stages).

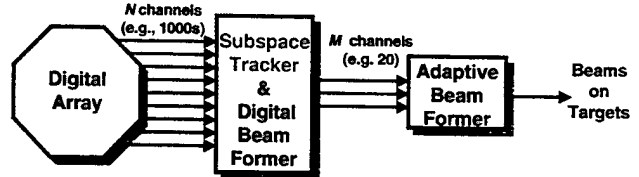


Figure 5. Feed-forward multistage ABF for very large digital arrays

The first stage performs both subspace tracking and digital beamforming. The subspace tracker estimates a basis for the rank-deficient jammer subspace. Traditionally, an SVD of the array data has been used to estimate this jammer subspace. However, the complexity of this factorization is too high to perform often (i.e., to use in a tracking scenario). Instead, an SVD-like factorization can be used. In fact, it was shown that both the jammer spectral energy (e.g., singular values) and an orthonormal basis for the jammer subspace can be tracked with only $O(NJ)$ operations per update [11]. Recently, other similar methods have also attained this desirable objective [12].

Once the subspace has been estimated (via a fast algorithm such as [11]), a set of jammer nulled beams can be created using the method of [11] (or perhaps more simply by projecting a set of prototype beams into the space orthogonal to the estimated jamming). These beams are applied to the element data*. The beamformed outputs are then processed using conventional beamspace ABF.

In this feed-forward architecture, there are several keys to low-cost operation. First, fast subspace tracking combined with digital beamforming requires far less computation than full SMI when $J < N$. Second, multistage adaptation adds robustness against inadequately nulled jamming (at the output of the first stage). This latter fact may be exploited to lower the complexity. For example, we may choose to perform only a small number of subspace updates every CPI. This will degrade the performance of our stage-one beamformer; overall performance, however, might still be maintained by the second stage. Moreover, the total weight computation complexity (for both stages) per CPI is only:

$$O(M^3) + O(NJ\xi) + \zeta P$$

where P is the complexity of creating the stage 1 beams using the most-current estimate of the jammer subspace, ζ is the rate at which these beams are updated, and ξ is the number of rank-1

* Note: Our combined subspace tracking and digital beamforming thus provides a computationally efficient for updating the adaptive weights. Astute readers will observe that there are some other traditional methods for achieving this goal (e.g., based upon updating the QR decomposition of the data matrix, or by exploiting the matrix inversion lemma). For $J < N$, however, these methods have higher complexity (per update) than the method described here.

subspace updates performed every CPI. Note that ξ could be small, e.g., one or even less than one. Likewise, ς may be less than ξ .

6. Evaluation

Here, we illustrate the potential offered by multistage ABF. We employ a 50 element uniform linear array ($N = 50$). The array is digitally transformed into six beams, including a single main beam (steered to 0°) and five other beams ($n' = 1$, $m' = 5$). Initially, the m' other beams had all-pass spatial responses.

We begin with an illustration of the jammer nulling potential of multistage ABF. Sixteen jammers are synthesized. They appear at intervals of 10 (i.e., at $k = 1, 11, 21, \dots$). Their angles are $-80^\circ, -70^\circ, -10^\circ, 10^\circ, \dots, 80^\circ$, in order of appearance. Each has a JNR of 30 dB per element. Figure 6 plots SINR loss over time for each of the multistage ABFs.

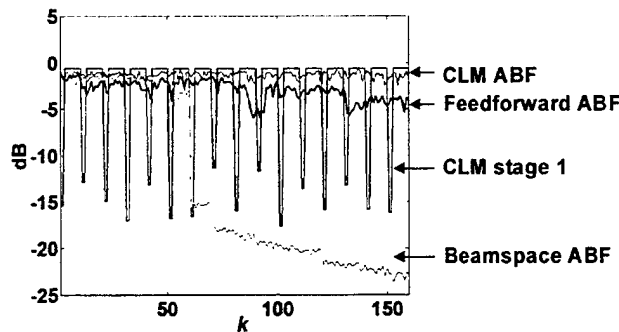


Figure 6. SINR Loss Comparison

First, consider closed-loop multistage ABF. As each new jammer appears, detection and initial estimation occur immediately, with acquisition completing within 2 CPIs. Observe that the output of the first stage (alone) does quite well after the jammers are acquired. During acquisition, however, the sidelobes in the first stage are too high to reject the strong jamming entirely. During this phase, it is the second stage that nulls the new jammers. The combined performance never deviates far from 0 dB.

Next, consider the feed-forward ABF. Here, a single rank-1 subspace update is performed each CPI. This is sufficient to track the very low-rank, slowly nonstationary interference. Performance is generally good throughout the simulation.

To put these multistage ABFs into context, Figure 6 also shows conventional beamspace ABF (i.e., a fixed digital beamformer producing a mainbeam and five omnidirectional auxiliaries, followed by SMI). In this case, the number of jammers exceeds $M - 1$ at $k = 61$. Henceforth, the conventional processor does not have enough adaptive degrees of freedom and performance clearly suffers.

To summarize Figure 6, both multistage ABFs successfully removed all 16 jammers with only six instantaneously adaptive DOFs. Conventional beamspace ABF (using the same number of adaptive DOFs) showed considerable degradation. To improve beamspace ABF to the level exhibited by our multistage beamformers would require many more adaptive DOFs and the associated hardware.

Next consider the effect of training set size and update rate. Figure 7 shows the effect of training set size on CLM ABF. Note that performance degrades gracefully, in a manner analogous to the Reed, Mallet and Brennan losses in SMI. Figure 8 shows the effects of both training set size and subspace update rate on the feed-forward ABF. The upper two curves use a single rank-one update per CPI. Performance is good, but as the update rate is decreased, performance degrades.

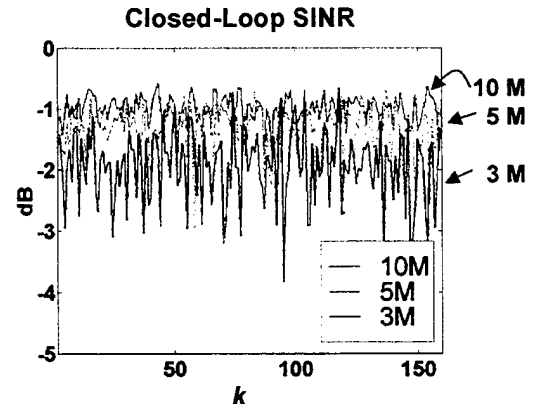


Figure 7. CLM SINR vs. size of stage 2 training set.

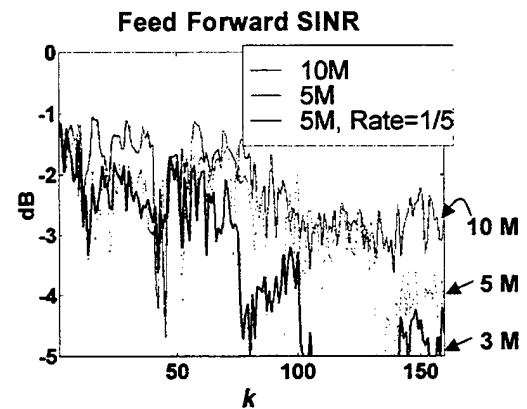


Figure 8. Feed-forward SINR for 1 update per CPI and 10M and 5M training. Also shown, 1 update every five CPI's and 5M training.

We use a second simulation to illustrate the initialization of the CLM processor in dense interference environment. Note that since CLM has access to only M instantaneously adaptive DOFs, it can not track highly nonstationary interference whose rank is too high. However, if the nonstationarity occurs in "bursts", a sectorized re-initialization mode can be used to recover the jammer subspace. Consider, for example, a scenario in which 8 jammers suddenly "turn on", but only 5 DOFs are available to track and/or null them. To estimate all 8 jammers, the signal space can be partitioned into sectors. Each sector, in sequence, is covered with beams. Detection and estimation is performed within each sector, initially acquiring only the strongest jammers, but later acquiring the weak ones. Figure 9 shows the performance of this mode.

Finally, we use a third simulation to illustrate the impact of uncompensated jammer motion on the CLM processor. If a

previously acquired jammer moves before its scheduled revisit time, and this motion is not compensated by re-steering the null, then jammer energy may leak through the stage-one digital beamformer. As mentioned earlier, robustness to this scenario can be gained by widening the jammer null. This is illustrated in Figure 10.

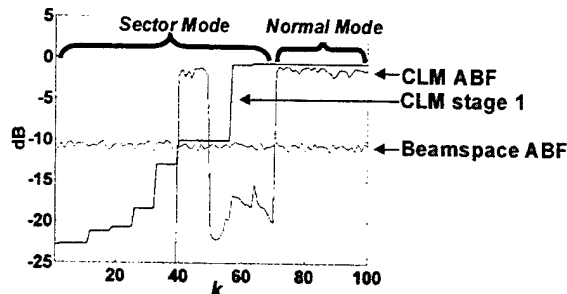


Figure 9. SINR during sector initialization mode.

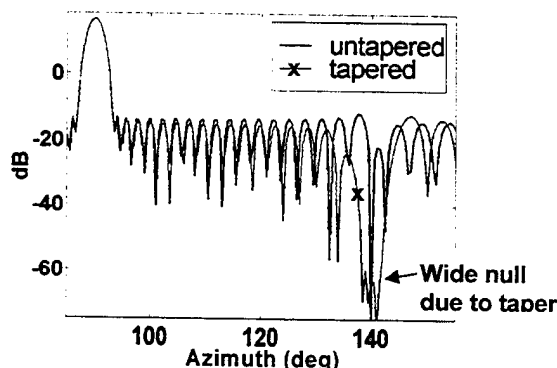


Figure 10. Illustration of tapered null.

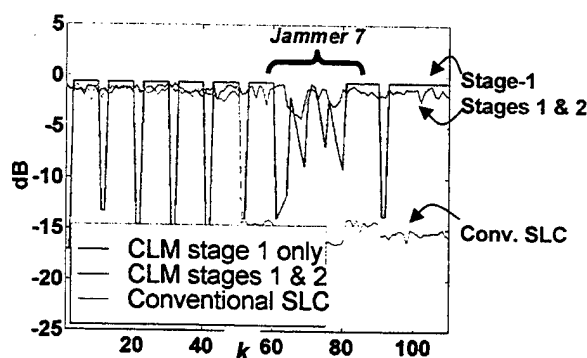


Figure 11. CLM SINR. The motion of jammer 7 is not intentionally compensated here. Instead, CLM is allowed to automatically track the jammer.

If significant jammer energy still manages to leak through the stage-one beamformer, CLM will detect and estimate the jammer again. The estimate will be associated with the prior jammer null, and a revisit will be automatically initiated. The outcome will be a null that is steered to track the jamming. This is illustrated in Figure 11. Here, there are six jammers present initially. A seventh jammer then appears and moves in an uncompensated fashion. As can be seen from Figure 11, a null is steered in stage one, but this null is soon "off." However, CLM

detects the error, correctly associates the error with the proper old null, and re-steers the null to restore cancellation. All the while, the second stage processor removes the jammer leakage, thus maintaining good end-to-end performance.

7. Summary

This work has outlined new multistage adaptive beamforming approaches. In the CLM case, our approach is to break the adaptive processor into two stages connected by a data link and a feedback control link. As each new jammer appears, cancellation is initially achieved through conventional beamspace adaptive processing. However, by carefully selecting the beamspace transformations, this job is soon passed on to the first stage. Thus, a relatively low DOF processor is used to control a much larger number of DOFs, reducing the required processing complexity. The architecture is computationally efficient, but requires that an accurate external array calibration be performed.

In the feed-forward case, two or more conventional ABFs are cascaded. Each stage reduces dimensionality, and thus the size, weight, power and cost of the processing hardware for the subsequent stages. To ease the burden on the initial (i.e., high dimensionality) stage, fast subspace tracking is used and updating is performed in a parsimonious manner.

- [1] E. Brookner, J.M. Howell, "Adaptive-Adaptive Array Processing," Proc. International Conference Radar 87, pp.257-63, 1987.
- [2] W.F. Gabriel, "Using Spectral Estimation Techniques in Adaptive Processing Antenna Systems," IEEE Trans. Antennas & Propagation, vol. AP-34, no. 3, pp 291-300, March 1986.
- [3] B.D. Van Veen, K.M. Buckley, "Beamforming: A Versatile Approach to Spatial Filtering," IEEE ASSP Magazine, pp. 4-24, April 1988.
- [4] M. Wax, T. Kailath, "Detection of signals by information theoretic criteria," IEEE Trans. Acoustics, Speech and Signal Processing, vol. ASSP-33, no. 2, pp. 387-392, April 1985.
- [5] D.J. Rabideau, "Closed-Loop Multistage Adaptive Beamforming," Proc. 33rd Asilomar Conf. on Signals, Systems, and Computers, pp. 98-102, 1999.
- [6] J. Eriksson, "Data Reduction in Sensor Array Processing Using Parameterized Signals Observed in Colored Noise," Proc. 30th Asilomar Conf. on Signals, Systems, and Computers, pp. 365-369, 1996.
- [7] M. Zatman, "Production of Adaptive Array Troughs by Dispersion Synthesis," Electronics Letters, vol. 31, no. 25, pp. 2141-2142, Dec. 7th 1995.
- [8] H.S. Eilts, R.T. Compton Jr., "The SINR performance of cascaded adaptive arrays," IEEE Int. Conf. on Communications. ICC '82. The Digital Revolution., pp.4F.4/1-5, vol.2, 1982.
- [9] T.C. Liu, B. Van Veen, "A modular structure for implementation of linearly constrained minimum variance beamformers," IEEE Trans. Sig. Proc., pp. 2342-2346, Oct. 1991.
- [10] G.H. Niezgoda, J.L.Krolik, "A multiple time scale modularized adaptive beamformer," IEEE Trans. Sig. Proc., pp. 1251-1256, May 1994.
- [11] D.J. Rabideau, "Fast, rank adaptive subspace tracking and applications," IEEE Trans. Sig. Proc., pp. 2229-2244, Sept. 1996.
- [12] E.C. Real, D.W.Tufts, J.W. Cooley, "Two algorithms for fast approximate subspace tracking," IEEE Trans. Sig. Proc., pp.1936-45, July 1999.

SPACE-TIME ADAPTIVE DETECTION OF DISTRIBUTED TARGETS IN HOMOGENEOUS ENVIRONMENT

E. Conte, A. De Maio

Università degli Studi di Napoli
"Federico II",
Dip. di Ingegneria Elettronica
e delle Telecomunicazioni,
Via Claudio 21, 80125 Napoli, Italy.
E-mail: conte@unina.it, a.demaio@unina.it

G. Ricci

Università degli Studi di Lecce,
Dip. di Ingegneria dell'Innovazione,
Via Monteroni, 73100 Lecce, Italy.
E-mail: giuseppe.ricci@unile.it

ABSTRACT

This paper deals with adaptive radar detection of range-spread targets (with unknown amplitudes) embedded in Gaussian noise with unknown covariance matrix. For estimation purposes, we assume that cells (referred to in the following as secondary data), free of signal components, are available. All of data vectors possess one and the same covariance matrix.

Detectors based upon the GLRT are designed; in particular, we propose two-step decision rules based on the following rationale: first assume that the structure (or the structure and the power level) of the covariance matrix is known and derive the GLRT over the cells under test, then plug the sample covariance matrix, based upon secondary data, into the previously derived detectors. We show that the newly-introduced decision schemes ensure the CFAR property with respect to the covariance matrix of the noise. The performance assessment highlights that these two-step detectors and the GLRT over the totality of data, previously derived by Kelly and Forsythe, have comparable performance. Hence, the two-step approach is to be preferred since it leads to simplified structures. Finally, we compare the proposed schemes with the one which assumes knowledge of the covariance matrix of the disturbance. The comparison confirms the suitability of these detectors to operate in real radar scenarios.

1. INTRODUCTION

A high resolution radar (HRR) can resolve a target into a number of scattering centers depending on the range extent of the target and the range resolution capabilities of the radar. In particular, the Multiple Dominant Scattering (MDS) centers, i.e. the individual parts of the target, may appear in a number of well separated range cells [1]. During the past decades, many results have been obtained in radar detection and imaging with HRR's. In particular, radar detection of distributed targets in white Gaussian noise of known spectral density level has been addressed in [2]. Therein, two detection structures have been proposed

and the results indicate that properly designed HRR's allow to significantly enhance the detection performance. The possible improvement depends upon two factors:

- a) increasing the range resolution of the radar reduces the amount of energy per cell backscattered by distributed clutter;
- b) individual parts of the useful target can be resolved and, since they appear in a number of well-separated cells, they introduce less fluctuations than an unresolved point-target.

The effects of the clutter reduction in a single range cell and of a MDS target model on the target detectability has been also studied by Nitzberg in [3]; he analyzed how the probability of detection of range-distributed targets depends upon the signal bandwidth in case of single pulse processing. In particular, he showed that the best performance is achieved when the radar bandwidth just resolves the individual scatterers; in fact, resolving the dominant scatterers introduce less fluctuation, but when the signal bandwidth is further increased the performance degrades as a consequence of the lack of knowledge about the position of the dominant scatterers within the extension of the target (the so-called collapsing loss).

Constant False Alarm Rate (CFAR) detection of distributed targets in Gaussian noise with unknown covariance matrix, based upon the Generalized Likelihood Ratio Test (GLRT), has been addressed in [4, 5, 6]. Therein, returns from different range cells are modeled as independent, identically distributed, Gaussian vectors with unknown covariance matrix; moreover, a set of secondary data, free of signal components, is available to estimate the spectral properties of the disturbance, see also [7].

In this paper, we still deal with the problem of detecting an extended target (with unknown amplitudes) across a bunch of cells (also referred to in the following as primary data) embedded in Gaussian noise with unknown covariance matrix. Again we resort to a set of secondary data which do not contain any useful target echo and assume an homogeneous environment, namely that all of cells possess one and the same covariance matrix. The last assumption refers to situations where the maximum spacing between any two

range cells is small compared with the scale over which power levels become different. Analysis of radar recordings has shown that such situation can be of practical interest for HRRs [8]. We address further the suitability of detectors designed according to the GLRT. The result proposed by Kelly and Forsythe, included for reader's ease, is generalized in that we resort to modified GLRT-based statistics, see also [9], a point fully clarified in the problem formulation. CFAR properties and detection capabilities of the newly-introduced detectors are successively investigated.

The paper is organized as follows: in the next section, section 2, we state the problem to be addressed and introduce the target and the noise models; in section 3 we derive the GLRT-based detectors; section 4 is devoted to the performance assessment of those receivers, also in comparison with previously proposed detectors. Section 5 contains some concluding remarks and hints for future research.

2. PROBLEM FORMULATION

We assume that data are collected from N sensors and deal with the problem of detecting the presence of a target across H range cells based upon the corresponding returns, z_t , $t = 1, \dots, H$, say. We suppose that the possible target is completely contained within those data. As in [7], it is assumed that a secondary data set z_t , $t = H + 1, \dots, H(K + 1)$, is available, that each of such snapshots does not contain any useful target echo, and that all of data possess one and the same covariance matrix.

The detection problem to be solved can be formulated in terms of the following binary hypotheses test:

$$\begin{cases} H_0: z_t = n_t, & t = 1, \dots, H(K + 1) \\ H_1: \begin{cases} z_t = \alpha_t p + n_t, & t = 1, \dots, H \\ z_t = n_t, & t = H + 1, \dots, H(K + 1) \end{cases} \end{cases}$$

where p denotes the steering vector and the α_t s, $t = 1, \dots, H$, are (unknown) deterministic parameters accounting for both the target and the channel effects.

As to the noise vectors, we assume that the n_t s, $t = 1, \dots, H(K + 1)$, are independent, zero-mean Gaussian vectors with covariance matrix given by

$$E[n_t n_t^\dagger] = M, \quad t = 1, \dots, H(K + 1), \quad (1)$$

where $E[\cdot]$ denotes statistical expectation and † conjugate transpose. Moreover, we suppose that the n_t s possess the circular property usually associated with I and Q pairs of a Wide-Sense Stationary process.

According to the Neyman-Pearson criterion, the optimum solution to the above hypotheses testing problem, is the Likelihood Ratio Test; but, for the case at hand, it cannot be implemented since total ignorance of the parameters $\alpha = (\alpha_1, \dots, \alpha_H)$ and M is assumed. We resort, instead, to GLRT-based decision strategies: strictly speaking, the GLRT is tantamount to replace the unknown parameters by their maximum likelihood estimates under each hypothesis, based upon the entirety of data [10]. Note that, it has no known optimality properties and, for point-like targets (i.e. $H = 1$), a simplified test statistic can achieve higher detection probabilities [9]. In fact, for that case, the GLRT

detector is not a Uniformly Most Powerful (UMP) Invariant test and, actually, a UMP-Invariant test does not exist as shown in [11]. Thus, it is also reasonable to investigate different strategies and, in particular, the one proposed in [9] which relies upon a two-step GLRT-based procedure: first assume that the covariance matrix M is known and derive the GLRT maximizing the Likelihood Ratio over α . Then, after the GLRT is derived, the sample covariance matrix, based upon secondary data, is inserted, in place of the true covariance matrix, into the test. A possible alternative has been conceived in [12]: in the first step assume that only the structure, Σ say, of the covariance matrix is known and, hence, derive the GLRT-based detector maximizing over both α and the power level, $2\sigma^2$ say. Finally, a completely adaptive detector is obtained by plugging the sample covariance matrix, based upon secondary data, in place of Σ into the test statistic derived for known Σ . In the following we investigate either alternatives to detect range-spread targets.

3. DERIVATION OF TWO-STEP GLRT-BASED DETECTORS

We first derive the GLRT based upon primary data assuming that the covariance matrix M or its structure Σ is known. Fully adaptive detectors are then obtained by substituting the unknown matrix by the sample covariance matrix based upon secondary data only.

Step 1. The pdf of the first H vectors is given by

$$f_{z_1, \dots, z_H}(z_1, \dots, z_H | M, H_0) = \frac{1}{[\pi^N \det(M)]^H} \exp[-tr(M^{-1} T_0)] \quad (2)$$

under H_0 and

$$f_{z_1, \dots, z_H}(z_1, \dots, z_H | M, \alpha, H_1) = \frac{1}{[\pi^N \det(M)]^H} \exp[-tr(M^{-1} T_1)] \quad (3)$$

under H_1 , respectively, wherein

$$\begin{cases} T_0 = \sum_{t=1}^H z_t z_t^\dagger \\ T_1 = \sum_{t=1}^H (z_t - \alpha_t p)(z_t - \alpha_t p)^\dagger \end{cases}$$

According to the GLRT, we replace the unknown parameters by their maximum likelihood estimates. To this end, denote M by $2\sigma^2 \Sigma$ where $2\sigma^2$ is the $(1, 1)$ -th component of the Toeplitz matrix M . The derivation is begun by writing the GLRT under the assumption that the covariance matrix or its structure only is known, namely considering the following decision rules

$$\frac{\max_{\alpha} f_{z_1, \dots, z_H}(z_1, \dots, z_H | \alpha, M, H_1)}{f_{z_1, \dots, z_H}(z_1, \dots, z_H | M, H_0)} \underset{H_0}{\overset{H_1}{>}} G \quad (4)$$

for known \mathbf{M} and

$$\frac{\max_{\alpha, 2\sigma^2} \int \mathbf{z}_1, \dots, \mathbf{z}_H (\mathbf{z}_1, \dots, \mathbf{z}_H | \alpha, 2\sigma^2 \Sigma, H_1)}{\max_{\alpha, 2\sigma^2} \int \mathbf{z}_1, \dots, \mathbf{z}_H (\mathbf{z}_1, \dots, \mathbf{z}_H | 2\sigma^2 \Sigma, H_0)} \quad (5)$$

$$\begin{matrix} H_1 \\ > \\ < \\ H_0 \end{matrix} G$$

for known Σ , respectively. Substituting the multivariate Gaussian density functions (2) and (3) in the previous formulas, and performing required maximizations, yields, after some algebra

$$\sum_{t=1}^H \frac{|\mathbf{p}^\dagger \mathbf{M}^{-1} \mathbf{z}_t|^2}{\mathbf{p}^\dagger \mathbf{M}^{-1} \mathbf{p}} \begin{matrix} H_1 \\ > \\ < \\ H_0 \end{matrix} G \quad (6)$$

for known \mathbf{M} and

$$\frac{\sum_{t=1}^H |\mathbf{p}^\dagger \Sigma^{-1} \mathbf{z}_t|^2}{\mathbf{p}^\dagger \Sigma^{-1} \mathbf{p} \sum_{t=1}^H \mathbf{z}_t^\dagger \Sigma^{-1} \mathbf{z}_t} \begin{matrix} H_1 \\ > \\ < \\ H_0 \end{matrix} G \quad (7)$$

for known Σ , respectively, with $|\cdot|$ denoting the modulus of a complex number. Note that when the covariance matrix is known the denominator of the Left-Hand-Side (LHS) of eqn. (6) is independent of the data and the test statistic reduces to the sum of the squared modula at the outputs of a bank of filters matched to $\mathbf{M}^{-1} \mathbf{p}$ whose inputs are the primary data.

Step 2. Assume $HK \geq N$. We can make detectors (6) and (7) fully adaptive, by plugging the maximum likelihood estimate of \mathbf{M} , based upon the secondary data \mathbf{z}_t , $t = H+1, \dots, H(K+1)$, i.e.

$$\widehat{\mathbf{M}} = \frac{1}{HK} \sum_{t=H+1}^{H(K+1)} \mathbf{z}_t \mathbf{z}_t^\dagger$$

in place of \mathbf{M} into (6) and of Σ into (7). Equivalently, we can substitute \mathbf{M} and Σ by \mathbf{S} , namely

$$\mathbf{S} = \sum_{t=H+1}^{H(K+1)} \mathbf{z}_t \mathbf{z}_t^\dagger.$$

The resulting decision rules, referred to in the following as Generalized Adaptive Matched Filter (GAMF) and Generalized Adaptive Subspace Detector (GASD), are thus given by

$$\sum_{t=1}^H \frac{|\mathbf{p}^\dagger \mathbf{S}^{-1} \mathbf{z}_t|^2}{\mathbf{p}^\dagger \mathbf{S}^{-1} \mathbf{p}} \begin{matrix} H_1 \\ > \\ < \\ H_0 \end{matrix} G \quad (8)$$

and

$$\frac{\sum_{t=1}^H |\mathbf{p}^\dagger \mathbf{S}^{-1} \mathbf{z}_t|^2}{\mathbf{p}^\dagger \mathbf{S}^{-1} \mathbf{p} \sum_{t=1}^H \mathbf{z}_t^\dagger \mathbf{S}^{-1} \mathbf{z}_t} \begin{matrix} H_1 \\ > \\ < \\ H_0 \end{matrix} G, \quad (9)$$

respectively. Note that for $H = 1$ the GAMF and the GASD reduce to the well-known AMF and ASD, respectively.

For future convenience the one-step GLRT, derived by Kelly and Forsythe [4], is reproduced here

$$\frac{\det(\sum_{t=1}^H \mathbf{z}_t \mathbf{z}_t^\dagger + \mathbf{S})}{\det[\sum_{t=1}^H (\mathbf{z}_t - \hat{\alpha}_t \mathbf{p})(\mathbf{z}_t - \hat{\alpha}_t \mathbf{p})^\dagger + \mathbf{S}]} \begin{matrix} H_1 \\ > \\ < \\ H_0 \end{matrix} G \quad (10)$$

where

$$\hat{\alpha}_t = \frac{\mathbf{p}^\dagger \mathbf{S}^{-1} \mathbf{z}_t}{\mathbf{p}^\dagger \mathbf{S}^{-1} \mathbf{p}}, \quad t = 1, \dots, H.$$

As a matter of fact, this detector is a special case of that proposed in [4] and, successively, reformulated in [5, 6]. In particular, in [5] Burgess and Van Veen recast the test statistic into a form advantageous for subspace processing applications while in [6] Bose and Steinhardt resorted to the principle of invariance. Furthermore, if we also assume that the radar is not able to resolve individual parts of a possible target, then $H = 1$ and detector (10) reduces to that proposed in [7].

Remarkably, either the one-step detector, the GAMF, and the GASD have the CFAR property with respect to \mathbf{M} , see [4] for the one-step GLRT. It is also apparent that the two-step detectors are simpler to implement than the plain GLRT. It remains to compare the two approaches in terms of obtainable performance. This is the object of the next section.

4. PERFORMANCE ASSESSMENT

To begin with we show that the probabilities of detection of the GAMF and the GASD are independent of the actual MDS model being in force. In fact, the following proposition holds true.

Proposition 1. The probability of detection (P_d) of the GAMF and that of the GASD depend upon

$$\alpha_1, \dots, \alpha_H, \mathbf{p}, \mathbf{M}$$

only through the signal-to-noise ratio (SNR) defined as

$$SNR = \frac{\sum_{t=1}^H |\alpha_t|^2}{N} \mathbf{p}^\dagger \mathbf{M}^{-1} \mathbf{p}.$$

Proof: first of all, following [7], we recast tests (8) and (9) in a more convenient form. To this end, denote by \mathbf{U} the unitary transformation aimed to rotate the vector $\mathbf{M}^{-\frac{1}{2}} \mathbf{p}$ onto the direction of $\mathbf{e}_1 = (1, 0, \dots, 0)$, by \mathbf{x}_t , $t = 1, \dots, H(K+1)$, the transformed whitened data vectors, and by $\widehat{\mathbf{C}}$ HK times the sample covariance matrix of the transformed secondary data, i.e.

$$\mathbf{U} : \mathbf{U} \mathbf{M}^{-\frac{1}{2}} \mathbf{p} = \sqrt{\mathbf{p}^\dagger \mathbf{M}^{-1} \mathbf{p}} \mathbf{e}_1,$$

$$\mathbf{x}_t = \mathbf{U} \mathbf{M}^{-\frac{1}{2}} \mathbf{z}_t, \quad t = 1, \dots, H(K+1),$$

$$\widehat{\mathbf{C}} = \sum_{t=H+1}^{H(K+1)} \mathbf{x}_t \mathbf{x}_t^\dagger.$$

Then, tests (8) and (9) can be re-written as

$$\sum_{t=1}^H \frac{|\mathbf{e}_1^\dagger \widehat{\mathbf{C}}^{-1} \mathbf{x}_t|^2}{\mathbf{e}_1^\dagger \widehat{\mathbf{C}}^{-1} \mathbf{e}_1} \begin{matrix} H_1 \\ > \\ < \\ H_0 \end{matrix} G \quad (11)$$

and

$$\frac{\sum_{t=1}^H |\mathbf{e}_1^\dagger \hat{\mathbf{C}}^{-1} \mathbf{x}_t|^2}{\mathbf{e}_1^\dagger \hat{\mathbf{C}}^{-1} \mathbf{e}_1 \sum_{t=1}^H \mathbf{x}_t^\dagger \hat{\mathbf{C}}^{-1} \mathbf{x}_t} \underset{H_0}{\overset{H_1}{>}} G, \quad (12)$$

respectively. Now decompose the vectors \mathbf{x}_t , $t = 1, \dots, H(K+1)$, into two components, an A component consisting of the first element only, $\mathbf{x}_{t,A}$, say, and a B component consisting of the rest of the vector, $\mathbf{x}_{t,B}$, say. Based upon the above decomposition, tests (11) and (12) can be recast as

$$\frac{\sum_{t=1}^H \left| \mathbf{x}_{t,A} - \sum_{k=H+1}^{H(K+1)} \mathbf{x}_{k,A} q_{t,k} \right|^2}{\sum_{k=H+1}^{H(K+1)} \left| \mathbf{x}_{k,A} - \sum_{i=H+1}^{H(K+1)} \mathbf{x}_{i,A} Q_{k,i} \right|^2} \underset{H_0}{\overset{H_1}{>}} \frac{G}{\sqrt{2}} \quad (13)$$

and

$$\frac{\sum_{t=1}^H \left| \mathbf{x}_{t,A} - \sum_{k=H+1}^{H(K+1)} \mathbf{x}_{k,A} q_{t,k} \right|^2}{\sum_{k=H+1}^{H(K+1)} \left| \mathbf{x}_{k,A} - \sum_{i=H+1}^{H(K+1)} \mathbf{x}_{i,A} Q_{k,i} \right|^2} \underset{H_0}{\overset{H_1}{>}} \quad (14)$$

$$\frac{G}{\sqrt{2(1-G)}} \sum_{t=1}^H \mathbf{x}_{t,B}^\dagger \mathbf{S}_{BB}^{-1} \mathbf{x}_{t,B},$$

respectively, with

$$q_{t,k} = \mathbf{x}_{k,B}^\dagger \mathbf{S}_{BB}^{-1} \mathbf{x}_{t,B},$$

$$Q_{k,i} = \mathbf{x}_{i,B}^\dagger \mathbf{S}_{BB}^{-1} \mathbf{x}_{k,B},$$

$$\mathbf{S}_{BB} = \sum_{t=H+1}^{H(K+1)} \mathbf{x}_{t,B} \mathbf{x}_{t,B}^\dagger.$$

To proceed further, note that, given the $\mathbf{x}_{t,BS}$, $t = 1, \dots, H(K+1)$, the numerator and the denominator of the tests are each other independent, moreover

- the denominator is a central χ^2 random variate with $2(HK+1-N)$ degrees of freedom;
- the numerator is the Euclidean norm squared of the H -dimensional vector

$$\mathbf{w} = \left(\mathbf{x}_{1,A} - \sum_{k=H+1}^{H(K+1)} \mathbf{x}_{k,A} q_{1,k}, \dots, \right.$$

$$\left. \mathbf{x}_{H,A} - \sum_{k=H+1}^{H(K+1)} \mathbf{x}_{k,A} q_{H,k} \right)$$

and, under H_1 , \mathbf{w} is a Gaussian vector with mean vector and covariance matrix given by

$$\sqrt{\mathbf{p}^\dagger \mathbf{M}^{-1} \mathbf{p}} \quad \boldsymbol{\alpha}$$

and

$$\mathbf{I}_H + \mathbf{X}_B^\dagger \mathbf{S}_{BB}^{-1} \mathbf{X}_B, \quad (15)$$

respectively, where $\mathbf{X}_B = (\mathbf{x}_{1,B}^*, \dots, \mathbf{x}_{H,B}^*)$.

Then, denote by \mathbf{U}_1 the unitary transformation aimed to rotate the vector $\boldsymbol{\alpha}$ onto the direction of \mathbf{e}_1 and introduce the transformed vector $\mathbf{v} = \mathbf{U}_1 \mathbf{w}$. It follows that, under H_1 and given the $\mathbf{x}_{t,BS}$, $t = 1, \dots, H(K+1)$, \mathbf{v} is a Gaussian vector with mean vector and covariance matrix given by

$$\sqrt{\sum_{t=1}^H |\alpha_t|^2 \mathbf{p}^\dagger \mathbf{M}^{-1} \mathbf{p}} \quad \mathbf{e}_1$$

and

$$\mathbf{I}_H + \mathbf{U}_1 \mathbf{X}_B^\dagger \mathbf{S}_{BB}^{-1} \mathbf{X}_B \mathbf{U}_1^\dagger, \quad (16)$$

respectively. Moreover, the sum at right-hand-side of eqn. (14) can be re-written as

$$\sum_{t=1}^H \mathbf{x}_{t,B}^\dagger \mathbf{S}_{BB}^{-1} \mathbf{x}_{t,B} = \text{tr} [\mathbf{X}_B^\dagger \mathbf{S}_{BB}^{-1} \mathbf{X}_B] = \text{tr} [\mathbf{U}_1 \mathbf{X}_B^\dagger \mathbf{S}_{BB}^{-1} \mathbf{X}_B \mathbf{U}_1^\dagger]. \quad (17)$$

Hence, given the $\mathbf{x}_{t,BS}$, $t = 1, \dots, H(K+1)$, the conditional value of P_d of detectors (13) and (14) can be written as

$$P_d | \mathbf{x}_{1,B}, \dots, \mathbf{x}_{H(K+1),B} = 1 - F_{|\mathbf{U}_1 \mathbf{x}_B^\dagger, \mathbf{S}_{BB}} \left(\frac{G}{\sqrt{2}}, \text{SNR} \right)$$

and

$$P_d | \mathbf{x}_{1,B}, \dots, \mathbf{x}_{H(K+1),B} = 1 - F_{|\mathbf{U}_1 \mathbf{x}_B^\dagger, \mathbf{S}_{BB}} \left(\frac{G}{\sqrt{2(1-G)}} \right) \times \text{tr} [\mathbf{U}_1 \mathbf{X}_B^\dagger \mathbf{S}_{BB}^{-1} \mathbf{X}_B \mathbf{U}_1^\dagger], \text{SNR} ,$$

respectively, where

$$F_{|\mathbf{U}_1 \mathbf{x}_B^\dagger, \mathbf{S}_{BB}}(\cdot, \text{SNR})$$

denotes the conditional Cumulative Distribution Function (CDF) of the LHS of either tests. In particular, previous notation highlights that the dependence of the conditional CDF upon the $\mathbf{x}_{t,BS}$, $t = 1, \dots, H(K+1)$, is confined to $\mathbf{U}_1 \mathbf{X}_B^\dagger$ and \mathbf{S}_{BB} .

In order to determine P_d we can first average out the $\mathbf{x}_{t,BS}$, $t = 1, \dots, H$, and then the $\mathbf{x}_{t,BS}$, $t = H+1, \dots, H(K+1)$. Following this guidance, we get

$$P_d = 1 - E_{\mathbf{x}_{H+1,B}, \dots, \mathbf{x}_{H(K+1),B}} E_{\mathbf{x}_{1,B}, \dots, \mathbf{x}_{H,B}}$$

$$\left[F_{|\mathbf{U}_1 \mathbf{x}_B^\dagger, \mathbf{S}_{BB}} \left(\frac{G}{\sqrt{2}}, \text{SNR} \right) \right]$$

for detector (13) and

$$P_d = 1 - E_{\mathbf{x}_{H+1,B}, \dots, \mathbf{x}_{H(K+1),B}} E_{\mathbf{x}_{1,B}, \dots, \mathbf{x}_{H,B}} \left[\right.$$

$$\left. F_{|\mathbf{U}_1 \mathbf{x}_B^\dagger, \mathbf{S}_{BB}} \left(\frac{G}{\sqrt{2(1-G)}} \text{tr} [\mathbf{U}_1 \mathbf{X}_B^\dagger \mathbf{S}_{BB}^{-1} \mathbf{X}_B \mathbf{U}_1^\dagger], \text{SNR} \right) \right]$$

for detector (14), respectively. To conclude the proof, it is then sufficient to observe that $\mathbf{U}_1 \mathbf{X}_B^\dagger$ is statistically equivalent to \mathbf{X}_B^\dagger and independent of \mathbf{S}_{BB} .

A detailed analysis of detector (10) and, in particular, closed form expressions for the probability of false alarm (P_{fa}) and the P_d , are reported in [4] and [5]. Therein, it is showed that also the P_d of (10) is independent of the actual MDS model being in force.

The remaining part of this section is devoted to the performance evaluation of the GAMF, the GASD, and the GLRT (10). To this end, we resort to standard Monte Carlo techniques and, in order to limit the computational burden, assume $P_{fa} = 10^{-4}$. Moreover, we assume that if the radar

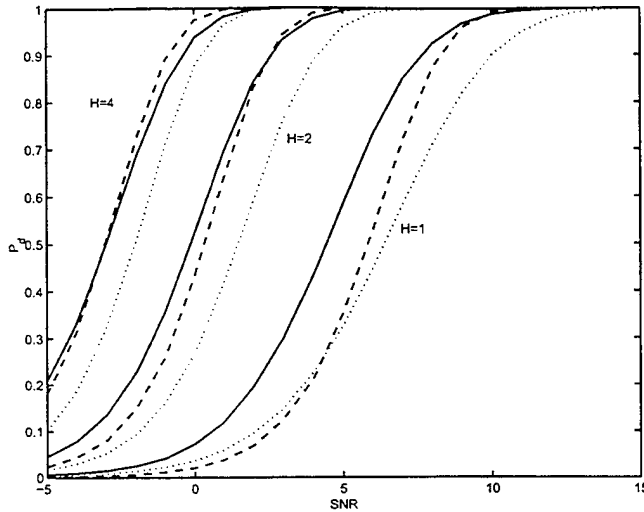


Figure 1: P_d versus SNR of the detector (10) (solid curves), the GAMF (dashed curves), and the GASD (dotted curves) for $N = 8$, $K = 16$, $P_{fa} = 10^{-4}$, and H as a parameter.

resolution is increased by a factor H the noise power per cell, $2\sigma_1^2$ say, decreases by the same factor, i.e. we set $\sigma_1^2 = \frac{\sigma^2}{H}$.

In particular, in figure 1 the P_d s of detector (10), of the GAMF, and of the GASD are plotted versus the SNR, for $N = 8$, $K = 16$ and several values of H . Note that $H = 1$ refers to unresolved targets. The figure shows that, increasing the radar resolution capabilities and suitably exploiting them, can produce a significant detection gain. Inspection of the figure also highlights that the corresponding curves of the GAMF and of the GLRT-based detector (10) intersect and, in particular, the GAMF outperforms the one-step GLRT for properly high values of P_d ; remarkably, for $H = 4$ the GAMF outperforms the GLRT for all values of P_d s of practical interest ($P_d > 0.5$). The GASD is, instead, poorer than the other two receivers, but the loss is always less than 2.5 dBs ($P_d = 0.9$, $H = 1$). Finally, the loss of the GAMF and the GASD with respect to detector (6), namely the one which possesses perfect knowledge of the covariance matrix M , can be read off figures 2 and 3 for $N = 8$, K as a parameter, $H = 2$ and $H = 4$, respectively. Inspection of the figures highlight that the loss of the proposed detectors, although not negligible, is acceptable for reasonable values of the sample size (HK).

5. CONCLUSIONS

In this paper, we have designed and assessed two-step GLRT-based decision rules to detect extended targets in homogeneous environment.

In particular, we have shown that

- the GAMF and the GASD have the CFAR property with respect to M ;
- GLRT detectors do not suffer collapsing loss;

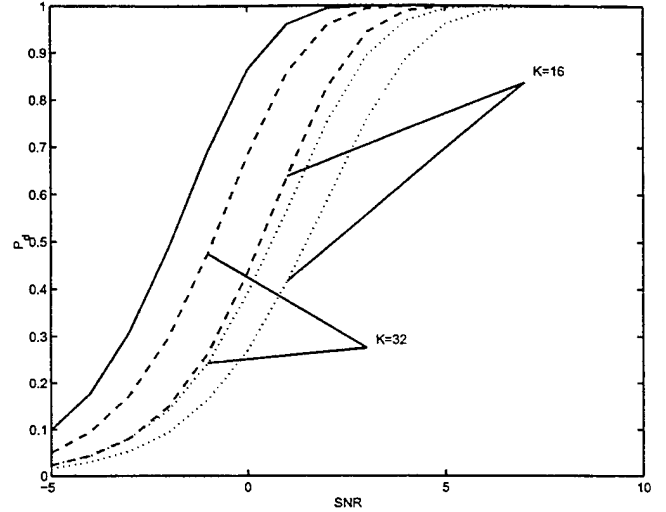


Figure 2: P_d versus SNR of detector (6) (solid curve), of the GAMF (dashed curves), and of the GASD (dotted curves) for $N = 8$, $P_{fa} = 10^{-4}$, $H = 2$, and K as a parameter.

- the performance of the GAMF is comparable with that of the one-step GLRT;
- the GASD has an acceptable loss with respect to the plain GLRT.

In conclusion, we can state that the modified approach is superior to the plain GLRT: in fact, it leads to simplified structures and, in case we resort to the GAMF, it does not experience any performance degradation. Nevertheless, although the GAMF outperforms the GASD in homogeneous environment, the latter is somewhat more robust than the former in that it keeps the CFAR property also when secondary data possess a common value of the power different from that of the cells under test [13].

It still remains to assess the capability of the proposed detectors in rejecting signals that are misaligned with the steering vector. This is the object of current studies.

6. REFERENCES

- [1] C. G. Backman: "Some recent developments in RCS Measurements techniques," *Proceedings of the IEEE*, Vol. 53, No. 8, pp. 962-972, August 1965.
- [2] P. K. Hughes II: "A High Resolution Radar Detection Strategy," *IEEE Trans on Aerospace and Electronic Systems*, Vol. 19, No. 5, pp. 663-667, September 1983.
- [3] R. Nitzberg: "Effect of a few Dominant Specular Reflectors Target Model Upon Target Detection," *IEEE Trans. on Aerospace and Electronic Systems*, Vol. 14, No. 4, pp. 670-673, July 1978.
- [4] E. J. Kelly and K. Forsythe: "Adaptive Detection and Parameter Estimation for Multidimensional Signal Models," *Tech. Report No. 848*, Lincoln Laboratories, April 19, 1989.

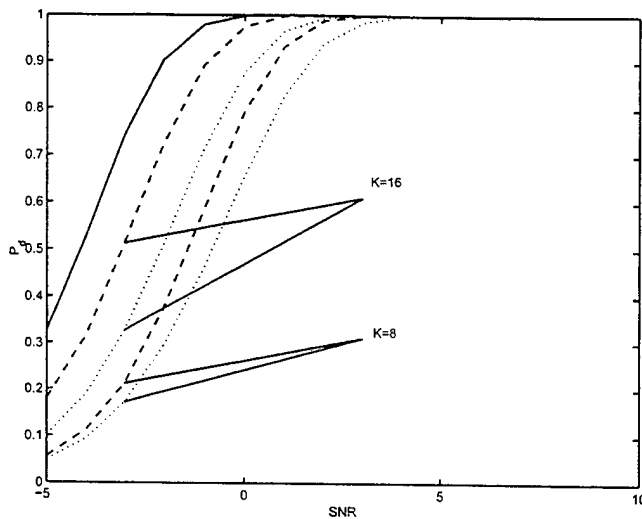


Figure 3: P_d versus SNR of detector (6) (solid curve), of the GAMF (dashed curves), and of the GASD (dotted curves) for $N = 8$, $P_{fa} = 10^{-4}$, $H = 4$, and K as a parameter.

- [5] K. A. Burgess and B. D. Van Veen: "Subspace-Based Adaptive Generalized Likelihood Ratio Detection," *IEEE Trans. on Signal Processing*, Vol. 44, No. 4, pp. 912-927, April 1996.
- [6] S. Bose and A. O. Steinhardt: "Adaptive Array Detection of Uncertain Rank One Waveforms," *IEEE Trans. on Signal Processing*, Vol. 44, No. 11, pp. 2801-2808, November 1996.
- [7] E. J. Kelly: "An Adaptive Detection Algorithm," *IEEE Trans. on Aerospace and Electronic Systems*, Vol. 22, No. 1, pp. 115-127, March 1986.
- [8] N. B. Pulsone and R. S. Raghavan: "Analysis of an Adaptive CFAR Detector in Non-Gaussian Interference," *IEEE Trans. on Aerospace and Electronic Systems*, Vol. 35, No. 3, pp. 903-916, July 1999.
- [9] F. C. Robey, D. R. Fuhrmann, R. Nitzberg and E. J. Kelly: "A CFAR Adaptive Matched Filter Detector," *IEEE Trans. on Aerospace and Electronic Systems*, Vol. 28, No. 1, pp. 208-216, January 1992.
- [10] H. L. Van Trees: *Detection, Estimation, and Modulation Theory*, Pt. 1, John Wiley & Sons, 1968.
- [11] S. Bose and A. O. Steinhardt: "Optimum Array Detector for a Weak Signal in Unknown Noise," *IEEE Trans. on Aerospace and Electronic Systems*, Vol. 32, No. 3, pp. 911-922, July 1996.
- [12] L. L. Scharf and L. T. McWhorter: "Adaptive matched subspace detectors and adaptive coherence," *Proceedings of the 30th Annual Asilomar Conference on Signals, Systems, and Computers*, Pacific Grove, CA, USA, November 1996.
- [13] E. Conte, A. De Maio, and G. Ricci: "Adaptive Detection of Distributed Targets in Partially-Homogeneous Environment," *IEEE Sensor Array and Multichannel*

EVALUATION OF REDUCED-RANK ADAPTIVE MATCHED FIELD PROCESSING FOR SHALLOW-WATER TARGET DETECTION *

Nigel Lee, Lisa M. Zurk, James Ward

MIT Lincoln Laboratory

244 Wood Street

Lexington, MA 02420

nigel@ll.mit.edu, zurk@ll.mit.edu, jward@ll.mit.edu

Abstract

This paper evaluates the performance of several reduced-rank adaptive matched field processing (AMFP) algorithms for passive sonar detection of quiet targets in littoral environments. Effective rank reduction improves the stability of adaptive beamformer weight calculation when the number of available snapshots is limited due to source motion and other nonstationarity in the data. Here, five reduced-rank algorithms with various criteria for subspace selection are systematically evaluated within a common simulation framework incorporating moving sources and either long or short observation times. For each simulation, the reduced-rank algorithms are compared for performance (measured by output signal-to-interference-plus-noise-ratio) versus subspace rank, with the full-rank minimum variance (MVDR) beamformer serving as a baseline. The algorithms each have different strengths and weaknesses, which are discussed in detail.

1 INTRODUCTION

Matched field processing (MFP) has been widely proposed as an array processing technique for passive sonar detection and localization with vertical line arrays in littoral environments. MFP exploits the coherent multipath of signals propagating in the shallow-water waveguide by incorporating propagation physics into the computation of "replica" (steering) vectors from which beamformer weights are derived, enabling target detection and accurate target localization in range, depth, and bearing.

For an array with N elements, each $N \times 1$ replica vector

\vec{v} is normalized such that $\vec{v}^H \vec{v} = N$. The MFP weight vector \vec{w} is derived from the replica vector \vec{v} , and the MFP output power is then computed as

$$P_{\text{MFP}}(\phi) = \vec{w}^H(\phi) \hat{\mathbf{K}} \vec{w}(\phi), \quad (1)$$

where ϕ represents spatial look direction (usually range and depth) and where

$$\hat{\mathbf{K}} = \frac{1}{L} \sum_{l=1}^L x_l x_l^H \quad (2)$$

is the sample covariance matrix, computed as a summation of outer products of $N \times 1$ data snapshots x_l .

The conventional, or Bartlett, MFP processor (CMFP) computes a weight vector that is a scaled version of the replica vector, $\vec{w}_c(\phi) = \vec{v}(\phi)/N$, where the scaling ensures the unity gain constraint, $\vec{w}^H(\phi) \vec{v}(\phi) = 1$. CMFP suffers from high strong-source sidelobes that can obscure detection and degrade localization accuracy.

The standard adaptive MFP (AMFP) processor, called **minimum-variance, distortionless response (MVDR)**, computes a weight vector that is a function of both the replica vector and the sample covariance matrix:

$$\vec{w}_m(\phi) = \frac{\hat{\mathbf{K}}^{-1} \vec{v}(\phi)}{\vec{v}^H(\phi) \hat{\mathbf{K}}^{-1} \vec{v}(\phi)}. \quad (3)$$

The MVDR output is then given by

$$P_{\text{MVDR}}(\phi) = \left\{ \vec{v}^H(\phi) \hat{\mathbf{K}}^{-1} \vec{v}(\phi) \right\}^{-1}. \quad (4)$$

Compared to CMFP, MVDR provides significant interference rejection and sidelobe suppression through the adaptive nulling of $\hat{\mathbf{K}}^{-1}$, resulting in superior target detection. However, MVDR output is very sensitive to mismatch because the action of $\hat{\mathbf{K}}^{-1}$ in (3) causes target self-nulling when the replica vectors $\vec{v}(\phi)$ are mismatched, and because

*This work was sponsored by DARPA-TTO under Air Force contract F19628-95-C-0002. Opinions, interpretations, conclusions, and recommendations are those of the authors and are not necessarily endorsed by the United States Air Force.

$\hat{\mathbf{K}}^{-1}$ itself may be estimated inaccurately when not enough snapshots are available for the computation of (2). It is the latter problem that is the focus of this paper.

Under the assumption of Gaussian noise statistics, Reed *et al.* [7] showed that the SINR power loss ρ incurred by using the sample covariance matrix $\hat{\mathbf{K}}$ to compute the MVDR output instead of the true data covariance matrix \mathbf{K} has expected value $\mathcal{E}(\rho) = (L - N + 2)/(L + 1)$, where L and N are defined as above. In practice, the number of snapshots L available to compute $\hat{\mathbf{K}}$ is limited by source motion and other nonstationarity in the data. However, SINR losses ρ of 3 dB or more are incurred if $L < 2N$, a significant constraint for large arrays.

One method of addressing both the self-nulling and the limited-snapshot problem in MVDR processing is to apply *diagonal loading* to the weight computation:

$$\tilde{\mathbf{w}}_{m_{DL}}(\phi) = \frac{(\hat{\mathbf{K}} + \sigma_d^2(\phi)\mathbf{I})^{-1}\tilde{\mathbf{v}}(\phi)}{\tilde{\mathbf{v}}^H(\phi)(\hat{\mathbf{K}} + \sigma_d^2(\phi)\mathbf{I})^{-1}\tilde{\mathbf{v}}(\phi)}, \quad (5)$$

where the *load level* $\sigma_d^2(\phi)$ is chosen to satisfy a white noise gain constraint [2] and is designed to minimize the effects of poorly estimated eigenvectors of $\hat{\mathbf{K}}$ in the weight computation. The diagonally-loaded MVDR output is then computed as in (4), with $\tilde{\mathbf{w}}_{m_{DL}}$ replacing $\tilde{\mathbf{w}}_m$. Diagonal loading significantly reduces the SINR power loss ρ (expressed above for unloaded MVDR), even when the number of snapshots L is less than the array size N (but still enough to capture all the source energy in the data).

In cases where the number of snapshots L is less than the array size N , however, $\hat{\mathbf{K}}$ is less than full-rank, and the inverse $\hat{\mathbf{K}}^{-1}$ must be replaced by an approximation $\hat{\mathbf{K}}^{-1}$. **Rank reduction** accomplishes this by first estimating $\hat{\mathbf{K}}$ with a reduced-rank approximation \mathbf{K}_R (of rank P , $P < \min\{N, L\}$) and then essentially performing the inversion in the lower-rank space. The combination of diagonal loading and rank reduction, then, provides meaningful AMFP output in “snapshot-starved” situations. In the following, several methods for determining the reduced-rank approximation \mathbf{K}_R are detailed, and the resulting reduced-rank AMFP algorithms are systematically evaluated by simulation, with the full-rank, diagonally-loaded MVDR (MVDR-DL) serving as a baseline.

2 RANK REDUCTION ALGORITHMS

The first two rank reduction algorithms examined here are eigenvector (EV) filtering algorithms. Let the eigenvector decomposition of $\hat{\mathbf{K}}$ be given as

$$\hat{\mathbf{K}} = \mathbf{U}\mathbf{\Sigma}\mathbf{U}^H = \sum_{i=1}^N \sigma_i^2 \tilde{\mathbf{u}}_i \tilde{\mathbf{u}}_i^H, \quad (6)$$

where $\mathbf{U} = [\tilde{\mathbf{u}}_1 \tilde{\mathbf{u}}_2 \dots \tilde{\mathbf{u}}_N]$ is an orthogonal matrix whose columns are comprised of the eigenvectors $\tilde{\mathbf{u}}_i$ of \mathbf{K} and $\mathbf{\Sigma} = \text{diag}(\sigma_1^2, \sigma_2^2, \dots, \sigma_N^2)$ is a diagonal matrix whose diagonal elements are comprised of the eigenvalues σ_i^2 of \mathbf{K} (usually ordered such that $\sigma_1^2 \geq \sigma_2^2 \geq \dots \geq \sigma_N^2$).

The EV filtering algorithms approximate $\hat{\mathbf{K}}$ with a rank- P approximation \mathbf{K}_R , where

$$\mathbf{K}_R = \mathbf{U}\mathbf{\Sigma}_R\mathbf{U}^H = \sum_{i=1}^P \sigma_{R_i}^2 \tilde{\mathbf{u}}_{R_i} \tilde{\mathbf{u}}_{R_i}^H, \quad (7)$$

and $\mathbf{\Sigma}_R = \text{diag}(\sigma_{R_1}^2, \sigma_{R_2}^2, \dots, \sigma_{R_P}^2, 0, \dots, 0)$. Note that $N - P$ eigenvalues have been set to zero (filtered) and the remaining P eigenvalues have been re-indexed to be the first P eigenvalues of $\mathbf{\Sigma}_R$ (so that there is an implicit reordering of the columns of \mathbf{U} in (7) as well).

The two EV filtering algorithms are distinguished by the criterion used to select which eigenvectors to retain in \mathbf{K}_R . The **signal coherence criterion (SCC)** [4] selects for each *look direction* all eigenvectors that have high correlation with the replica vector $\tilde{\mathbf{v}}(\phi)$, i.e.,

$$|\tilde{\mathbf{u}}_i^H \tilde{\mathbf{v}}(\phi)|^2 \geq \gamma |\tilde{\mathbf{v}}(\phi)|^2, \quad (8)$$

where γ is some scalar constant; setting $\gamma = 0.5$, for example, retains those eigenvectors with correlation within 3 dB of the maximum. If, for a given replica vector, no eigenvectors satisfy (8), SCC reverts to the full-rank MVDR-DL output (full nulling). Note that the criterion (8) is such that both the reduced-rank subspace and the dimension P of the subspace *will vary* with spatial parameters ϕ . For SCC, then, the only eigenvectors of interest are those that have high correlation with the replica vector in the look direction; all other directions have an infinite null place on them.

The **direct form (DF)** algorithm [8] retains the P eigenvectors-eigenvalue pairs that maximize, for each $\tilde{\mathbf{v}}(\phi)$, the ratio

$$|\tilde{\mathbf{u}}_i^H \tilde{\mathbf{v}}(\phi)|^2 / \sigma_i^2. \quad (9)$$

The DF criterion again is such that the subspace choice varies with spatial parameters ϕ , although the rank P is fixed for all ϕ . The DF criterion selects the subspace that minimizes MVDR output power over all P -dimensional eigenvector bases, which maximizes output SINR under ideal conditions. Practically, however, the DF criterion needs to be applied subsequent to diagonal loading to reduce the sensitivity of (9) to small eigenvalues (and corresponding eigenvectors, which may be inaccurately estimated) during subspace selection. Because both SCC and DF select a different subspace for each look direction, both algorithms perform extremely well when the replica vectors and eigenvectors in (8) and (9) are estimated accurately.

Once \mathbf{K}_R is determined, the reduced-rank MVDR

weight vector $\vec{w}_R(\phi)$ is computed as

$$\vec{w}_R(\phi) = \frac{\check{\mathbf{K}}_R^{-1} \vec{v}(\phi)}{\vec{v}^H(\phi) \check{\mathbf{K}}_R^{-1} \vec{v}(\phi)}, \quad (10)$$

where

$$\check{\mathbf{K}}_R^{-1} = \sum_{i=1}^P (\sigma_{R_i}^2 + \sigma_d^2(\phi))^{-1} \vec{u}_{R_i} \vec{u}_{R_i}^H \quad (11)$$

(cf. equation (7)). The reduced-rank MVDR output is then computed as

$$P_{\text{MVDR}_{\text{RR}}}(\phi) = \vec{w}_R^H(\phi) \hat{\mathbf{K}} \vec{w}_R(\phi). \quad (12)$$

A third EV-based algorithm that takes a different approach to rank reduction is the **dominant mode rejection (DMR)** algorithm [5]. In the DMR algorithm, \mathbf{K}_R is constructed by retaining the largest P eigenvalues of $\hat{\mathbf{K}}$, but the remaining $N-P$ small eigenvalues are *averaged* instead of *filtered*. Thus, $\mathbf{K}_R = \mathbf{U} \Sigma_R \mathbf{U}^H$, where $\Sigma_R = \text{diag}(\sigma_1^2, \sigma_2^2, \dots, \sigma_P^2, \alpha, \alpha, \dots, \alpha)$ and α is the average of the smallest $N-P$ eigenvalues. The reduced-rank MVDR weight vector \vec{w}_R is then computed as in (10) and the reduced-rank MVDR output $P_{\text{MVDR}_{\text{RR}}}(\phi)$ as in (12). The DMR algorithm is such that adaptive nulling still occurs in (10) in the directions of the eigenvectors with highest-energy eigenvalues (the “dominant modes”), but the averaging of the “noise” eigenvalues reduces sensitivity to poorly estimated noise eigenvectors. DMR selects a fixed reduced-rank subspace for every look direction, so it is computationally fast compared to SCC and DF.

Cox and Pitre [1] proposed a modified version of DMR that employs “mismatch protection,” where for each look direction ϕ , eigenvectors having high correlation with the replica vector $\vec{v}(\phi)$ (measured by a criterion similar to (8)) are excluded from consideration as dominant modes. While this prevents self-nulling of targets of interest, it also allows sidelobe leakage from interferers in the directions of the “protected” eigenvectors. For this reason, DMR is implemented here without mismatch protection.

The last two reduced-rank algorithms examined in this paper are based on the **modal decomposition (MD)** [9] of $\hat{\mathbf{K}}$. Here, both data and replica vectors are transformed from phone space into mode space:

$$\vec{v}_m = \mathbf{T}_m \vec{v} \quad (13)$$

$$\mathbf{K}_m = \mathbf{T}_m \mathbf{K} \mathbf{T}_m^H, \quad (14)$$

where \vec{v}_m is the “mode replica” vector, \mathbf{K}_m is the modal covariance matrix, and $\mathbf{T}_m = (\mathbf{Q}^H \mathbf{Q})^{-1} \mathbf{Q}^H$ is the mode transformation matrix derived from the mode space matrix \mathbf{Q} , whose columns are mode functions sampled at the depths of the vertical line array.

Mode filtering then takes place in the mode domain, with \mathbf{K}_R computed by retaining P rows and columns of \mathbf{K}_m and deleting the other $N-P$ rows and columns. The advantage of transforming into mode domain is that the mode functions have an easily understood physical meaning. For example, retaining low-order modes filters out surface energy, because only higher-order modes are excited near the surface. Thus, the **mode-order (MDO)** algorithm is an MD-based algorithm that selects as its reduced-rank subspace the P lowest-order modes, a subspace based on physical considerations and essentially independent of the data. A more sophisticated (but still data-independent) mode-based algorithm is the **mode-select (MDS)** algorithm, which selects a position-dependent subspace of modes, depending on which modes are most excited at each range and depth according to the propagation model.

Once \mathbf{K}_R has been computed, the reduced-rank MVDR weight vector is computed in the mode domain as

$$\vec{w}_{m_R}(\phi) = \frac{\check{\mathbf{K}}_R^{-1} \vec{v}_m(\phi)}{\vec{v}_m^H(\phi) \check{\mathbf{K}}_R^{-1} \vec{v}_m(\phi)}, \quad (15)$$

and reduced-rank “matched mode” power is given by

$$P_{\text{MODE}_{\text{RR}}}(\phi) = \vec{w}_{m_R}^H(\phi) \hat{\mathbf{K}}_m \vec{w}_{m_R}(\phi). \quad (16)$$

Note that the mode functions in \mathbf{Q} are not orthogonal unless the vertical line array spans the water column. Thus, the mode transformation \mathbf{T}_m may not be orthogonal, and this needs to be accounted for in comparing matched mode output in (16) to matched field output in (1). In the simulations presented here, however, the vertical line arrays span most of the water column and the modes vectors are approximately orthogonal.

3 EVALUATION OF REDUCED-RANK AMFP ALGORITHMS

In order to evaluate the various reduced-rank AMFP algorithms, the following simulation analysis was performed. Simulated data was generated with a strong surface interferer at depth 6m moving at 6 m/s toward the array and a quieter submerged target at depth 30m moving at 3 m/s away from the array. The array was assumed to be a bottom-moored, vertical line array with $N=30$ elements separated by 5.7m and total aperture $\approx 170\text{m}$. Replica vectors were computed with environmental parameters and bathymetry for the Santa Barbara channel, using data collected during the 1998 Santa Barbara Channel Experiment (SBCX); water depth for the Santa Barbara channel was approximately 200m. The replica vectors were computed using output from the KRAKEN normal mode propagation model [6], with an adiabatic approximation to account for range-dependent bathymetry. The simulations assumed *no environmental mismatch*, meaning that a simulated source at a

given location was exactly matched to the replica vector at that location. Data was simulated for 101 seconds and processed at a frequency of 235 Hz, using a 1-second FFT window.

In Simulation 1, all 101 snapshots were used to compute the sample covariance matrix. Figure 1 shows the CMFP and full-rank MVDR-DL range-depth ambiguity surfaces assuming interferer power 140 dB, target power 130 dB, transmission loss ≈ 64 dB, and noise power 70 dB. The input (phone-level) SNR was thus $(130 - 64) - 70 = -4$ dB. Note that while the MVDR-DL background is lower than the CMFP background (as expected), the motion of the interferer over 101 snapshots causes a spreading of the interferer energy that almost entirely masks the weaker submerged target. For these sim-

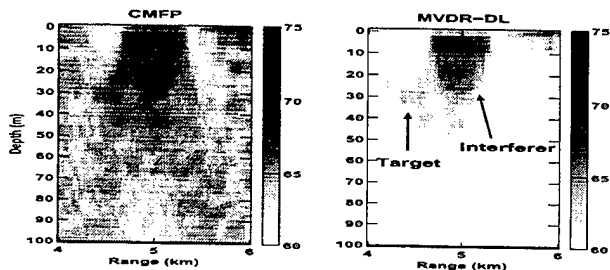


Figure 1. MFP ambiguity surfaces from 101s of data. Gray scale units are dB re $1 \mu\text{Pa}/\text{Hz}$.

ulations, output signal power for an ambiguity surface was measured by the power at the midpoint of the known target path, while output noise was measured as the 75th percentile of the ordered output powers of the entire surface. Defined in this way, the MVDR-DL output signal was 63.3 dB, while the output noise was 59.5 dB, resulting in an output SINR of 3.8 dB. Note that this definition of output SINR does not necessarily take into account source localization.

Figure 2 plots the output SINR of the five reduced-rank AMFP processors as a function of processor rank. Because interference motion over 101 snapshots consumes several adaptive degrees of freedom, little is gained over the baseline, full-rank MVDR-DL by performing rank reduction. In this example, the best performance was obtained by the Rank-10 MDO, for which a subspace with the ten lowest-order modes provided the best combination of filtering interferer energy at the surface and retaining target energy. As the rank of the MDO processor increased (allowing successively higher-order modes), more target energy was retained but less interferer energy was filtered. The proper number of low-order modes to retain may be predetermined from physical considerations based on the parameters of the problem (source depths, water depth, etc.); this is the utility of mode-based algorithms.

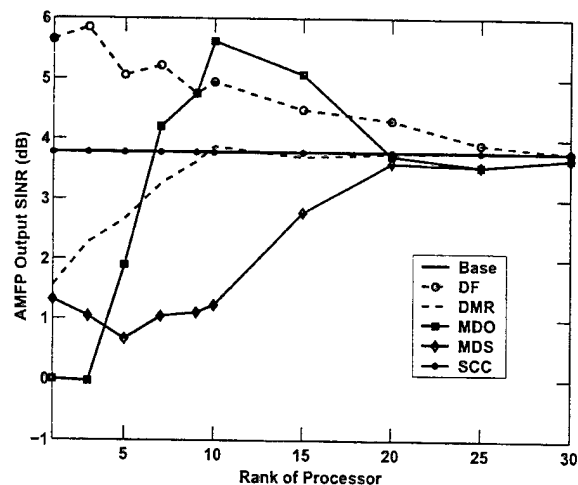


Figure 2. Reduced-rank AMFP output SINR versus processor rank. Base (full-rank MVDR-DL) and SCC are independent of rank and are identical for this example.

The only other algorithm to attain better performance than the baseline was DF, which will always perform better than the baseline as long as the target eigenvectors are selected in the target look direction. The nature of the DF criterion (9) is such that sources will appear in fewer look directions than in the full-rank baseline, because source energy is filtered if not retained. In Simulation 1, a DF rank of 3 was needed to retain the target in the target look direction – thus the jump in performance at rank 3. Note that the SCC algorithm, which also selects variable subspaces for each look direction, also will perform better than the baseline as long as the target eigenvectors are selected by (8) in the target look direction. For this example, the SCC output was identical to the baseline, meaning that no eigenvectors passed the criterion (8) in any look direction; this again was due to source motion.

Figure 3 shows the ambiguity surfaces for the two best reduced-rank AMFP processors, Rank-7 DF and Rank-10 MDO. Note that in the MDO surface there is a broadening of the target peak. This “widening of beams” is characteristic of mode-based processing and can be considered advantageous in countering motion effects over long observation times.

In Simulation 2, only 21 snapshots in the middle of the time interval were used to compute the sample covariance matrix (but the simulation data was otherwise the same as in Simulation 1). Figure 4 shows ambiguity surfaces for CMFP and full-rank MVDR-DL. Because the original sample covariance $\hat{\mathbf{K}}$ (30×30) was rank-21 in this case, both $\hat{\mathbf{K}}$ and the replica vectors $\vec{v}(\phi)$ were projected onto the sub-

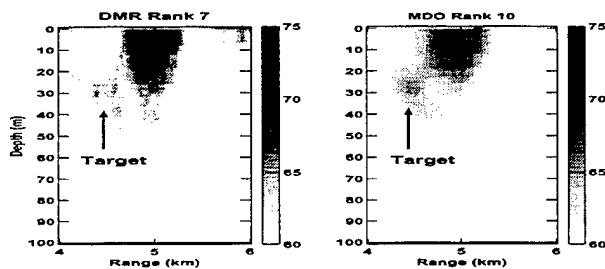


Figure 3. Reduced-rank AMFP ambiguity surfaces from 101s of data. Gray scale units are dB re 1 μ Pa/Hz.

space spanned by the principal 21 eigenvectors¹. Thus, "full-rank" MVDR-DL has dimension 21 here and already involves some rank reduction from the original dimension of 30. Note that with 21 snapshots, source motion is much

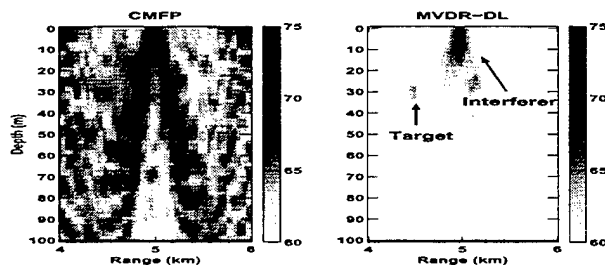


Figure 4. MFP ambiguity surfaces from 21s of data. Gray scale units are dB re 1 μ Pa/Hz.

less of an effect and the source peaks (especially the target peak) are much more localized in the MVDR-DL ambiguity surface. MVDR-DL output SINR was computed at 8.43 dB, an improvement of almost 5 dB from Simulation 1.

Figure 5 plots the output SINR of the five reduced-rank AMFP processors as a function of processor rank. First, note that DMR performance approaches the baseline as the rank approaches the maximum of 21. This is because K_R constructed using the DMR approximation becomes closer to \hat{K} as the rank increases. However, note that DMR approaches within 1 dB of the baseline once the rank is greater than or equal to the number of "dominant modes" associated with the two sources – here, a rank of 7.

The DF algorithm, on the other hand, performs extremely well for low ranks: with less source motion over 21 snapshots, the criterion (9) effectively selects the target eigenvectors at the target location and selects only noise

¹ The deleted subspace contains essentially zero energy but would affect adaptive weight computation if not deleted.

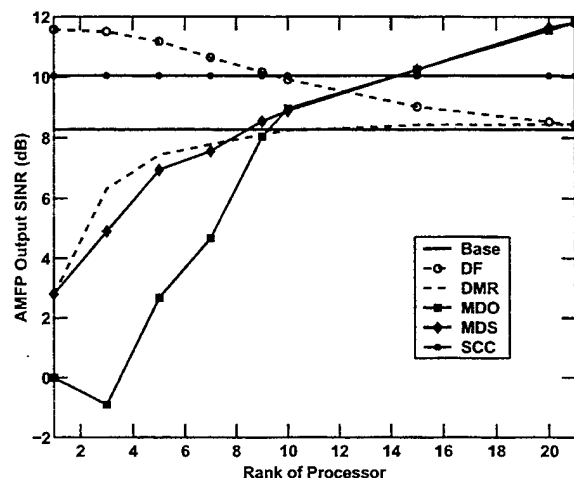


Figure 5. Reduced-rank AMFP output SINR versus processor rank. Base (full-rank MVDR-DL) and SCC are independent of rank.

eigenvectors at "background" locations. As the processor rank increases, the DF processor loses this resolution between target and background locations and performance approaches the baseline. Similarly, the SCC criterion (8) for Simulation 2 selects the target eigenvectors at the target location and nowhere else, resulting in a performance increase over the baseline².

Finally, the mode processors MDO and MDS require higher ranks to achieve good performance, but performance is comparable at rank 9 or so, still significant given that the subspaces are selected independent of the data³. Figure 6 shows selected reduced-rank ambiguity surfaces for this example.

4 DISCUSSION

This paper examined several reduced-rank adaptive matched field processing algorithms for detecting quiet targets in littoral environments. Using simulated data with a strong, moving surface interferer and a quieter, moving submerged target, it was demonstrated that process-

² SCC does not converge to the baseline as rank approaches 21 because SCC does not have constant rank versus look direction.

³ The fact that the MDO/MDE curves approach a higher output SINR as the rank approaches 21 is somewhat misleading because there is a different rank-21 baseline MVDR-DL in mode space, formed by projecting the modal covariance K_m and mode-space replicas onto the subspace spanned by the 21 lowest-order modes. The projected (21×21) modal covariance is significantly nonorthogonal, leading to artificially low AMFP output powers in certain look directions. The higher output SINR for the mode methods in the baseline/limit is thus due to artificially low output noise values in the ambiguity surface.

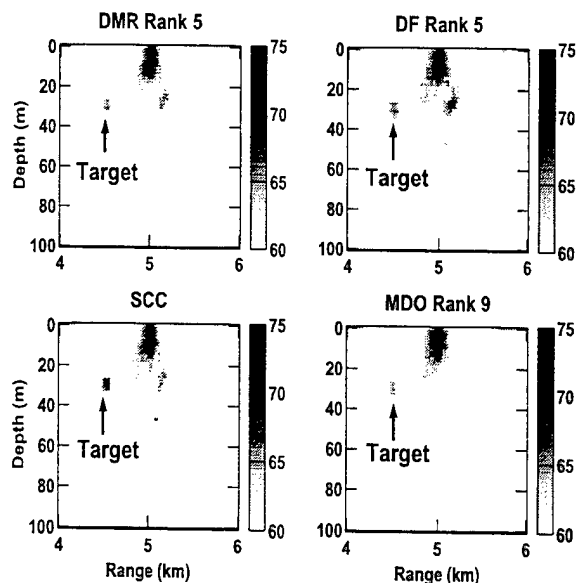


Figure 6. MFP ambiguity surfaces from 21s of data. Gray scale units are dB re 1 μ Pa/Hz.

ing over shorter observation intervals effectively combats the effect of source motion and produces better AMFP detection performance. It is with shorter observation intervals (and the accompanying scarcity of snapshots), however, that rank reduction is important in computing adaptive weights. Among the reduced-rank AMFP algorithms investigated, best performance was shown by those algorithms that vary the reduced-rank subspace with look direction, the direct form (DF), signal coherence criterion (SCC), and mode-select (MDS) algorithms. However, environmental mismatch was not incorporated into this study, and all three algorithms depend on accurate propagation models. Sensitivity of the algorithms to environmental mismatch is thus a topic for future study. By contrast, the other two algorithms, the dominant mode rejection (DMR) and mode-order (MDO) algorithms, compute a single reduced-rank subspace for every look direction and thus are both faster and simpler than the others. Predictably, these constant-subspace algorithms do not perform as well in the best case (Simulation 2).

Mode-space rank reduction allows subspace choices motivated by physical considerations essentially independent of the data. Thus, the mode-order (MDO) algorithm, implemented here by selecting low order modes that are presumably only excited below surface depths, was able to achieve slightly better performance than the others in Simulation 1 for a long observation time, where interferer motion prevented effective rank reduction in the eigenvector domain.

Selection of reduced-rank subspaces that are indepen-

dent of data also provides some degree of robustness for very-low-snapshot cases, where criteria such as SCC and DF that depend on eigenvector correlations may become inaccurate. Degradation of reduced-rank AMFP performance as the number of snapshots becomes even smaller relative to the array size is thus another topic of further study, one that becomes increasingly important the larger the array size.

Finally, the algorithms need to be validated on real data. Initial results from the SBCX data set previously shown by the authors [3] indicate that reduced-rank AMFP can indeed be applied effectively on real data. Further validation on more difficult cases is forthcoming.

References

- [1] H. Cox and R. Pitre. Robust DMR and multi-rate adaptive beamforming. In *1997 31st Asilomar Conference*, pages 920–924, 1997.
- [2] H. Cox, R. Zeskind, and M. Owen. Robust adaptive beamforming. *IEEE Trans. on Acoustics, Speech, and Signal Processing*, 35(10):1365–1376, October 1987.
- [3] N. Lee, L. Zurk, and J. Ward. Evaluation of reduced-rank, adaptive matched field processing algorithms for passive sonar detection in a shallow-water environment. In *1999 33rd Asilomar Conf.*, pages 876–880, 1999.
- [4] Y. Lee et al. Robust adaptive matched-field-processing. In *Proceedings of the Conference on Oceans '93*, pages 387–392, 1993.
- [5] N. Owsley. Sonar array processing. In S. Haykin, editor, *Array Signal Processing*. Prentice-Hall, New Jersey, 1985.
- [6] M. Porter. The KRAKEN normal mode program. Technical Report SM-245, SACLANT Undersea Research Centre, 1991.
- [7] I. Reed, J. Mallett, and L. Brennan. Rapid convergence rate of adaptive arrays. *IEEE Trans. on Aerospace and Electronic Systems*, 10(6):853–863, 1974.
- [8] J. Ward, A. Baggeroer, and L. Zurk. Rapidly adaptive matched field processing for nonstationary environments. In *1998 Adaptive Sensor Array Processing Workshop*, Lexington, MA, March 1998.
- [9] T. Yang. Effectiveness of mode filtering: A comparison of matched-field and matched-mode processing. *J. of the Acoust. Soc. of America*, 87(5):2072–2084, 1990.

RADAR IMAGING USING A WIDEBAND ADAPTIVE ARRAY

Mark Curry, Yasuo Kuga

Dept. of Electrical Eng., Box 352500, University of Washington, Seattle, WA, USA
curryma@gte.net, kuga@ee.washington.edu

Introduction

The focus of this paper is to investigate the application of wideband adaptive array processing techniques to the problem of radar imaging. In particular we are interested in joint range-angle estimation with angular resolution improvement for small, relative to λ , antennas. The simulations and experimental results indicate that this approach is viable in a practical sense, and yields significant angular resolution improvement over conventional methods.

The approach uses conventional Fourier techniques for downrange information and uses adaptive beamforming for the azimuth dimension. The basic approach is to transmit a wideband set of continuous wave signals, then apply spatial resampling to the received data to correct for the fixed element spacing, then Fourier transform this data to extract range information. We then have a spectral estimation problem at each range cell. By using data associated with each range bin, the angular spectrum is computed using a minimum variance spectral estimate. In general, adaptive array theory is based on the narrow band requirement that the array aperture size is much less than the inverse relative bandwidth. This implies that plane waves are parameterized primarily by their angle of arrival. For this work the narrowband assumption is not valid since we will be using bandwidths of at least 20% of the carrier frequency. Spatial resampling can estimate the array data that would occur if the antenna spacing were varied physically as a function of frequency. See [2] for a discussion of spatial resampling applied to underwater acoustics. Another problem that must be addressed is that parametric spectral estimation methods require a covariance matrix to be estimated from multiple, uncorrelated snapshots of the array output. We introduce a method that amounts to an induced Doppler shift that can be used to generate the required data necessary for angular spectral estimates. The final result is a range-angle plot of backscattered energy.

Signal Model and Formulation

Consider the case of a superposition of plane waves incident upon a receiving array. These plane waves are the backscattered energy from objects in the field of view of

the transmitter. Assume objects are in the far field so the plane wave assumption is valid. The incident plane waves can be parameterized by their angle of arrival as shown in Figure 1.

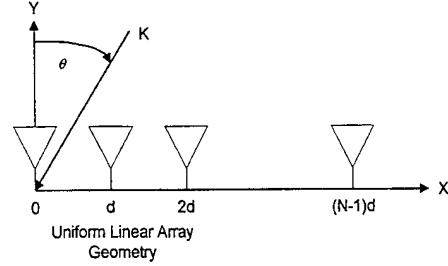


Figure 1. Uniform linear array geometry.

A narrowband incident field with wavenumber vector \vec{k} is present. $|\vec{k}| = k = 2\pi f / c_0$, where c_0 is the free space velocity. In the X-Y plane $\vec{k} = k(\sin \theta, \cos \theta)^T$, with θ measured clockwise from the Y-axis. The sensor positions are given by $\vec{r} = (x_n \ y_n)^T$. The output of each sensor is then given by

$$V(\vec{k}, \vec{r}) = Ae^{-j\vec{k}^T \vec{r}} \quad (1)$$

Applying this to the uniform linear array geometry above yields the baseband output at each sensor as

$$V(n) = Ae^{-jknd \sin \theta}, n \in 0 : N-1 \quad (2)$$

with d the inter-element distance.

Given that range information requires signal bandwidth, consider a point target at a distance r_0 from the origin. A CW transmitter radiates a field that is scattered by the target back to the receiver. The target is modeled as a delta function with backscattering amplitude, $A(r_0) = A = 1$, at the receiver.

$$B(r) = A(r_0)\delta(r - r_0) \quad (3)$$

The transmitter generates a CW signal at frequency f_m ,

with round trip travel time given by $\tau_0 = \frac{2r_0}{c_0}$. For

frequency f_m the received signal is:

$$V_o = Ae^{-j2\pi f_m(2r_o/c_o)} = Ae^{-j2\pi m\Delta f(2r_o/c_o)}, \quad (4)$$

where $\Delta f = \frac{f_{BW}}{M}$ and f_{BW} is the total bandwidth used and M is the number of steps. This equation is the discrete (spatial) frequency Fourier transform of the target position r_o . Note that $\frac{f_{BW}}{c_o}$ has units of cycles per unit distance, or cycles per meter for example. Therefore a point target at position r_o is transformed to M samples of a complex exponential of 'frequency', $\frac{2\Delta f}{c_o} r_o$ or $\frac{2f_{BW}}{Mc_o} r_o$. To convert this signal to the spatial domain, apply the inverse Fourier transform, which yields

$$I(n) = A \sum_{m=0}^{M-1} e^{-j2\pi m(2f_{BW}r_o/Mc_o)} e^{j2\pi m(n/M)}. \quad (5)$$

This equation describes a *SINC* function with peak at $n = \text{round}(\frac{2f_{BW}}{c_o} r)$, where $\text{round}()$ signifies rounding to the nearest integer and r is an arbitrary distance. The *SINC* function provides interpolation for range values that are non-integer values of $\frac{2f_{BW}}{c_o} r$. Increasing the

bandwidth, f_{BW} , will increase the resolution but reduces the maximum usable range due to aliasing. This method of ranging is called FM-CW ranging and is well known for imaging stationary scenes. The free space medium is linear so superposition holds, allowing the extension of one target to multiple targets or in our case scatterers distributed in range (and angle). As will be shown in the next section increasing bandwidth, f_{BW} , also affects the spatial spectrum.

We then combine the FM-CW technique with the angle of arrival results to describe the antenna outputs for the M , CW linear stepped frequencies, with angles of arrival from $-\pi/2$ to $\pi/2$, incident upon N antenna elements. Combining Eq(2) and Eq(4), and letting $A=1$, the baseband antenna output for frequency m and element n , for one emitter at range r_o and angle θ is

$$V_o(n, m) = e^{-j2\pi m\Delta f \frac{2r_o}{c_o}} e^{-j2\pi \frac{f_o}{c_o} nd \sin \theta} e^{-j2\pi (\frac{m}{M} - \frac{1}{2}) \frac{f_{BW}}{c_o} nd \sin \theta}. \quad (5)$$

Transmit frequency, $f_m = f_o + (m - \frac{M}{2})\Delta f$ and f_o is the center frequency of the antenna. The first exponential term describes the phase information for range, and the second and third terms describe the inter-element phase due to the incidence angle. The second term describes the linear phase shift across the array for incidence angle θ , which is independent of frequency. However the third term shows an additional phase across the array which is dependent on frequency $m\Delta f$. The affect of the last term is to cause the angle of arrival to appear to vary as the incident field wavelength changes. The angle of arrival sweeps linearly from

$$\begin{aligned} & \frac{2\pi f_o}{c_o} (1 - \frac{f_{BW}}{2f_o}) d \sin \theta \text{ radians} \\ \text{to} & \frac{2\pi f_o}{c_o} (1 + \frac{f_{BW}}{2f_o}) d \sin \theta \text{ radians.} \end{aligned} \quad (6)$$

The angular sweep is proportional to the true angle. For large angles of arrival the angular broadening is greatest. Targets are smeared in range by the third term also. Conventional delay and sum beamforming correctly accounts for both of these affects, but for small antennas the angular resolution will be poor. The set of received signal samples from M frequencies, at N outputs of the antenna array is formed into a matrix for processing.

Spatial Resampling

The array outputs must be properly focussed so that the angle of arrival of a single plane wave for any given frequency m will be constant. This is accomplished by resampling the array outputs to correct for the constant element spacing d . See [4] for discussion of spatial resampling techniques applied to wideband angle of arrival estimation for uncorrelated signals. For joint range-angle estimation we have the additional requirement that the antenna phase center for each resampled array output must remain fixed at the center of the array. The spatial resampling concept is motivated by treating the outputs of the N element linear array as the result of spatially sampling a continuous linear array. The resampling is accomplished by approximating a continuous array by interpolation of the given data and then extracting the required samples at the new sampling interval required for each temporal frequency m . Interpolation is accomplished by inserting $K - 1$ zeros between samples, where K is the interpolation factor, to produce a vector of length KN . A linear phase, low pass filter is applied to the data. This filter has a cutoff frequency of $\frac{\theta}{K}$, where

θ is the maximum normalized spatial angle, typically $\pm \pi/2$. A fast implementation utilizes the polyphase filtering architecture [3]. The resampling process will create a set of data that contains samples at varying distances from the antenna phase center. To prevent the algorithm from trying to sample beyond the ends of the

array we introduce a scale factor $\beta = \frac{f_{\min}}{f_o}$, which has

the affect of making the interpolated array spacing d appear fractionally smaller than the original by β . Consequently the steering vectors used later for angular spectrum estimation will be corrected by β also. Combining these ideas with the bandwidth relation in (6) it is easily shown that the resampled data for element n , and frequency m , from the interpolated array is given by

$$Y(n, m) = X_{interp} \left(\text{round} \left(\frac{KN}{2} \right) + \frac{K \left(n - \frac{N}{2} \right)}{1 + \frac{BW}{f_o} \left(\frac{m - \frac{M}{2}}{M} \right) \frac{f_{\min}}{f_o}} \right) \quad (7)$$

where $X_{interp}(\cdot)$ is the interpolated array of length KN . \mathbf{Y} is a matrix of size M by N . The offsets into the interpolated array are all relative to the array center at $\frac{KN}{2}$. This procedure amounts to interpolation followed by decimation of the original data.

Angular Spectrum Estimation

This section outlines the minimum variance spectral estimation method used to derive the angular spectrum at each range bin. Consider an array of N sensors whose location and directional characteristics are known. Assume that there are multiple signal sources whose statistical characteristics are uncorrelated. A simple model for the received signal $y(t)$ at the output of each element can be expressed by:

$$\mathbf{y}(t) = \sum_{l=1}^L \mathbf{a}(\psi_l) x_l(t) + \mathbf{n}(t), \quad t = 1, \dots, M. \quad (8)$$

The vector $\mathbf{a}(\psi_l)$ is the spatial signature ($N \times 1$) that depends upon the angle of arrival ψ and x is a scalar associated with the l th signal source and incorporates the time variation of the signal. Assume there are L signal sources and M uncorrelated snapshots. $\mathbf{n}(t)$ is additive Gaussian noise. The signal received by the sensors is $\mathbf{y}(t)$ and it is an $N \times 1$ complex vector. As evident, the signal $\mathbf{y}(t)$ is a linear combination of the spatial signature and the additive noise. When the geometry of the array is linear with equally spaced sensors, the steering vector of the l th signal source is

$\mathbf{a}(\psi_l) = [1 \ e^{ja(\psi_l)} \ e^{j2a(\psi_l)} \ \dots \ e^{j(N-1)a(\psi_l)}]^T$, where $a(\psi_l) = kd \sin \psi_l$ represents spatial frequency, and d denotes sensor spacing. The source signal $x(t)$ and the noise $\mathbf{n}(t)$ are white Gaussian distributed with zero mean, statistically independent of the field signal(s). Consequently we have:

$$\begin{aligned} E[x(t)] &= 0, \quad E[x(t)x'(t)] = \mathbf{I}, \\ E[\mathbf{n}(t)] &= 0, \quad E[\mathbf{n}(t)\mathbf{n}'(t)] = \sigma^2 \mathbf{I} \end{aligned} \quad (9)$$

where ' represents conjugate transposition. The stationarity assumption extends to both it's temporal and spatial properties. The spatial covariance matrix can be expressed as follows:

$$\begin{aligned} \mathbf{R} &= E[\mathbf{y}(t)\mathbf{y}^H(t)] = \mathbf{A}(\Psi)\mathbf{A}^H(\Psi) + \sigma^2 \mathbf{I} \\ &= \sum_{l=1}^L \mathbf{a}(\psi_l)\mathbf{a}^H(\psi_l) + \sigma^2 \mathbf{I} \end{aligned} \quad (10)$$

The rank of the covariance matrix increases by one for each incident plane wave.

For the linear array, the steering vector steers the beamformer to the assumed propagation direction of the incident field. The general form for the steering vector is:

$$\mathbf{e} = \begin{bmatrix} e^{-jk_0^0 \cdot \bar{x}_0} \\ \vdots \\ e^{-jk_{N-1}^0 \cdot \bar{x}_{N-1}} \end{bmatrix} \quad (11)$$

The notation \bar{k}_m^0 denotes the phase shift due to the wave's propagation at each sensor.

Adaptive Beamforming

The basic approach here is to solve a constrained, minimum mean-squared error, optimization problem. Many algorithms have been developed using this concept. The received signal $y(t)$ from antenna array is expressed as:

$$\mathbf{y}(t) = \mathbf{a}(\psi)x(t) + \mathbf{n}(t) \quad (12)$$

where \mathbf{a} is the spatial signature of the desired signal. Using the conventional beamforming approach described above, we may form a weight vector \mathbf{w} focus the array:

$$\hat{x}(t) = \mathbf{w}^H \mathbf{y}(t) \quad (13)$$

The objective is to maximize the output signal to interference-plus-noise ratio (SINR). For constrained optimization, instead of maximizing the output SINR directly, we minimize the mean-squared value of the weighted observations,

$$P_0 = E[|\mathbf{w}^H \mathbf{y}|^2] = \mathbf{w}^H \mathbf{R} \mathbf{w} \quad (14)$$

subject to a look-direction gain constraint.

Minimum Variance Beamforming

Consider an ideal, unit-amplitude signal, assumed to be propagating in the direction $\bar{\xi}$. The notation for this signal is $\mathbf{e}(\bar{\xi})$. The idea is to apply the weight vector \mathbf{w} to the sensor output. Any signal from the direction specified by \mathbf{e} should have unit gain. Noise and signal propagating from other direction should be suppressed. In this case, the constraint optimization problem is:

$$\min_{\mathbf{w}} E[|\mathbf{w}^H \mathbf{y}|^2] \quad \text{subject to } \text{Re}[\mathbf{e}^H \mathbf{w}] = 1 \quad (15)$$

where the constraint $\text{Re}[\mathbf{e}^H \mathbf{w}] = 1$ ensures that the ideal signal has unit gain. The optimum weight vector that solves the optimization problem is given by [1]:

$$\mathbf{w}_0 = \frac{\mathbf{R}^{-1} \mathbf{e}}{\mathbf{e}^H \mathbf{R}^{-1} \mathbf{e}} \quad (16)$$

It is evident that the optimum weight vector depends on two parameters: the correlation matrix \mathbf{R} and the direction of propagation $\bar{\xi}$. As different directions are scanned, the weights adapt to the signal and noise component of the observations. The beamformer output power is $P = \mathbf{w}_0^H \mathbf{R} \mathbf{w}_0$, in the assumed propagation direction. The output power of the minimum variance beamformer is:

$$P^{MV}(\bar{\xi}) = [\mathbf{e}^H(\bar{\xi}) \mathbf{R}^{-1} \mathbf{e}(\bar{\xi})]^{-1} \quad (17)$$

Covariance Matrix Estimation

To estimate \mathbf{R} from the available data, it must be derived from I.I.D. samples of \bar{x} , the observed data. The approach utilized for deriving multiple snapshots is perhaps the most important one for imaging since it can yield an array that does not sacrifice degrees of freedom as is required for sub-array averaging. This technique is based on the use of a set of orthogonal, closely spaced, sub-frequencies around each frequency m . If the transmitter is swept around each of M frequencies, in L steps of step size DI/L , then the L sub-frequencies form an orthogonal set over a narrow frequency band. D is defined as the total bandwidth of the induced Doppler shift. Thus we have created a set of receive vectors \bar{x}_{ml} , that are uncorrelated signals to be used in (16). The total bandwidth utilized by the system is the same although it has been more finely divided. The resulting data cube is of size $N * M * L$. Ideally L would be equal to $2N$ since it can be shown that this value yields estimates of \mathbf{R} that are within 3dB of optimal. The resampling process is carried out for each frequency f_{ml} , as described above. After range compression is applied using the FFT (Fast Fourier Transform), the corresponding groups of \bar{x}_{ml} are used to build \mathbf{R} for that range bin, as shown by

$$\mathbf{R}_m = \frac{1}{L} \sum_{l=0}^{L-1} \bar{x}_{m+l-\frac{L}{2}} \bar{x}_{m+l-\frac{L}{2}}^* \quad (18)$$

Next is a brief description of forward-backward averaging, which is an effective way to improve a correlation matrix estimate. A ULA (uniform linear array) steering vector remains invariant up to a scaling if it's elements are reversed and complex conjugated. Let \mathbf{J} be an $N \times N$ exchange matrix whose components are zero except for the anti-diagonal. Then for the ULA it holds that $\mathbf{J} \bar{s}^*(\phi) = e^{-j(N-1)\rho} \bar{s}(\phi)$.

The backward array correlation matrix is therefore $\mathbf{R}_b = \mathbf{J} \mathbf{R}^* \mathbf{J}$. By averaging this matrix with the normal one we get the new correlation matrix

$$\mathbf{R}_{FB} = \frac{1}{2} (\mathbf{R} + \mathbf{J} \mathbf{R}^* \mathbf{J}) \quad (19)$$

By combining the methods outlined above we are able to estimate \mathbf{R} with a great deal of robustness. In general, \mathbf{R} will be full rank but may have a high condition number.

We wish to obtain reasonable estimates in all normal imaging environments, so for this reason we include a user controllable amount of diagonal loading $\sigma^2 \mathbf{I}$, added to \mathbf{R} to set the dynamic range of the image.

Jammer Suppression

Jammers or unintentional interferers are removed by simply turning off the transmitter and using the captured data as an estimate of the jammer AOA and temporal frequency. The Fourier transforms of the jammer signals are used to form angular covariance matrices at each range bin in the same manner as for imaging. Each \mathbf{R} matrix is then used to form an orthogonal subspace projection matrix, \mathbf{Q} , which is used to project out the interference at each range bin.

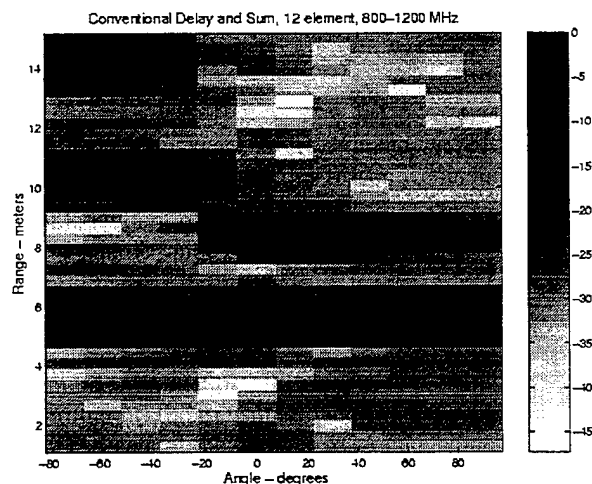


Figure 2. Conventional beamforming, using a 12-element array with 8 targets.

Computer Simulation Results

A computer simulation has been created to verify the proposed scheme for adaptive imaging. Figure 2 shows an image created by performing conventional beamforming on a 12-element array, using 800-1200 MHz bandwidth, and 40 frequency steps. The 8 targets are not discernible due to the antenna sidelobes. The 5 targets at 5 meters downrange are not separable. Figure 3 uses a 12-element array and 4 sub-frequencies but uses spatial resampling to achieve the best possible imaging. All targets are clearly discernible above the noise floor.

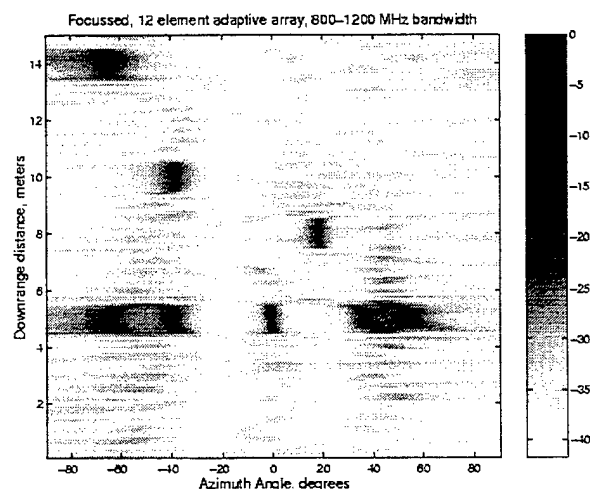


Figure 3. Resampled, 12 element array with 8 targets.

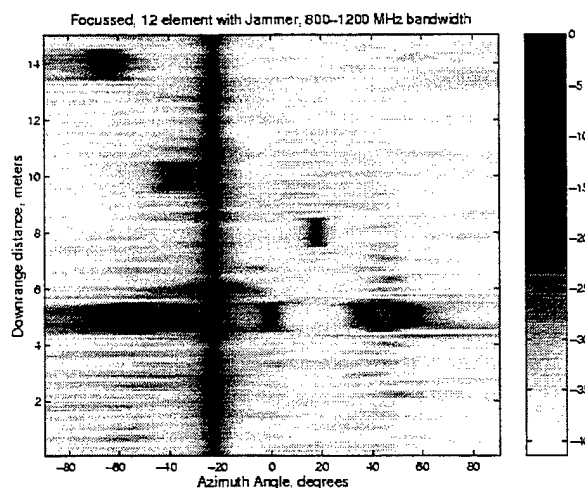


Figure 4. Same as Fig. 3, plus jammer.

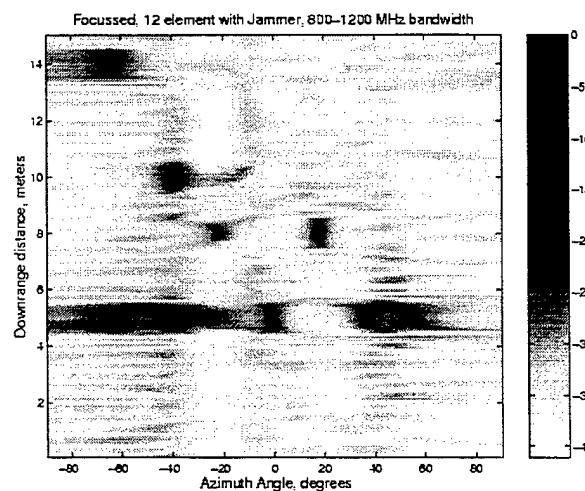


Figure 5. Same as Fig. 4 with jammer suppression.

Experimental Results

The imaging system consists of a 4-element uniform linear array for receive, and a wide beamwidth horn antenna for the transmitter. The source is stepped from 800 MHz to 1200 MHz in 80 increments. The system center frequency is, $F_c = 1$ GHz or approximately 33cm wavelength and $\lambda_c = c_0/F_c$. Transmit power is 5dBm into the horn antenna. The receiver consists of 4 vertical half wave at λ_c , dipoles, spaced at half wave at λ_c intervals, followed by matched (equal group delay) receive channels, with 60dB gain, and each mixed to a 102.5 KHz IF frequency. The transmitted signal is tapped off at the antenna and mixed by the LO to 102.5 KHz to form the reference signal. The 5 signal channels are sampled at 10 KHz each, thus converting each signal to 2.5 KHz discrete time due to undersampling. This signal, being $1/4$ of the sample rate is then converted to complex baseband by mixing with digital quadrature oscillators, followed by low pass filtering. Finally, one set of 4 complex signals, representing S_{21} for each antenna is created by dividing each channel's baseband signal by the reference signal to derive the round trip phase and amplitude response at each antenna element for each frequency. The system is placed in an anechoic chamber for testing. Test objects consist of various metal cylinders, approximately 1-2 wavelength in size and placed from 3 to 8 meters away. It should be noted that our anechoic chamber is not highly effective at absorbing energy at 1GHz, so there is some clutter energy.

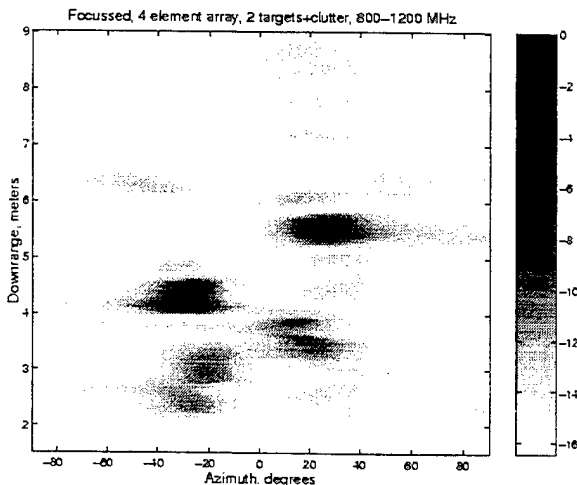


Figure 6. One target at 4.5m downrange and -30° crossrange, A larger cylindrical object is at 5.5m downrange and 25° crossrange.

The experimental array uses the same frequency and bandwidth parameters as the simulation except has 4 elements, utilizes forward-backward averaging, and 4 sub-frequencies. This array could benefit from using more sub-frequencies to improve the estimate of \mathbf{R} , but system constraints restricted the available data storage. Future hardware will allow more data storage as well as additional antenna elements. Diagonal loading is used to set the dynamic range of the image and stabilize the correlation matrix estimates. Figure 6 shows a image of 2 targets in the chamber. The available space is fairly small, consequently the target scenario is simple. Figure 5 shows a higher level of near field clutter as well as some emitted signal from the transmitter horn.

Conclusion

This paper has outlined an approach for radar imaging using wideband array processing techniques. In particular the use of spatial resampling to convert signals to a narrowband model, and an induced Doppler shift for angular spectrum estimation are combined for imaging. Simulations were validated by an experimental 4-element, stepped CW system. Ongoing work will investigate performance issues, antenna element dispersion and calibration. A twelve element system is currently being developed for further study of this approach. This approach may be useful for radar applications that utilize conformal antennas or foliage penetration systems that utilize low frequencies for imaging and area surveillance.

References

1. J.Capon, "High Resolution Frequency-Wavenumber Spectrum Analysis", Proceedings of the IEEE, 57:1408-1418, 1969
2. J.Krolik and D.Swinger, "Focused Wide-Band Array Processing by Spatial Resampling", IEEE Trans. Acoust., Speech, Signal Processing, vol. 38, No. 2, pp. 356-360, 1990.
3. R.A. Roberts and C.T. Mullis, "Digital Signal Processing", (Addison-Wesley), pp.447-448, 1987
4. S. Haykin, Editor, "Advances in Spectrum Analysis and Array Processing", (Prentice-Hall), VOL. I and II, 1991

Novel Impact Echo Imaging Technique Using Multiresolution Enhancements in Temporal and Spatial Domains

Amjed S. Al-Fahoum and Ali M. Reza

Department of Electrical Engineering and Computer Science

University of Wisconsin-Milwaukee

P. O. Box 784, Milwaukee WI 53201-0784, USA

afahoum@uwm.edu, reza@uwm.edu

ABSTRACT

Echo imaging techniques have been shown to be effective in both demonstrating the reflectivity patterns and detecting different kind of flaws in many engineering fields. Further modifications in such approaches depend solely on the variability of the medium under investigation, the temporal resolution of the source waves and the spatial resolution of the source-receiver array. Impact echo imaging aimed at high resolution gains using conventional processing techniques (deconvolution and migration) suffers from inherent problems such as noise degradation, nonstationarity of the mediums, incompleteness of the data set, and exactness of the modeling parameters. In this work, we intuitively propose a new imaging approach that employs the apriori knowledge of the medium to predict a robust modeling structure of the medium. This model will then be used in an optimum way to minimize the squared error between the observed data and the exact medium. To guarantee a solution for this ill posed inverse problem, the exact medium is constrained to satisfy the predicted model and the normal equations resulted from this minimization process are weighted by a positive definite function to maintain stability and prevent divergence. To achieve high temporal resolution, we utilize from the ability of wavelet transform in decomposing the data into non-overlapping spectral bands and performing both time varying spectral prewhitening and adaptive deconvolution to suppress the source signature. For high spatial resolution, we will perform the constrained estimation approach in each sub-domain to minimize the computational effort. To evaluate the performance of the proposed approach, we will conduct a comparative study that manifests the achievements and the limitations of this approach over the conventional echo imaging techniques. To demonstrate the effectiveness of our approach in handling near field and far field problems, we apply this technique to detect various flaws in post-tensioned concrete bridge structures.

1. INTRODUCTION

Echo imaging techniques aiming at high-resolution reconstructions are recently paid attention to the ill posed problem in the reconstructed data. The existence of high frequency contribution with zero Eigen value clustering makes the solution for the inverse problem unstable, and so spurious noise and miss positioned reflectors will appear in the reconstructed images. The conventional way to solve such problem is to use either Tikhonov regularization theory

[1], diagonal loading in array processing [2], and spectral prewhitening [3]. Several researchers look to this problem from different prospective. In [4] a constrained maximum smoothness approach using Tikhonov regularization theory was considered to reconstruct incomplete seismic data. The assumption of maximum smoothness and the penalizing procedure used there makes this idea appealing. However, such approach depends on an expensive iterative technique, data dependent regularization process, and noise free environment. Bounding the total variation of the reflectivity pattern by reducing the requirement of maximum smoothness is considered by [5], and [6]. While in this way, data dominated by spatially high frequencies can be reconstructed. Imposing unsupervised bounds on the model parameter variations will distort image details. Moreover, for fast processing a preconditioning approach is necessary that minimizes the distance between the system Eigen values clusters and reduces the system's matrix condition number. Such preconditioning procedure is expensive and requires using another calculation space. The weakness of the total variation approach can be resolved by introducing a stabilizer function that limits the area where significant variations of the model parameters and/or discontinuity occur. Such stabilizer is proposed by [7] and used to penalize dispersed and smoothed distribution of the parameters with all values different from the apriori model. While well-focused distribution with a small departure from the apriori model has a small penalty function. Although, such approach is convincing, it tends to produce the smallest possible anomalous domain. To overcome this problem another penalizing constraint is applied on the material property to limit the model variation with respect to its background, the existence of noise limits such achievement and tends to smudge the image.

In this work, we propose another approach that addresses the difficulties that faces echo imaging problem utilizing from parametric modeling approach that uses regularization techniques in numerical linear algebra. Herein, we will focus on the mathematical formulation of the imaging approach, limitations of conventional techniques to cope with image non smoothness characteristics, robustness of the imaging approach to small perturbations in data domain, and elegantly propose a robust fast convergence solution that focuses image variations without disturbing its details. This is achieved by combining preconditioning conjugate gradient solver, temporal-spectral weighting domain (Wavelet), and nearly optimal nonlinear

estimator. In this case, the problem is divided into minor problems that are highly decoupled. Applying a denoising approach to remove parameter variation due to noise and constraining high frequency components in horizontal, vertical, and detail domains tends to reform centered clusters that has an improved condition numbers. As a result, a considered improvement in temporal-spectral resolution of the reconstructed images is achieved. This modification on both reconstruction and computational requirement is achieved due to the ability of wavelet domain to cope with noise, wavelet bases nearly matches eigen vectors in low frequency domain which tends to minimize the number of energy based coefficients. Using conjugate gradient solver that needs $O(n)$ computations, where n is the number of nonzero coefficients makes the convergence faster. Moreover, decomposing the domain into less correlative sub domains that its features are locally estimated and filtered, will resolve image details and minimize the effect of parameters perturbations.

The paper is organized into four sections. The first section formulates the echo-imaging problem in time-space domain and points the difficulties associated with parameterized inversion. In section 2, the problem will be formulated in the wavelet domain and the concept of nearly optimal nonlinear estimator will be introduced. In section 3, preliminary results of applying the echo imaging approach to reconstruct reflectivity structures of post tensioned concrete bridges will be addressed. The last section summarizes the concepts achieved in this work.

2. Problem Formulation

Modeling and imaging of the synthetic data is escorted by the noisy influence of the source-receiver geometry and both coherent and non-coherent noise at the array surface. The synthetic data at the surface of the array characterizes the intertwined relation between both the reflectivity structure of the model (m) and the noise (n). To distinguish the model, data should be mapped into separate spaces that perfectly characterize one from the other. Let us formulate the modeling problem:

$$d(t, x) = T(z, x, t) * m(z, x) + n(t, x) \quad (1)$$

In equation (1) d represents the synthetic data at the array surface, T is a transfer function that represents the characteristics of the propagated waves through the imaged medium. This function is implicitly achieved by solving the wave equation in elastic medium [9]. While (*) is a convolution operator, (m) is the reflectivity model, and (n) is an additive white Gaussian noise. Equation (1) can be represented in matrix form as follows:

$$\bar{d} = T\bar{m} + \bar{n} \quad (2)$$

Equation (2) shows that the model can be resolved if and only if (T^{-1}) is bounded and $(T^{-1}\bar{n})$ is located in a non-overlapped space with \bar{m} . Based on the solution of the wave equation, (T^{-1}) is not bounded and $(T^{-1}\bar{n})$ is not white any more. Due to instability of the inverse operator the power of the noise is considerably amplified with the increase of spatial and temporal frequencies. The conventional way of solving this problem is by using preprocessing steps to diminish the noise

contribution on the data and then using an adjoint operator of (T) to approximate its inverse [10]. The imaging (migration) of the estimated reflectors can be determined by:

$$m_{est} = \bar{T}Tm \quad (3)$$

In equation (3) (\bar{T}) is the complex conjugate transpose of (T) . The matrix $(\bar{T}T)$ is a linear filter matrix that represents a Hessian matrix for the denoised data correlation matrix $(E(\bar{d}d) = \bar{m}\bar{T}Tm)$. Equation (3) represents the formal migration technique called Kirchhoff [10]. Since the Hessian matrix has both non-unity diagonal elements due to the existence of spreading losses unaccounted for during imaging and non-zero off-diagonal elements due to both correlation of neighborhood pixels and non-smoothness of model parameters, Kirchhoff imaging cannot correctly reconstruct the actual model [9]. Kirchhoff imaging approximation is preferable when the source-receiver geometry is very dense, reflectivity structure is smooth, and the recording aperture is wide. Normally, these conditions are rarely available and applying this approach yields imaging artifacts that give fake reflectors and distort structure details. However, this approach still can be used if we manage how to use the apriori information of the model history and the enhanced performance of Tikhonov theory. We will keep our weak assumption that data is perfectly noise free, and formulate a constrained regularization process that mimics the constrained adaptive beamformer to limit the variations of out of aperture data, to force the model to be focused on known data points, and to penalize those events that diverge from our apriori model. Starting by a normal regularization process that tends to find the optimal model that minimizes the data energy subject to minimum total variation energy. The parametric function is:

$$P(m) = \|Tm - d\|^2 + \alpha \|m - m_{apr}\|^2 \quad (4)$$

The model that minimizes equation (4) is:

$$m = [\bar{T}T + \alpha I]^{-1}(\bar{T}d + \alpha m_{apr}) \quad (5)$$

Using constrained stabilizing function, by applying a constrained matrix that depends on the apriori knowledge of the model, equation (5) becomes:

$$m = [\bar{T}T + \alpha \bar{C}C]^{-1}(\bar{T}d + \alpha \bar{C}Cm_{apr}) \quad (6)$$

if $\alpha = 0$ in equation (6), then $m = (\bar{T}T)^{-1}\bar{T}d$ which is the least square imaging. Due to the ill posed structure of the Hessian matrix, this solution may lead to spurious oscillations around sharp features. Applying the constrained least square imaging leads to some form of Wiener filtering. The solution of equation (6) is not trivial, where the system usually has the following characteristics:

- The Hessian matrix has wide distribution of Eigen structures and $(\bar{C}C)$ approximates noise covariance matrix that tends to remove zero-clustered Eigen values.
- Hessian matrix is symmetric positive definite.
- Hessian matrix depends on source-receiver geometry, aperture limitations, medium acoustical impedances, spectral weighting due to amplitude losses, and autocorrelation function of source signature.

- d. The regularization term has sparse distribution that limits the achievement of fast transform methods.
- e. To minimize the regularized term energy, Low values of α is to be used that will lead to the ill posed problem.

Based on these characteristics of equation (6), the best approach is to use an iterative procedure that achieves the best estimate of (m) . Conjugate gradient techniques can be used to achieve (m) , but due to (e) the application of conjugate gradient will be very slow and so a preconditioned conjugate gradient solver is required [11]. Preconditioning is applied to improve the condition number of the regularized Hessian matrix. Let us assume that there exists a symmetric, positive-definite matrix M that approximates $[\bar{T}T + \alpha\bar{C}C]$, then if $k(M^{-1}[\bar{T}T + \alpha\bar{C}C]) \ll k([\bar{T}T + \alpha\bar{C}C])$ we can iteratively solve the preconditioned regularized problem much faster than equation (6). Where $k(A)$ is the condition number of the matrix A . A good choice for the preconditioning matrix is the diagonal matrix $M = 1/\sqrt{\text{diag}(\bar{T}T + \alpha\bar{C}C)}$. Rewriting equation (6) using $\hat{T} = TM$, $\hat{C} = CM$, and $\hat{m} = M^{-1}m$:

$$(\hat{T}\hat{T} + \alpha\hat{C}\hat{C})\hat{m} = \hat{T}d + \alpha\hat{C}Cm_{apr} \quad (7)$$

Solving equation (7) using conjugate gradient technique requires number of iterations $i \leq \left\lceil \frac{1}{2} \sqrt{k} \ln\left(\frac{2}{\epsilon}\right) \right\rceil$, where ϵ represents the factor by which the residuals is minimized. Using $\epsilon = 0.001$ requires number of iteration $i \leq 3.8\sqrt{k}$, and a matrix-vector multiplication requires $O(l)$ operations, where (l) is the number of nonzero entries in the matrix. In our problem k is not a small value even for the preconditioned problem $k \geq 10^4$. The complexity of the considered algorithm without considering the influence of band-limited noise on the problem is still very high. The influence of noise on the system is not trifling and prefiltering process is not enough to resolve signal arrivals from noise.

3. Wavelet Based Noise Removal and Imaging

To enhance signal predictions and to improve Eigen structures clustering of the regularized Hessian matrix a wavelet-based approach is proposed. Our approach is utilizing from section 2 results and incorporating the prior knowledge on the reflectivity pattern through simple models, which defines a set of wavelet coefficients where (m) is guaranteed to be there. The estimator is optimized by minimizing the maximum risk of the entire wavelet coefficients. Let us revisit the synthetic data modeling of equation (2) and apply the adjoint operator (\bar{T}) to it:

$$\bar{T}d = \bar{T}Tm + \bar{T}n \quad (8)$$

The left side of equation (8) is part of the solution of equation (7), to minimize the variation between estimated model and actual one the second term of equation (8) needs to be removed. It may drastically deteriorate the clustering

efficiency achieved by the regularization term and so enhance the instability probability. The second term of equation (8) is no longer white but it is still Gaussian due to the linearity of the operator (\bar{T}) . The problem is now how to remove the growing effect of noise at high frequencies. Similar approach is studied by [12] and clarified by [13]. The difference here is that noise grows up with the increase of spatial and temporal frequencies, which limits the use of a thresholding estimator with nearly minimax risk. In order to achieve our goals a nonlinear estimator based on linear estimation theory and thresholding is to be achieved, then bounded scale variation to be determined. Transforming equation (8) using orthogonal wavelet bases leads to:

$$W_{Td} = W_{Tm} + W_{Tn} \quad (9)$$

The subscripts in equation (9) are used to indicate filtered parameters. Applying the same concepts of [14] for linear least square estimator where $\hat{W}_m = QW_d$, the optimal linear operator Q is determined by:

$$Q = [R_m + R_n]^{-1} R_m \quad (10)$$

In equation (10), R_m and R_n are diagonal correlation matrices for the reflectivity model and the noise. Since correlation matrices of either the model or the noise are not available. We follow the same procedure described on [14] to get an estimate of the filtered model correlation matrix and noise correlation matrix. The problem in this approach occur when the diagonal elements of Q is dominated by the noise power. To limit such effect, we use a nonlinear version of the estimator that employs a hard thresholding process for those noisy events. For a Gaussian random variable, [15] proved that using a threshold $Th = \sigma\sqrt{2\log_e L}$, the thresholding risk is not much above that of linear minimax risk, where σ is the noise standard deviation and L is the length of the data set. Due to the structure of our problem, different thresholds are used, where low frequency data can be processed using $Th = \sigma\sqrt{2\log_e(L/2)}$, while the threshold for high frequency data is determined by the maximum absolute value of the wavelet coefficient in the range $[L/2, L]$:

$$Th = \begin{cases} \sigma\sqrt{2\log_e(L/2)} & \text{if } \sigma\sqrt{2\log_e(L/2)} \leq \max |W_d| \\ \infty & \text{else} \end{cases} \quad (11)$$

Decomposing this range may achieve better results where our goal is to limit the influence of those data that lies at the border of the Nyquist frequency with a marginal zone that ensures their removal. Using equation (11) can still achieve improved results. The values of σ_1 and σ_2 are achieved by $\sigma_i = \frac{1}{0.675} \text{median}(\text{abs}(\theta_i))$, where θ_1 spans low frequency wavelet coefficients and θ_2 spans high frequency wavelet coefficients. The thresholded nonlinear estimator is now:

$$\hat{W}_m = \begin{cases} QW_d & |QW_d| \geq Th \\ 0 & |QW_d| < Th \end{cases} \quad (12)$$

The reconstructed wavelet coefficients are highly clustered in a way that strengthen the energy in limited number of coefficients that approximate the eigen values within that band. This reformation process will inherently improve the convergence of the conjugate gradient solver discussed in section 2. Moreover, due to the properties of wavelet domain, different wavelet levels have minor correlative properties, which define each band as a distinct problem that needs to be iteratively reconstructed. Using this approach adds the flavor of nearly optimal noise removal and fast convergence.

4. Results and Discussion

In this section an experimental simulation investigation will be carried out to evaluate the performance of the developed wavelet based echo-imaging technique. To generalize the results of simulation, the influence of various flaw types within the post tensioning ducts and within concrete structural elements used in highway bridges will be included. The velocity and density models are adopted from [16]. The force time function resulting from the impact of a solid sphere on a solid body can be approximated as a half-cycle sine wave with $F(t) = F_{\max} \sin\left(\frac{\pi t}{t_c}\right)$, where F_{\max} is the maximum applied

impact force, and t_c is the contact time for the impact. The impact time is of great influence on the achieved results, where it determines the minimum size of the discontinuity or flaw that can be resolved vertically [16]. Since the source waveform is deterministic, using the wavelet domain to vertically deconvolve the received data will greatly improve the vertical resolution and remove the distortion effect of the source waveform on the synthetic data.

To demonstrate the efficiency of the proposed approach in enhancing both horizontal and vertical resolution of the reconstructed images a 12-point diffractor model is used. The reflectivity value of each one is assumed to be 1. The propagation velocity is chosen to be the compressional velocity of the concrete medium. The space between receivers is 5 cm and the aperture is limited by 5-m. Figure 1 shows respectively the model, zero-offset synthetic data, the image using Kirchhoff migration [10], the image using [8], the image using [7], and the image using our approach. As shown in Figure 1 the proposed approach shows focused image with less artifacts than the other algorithms. Figure 2 shows reconstructed images of the same model contaminated by Gaussian noise, the synthetic data has $SNR = 10dB$. The proposed approach shows the ability of removing the noise with affecting the actual positions of the diffractors. Other techniques show spurious events that smear diffractor locations and degrade their imaging capability. To improve the performance of other techniques, we performed wiener filtering to the data and then applied them. The results show better localization to the actual diffractors and noisy events that mimic them.

In this part of the paper, two post-tensioned concrete structures with flaws will be studied. The first specimen represents a 3.66-m by 1.22-m by .39-m-thick (12-ft by 4-ft by 15.5-in-thick) concrete slab containing one 76-mm (3-in) diameter straight corrugated steel-grouted duct and one 76-mm (3-in) diameter

straight corrugated PVC-grouted duct with a wall thickness of 1.6-mm (1/16 -in). Voids were introduced inside these ducts, including three voids with sizes of 0.13, 0.28, and 0.46 m long (5, 11, and 18 in long) in the steel duct, and two voids with sizes of 0.15 and 0.47 m long (6 and 18.5 in long) in the PVC duct. This model was used to evaluate the reliability of the technique in detection of voids inside post-tensioning ducts. Figure 3 shows the reflectivity model of specimen 1, synthetic data with $SNR = 10$, and the wavelet based image. The parameters involved in this experiment are: spatial sampling $\Delta x = 5cm$, the impact time is $t_c = 20\mu s$, and sampling time $dt = 2\mu s$. The results ensure the ability of the imaging process in determining the exact location of the voids and their actual sizes. A noticeable limitation appears at high spatial frequencies where both signal and noise shares the same spectrum; the imaging technique tries to focus the events while opposed by noise. This limitation is confined by Δx and so can be enhanced by decomposing the high frequency events using wavelet packet bases that will significantly reduce the influence of high frequency noise but will increase the computational complexity. Also, reducing Δx will be significant but such improvement will limit the feasibility of the process. Since apriori knowledge of the structure is highly correlated with the age of the bridge, applying predictive techniques to estimate the data between consecutive sensors will resolve the problem.

The second specimen is a 0.91-m by 0.76-m-deep by 7.32-m-long (3-ft by 2.5-ft-deep by 24-ft-long) concrete beam containing one longitudinal 76-mm (3-in) diameter draped corrugated galvanized steel duct and one 76-mm (3-in) and 1.6-mm-thick (1/16 -in-thick) PVC duct, which was also draped in the longitudinal direction. Both longitudinal ducts contained nine 12.7-mm (0.5-in) diameter pre-stressing strands. There are also three diffractors with sizes of 0.15, 0.3, and 0.47 m long (6, 12, and 18.5 in long) in the PVC duct. This model is used to evaluate the reliability of the technique in imaging deep post tensioned members and differentiating different flaw shape and sizes. As shown in Figure 4, the existence of the flaws smears the synthetic data and shows an impulse that spread all over the z domain at each location of these flaws. The reason is that the reflectivity values at these locations are so small with plus and minus polarities. Such values with sharp edges will cause unstable effect in the wave equation that will drive it to its extreme conditions and so unstable results achieved. The reconstructed image conserve both sharp and smooth details and elegantly diminish the effect of the noise. The exact locations in deep and within the concrete beam are also detected. Increasing the spatial frequency and applying the nonlinear wavelet estimator on wavelet packet will significantly improve both temporal and spatial resolutions. Our observations indicate combining both predictive estimation and wavelet imaging will maximize the efficiency of this technique.

5. Conclusions

A novel imaging technique that preserves both temporal and spatial details is proposed. The imaging approach utilizes from the apriori history of the reflectivity pattern and uses this

information in an optimum way to estimate the corresponding structure of the model. It applies a constrained parameterization process that attends to minimize the total variation of the model with respect to its history. Due to the limitation of aperture, incompleteness of data set, and variability of medium parameters, data will be dominated by high spatial frequencies where noise there grows as function of data lengths. Such occurrence will degrade the optimization process and enhance probability of instability. To overcome these deficiencies, a wavelet based imaging approach is anticipated that applies a nonlinear estimation process to separate signal components from noise corruptions. The algorithm shows superior results when compared with standard and developed imaging techniques especially in the presence of noise and complex interfaces medium. The algorithm was applied successfully on concrete bridge structures. The detection of various flaws inside and beneath post-tensioned beams is demonstrated. To enhance the manifestation of the considered approach we suggest applying predictive interpolation techniques to reduce the spatial sampling interval and using wavelet packet to minimize the weight of high frequency noise that deteriorate the efficiency of the nonlinear estimator.

6. References

- [1] A. N. Tikhonov, and V. Y. Arsenin, "Solution of ill posed problems", V. H. Winston and Sons, 1977.
- [2] B. D. Carlson" Covariance matrix estimation errors and diagonal loading in adaptive arrays", IEEE Trans. Aerosp. Electron. Sys., 1988, AES-24: pp. 397-401.
- [3] Yilmaz, O., 1987," Seismic data processing", Society of Extrapolation Geophysicists.
- [4] T. Nemeth; C. Wu; G. T. Schuster "LEAST-SQUARES MIGRATION OF INCOMPLETE REFLECTION DATA", Geophysics v 64 n 1,1999, pp 208-221.
- [5] L. I. Rudin, S. Osher and E. Fatmi " Nonlinear total variation based noise removal algorithms" Physica D, 60, 1992, pp. 259-268.
- [6] C. R. Vogel , and M. E. Oman " Fast total variation based reconstruction of noisy, blurred images", IEEE Trans. Image Processing, 7, 1998, pp. 813-824.
- [7] O. Portniaguine, and M. S. Zhdanov," Focusing geophysical inversion images", Geophysics v 64 n 3,1999, pp 874-887.
- [8] V. K. Madiseti, and D. G. Messerschmitt " Seismic migration algorithms in parallel computers", IEEE Trans. Signal Processing. Vol. 39. no. 7., 1991, pp. 1642-1654.
- [9] A. S. Al-Fahoum, " Impact Echo-Imaging For Nondestructive Detection Of Flaws In Post-Tensioned Concrete Structures" Ph.D. Proposal, EE Dept., UWM, 1999.
- [10] J. F. Claerbout, "Earth soundings analysis: Processing versus inversion", Blackwell Science Ltd, 1996.
- [11] J. C. Gilbert, and J. Nocedal, " Global convergence properties of conjugate gradient methods for optimization", SIAM journal on optimization 2, no. 1,1992, pp. 21-42.
- [12] D. Donoho" Nonlinear solution of linear inverse problems by wavelet-vaguelette decompositions", J. of Appl. And Comput. Harmonic Analysis, 2(2),1995, pp. 101-126.
- [13] F. Abramovich, and B. W. Silverman," Wavelet decomposition approach to statistical inverse problems", Biometrika, 85(1), 1998, pp. 115-129.
- [14] A. S. Al-Fahoum, and A. M. Reza" Combined Edge Crispiness and Statistical Differencing for Deblocking JPEG Compressed Images"Submitted to IEEE Trans. On IP, 1999.
- [15] D. Donho, and I. Johnstone, " Ideal spatial adaptation via wavelet shrinkage", Biometrika, 81, 1994, pp. 425-455.
- [16] A. Ghorbanpoor,"Evaluation of Post-Tensioned concrete Bridge Structures by the Impact echo-Technique", FHEWA-RD-92-096, U.S. Department of transportation, 1993.

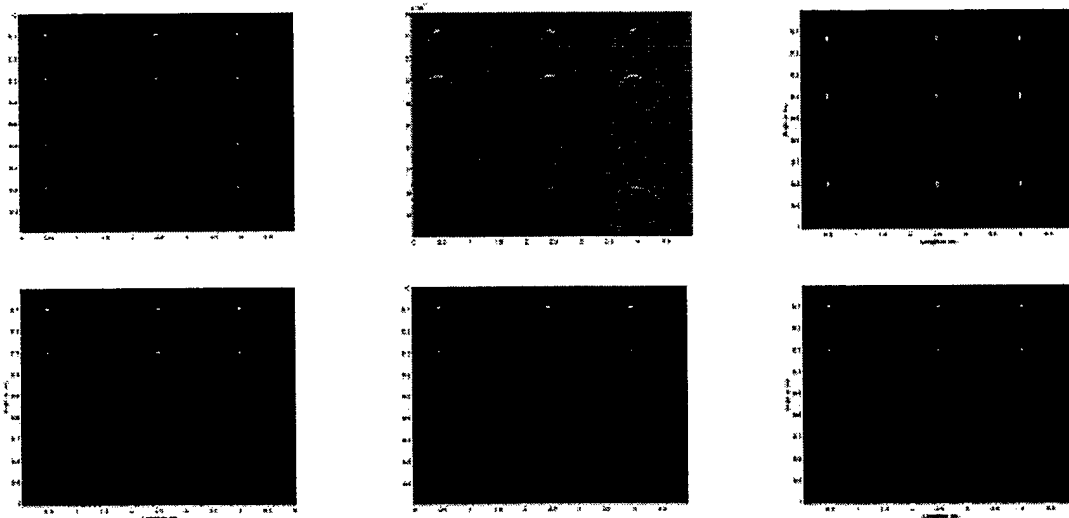


Figure1 A 12-point diffractor model, synthetic data, and comparison between four different imaging techniques.

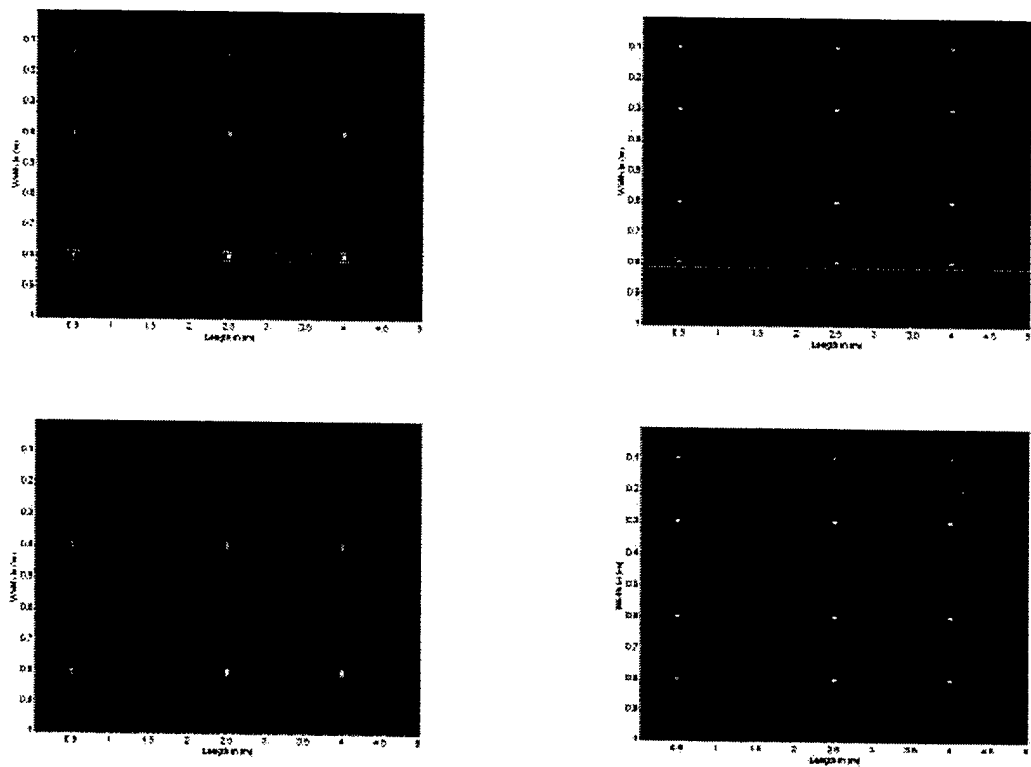


Figure 2 Imaging the noisy 12-point diffractor model using four different imaging techniques.

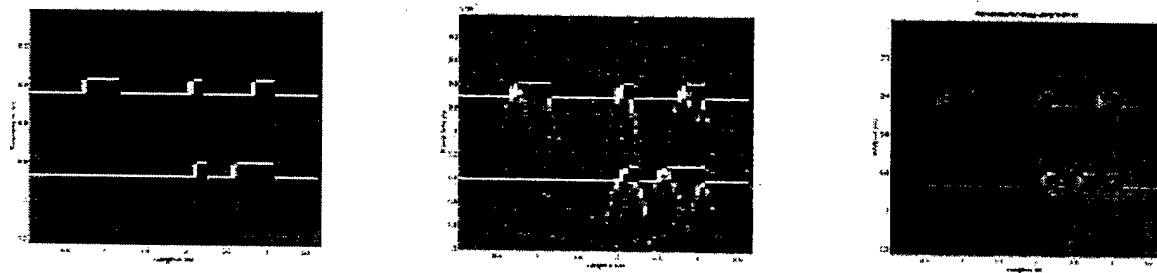


Figure 3 L) Concrete slab with partially grouted metal and plastic ducts. M) Synthetic data with $SNR = 10dB$ and R) Image using wavelet based approach.

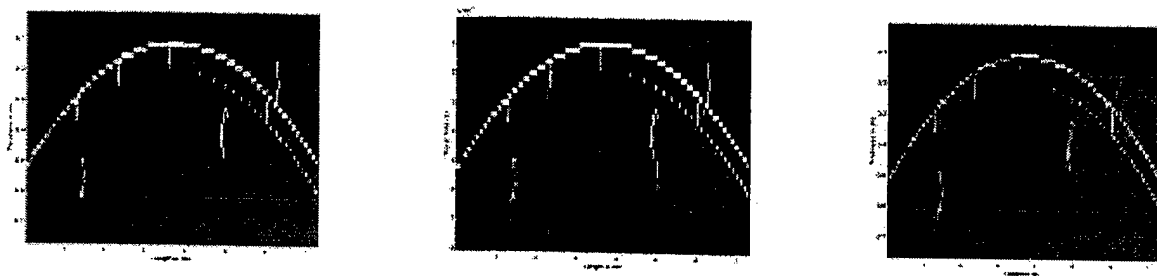


Figure 4 L) Large concrete beam with draped and crossed metal and plastic ducts. M) Synthetic data with $SNR = 10dB$ and R) Image using wavelet based approach.

ADAPTIVE BEAMPATTERN CONTROL USING QUADRATIC CONSTRAINTS FOR CIRCULAR ARRAY STAP

Kristine L. Bell, Harry L. Van Trees, and Lloyd J. Griffiths

School of IT & Engineering, George Mason University
Fairfax, VA 22030-4444, USA

kbell@gmu.edu, hlvan@gmu.edu, griffiths@gmu.edu

ABSTRACT

A general framework for adaptive and non-adaptive space-time beampattern synthesis using quadratic beampattern constraints with minimum mean-square error (MMSE) and linearly constrained minimum variance (LCMV) beamforming is presented. Main beam and sidelobe pattern control is achieved by imposing a set of inequality constraints on the weighted mean-square error between the adaptive pattern and a desired beampattern over a set of angle-Doppler regions. An iterative procedure for satisfying the constraints is developed which can be applied as post-processing to standard MMSE or LCMV beamformers. The algorithm is used to synthesize a nearly uniform sidelobe level quiescent pattern for the circular UHF Electronically Scanned Array (UESA), and to control sidelobe levels for the same array in an adaptive manner. Performance results using data provided by Lincoln Lab show that under low sample support conditions, sidelobes can be effectively suppressed while maintaining high signal-to-interference plus noise ratio, and deep nulls on clutter and interferers.

1. INTRODUCTION

Space-Time Adaptive Processing (STAP) used in airborne radar systems combines signals from N antenna array elements and M pulses to adaptively suppress clutter and jamming in both the space (angle) and time (Doppler frequency) dimension. Traditionally, STAP systems have used a rotating linear array configuration, however a fixed circular ring array is currently under development under the UHF Electronically Scanned Array (UESA) program sponsored by the Office of Naval Research (ONR). The array consists of 54 directional antenna elements with suppressed backlobes. Only 20 of the elements will be used at a time to transmit and receive [2]. With this configuration, the antenna can be scanned mechanically in 6.67° increments by choosing the appropriate 20-element sector, and scanned electronically

$\pm 3.33^\circ$ with the chosen sector of elements. The circular array configuration has the potential to provide continuous 360° availability, however it has some potentially negative impacts for STAP algorithms [2]. First, the clutter rank is increased in a manner similar to the increase from misalignment with the velocity vector in linear arrays. Second, the clutter locus varies with range. This decreases the number of range gates that can be averaged to reliably estimate the clutter covariance matrix.

The foundation of most STAP techniques is the Minimum Variance Distortionless Response (MVDR) processor [1]. The standard MVDR processor weights are designed to minimize the processor output power subject to a linear distortionless constraint in the angle-Doppler steering direction. The same weights can be obtained, to within a scale factor, using the minimum mean square error (MMSE) criterion, where the weights are designed to minimize the mean square error (MSE) between the processor output and a reference signal [3]. The MVDR/MMSE beamformer can have unacceptably large sidelobes and mainlobe squinting due to sensor perturbations, pointing error, and low sample support. In radar systems, this behavior can lead to increased false alarms from clutter and unexpected interferers.

To mitigate this problem, a general framework was developed for adaptive and non-adaptive beampattern synthesis for non-linear arrays based on minimum mean-square error (MMSE) beamforming with quadratic beampattern constraints (QPC) [4]. In this technique, main beam and sidelobe pattern control is achieved by imposing a set of inequality constraints on the weighted mean-square error between the adaptive pattern and a desired beampattern over a set of angle-Doppler regions. The algorithm uses an iterative procedure for satisfying the constraints which can be applied as post-processing to standard STAP processors. In this paper, we extend the results to linearly constrained minimum variance (LCMV) processing, and present circular array STAP results with data provided by MIT Lincoln Lab [5].

This research was supported by ONR Grant #N00014-99-1-0691.

2. LCMV BEAMFORMING WITH QUADRATIC PATTERN CONSTRAINTS

Quadratic pattern constraints were first introduced in the minimum variance, or minimum output power framework. In [6] and [7], processor output power is minimized subject quadratic pattern constraints, while in [8] and [9], the output power is minimized subject to the standard distortionless constraint as well as quadratic pattern constraints. In [4], we used a MMSE approach in which the MSE between a reference signal and the array output is minimized (the standard MMSE beamforming criterion [3]) subject to a set of quadratic pattern constraints.

An important feature of the MMSE-QPC formulation in [4] is the specification of multiple quadratic pattern constraints. By proper choice of the number of constraints, the angle-Doppler regions to which they apply, and the desired beampatterns in those regions, the level of pattern control can be traded off against algorithmic complexity. At one extreme, low-complexity techniques can be obtained based on one or two constraints similar to the adaptive pattern control methods in [6]-[9]. At the other extreme, we can achieve tight pattern control using many constraints, in a manner similar to the technique in [10]. Between the two extremes, an approach using several constraints was shown to achieve good pattern control and maintain a high SINR with reasonable complexity.

Furthermore, the MMSE solution allowed development of an computationally efficient iterative procedure for satisfying the constraints which can be applied as post-processing to the standard MMSE STAP processor. However, there are cases where linear main beam constraints or sidelobe null constraints are necessary, and we would like to develop an iterative QPC technique for LCMV beamforming.

2.1. Direct LCMV Problem Formulation

We assume a STAP model with N antenna elements and M pulses. Let $\mathbf{v}(\theta, \phi, \omega)$ denote $NM \times 1$ space-time array response vector to a signal arriving with elevation angle θ , azimuth angle ϕ , and Doppler frequency ω . We partition azimuth angle-Doppler space into r sectors, $\Omega_1, \dots, \Omega_r$, as shown in Figure 1. In this illustration, the elevation angle space has only one partition and the sectors are cubes, however more general partitions of azimuth angle, elevation angle, and Doppler space can be used. Let $B_{d,i}(\theta, \phi, \omega) = \mathbf{w}_{d,i}^H \mathbf{v}(\theta, \phi, \omega)$ be a desired beampattern in the region Ω_i , and $\mathbf{w}_{d,i}$ be the corresponding weight vector. The MSE between the beampattern generated by the adaptive weight vector \mathbf{w} and the desired beampattern over the region Ω_i is given by

$$\epsilon_i^2 = \int_{\Omega_i} |\mathbf{w}^H \mathbf{v}(\theta, \phi, \omega) - \mathbf{w}_{d,i}^H \mathbf{v}(\theta, \phi, \omega)|^2 d\Omega. \quad (1)$$

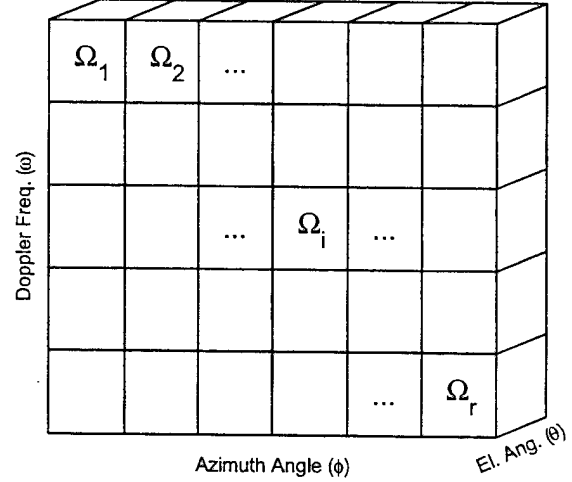


Figure 1: Partition of Angle-Doppler space

The error can be written compactly as

$$\epsilon_i^2 = (\mathbf{w} - \mathbf{w}_{d,i})^H \mathbf{Q}_i (\mathbf{w} - \mathbf{w}_{d,i}) \quad (2)$$

where

$$\mathbf{Q}_i = \int_{\Omega_i} \mathbf{v}(\theta, \phi, \omega) \mathbf{v}(\theta, \phi, \omega)^H d\Omega. \quad (3)$$

Thus the pattern error is a quadratic function of the adaptive weight vector.

Adaptive weights are designed according to the standard LCMV criterion, while limiting the deviations from the desired pattern using quadratic pattern constraints. Let \mathbf{C} be the $NM \times d$ constraint matrix and \mathbf{f} be the $d \times 1$ vector of constraint values. The LCMV-QPC optimization problem is

$$\begin{aligned} \min \quad & \mathbf{w}^H \mathbf{R}_x \mathbf{w} \quad \text{st.} \quad \mathbf{C}^H \mathbf{w} = \mathbf{f} \\ \text{st.} \quad & (\mathbf{w} - \mathbf{w}_{d,i})^H \mathbf{Q}_i (\mathbf{w} - \mathbf{w}_{d,i}) \leq L_i \quad i = 1, \dots, r \end{aligned} \quad (4)$$

The optimization is straightforward, however the solution is somewhat complex. For notational convenience, define

$$\mathbf{R}_Q = \mathbf{R}_x + \sum_{i=1}^r \lambda_i \mathbf{Q}_i \quad (5)$$

$$\mathbf{w}_Q = \sum_{i=1}^r \lambda_i \mathbf{Q}_i \mathbf{w}_{d,i}. \quad (6)$$

The LCMV-QPC solution is given by

$$\begin{aligned} \mathbf{w} = & \mathbf{R}_Q^{-1} \mathbf{C} \left(\mathbf{C}^H \mathbf{R}_Q^{-1} \mathbf{C} \right)^{-1} \left(\mathbf{f} - \mathbf{C}^H \mathbf{R}_Q^{-1} \mathbf{w}_Q \right) \\ & + \mathbf{R}_Q^{-1} \mathbf{w}_Q. \end{aligned} \quad (7)$$

This is the multiple constraint extension of the quadratically constrained MVDR processor developed in [8], [9]. In

this processor a sum of 'loading' matrices $\mathbf{Q}_i, i = 1, \dots, r$ are added to the sample covariance matrix, and a weighted sum of desired weight vector terms $\mathbf{Q}_i \mathbf{w}_{d,i}, i = 1, \dots, r$ appears as well. The loading terms balance the adaptive pattern with the desired pattern. The relative contribution of these terms can be adjusted to achieve pattern control while maintaining high signal-to-interference-plus-noise ratio (SINR). There are a set of optimum loading levels $\lambda_i, i = 1, \dots, r$ which satisfy the constraints, however there is no closed form solution for the loading levels, even when $r = 1$. It can be shown that the mean-square pattern error decreases with increasing λ_i , but at the expense of decreased interference suppression. The loading levels must be chosen judiciously to achieve pattern control while maintaining high signal-to-interference-plus-noise ratio (SINR).

In [4], an iterative procedure was for computing the optimum loading levels in the quadratically constrained MMSE processor. It was based on a first order Taylor series approximation of the weight vector for small loading increments. This technique can be applied in principle to the quadratically constrained LCMV weights, but the result does not have the elegance and computational efficiency of the MMSE solution. The Generalized Sidelobe Canceller (GSC) [11] form of the LCMV processor provides the key to a better solution.

2.2. GSC LCMV Problem Formulation

In the GSC, the weights are partitioned into a fixed constrained weight vector \mathbf{w}_c , and a reduced dimension adaptive weight vector, \mathbf{w}_a . The relationship to the total weight vector is

$$\mathbf{w} = \mathbf{w}_c - \mathbf{B}\mathbf{w}_a, \quad (8)$$

where \mathbf{B} is the $NM \times (NM - d)$ blocking matrix orthogonal to \mathbf{C} and \mathbf{w}_c is given by

$$\mathbf{w}_c = \mathbf{C}(\mathbf{C}^H \mathbf{C})^{-1} \mathbf{f}. \quad (9)$$

Any weight vector with this form satisfies the constraint $\mathbf{C}^H \mathbf{w} = \mathbf{f}$, therefore the optimization problem becomes

$$\begin{aligned} \min \quad & (\mathbf{w}_c - \mathbf{B}\mathbf{w}_a)^H \mathbf{R}_x (\mathbf{w}_c - \mathbf{B}\mathbf{w}_a) \\ \text{s.t.} \quad & (\mathbf{w}_c - \mathbf{B}\mathbf{w}_a - \mathbf{w}_{d,i})^H \mathbf{Q}_i (\mathbf{w}_c - \mathbf{B}\mathbf{w}_a - \mathbf{w}_{d,i}) \leq L_i \\ & i = 1, \dots, r \end{aligned} \quad (10)$$

Defining

$$\mathbf{R}_B = \mathbf{B}^H \mathbf{R}_x \mathbf{B} \quad (11)$$

$$\mathbf{Q}_{B,i} = \mathbf{B}^H \mathbf{Q}_i \mathbf{B} \quad (12)$$

$$\mathbf{w}_B = \mathbf{B}^H \mathbf{R}_x \mathbf{w}_c \quad (13)$$

$$\mathbf{q}_{B,i} = \mathbf{B}^H \mathbf{Q}_i (\mathbf{w}_c - \mathbf{w}_{d,i}), \quad (14)$$

the constraints can also be written as

$$\mathbf{w}_a^H \mathbf{Q}_{B,i} \mathbf{w}_a - 2\Re(\mathbf{q}_{B,i}^H \mathbf{w}_a) \leq \eta_i \quad i = 1, \dots, r \quad (15)$$

where

$$\eta_i = L_i - (\mathbf{w}_c - \mathbf{w}_{d,i})^H \mathbf{Q}_i (\mathbf{w}_c - \mathbf{w}_{d,i}). \quad (16)$$

The solution is given by

$$\mathbf{w}_a = \left(\mathbf{R}_B + \sum_{i=1}^r \lambda_i \mathbf{Q}_{B,i} \right)^{-1} \left(\mathbf{w}_B + \sum_{i=1}^r \lambda_i \mathbf{q}_{B,i} \right). \quad (17)$$

This is similar in form to the MMSE-QPC solution in [4], and it is now straightforward to derive an iterative update procedure for this weight vector.

2.3. Iterative Implementation

The algorithm is initialized with the standard GSC weights $\mathbf{w}_a^{(0)} = \mathbf{R}_B^{-1} \mathbf{w}_B$. At each iteration, the pattern errors are computed and checked against the constraints. If a constraint is exceeded, the loading for that sector is increased by an incremental factor $\Delta_i^{(p)}$, i.e. $\lambda_i^{(p)} = \lambda_i^{(p-1)} + \Delta_i^{(p)}$. The the covariance matrix and weights are updated according to

$$\mathbf{R}_B^{(p)} = \mathbf{R}_B + \sum_{i=1}^r \lambda_i^{(p)} \mathbf{Q}_{B,i} \quad (18)$$

$$\mathbf{w}_B^{(p)} = \mathbf{w}_B + \sum_{i=1}^r \lambda_i^{(p)} \mathbf{q}_{B,i} \quad (19)$$

$$\mathbf{w}_a^{(p)} = \left(\mathbf{R}_B^{(p)} \right)^{-1} \mathbf{w}_B^{(p)}, \quad (20)$$

This is a computationally expensive procedure because the covariance matrix is inverted at each iteration. However, if the incremental loading levels are small, the update can be accomplished without re-inverting the matrix. Let $\mathbf{S}^{(p)}$ denote the covariance matrix inverse at the p th iteration,

$$\begin{aligned} \mathbf{S}_B^{(p)} &= \left(\mathbf{R}_B^{(p)} \right)^{-1} = \left(\mathbf{R}_B^{(p-1)} + \sum_{i=1}^r \Delta_i^{(p)} \mathbf{Q}_{B,i} \right)^{-1} \\ &= \left(\left(\mathbf{S}_B^{(p-1)} \right)^{-1} + \sum_{i=1}^r \Delta_i^{(p)} \mathbf{Q}_{B,i} \right)^{-1}. \end{aligned} \quad (21)$$

The GSC steering vector at each iteration can be written as

$$\mathbf{w}_B^{(p)} = \mathbf{w}_B^{(p-1)} + \sum_{i=1}^r \Delta_i^{(p)} \mathbf{q}_{B,i}. \quad (22)$$

Using (21) and (22) in (20), the adaptive weight vector is given by

$$\begin{aligned} \mathbf{w}_a^{(p)} &= \mathbf{S}_B^{(p)} \mathbf{w}_B^{(p)} \\ &= \left(\left(\mathbf{S}_B^{(p-1)} \right)^{-1} + \sum_{i=1}^r \Delta_i^{(p)} \mathbf{Q}_{B,i} \right)^{-1} \cdot \\ &\quad \left(\mathbf{w}_B^{(p-1)} + \sum_{i=1}^r \Delta_i^{(p)} \mathbf{q}_{B,i} \right). \end{aligned} \quad (23)$$

Expanding this expression in a first order Taylor series approximation as in [4], $\mathbf{w}_a^{(p)}$ can be updated by:

$$\mathbf{w}_a^{(p)} = \mathbf{w}_a^{(p-1)} - \mathbf{S}_B^{(p-1)} \sum_{i=1}^r \Delta_i^{(p)} \left(\mathbf{Q}_{B,i} \mathbf{w}_a^{(p-1)} - \mathbf{q}_{B,i} \right). \quad (24)$$

Similarly, the matrix inverse update is

$$\mathbf{S}_B^{(p)} = \mathbf{S}_B^{(p-1)} - \mathbf{S}_B^{(p-1)} \left(\sum_{i=1}^r \Delta_i^{(p)} \mathbf{Q}_{B,i} \right) \mathbf{S}_B^{(p-1)}. \quad (25)$$

One way to achieve fast convergence while ensuring that the small update assumption is valid is to let $\Delta_i^{(p)}$ be a fraction of the of the current loading value, i.e. $\Delta_i^{(p)} = \alpha \lambda_i^{(p)}$, where α in the range 0.3 to 0.5 seems to work well. This requires that the initial loading level be non-zero. One possibility is to initialize all of the loading levels to some small value, i.e. $\lambda_i^{(0)} = \lambda_0, i = 1, \dots, r$. The algorithm is initialized by

$$\mathbf{S}_B^{(0)} = \left(\mathbf{R}_B + \lambda_0 \sum_{i=1}^r \mathbf{Q}_{B,i} \right)^{-1} \quad (26)$$

$$\mathbf{w}_a^{(0)} = \mathbf{S}_B^{(0)} \left(\mathbf{w}_B + \lambda_0 \sum_{i=1}^r \mathbf{q}_{B,i} \right). \quad (27)$$

At each iteration, the weights are updated by

1. for $i = 1, \dots, r$

$$\text{if } \mathbf{w}_a^{(p-1)H} \mathbf{Q}_{B,i} \mathbf{w}_a^{(p-1)} - 2\Re e \left(\mathbf{q}_{B,i}^H \mathbf{w}_a^{(p-1)} \right) > \eta_i$$

$$\text{then } \Delta_i^{(p)} = \alpha \lambda_i^{(p)}, \text{ else } \Delta_i^{(p)} = 0$$

$$\lambda_i^{(p)} = \lambda_i^{(p-1)} + \Delta_i^{(p)}$$

2. $\mathbf{Q}_B^{(p)} = \sum_{i=1}^r \Delta_i^{(p)} \mathbf{Q}_{B,i}$ (28)

3. $\mathbf{q}_B^{(p)} = \mathbf{Q}_B^{(p)} \mathbf{w}_a^{(p-1)} + \sum_{i=1}^r \Delta_i^{(p)} \mathbf{q}_{B,i}$ (29)

4. $\mathbf{w}_a^{(p)} = \mathbf{w}_a^{(p-1)} - \mathbf{S}_B^{(p-1)} \mathbf{q}_B^{(p)}$ (30)

5. $\mathbf{S}_B^{(p)} = \mathbf{S}_B^{(p-1)} - \mathbf{S}_B^{(p-1)} \mathbf{Q}_B^{(p)} \mathbf{S}_B^{(p-1)}$. (31)

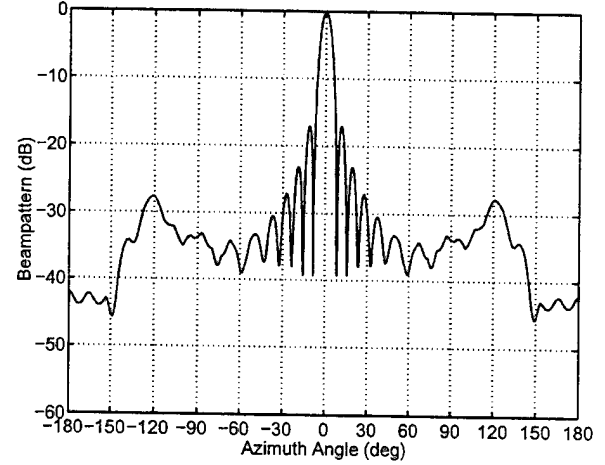


Figure 2: UESA Conventional Spatial Beampattern

Both the MMSE-QPC and LCMV-QPC techniques can be used for non-adaptive pattern synthesis by letting $\mathbf{R}_x = \mathbf{I}$. They generalize the techniques in [10] and [12] for developing low sidelobe quiescent patterns for arbitrary arrays, and can be used for developing a tapered steering vector for use in the adaptive methods.

3. EXAMPLES

In the MIT Lincoln Lab data set [5], there are $N = 20$ elements and $M = 18$ pulses with a 300 Hz pulse repetition frequency. The UESA spatial beampattern is shown in Figure 2 and the space-time beampattern is shown in Figure 3.

First, the MMSE-QPC technique was used to synthesize a -35 dB uniform sidelobe level quiescent pattern steered to $\phi = 0^\circ$ and $\omega = 0$ Hz for a range of 50 km, which corresponds to $\theta = -10.5^\circ$. Angle-Doppler space was partitioned into one elevation angle sector $\theta \in (-11^\circ, -2^\circ)$, 11 azimuth angle sectors $\phi \in (-12^\circ, 12^\circ), \pm(12^\circ, 30^\circ), \pm(30^\circ, 60^\circ), \pm(60^\circ, 100^\circ), \pm(100^\circ, 140^\circ), \pm(140^\circ, 180^\circ)$, and 5 Doppler sectors $\omega \in (-30, 30), \pm(30, 90), \pm(90, 150)$ Hz for a total of $1 \times 11 \times 5 = 55$ sectors. The desired pattern was set to zero outside of the mainlobe region, and the constraint levels were set to -35 dB times the volume of the sector. No constraint was used in the mainlobe region. The loading levels were initially set to $\lambda_0 = 10$ dB, and then iteratively increased in the sectors where the constraint was not met using $\alpha = 1.5$. The algorithm converged in five iterations. The final -35 dB sidelobe level pattern steered to $\phi = 0^\circ, \omega = 60$ Hz is shown in Figure 4.

Next, a scenario with two 30dB interference-to-noise ratio (INR) jammers at 60° and -20° , in addition to clutter, was considered. An 8 km training window (200 snapshots) was used to estimate the covariance matrix. The standard MMSE/LCMV processor weights were computed by

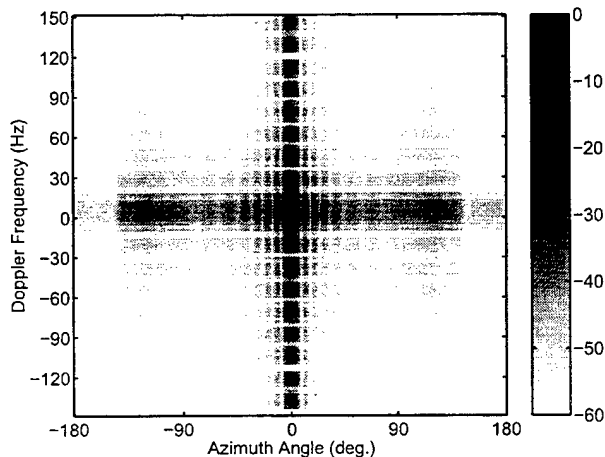


Figure 3: UESA Conventional Space-Time Beampattern

adding -30 dB diagonal loading to allow the covariance matrix to be inverted. The resulting space-time beampattern, and beampattern cuts are shown in Figures 5 and 8. The beamformer has put nulls on the clutter ridge and the two jammers, however the sidelobes are quite high.

The MMSE-QPC adaptive beamformer was used to reduce the sidelobes. The quiescent weights derived in the first example was used as the tapered steering vector. The initial loading levels were set to $\lambda_0 = 0.0013$, and then iteratively increased using $\alpha = 0.8$. In six iterations, the MMSE-QPC is able to reduce the sidelobes below the -35 dB level while maintaining a well behaved main-beam, and deep clutter and jammer nulls. The final beampattern is shown in Figures 6 and 9.

For comparison, the LCMV-QPC procedure was also applied to this scenario using the same initial loading levels and increment factor. The final patterns achieved in eight iterations are shown in Figures 7 and 10. The LCMV processor required a few more iterations because it started with higher sidelobes than the tapered MMSE processor, however it has a slightly higher SINR.

4. REFERENCES

- [1] J. Ward, "Space-Time Adaptive Processing for Airborne Radar," MIT Lincoln Laboratory Technical Report 1015, Dec. 1994.
- [2] M. Zatman, "Circular Array STAP," *IEEE Intl. Radar Conference (RADAR '99)*, Boston, MA, May 1999.
- [3] B. D. Van Veen and K. M. Buckley, "Beamforming: A Versatile Approach to Spatial Filtering," *IEEE Acoust., Speech, Sig. Process. Magazine*, pp. 4-24, Apr. 1988.
- [4] K. L. Bell and H. L. Van Trees, "Adaptive and Non-Adaptive Beampattern Control Using Quadratic Beam-

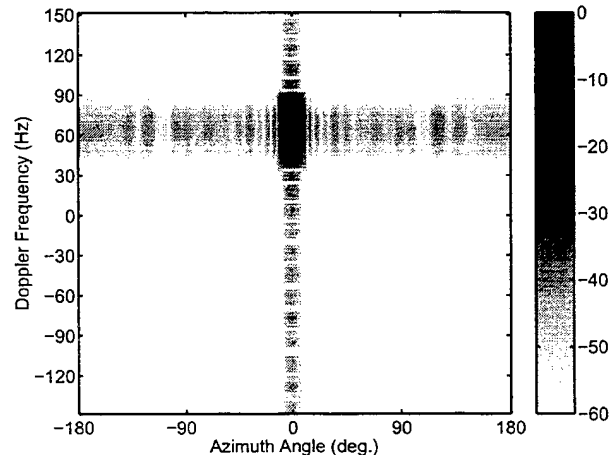


Figure 4: Low Sidelobe Level Quiescent Beampattern

pattern Constraints," *33rd Asilomar Conf. on Signals, Systems, and Computers*, Pacific Grove, CA, Oct. 1999.

- [5] M. Zatman and B. Freburger, "Circular STAP Data Package," May 17, 1999.
- [6] M. H. Er and A. Cantoni, "A New Approach to the Design of Broadband Element Space Antenna Array Processors," *IEEE J. Oceanic Eng.*, vol. 10, pp. 231-240, July 1985.
- [7] B. D. Van Veen, "Minimum Variance Beamforming with Soft Response Constraints," *IEEE Trans. Sig. Process.*, vol. 39, no. 9, pp. 1964-1972, Sept. 1991.
- [8] D. T. Hughes and J. G. McWhirter, "Sidelobe Control in Adaptive Beamforming Using a Penalty Function," *Fourth Intl. Symp. on Sig. Process. and Appl. (ISSPA '96)*, Gold Coast, Australia, Aug. 1996.
- [9] D. T. Hughes and J. G. McWhirter, "Using the Penalty Function Method to Cope with Mainbeam Jammers," *Third Intl. Conf. on Sig. Process. (ICSP '96)*, Beijing, China, Oct. 1996.
- [10] P. Y. Zhou and M. A. Ingram, "A New Synthesis Algorithm with Application to Adaptive Beamforming," *9th IEEE Workshop on Stat. Sig. and Array Processing*, Portland, OR, Sept. 1998.
- [11] L. J. Griffiths and C. W. Jim, "An Alternative Approach to Linearly Constrained Adaptive Beamforming," *IEEE Trans. Antennas Propagat.*, vol. 30, no. 1, pp. 27-34, Jan. 1982.
- [12] C. A. Olen and T. T. Compton, Jr., "A Numerical Pattern Synthesis Algorithm for Arrays," *IEEE Trans. Antennas Propagat.*, vol. 38, no. 10, pp. 1666-1676, Oct. 1990.

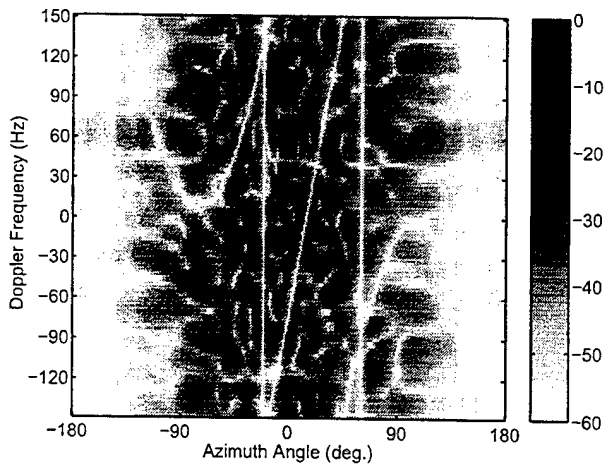


Figure 5: Initial Adaptive Beampattern

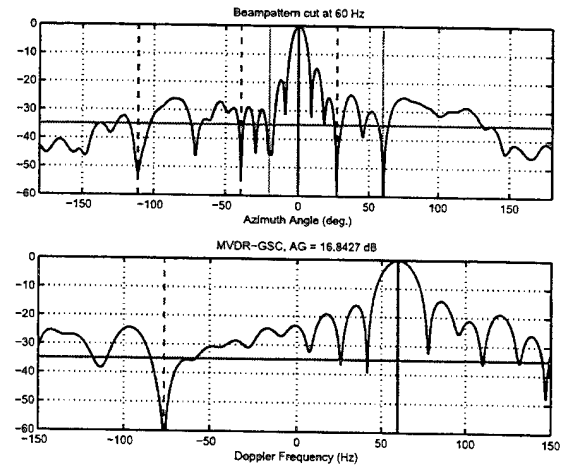


Figure 8: Initial Adaptive Beampattern

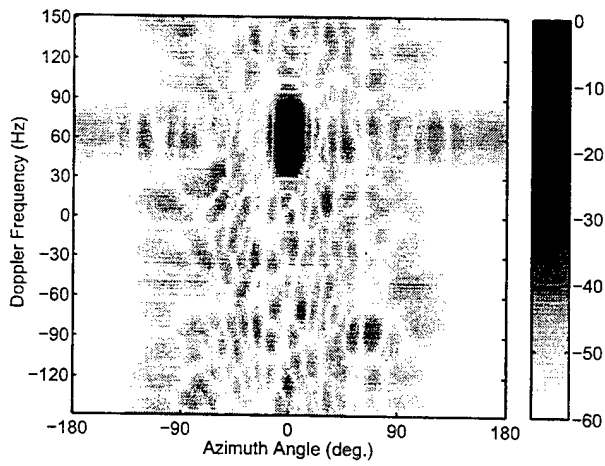


Figure 6: Final Adaptive Beampattern

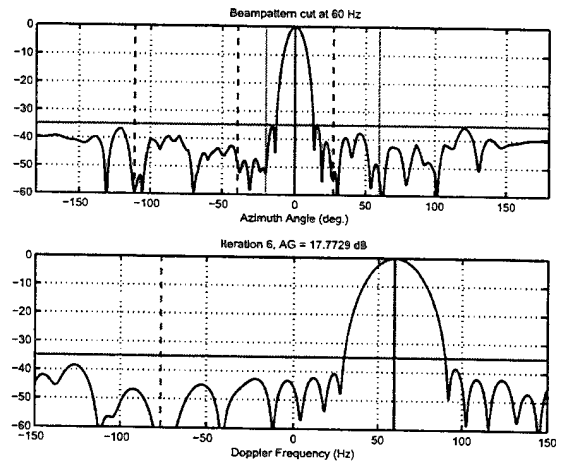


Figure 9: Initial Adaptive Beampattern

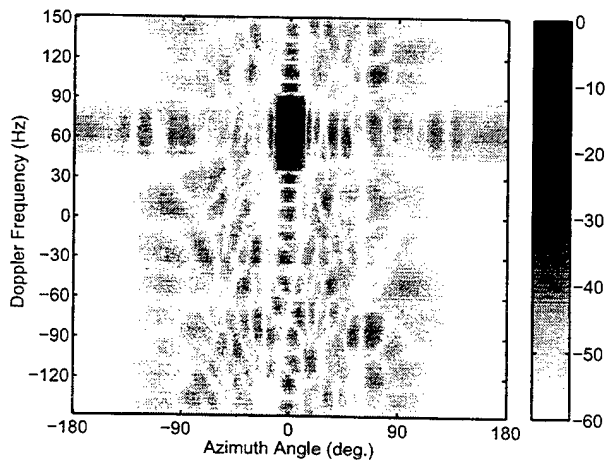


Figure 7: Final Adaptive Beampattern

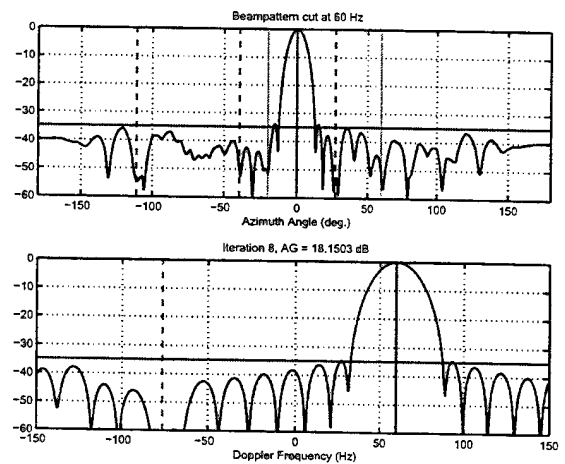


Figure 10: Final Adaptive Beampattern

PARAFAC-STAP FOR THE UESA RADAR¹

Tao Li
Dept. of Elec. Eng.
University of Virginia
Charlottesville, VA 22903
Email: tl7d@virginia.edu

Nicholas D. Sidiropoulos
Dept. of ECE, 200 Union St. S.E.
University of Minnesota
Minneapolis, MN 55455
Email: nikos@ece.umn.edu

Georgios B. Giannakis
Dept. of ECE, 200 Union St. S.E.
University of Minnesota
Minneapolis, MN 55455
Email: georgios@ece.umn.edu

ABSTRACT

Space-Time Adaptive Processing (STAP) algorithms that built on Wiener filtering ideas work well in stationary or quasi-stationary clutter environments, but may fail to perform satisfactorily when clutter statistics are appreciably range-dependent. The UESA (UHF Electronically Steered Array) radar under development by the Navy employs a circular array, for which clutter statistics exhibit range-dependence due to elevation dependence. This paper proposes a novel small sample-support clutter modeling and mitigation algorithm building on parallel factor (PARAFAC) analysis tools. The proposed PARAFAC-STAP compares favorably to Pulse-Repetition Staggered STAP (PRSTAP), and provides very encouraging blind target detection and Doppler estimation results, even at low target-to-clutter power ratios.

1. INTRODUCTION

The UESA (UHF Electronically Steered Array) circular array under development by the Navy affords 360 degree coverage without requiring mechanical rotation. A drawback of circular arrays is that near/mid-range interference statistics are appreciably range-dependent, due to elevation dependence. This means that the sample support available for estimating the clutter covariance from adjacent range bins is limited, which can significantly affect the performance of linear STAP algorithms [13], [8], [4] that build on Wiener filtering ideas.

The fully adaptive STAP [1], [13] is optimal (in the sense of maximizing SINR / prob. of detection for a given false alarm rate) provided that the target signal parameters (Doppler, azimuth / elevation, range) and the interference covariance matrix are known. In practice however, these parameters need to be estimated, hence the fully adaptive STAP can be viewed as a performance bound. In a stationary environment, proper estimation of the interference covariance matrix requires at least $2JK$ training samples, J being the number of antenna elements and K the number of pulses per dwell [7]. For typical J, K values this translates to anywhere from several hundred to several thousand samples. The UESA array exhibits clutter range-dependence due to elevation-dependence. More generally, real-world clutter is often not homogeneous in range, and assuming stationarity over hundreds or thousands of range gates can be unrealistic [13]. It is therefore of interest to develop STAP algorithms capable of performing well with only limited sample support (e.g., under 100 range gates). This paper develops such an algorithm based on PARALLEL FACTOR (PARAFAC) analysis tools. PARAFAC is a common name for low-rank decomposition of three- and higher-way arrays. Unlike low-rank matrix (two-way array) decompositions which are inherently non-unique, low-rank three-way array decomposition is inherently unique, under mild conditions. This allows us to model clutter in the neighborhood of a certain range gate of interest, and blindly extract

Doppler, spatial, and range profiles for the clutter patches in the vicinity of the given range gate. This is achieved by joint least squares (LS) PARAFAC fitting of the 3-D radar data within a small batch of range gates. The overall algorithm consists of: (i) LS beamforming in the look direction (this serves to reduce clutter rank and improve target-to-clutter ratio); (ii) LS PARAFAC fitting and extraction of clutter Doppler and Spatial components; (iii) clutter estimation for the range gate of interest by LS projection of the received range gate data onto the spatial-Doppler span of the clutter; and (iv) clutter removal and target Doppler estimation. PARAFAC affords reliable blind target detection down to -40 dB target-to-clutter ratio, using realistic circular array clutter data. An adaptive implementation of the proposed PARAFAC-STAP algorithm has also been developed, and it brings complexity down to PRSTAP-like levels.

The rest of this paper is structured as follows. Section 2 develops the baseband-equivalent clutter model and shows that, under certain assumptions, beamspace clutter can be modeled by PARAFAC. Section 3 provides brief but necessary background on PARAFAC and the uniqueness of low-rank decomposition of three-way arrays. Section 4 develops the proposed PARAFAC-STAP algorithm, while Section 6 provides simulation results using a realistic circular array radar dataset², including comparison with PRSTAP, one of the leading STAP algorithms. Section 5 develops a fast adaptive variant of the basic PARAFAC-STAP algorithm. Conclusions are drawn in Section 7.

2. BASEBAND-EQUIVALENT MODEL FOR PULSE-COMPRESSED DATA

Consider an airborne radar system that employs M antenna elements arranged in a Uniform Circular Array (UCA) configuration, as shown in Figure 1. At any given point in time, a subset of $J < M$ antenna elements are actually utilized for both transmit and receive. Active elements are denoted with a triangle, whereas inactive elements are denoted with a thin line in Figure 1. Let K be the number of pulses per dwell, f_r the pulse repetition frequency, and f_o the operating carrier frequency. Following transmit-pulse matched filtering (*pulse compression*), the baseband-equivalent received data for a point scatterer at a given range gate is a $JK \times 1$ space-time snapshot

$$\mathbf{z} = \alpha \mathbf{v}(\phi, \theta, f) + \mathbf{x}, \quad (1)$$

where

$$\mathbf{v}(\phi, \theta, f) = \mathbf{c}(f) \otimes \mathbf{b}(\phi, \theta) \quad (2)$$

is the space (\mathbf{b}) - time (\mathbf{c}) steering vector, α , ϕ , θ , and f denote amplitude, azimuth, elevation, and Doppler frequency, \otimes denotes the Kronecker product, and \mathbf{x} models clutter, jamming, and thermal noise interfering with the radar's operation. Assuming that the UCA is composed of identical omni-directional antenna elements

¹Supported by ONR/CSTAP N/N00014-99-1-0693

²Courtesy of Dr. M. Zatman, part of the ONR/CSTAP package.

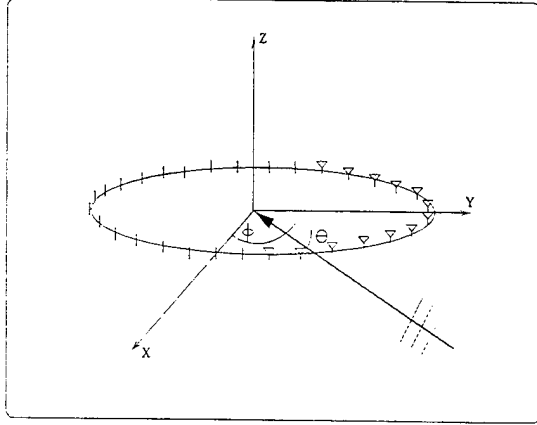


Figure 1: UCA geometry.

spaced uniformly along the circumference, the spatial steering vector is given by

$$\mathbf{b}(\phi, \theta) = \begin{bmatrix} \exp(j \frac{2\pi r}{\lambda_0} \cos \theta \cos(\phi - \beta_1)) \\ \exp(j \frac{2\pi r}{\lambda_0} \cos \theta \cos(\phi - \beta_2)) \\ \vdots \\ \exp(j \frac{2\pi r}{\lambda_0} \cos \theta \cos(\phi - \beta_J)) \end{bmatrix}, \quad (3)$$

$$\beta_j = \beta_1 + \frac{2\pi(j-1)}{M}, \quad j = 1, 2, \dots, J, \quad (4)$$

where r is the radius of the UCA, and β_j is the azimuth of the j -th active element ($j = 1$ is the reference element). The temporal steering vector is given by

$$\mathbf{c}(f) = [e^{j2\pi f T_r} e^{j2\pi 2f T_r} \dots e^{j2\pi K f T_r}]^T, \quad (5)$$

where $T_r = 1/f_r$ is the pulse repetition period, and f is the Doppler frequency, which is a function of scatterer azimuth and elevation parameters, and relative scatterer to airborne platform velocity. For a stationary point scatterer,

$$f(\phi, \theta, v) = \frac{2v}{\lambda_0} \sin \phi \cos \theta, \quad (6)$$

where v is the platform's velocity and λ_0 is the carrier wavelength.

The interference term \mathbf{x} in (1) consists of clutter, jamming and thermal noise

$$\mathbf{x} = \mathbf{x}_c + \mathbf{x}_j + \mathbf{x}_t, \quad (7)$$

which are usually assumed to be uncorrelated with one another [13]. In the absence of jamming, clutter is the dominant interference term in (7). Under certain conditions [13], clutter can be modeled as a sum of F components

$$\mathbf{x}_c = \sum_{k=1}^F a_k \mathbf{v}(\phi_k, \theta_k, f(\phi_k, \theta_k, v_k)) \quad (8)$$

$$= \sum_{k=1}^F a_k \mathbf{c}(f(\phi_k, \theta_k, v_k)) \otimes \mathbf{b}(\phi_k, \theta_k), \quad (9)$$

where v_k is used to denote the relative velocity vector for the k -th component. Let us re-arrange (9), using that³ $\mathbf{c} \otimes \mathbf{b} = \text{vec}(\mathbf{b}\mathbf{c}^T)$:

$$\mathbf{X}_c = \text{vec}_{J,K}^{-1}(\mathbf{x}_c) \quad (10)$$

$$= \begin{bmatrix} \mathbf{b}_1 & \mathbf{b}_2 & \dots & \mathbf{b}_F \end{bmatrix} \begin{bmatrix} a_1 & 0 & \dots & 0 \\ 0 & a_2 & 0 & \vdots \\ \vdots & 0 & \ddots & 0 \\ 0 & \dots & 0 & a_F \end{bmatrix} \begin{bmatrix} \mathbf{c}_1^T \\ \mathbf{c}_2^T \\ \vdots \\ \mathbf{c}_F^T \end{bmatrix} \quad (11)$$

$$\text{or} \quad \mathbf{X}_c = \mathbf{B}(\phi, \theta) \text{diag}(\mathbf{a}) \mathbf{C}^T(\phi, \theta, \mathbf{v}),$$

where $\mathbf{b}_k := \mathbf{b}(\phi_k, \theta_k)$, $\mathbf{c}_k := \mathbf{c}(f(\phi_k, \theta_k, \mathbf{v}))$, ϕ, θ, \mathbf{v} , and \mathbf{a} are $F \times 1$ vectors of azimuth, elevation, velocity, and amplitude parameters for the F clutter components, $\mathbf{B}(\phi, \theta)$ is a $J \times F$ matrix that holds all spatial steering vectors, and $\mathbf{C}(\phi, \theta, \mathbf{v})$ is a $K \times F$ matrix that holds the respective Doppler vectors. For a total of I range gates, the data can be modeled as (dropping the subscript c for brevity)

$$\mathbf{X}_i = \mathbf{B}(\phi_i, \theta_i) \text{diag}(\mathbf{a}_i) \mathbf{C}^T(\phi_i, \theta_i, \mathbf{v}_i), \quad i = 1, \dots, I.$$

Notice that \mathbf{B} and \mathbf{C} depend on range through the azimuth, elevation, and velocity parameter vectors⁴. For high range-resolution radar (like the UESA system that supports range resolution down to approximately 40 meters) it is reasonable to assume that \mathbf{B} and \mathbf{C} remain approximately invariant over a small number of contiguous range gates, and only the clutter component proportions \mathbf{a}_i change with range. That is, the space-Doppler clutter locus remains approximately invariant for a small (e.g., in the order of 20-100) number of range gates. This is well-motivated for spatially beamformed data, which only exhibit a few spatio-temporal modes, determined primarily by the spatial mainlobe/sidelobes, with some residual Doppler variation due to clutter scintillation. It is also well-motivated for discrete coherent scatterers, whose physical dimensions span a proportional number of range gates. With this assumption, the data model for I range gates can be written as

$$\mathbf{X}_i = \mathbf{B} \mathbf{D}_i(\mathbf{A}) \mathbf{C}^T, \quad i = 1, \dots, I, \quad (12)$$

where \mathbf{A} is an $I \times F$ matrix that holds the component profiles for the I ranges, and $\mathbf{D}_i(\mathbf{A})$ is a diagonal matrix holding the i -th row of \mathbf{A} on its diagonal. Equation (12) can be viewed as a rank- F decomposition of the three-way data array constructed by laying out the \mathbf{X}_i 's parallel to each other along range. Interestingly, low-rank decomposition of three-way arrays is unique - that is, \mathbf{A} , \mathbf{B} , and \mathbf{C} can be essentially uniquely determined from the \mathbf{X}_i 's, under a relatively mild rank-like condition. PARALLEL FACTOR (PARAFAC) analysis is a common name for low-rank decomposition of such three-way arrays, and it is reviewed next.

3. PARAFAC

The pioneering work of Cattell (published in *Psychometrika* in '44) formed the basis for the development of PARAFAC by R.A. Harshman [3] in 1970. Although PARAFAC is widely adopted as a powerful analysis tool in Chemometrics and Psychometrics, it was only recently introduced to the signal processing and communications community by Sidiropoulos *et al* [11, 12, 10].

Consider an $I \times J \times K$ three-way array $\underline{\mathbf{X}}$ with typical element $x_{i,j,k}$, and the F -component trilinear decomposition:

$$x_{i,j,k} = \sum_{f=1}^F a_{i,f} b_{j,f} c_{k,f}. \quad (13)$$

In (13), $\underline{\mathbf{X}}$ is expressed as a sum of F rank-one three-way factors; a schematic of such decomposition is given in Figure 2. Analogous to the definition of matrix (two-way array) rank, the rank of three-way array $\underline{\mathbf{X}}$ is defined as the minimum number of rank-one (three-way) components needed to decompose $\underline{\mathbf{X}}$.

³ $\text{vec}(\cdot)$ stacks the columns of its matrix argument in a tall vector; similarly $\text{vec}_{J,K}^{-1}(\cdot)$ performs the inverse operation, producing a $J \times K$ matrix out of its vector argument, which is assumed to be $JK \times 1$.

⁴ It is implicitly assumed here that F is appropriate to model clutter throughout the I range gates of interest. This can be achieved by picking $F := \max(F_1, \dots, F_I)$, with obvious notation.

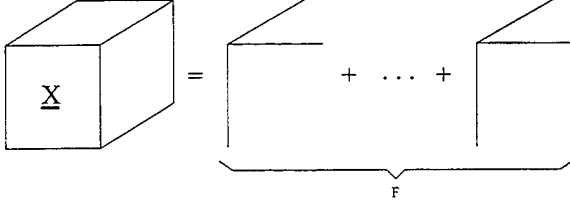


Figure 2: PARAFAC model

Let \mathbf{A} be an $I \times F$ matrix with typical element $a_{i,f}$, \mathbf{B} be a $J \times F$ matrix with typical element $b_{j,f}$, \mathbf{C} be a $K \times F$ matrix with typical element $c_{k,f}$, and $\mathbf{D}_i(\mathbf{A})$ denote a diagonal matrix containing the i -th row of \mathbf{A} . Define $J \times K$ matrices \mathbf{X}_i , $I \times K$ matrices \mathbf{Y}_j , and $I \times J$ matrices \mathbf{Z}_k with corresponding typical elements $\mathbf{X}_i(j, k) := \mathbf{Y}_j(i, k) := \mathbf{Z}_k(i, j) := x_{i,j,k}$. Then Equation (13) can be written in three equivalent ways in terms of systems of matrix equations, corresponding to three different ways of “slicing” the data cube in Figure 2 along a given axis:

$$\mathbf{X}_i = \mathbf{B}\mathbf{D}_i(\mathbf{A})\mathbf{C}^T, i = 1, 2, \dots, I, \quad (14)$$

$$\mathbf{Y}_j = \mathbf{A}\mathbf{D}_j(\mathbf{B})\mathbf{C}^T, j = 1, 2, \dots, J, \quad (15)$$

$$\mathbf{Z}_k = \mathbf{A}\mathbf{D}_k(\mathbf{C})\mathbf{B}^T, k = 1, 2, \dots, K. \quad (16)$$

In addition to the sliced model representations above, several two-way representations (corresponding to different ways of unfolding the three-way structure \mathbf{X} into block-row “matricized” form) are possible. For example,

$$\mathbf{X}^{(JI \times K)} = \begin{bmatrix} \mathbf{X}_{i=1} \\ \mathbf{X}_{i=2} \\ \vdots \\ \mathbf{X}_{i=I} \end{bmatrix} = \begin{bmatrix} \mathbf{B}\mathbf{D}_1(\mathbf{A}) \\ \mathbf{B}\mathbf{D}_2(\mathbf{A}) \\ \vdots \\ \mathbf{B}\mathbf{D}_I(\mathbf{A}) \end{bmatrix} \mathbf{C}^T = (\mathbf{A} \odot \mathbf{B}) \mathbf{C}^T, \quad (17)$$

where the superscript $(JI \times K)$ means that the matrix is of size $JI \times K$, and the j -index (J goes first in the product JI) runs faster than the i -index along its columns, and the symbol \odot stands for the Khatri-Rao (column-wise Kronecker) product.

3.1. k-rank

The concept of k-rank [3] is instrumental for PARAFAC.

Definition 1 Consider a matrix $\mathbf{B} \in \mathbb{C}^{J \times F}$. If $\text{rank}(\mathbf{B}) = r$, then \mathbf{B} contains a collection of r linearly independent columns. Moreover, if every $\ell \leq F$ columns of \mathbf{B} are linearly independent, but either there exists a collection of $\ell + 1$ linearly dependent columns or $\ell = F$, then \mathbf{B} has k-rank $k_{\mathbf{B}} = \ell$. Note that $k_{\mathbf{B}} \leq \text{rank}(\mathbf{B})$, $\forall \mathbf{B}$.

3.2. Identifiability

A distinguishing feature of the trilinear model is its uniqueness. Under mild conditions and unlike the unconstrained bilinear model ($\mathbf{Z} = \mathbf{A}\mathbf{B}^T$), the trilinear model is essentially unique - that is $\mathbf{A}, \mathbf{B}, \mathbf{C}$ are identifiable without unitary matrix ambiguities.

Theorem 1 (R-[5]; C-[12]) Given $\mathbf{X}_i = \mathbf{B}\mathbf{D}_i(\mathbf{A})\mathbf{C}^T$, $i = 1, 2, \dots, I$, $\mathbf{A} \in \mathbb{C}^{I \times F}$, $\mathbf{B} \in \mathbb{C}^{J \times F}$, $\mathbf{C} \in \mathbb{C}^{K \times F}$, if:

$$k_{\mathbf{A}} + k_{\mathbf{B}} + k_{\mathbf{C}} \geq 2(F + 1) \quad (18)$$

then: \mathbf{A}, \mathbf{B} , and \mathbf{C} are unique up to permutation and (complex) scaling of columns.

3.3. Trilinear Alternating Least Squares Regression

The principle of Alternating Least Squares (ALS) can be used to fit the trilinear model in (13) on the basis of noisy observations $\tilde{x}_{i,j,k}$. The basic idea behind ALS is simple: In each step, update *one* matrix, using least squares (LS) *conditioned* on previously obtained estimates for the remaining matrices; proceed to update the other matrices; repeat until convergence. A basic trilinear ALS (TALS) algorithm is outlined in [12]. The trilinear ALS method is appealing primarily because it is guaranteed to converge monotonically, but also because it is conceptually simple (no parameters to tune, each step solves a standard LS problem) and provides good performance [9].

Least squares fitting of (17) (and ML parameter estimation, when the noise is modeled as i.i.d. Gaussian and all other parameters are treated as deterministic unknowns) amounts to:

$$\min_{\mathbf{A}, \mathbf{B}, \mathbf{C}} \left\| \begin{bmatrix} \tilde{\mathbf{X}}_1 \\ \vdots \\ \tilde{\mathbf{X}}_I \end{bmatrix} - \begin{bmatrix} \mathbf{B}\mathbf{D}_1(\mathbf{A}) \\ \vdots \\ \mathbf{B}\mathbf{D}_I(\mathbf{A}) \end{bmatrix} \mathbf{C}^T \right\|_F^2, \quad (19)$$

where $\tilde{\mathbf{X}}_i$, $i = 1, \dots, I$ are the noisy slabs, and $\|\cdot\|_F$ stands for the Frobenius norm. It follows that the conditional least squares update for \mathbf{C} is:

$$\hat{\mathbf{C}}^T = \begin{bmatrix} \hat{\mathbf{B}}\mathbf{D}_1(\hat{\mathbf{A}}) \\ \vdots \\ \hat{\mathbf{B}}\mathbf{D}_I(\hat{\mathbf{A}}) \end{bmatrix}^\dagger \begin{bmatrix} \tilde{\mathbf{X}}_1 \\ \vdots \\ \tilde{\mathbf{X}}_I \end{bmatrix}, \quad (20)$$

where $(\cdot)^\dagger$ stands for pseudo-inverse, and $\hat{\mathbf{A}}, \hat{\mathbf{B}}$ denote previously obtained estimates of \mathbf{A} and \mathbf{B} . One may now resort to the complete symmetry of the trilinear model (cf. Equation (13)) and data reshaping (cf. Equations (14), (15), (16)) to figure out corresponding conditional LS updates for \mathbf{A} and \mathbf{B} .

4. PROPOSED ALGORITHM: PARAFAC-STAP

The proposed PARAFAC-STAP algorithm consists of several steps, which are discussed next. The basic idea is to isolate a small batch of contiguous range gates around a given “target” range gate of interest, exclude the target range gate, and fit a rank- F PARAFAC model to the remaining data in the batch. This will recover an estimate of the clutter’s spatio-temporal steering vectors in the neighborhood of the target range gate. Using these vectors, the clutter’s contribution in the range gate of interest can be estimated in a least squares sense, and subsequently removed from the data. What remains is an estimate of the rank-1 target contribution if a target is present.

The method capitalizes on the following observation: if the target is away from the clutter ridge, then its (rank-1) contribution cannot be spanned by clutter components, and this provides means for separation even at very low target-to-clutter power ratios.

4.1. Step one: Least Squares Beamforming

The first step in the overall algorithm is to compute a least squares beamformer for a desired look direction, and then beamform the received data. This serves a two-fold purpose:

1. Clutter rank (F) is reduced by beamforming, which ensures that a low-rank PARAFAC model is appropriate; and
2. The target-to-clutter power ratio is improved, by filtering out clutter from other than the look direction. This is especially important for low target-to-clutter ratios (in the neighborhood of -30 to -40 dB is not unusual).

The least squares beamformer *per se* can be computed off-line, and the weights stored for later retrieval. The formulation is as follows. Given a UCA steering vector \mathbf{sv}_{look} for a particular look direction of interest, and a set of n additional steering vectors corresponding to a quantization of the (azimuth, elevation) horizon, find a $J \times J$ beamformer to

$$\min_{\mathbf{W}} \|\mathbf{S}_{desired} - \mathbf{W}\mathbf{S}_{measured}\|_F^2, \quad (21)$$

where

$$\mathbf{S}_{desired} = \left[\begin{pmatrix} \mathbf{sv}_{look} \end{pmatrix} \begin{pmatrix} \vdots \\ 0 \\ \vdots \end{pmatrix} \cdots \begin{pmatrix} \vdots \\ 0 \\ \vdots \end{pmatrix} \right], \quad (22)$$

and

$$\mathbf{S}_{measured} = \left[\begin{pmatrix} \mathbf{sv}_{look} \end{pmatrix} \begin{pmatrix} \mathbf{sv}_1 \end{pmatrix} \cdots \begin{pmatrix} \mathbf{sv}_n \end{pmatrix} \right]. \quad (23)$$

This is a standard least squares problem, whose solution is ($n > J$)

$$\mathbf{W} = \mathbf{S}_{desired} \mathbf{S}_{measured}^\dagger. \quad (24)$$

Applying the beamforming transformation to each range gate of \mathbf{X} , we obtain

$$\mathbf{X}_i^{(b)} = \mathbf{W}\mathbf{X}_i, \quad i = 1, 2, \dots, I, \quad (25)$$

from which we construct the beamformed three-way array $\mathbf{X}^{(b)}$.

4.2. Step two: PARAFAC fitting

The goal of this step is to extract a local PARAFAC model for clutter in the vicinity of a target range gate of interest. Towards this end, we select a neighborhood of length I range gates and fit an F -component PARAFAC model to the beamspace data around but excluding the range gate of interest. This is illustrated in Figure 3. The selection of appropriate I and F is an important step. Our experiments show that the selection of I is not crucial - any choice between e.g., 20 and 40 provides good results. The choice of F is far more complicated - F is the essential rank of the three-way data array, and rank determination is a difficult problem. In our experiments, we selected F using split-half analysis, then tested the results for consistency across range space. We will revisit this issue in the simulations section.

Let \mathbf{X}_b be the selected data, excluding the range gate of interest. Invoke the *comfac* fast least squares PARAFAC fitting algorithm in [2]

$$[\mathbf{A}, \mathbf{B}, \mathbf{C}] = \text{comfac}(\mathbf{X}_b, [I-1, J, K], F), \quad (26)$$

to recover joint least squares estimates of the clutter range profiles $\mathbf{A} : ((I-1) \times F)$, spatial profiles $\mathbf{B} : J \times F$, and Doppler profiles $\mathbf{C} : K \times F$.

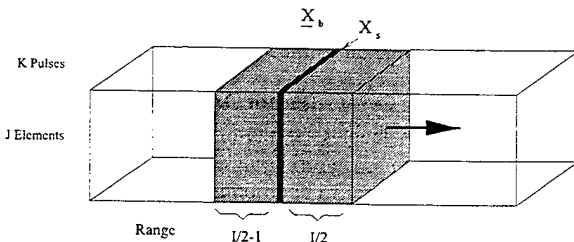


Figure 3: PARAFAC-STAP Illustration

4.3. Step three: Least Squares Interpolation

The goal of this step is to estimate the clutter contribution for the range gate of interest from the local clutter parameters extracted in the previous step. The clutter range profiles (\mathbf{A}) extracted in step two are typically very rapidly varying, and are therefore useless for interpolation purposes. However, the spatial (\mathbf{B}) and Doppler (\mathbf{C}) profiles remain approximately invariant over a small number of range gates, and they can be used to estimate clutter in the missing slice. This task can be formulated as a least squares problem

$$\min_{\mathbf{D}} \|\mathbf{X}_s - \mathbf{B}\mathbf{D}\mathbf{C}^T\|_F^2,$$

where \mathbf{X}_s is the data in the range gate of interest. The solution of this problem is given by:

$$\begin{aligned} \hat{\mathbf{d}}_{LS} &= (\mathbf{C} \odot \mathbf{B})^\dagger \text{vec}(\mathbf{X}_s), \\ \hat{\mathbf{D}}_{LS} &= \text{diag}(\hat{\mathbf{d}}_{LS}). \end{aligned} \quad (27)$$

4.4. Step four: Target Doppler Spectrum Estimation

In this final step, the estimated clutter contribution in the range gate of interest is removed from the range gate data to reveal the target's contribution, if any. Accordingly, if a target is present

$$\hat{\mathbf{X}}_t = \mathbf{X}_s - \mathbf{B}\hat{\mathbf{D}}_{LS}\mathbf{C}^T, \quad (28)$$

provides an estimate of its rank-1 contribution. The unknown pure target contribution is of the form $\mathbf{b}(\phi_t, \theta_t)\mathbf{c}^T(f_t)$. Given $\hat{\mathbf{X}}_t \approx \mathbf{b}(\phi_t, \theta_t)\mathbf{c}^T(f_t)$, $\mathbf{c}(f_t)$ can be estimated in a variety of ways. A simple way to do it in MATLAB is to take the right singular vector corresponding to the strongest singular value of $\hat{\mathbf{X}}_t$, and e.g., compute its periodogram. This periodogram can be used to determine if a target is present (if it is, then the periodogram should be approximately unimodal) and estimate its Doppler. More sophisticated parametric techniques can also be utilized.

5. ADAPTIVE TRILINEAR ALTERNATING LEAST SQUARES (A-TALS)

The result in (27) is useful not only in deriving the LS estimate of the clutter component weights in the range gate of interest, but also in developing fast least squares algorithms for fitting the general PARAFAC model. This is particularly important in our present context, because the processing in steps one to four above has to be repeated for every single range gate of interest - which quickly builds up to a formidable task.

The basic idea behind A-TALS is simple. Once processing for a certain range gate is complete, the entire $I \times J \times K$ cube is shifted to the right by a single range gate. One can then use (27) to LS-predict the component weights for the next data slice in line.

In MATLAB notation, using $\hat{\mathbf{d}}_{LS,interp}$ to denote the optimal weights previously computed for the interpolated slice, and $\hat{\mathbf{d}}_{LS,predict}$ the weights for the new slice

$$\mathbf{A}_{new}(1 : (I/2) - 1, :) = \mathbf{A}(2 : (I/2), :), \quad (29)$$

$$\mathbf{A}_{new}((I/2), :) = \hat{\mathbf{d}}_{LS,interp}^T, \quad (30)$$

$$\mathbf{A}_{new}((I/2) + 1 : I - 2, :) = \mathbf{A}((I/2) + 2 : I - 1, :), \quad (31)$$

$$\mathbf{A}_{new}(I - 1, :) = \hat{\mathbf{d}}_{LS,predict}^T. \quad (32)$$

\mathbf{A}_{new} , along with the existing estimates for \mathbf{B} and \mathbf{C} is then used to initialize the LS fitting procedure for the shifted data. The result is an algorithm that achieves the same results as the batch algorithm in [2], but is an order of magnitude faster: typically 2-3 iterations are sufficient for convergence, due to smooth variation in \mathbf{B} , \mathbf{C} .

6. SIMULATION RESULTS

We conducted a series of simulation experiments (we can only show some of them due to limited space) using the circular STAP data package developed for the UESA radar by Dr. M. Zatman, and distributed to ONR/CSTAP participants. The data package contains simulated clutter data for typical UESA system parameters. Throughout, the following system parameters are in effect: $J = 20$ active antenna elements, $K = 18$ pulses, carrier frequency $f_c = 435$ MHz, platform velocity $v = 100$ m/s, pulse repetition frequency $f_r = 300$ Hz.

The parameter I determines the length of the neighborhood chosen for clutter model fitting. I should not be too small, as this may violate the required identifiability conditions. On the other hand, I cannot be too big, for otherwise the invariance of \mathbf{B} and \mathbf{C} will no longer be valid, due to UCA range dependence. We found through experimentation that the choice of I is not critical, with values between 20 and 40 providing similar results. We therefore chose $I = 32$. Performance is more sensitive to the choice of F . As previously mentioned, F is the essential rank of the three-way data array. For our simulations, we selected $F = 9$ using split-half analysis, and also experimented with various values of F . The results show that F should be roughly between 8 and 12 for best detection performance. Rank determination is a difficult problem, and there is more work to be done in this direction.

In our first series of experiments, we injected a target at a certain range gate, and applied the proposed PARAFAC-STAP algorithm to the mixed clutter/target data. Figures 4 depict the target Doppler spectrum (top) and Doppler spectra extracted from the target slice using SVD before clutter mitigation (middle) and after PARAFAC-STAP clutter mitigation with target to clutter power ratio $\text{TCR} := 10 \log_{10} \frac{\|\mathbf{x}_t\|_F^2}{\|\mathbf{x}_c\|_F^2}$ set to -40 dB. Notice how well PARAFAC-STAP performs, even at this low TCR (all 1-D plots normalized to [0,1]-range). Another example (target Doppler closer to clutter ridge) is given in Figure 5.

In our second series of experiments, we constructed a synthetic target Doppler-range template consisting of three identical targets injected to the test range gates at near/mid-range. Figures 6 and 7 show before and after PARAFAC-STAP clutter mitigation results for mid-range, $\text{TCR} = -40$ dB. Observe that the inserted targets can be easily detected after PARAFAC-STAP clutter mitigation. As a line of comparison, Figure 8 shows PRSTAP results for the same dataset, using about 20 times more training samples than PARAFAC-STAP.

Figure 9 gives the CPU time comparison between PARAFAC-STAP (batch version) and its adaptive version developed in Section 5. Both algorithms provide the same fit, but the adaptive one is an order of magnitude faster.

7. CONCLUSIONS

Motivated by the need to develop novel STAP algorithms for the UESA radar, we proposed a small sample-support clutter modeling and mitigation algorithm that circumvents the clutter covariance estimation step common to all Wiener-based STAP algorithms. The proposed STAP algorithm builds on PARAFAC analysis tools, and reduces the required sample support from several hundreds to a few dozen samples. PARAFAC-STAP compares favorably to PRSTAP, and can provide reliable detection results even at low TCR, without assuming knowledge of the target's Doppler. We also developed an adaptive version of PARAFAC-STAP which does not compromise performance while bringing overall complexity

down to PRSTAP-like levels. PARAFAC-STAP can be a useful tool in other nonstationary environments, beyond the specific UESA circular array application that motivated our work.

8. REFERENCES

- [1] L. E. Brennan, I. S. Reed, "Theory of adaptive radar", *IEEE Transaction on Aerospace and Electronic Systems*, vol. 9, March 1973, pp.237-252.
- [2] R. Bro, N. D. Sidiropoulos, and G. B. Giannakis, "A Fast Least Squares Algorithm for Separating Trilinear Mixtures", in *Proc. ICA99 - Int. Workshop on Independent Component Analysis and Blind Signal Separation*, Jan. 11-15, 1999, Aussois, France, pp. 289-294.
- [3] R. A. Harshman, "Foundations of the PARAFAC procedure: Model and conditions for an 'explanatory' multi-mode factor analysis", *UCLA Working Papers in Phonetics*, 16:1-84, Dec. 1970.
- [4] E. J. Kelly "An Adaptive Detection Algorithm" *IEEE Aerospace and Electronic Systems* vol. AES-22, No. 1 March, 1986, pp. 115-127.
- [5] J. B. Kruskal, "Three-Way Arrays: Rank and Uniqueness of Trilinear Decompositions, with Application to Arithmetic Complexity and Statistics", *Linear Algebra and Its Applications*, 18:95-138, 1977.
- [6] C. P. Mathews and M. Zoltowski, "Eigenstructure Techniques for 2-D Angle Estimation with Uniform Circular Arrays", *IEEE Trans. Signal Proc.*, 49(2): 2395-2407, Sept. 1994.
- [7] I. S. Reed, J. D. Mallett, and L. E. Brennan, "Rapid Convergence Rate in Adaptive Arrays" *IEEE Trans. on Aerospace and Electronic Systems*, AES-10, No. 6 Nov., 1974.
- [8] F. C. Robey, D. R. Fuhrmann, E. J. Kelly, and R. Nitzberg, "A CFAR Adaptive Matched Filter Detector", *IEEE Trans. on Aerospace and Electronic Systems* vol. 28, No.1, 1992, pp. 208-216.
- [9] N. D. Sidiropoulos, and R. Bro, "PARAFAC Techniques For Separation", *Signal Processing Advances in Wireless Communications*, Prentice-Hall, to appear in 2000.
- [10] N. D. Sidiropoulos, R. Bro, and G. B. Giannakis, "Parallel Factor Analysis in Sensor Array Processing", *IEEE Trans. Signal Processing*, submitted Jan 5, 1999.
- [11] N. D. Sidiropoulos, G. B. Giannakis, and R. Bro, "Deterministic Waveform-Preserving Blind Separation of DS-CDMA Signals Using an Antenna Array", *Proc. of IEEE SP Workshop on Statist. Signal and Array Proc.* pp. 304-307, Portland, Oregon, Sept. 14-16, 1998.
- [12] N. D. Sidiropoulos, G. B. Giannakis, and R. Bro, "Blind PARAFAC Receivers for DS-CDMA Systems", *IEEE Trans. Signal Processing*, March 2000.
- [13] J. Ward, "Space-time adaptive processing for airborne radar", *MIT Lincoln Laboratory Technical Report 1015*, 13 Dec. 1994.

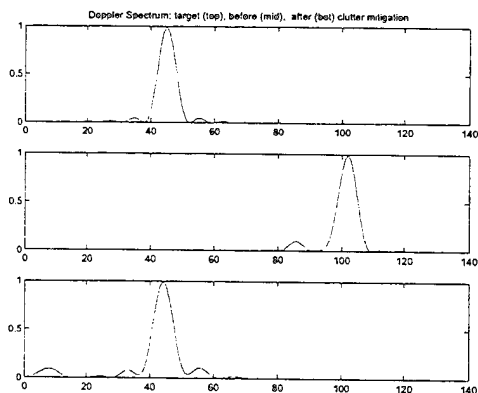


Figure 4: TCR=-40 dB, I=32, F=9.

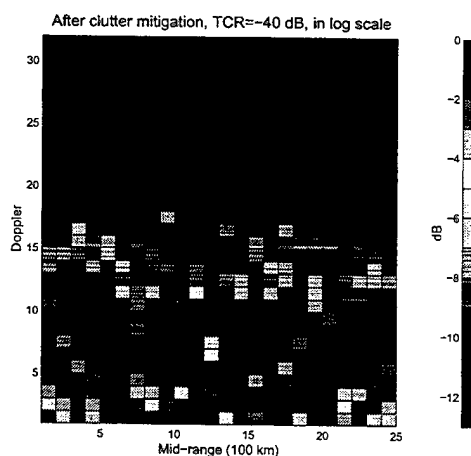


Figure 7: TCR=-40 dB, mid-range, after clutter mitigation

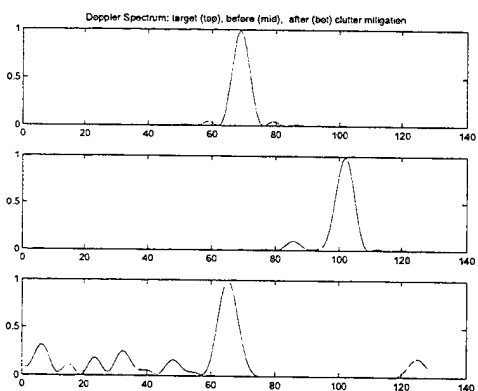


Figure 5: TCR=-40 dB, I=32, F=9, target Doppler close to clutter ridge.

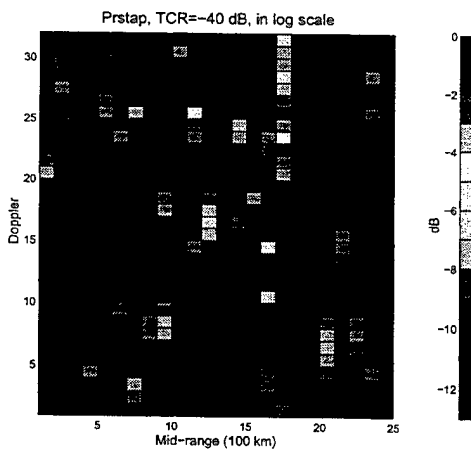


Figure 8: TCR=-40 dB mid-range, PRSTAP algorithm

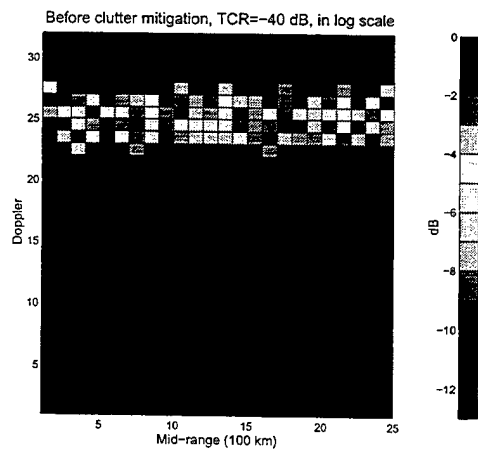


Figure 6: TCR=-40 dB, mid-range, before clutter mitigation

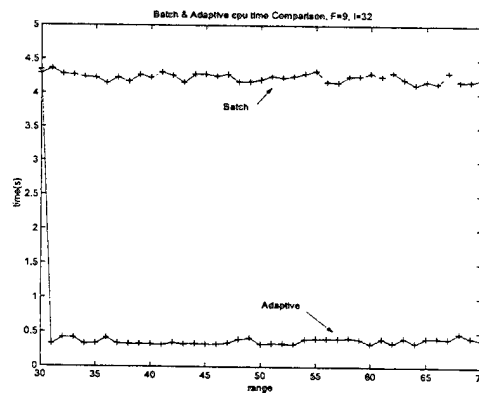


Figure 9: CPU time comparison, batch vs. adaptive.

ADAPTIVE PROCESSING OF ELEMENT-DIGITISED AIRBORNE-INTERCEPT PHASED ARRAY RADAR

J. L. Mather[†], H. D. Rees[†], M. Cook[‡], J. Wood[‡]

[†] Signal Processing Group, DERA, St. Andrew's Road, Malvern, Worcs., WR14 3PS, U.K.

[†] Email: mather@signal.dera.gov.uk Internet: <http://spg.dera.gov.uk/>

[‡] BAES Ltd, Marconi Research Centre, Chelmsford, UK.

Abstract

We describe a novel multi-layer ("domain factorisation") adaptive beamforming method, for element-digitised array radar (EDAR). This enables adaptive beamforming weights for an array of many hundreds or thousands of elements to be calculated with realistic sample support and computational workload. Range-dependent gain adaption (RDGA) coupled with adaptive weighting of each element of the array permits much more effective cancellation of clutter and jamming than sub-array based space-time adaptive processing. Simulations of airborne intercept (AI) radar demonstrate the power of this approach for detection of small targets against severe clutter and jamming.

If a strong target echo is present, it is bound to contribute to one or more of the range-gated adaptive weight calculations, and there is a danger of target cancellation. We show how this may be dealt with by excising target line spectral contributions from the data used for weight calculation.

1. Introduction

The performance and availability of digital technology - from analogue-to-digital converters (ADCs) to digital signal processing - continue to increase, whilst costs plummet. There has been similar progress in the technology for producing microwave integrated circuits.

As a result, it is now realistic to consider element-level digitisation for large phased array radars, as opposed to the current state-of-the-art, which is based on sub-array digitisation. Benefits include

- improved ability to compensate for mismatches in analogue components (or the ability to use cheaper, less well-matched analogue components);
- the ability to form multiple simultaneous low-sidelobe receive-beams, accelerating surveillance; and
- new opportunities for the design of the adaptive beamforming system, offering improved cancellation of unwanted signals.

The challenge is to exploit the additional degrees of freedom without demanding unrealistic numbers of data samples, and without requiring unrealistically high levels of computation for calculation of the beamforming weights.

In this paper, we concentrate on adaptive beamforming in a fully-digitised forward-looking airborne phased array, such as might be fitted in a fighter aircraft. Section 2 reviews the basic processing scheme [1], and suggests methods for preventing cancellation of strong target echoes. Section 3 provides simulation results to illustrate typical performance. We also illustrate the effect of calibration errors on clutter cancellation.

2. Element Digitised Array Radar

2.1 Cancellation of Clutter From Airborne Radar

In simple terms, detection of targets by an airborne radar may be limited by (a) thermal noise; (b) jamming or other interference; (c) clutter. For a particular power-aperture product, thermal noise sets the ultimate limit. In phased arrays, fixed taper weighting can keep sidelobe gains low, reducing sensitivity to sidelobe jamming and clutter. However, at low altitude, clutter breaks through and masks targets. Phased arrays can be designed to adapt their gain to the environment. To date, in large arrays, individual elements have been grouped into (typically 16) sub-arrays, the outputs of which are weighted adaptively and then summed. Due to the small number of degrees of freedom, it is possible to suppress only a limited number of point-source jammers. Spatial adaption has been largely ignored for cancellation of distributed clutter.

Two approaches can be taken to increase the number of degrees of freedom. Firstly, a tapped delay line can be used on each sub-array output to create a Doppler-frequency dependent weight vector. This leads to space-time adaptive processing (STAP) [2], which is very well suited to removing the clutter seen from a sideways-looking airborne radar. A second method is to increase the number of sub-arrays. This can be increased until the array is completely digitised. However, if the usual sample-matrix inversion adaptive algorithm is similarly extended, element digitised

adaptive beamforming becomes impractical for large arrays because too many data samples are required to estimate the covariance matrix, and the number of digital operations to invert the covariance matrix becomes too large. Below, we describe a processing architecture that allows us to calculate element-level weights without these problems.

2.2 Range Dependent Gain Adaption (RDGA)

Within a single range gate, clutter observed by the radar subtends a limited solid angle. Range dependent gain adaption (RDGA) involves calculating an adapted beamforming weight vector for each range gate. Thus, it is not necessary to maintain ultra-low sidelobes for all angles of arrival - only for angles corresponding to the clutter within the range gate of interest. An $n \times m$ matrix of data is used to calculate the weight vector, where n is the number of antenna elements and m is the number of pulses. At high PRF, range ambiguous clutter returns are received. This is indicated in Fig. 1, where the radar is at an altitude h above a flat earth. A target is at a distance of $R_t = n_t R_a + d_t$, where n_t is an integer, R_a is the range ambiguity given by $R_a = cT/2$, T is the pulse repetition interval (PRI) and $c = 3 \times 10^8$ m/s. After an initial period of n_t pulses has elapsed, the target return lies in all m samples. Each sample contains clutter from rings on the ground located between distances of $R_a + d_t - a$ to $R_a + d_t + a$, $2R_a + d_t - a$ to $2R_a + d_t + a$, ..., $pR_a + d_t - a$ to $pR_a + d_t + a$, where $a = c\tau/2$ and τ is the pulse length.

To cancel the clutter spatially, broad gain minima must be formed over the clutter bands. Sidelobes may increase in other directions. This reduces array efficiency, but does not increase sensitivity to other interference since signals corresponding to intermediate ranges have been gated out. Although we have described a high pulse-repetition-frequency (HPRF) mode of operation, the method can be extended easily for low and medium PRF. (Section 3 includes results from a medium PRF simulation.)

2.3 Domain Factorisation

In this paper, we consider a planar array of $n = 1387$ elements, whose locations are shown in the bottom right of Fig. 2. We assume that all elements have been matched,

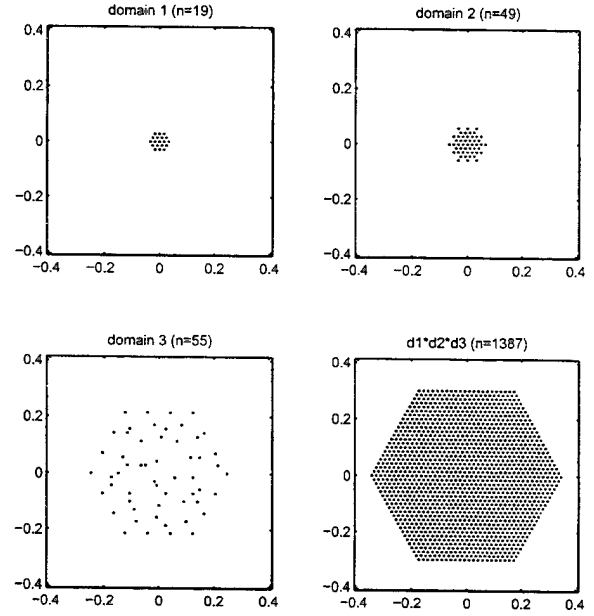


Figure 2. Three-layer domain factorisation of a 1387 element X-band array. Axes show dimensions in metres.

using digital correction. Element-level weights are calculated by breaking down the processing into smaller stages, or *domains*, as illustrated in Fig. 2. The first domain, shown in the top left of Fig. 2, consists of $n_1=19$ elements taken around the array centre. The second domain, of $n_2=49$ points, is shown in the top right of Fig. 2. The third domain, of $n_3=55$ points (in randomised positions, to minimise grating effects [1]) is shown at the bottom left. In domain q , a weight vector $w^{(q)}$ of dimension $n_q \times 1$ is calculated

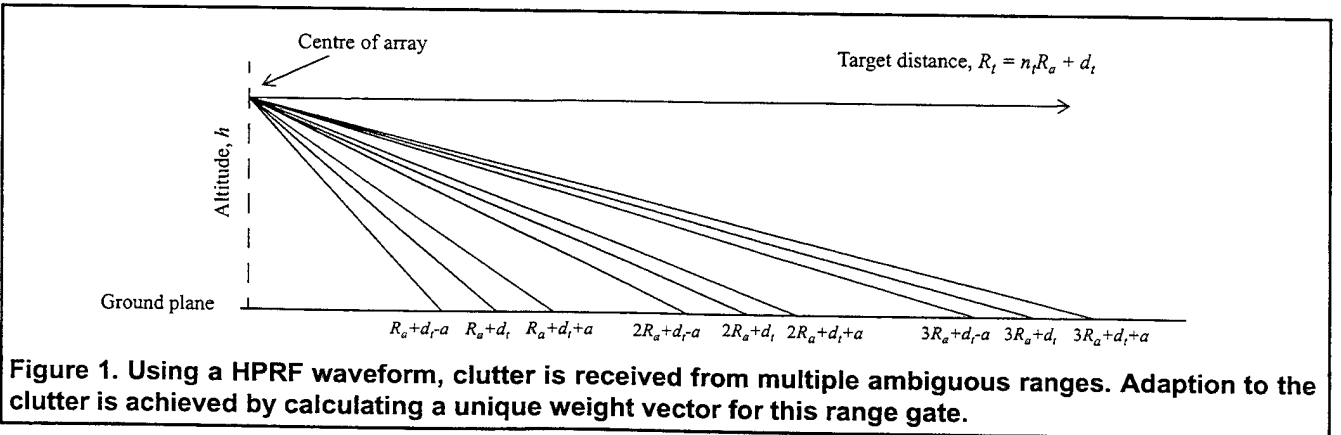


Figure 1. Using a HPRF waveform, clutter is received from multiple ambiguous ranges. Adaption to the clutter is achieved by calculating a unique weight vector for this range gate.

adaptively from an $n_q \times m$ matrix of signals $X^{(q)}$, where m is the number of time samples.

Define the data at a single domain element to be the $1 \times m$ vector $x(r)$ where r is the position vector of the element. The $n_1 \times m$ matrix $X^{(1)}$ which is used to calculate the weights in domain 1 is given by

$$X^{(1)} = \begin{bmatrix} x_1^{(1)} & x_2^{(1)} & \dots & x_{n_1}^{(1)} \end{bmatrix}^T, \quad (1)$$

where T denotes the matrix transpose. $x_i^{(1)}$ is the data time-series from the i^{th} element in domain 1, given by $x_i^{(1)} = x(r_i^{(1)})$, where $r_i^{(1)}$ is the position vector of the i^{th} element.

Having obtained the domain 1 weight vector $w^{(1)} = [w_1^{(1)} \ w_2^{(1)} \ \dots \ w_{n_1}^{(1)}]^T$, shifted versions of domain 1 then form n_2 overlapping sub-arrays, centred about the domain 2 points. The inputs to domain 2 are then

$$x_j^{(2)} = \sum_{i=1}^{n_1} w_i^{(1)} x(r_i^{(1)} + r_j^{(2)}), \quad (2)$$

where $r_j^{(2)}$ is the position vector of the j^{th} point in domain 2 and $j=1, 2 \dots n_2$. The $n_2 \times m$ matrix of domain 2 data is

$$X^{(2)} = \begin{bmatrix} x_1^{(2)} & x_2^{(2)} & \dots & x_{n_2}^{(2)} \end{bmatrix}^T. \quad (3)$$

The weight vector $w^{(2)} = [w_1^{(2)} \ w_2^{(2)} \ \dots \ w_{n_2}^{(2)}]^T$ is then calculated by adapting to the data in $X^{(2)}$. The input signals to domain 3 are

$$x_k^{(3)} = \sum_{i=1}^{n_1} \sum_{j=1}^{n_2} w_i^{(1)} w_j^{(2)} x(r_i^{(1)} + r_j^{(2)} + r_k^{(3)}), \quad (4)$$

where $r_k^{(3)}$ is the position vector of the k^{th} point in domain 3, and $k=1, 2 \dots n_3$. The $n_3 \times m$ data matrix for domain 3 is

$$X^{(3)} = \begin{bmatrix} x_1^{(3)} & x_2^{(3)} & \dots & x_{n_3}^{(3)} \end{bmatrix}^T. \quad (5)$$

From $X^{(3)}$, a weight vector $w^{(3)} = [w_1^{(3)} \ w_2^{(3)} \ \dots \ w_{n_3}^{(3)}]^T$ is calculated, and the $1 \times m$ output from the array is

$$y = \sum_{i=1}^{n_1} \sum_{j=1}^{n_2} \sum_{k=1}^{n_3} w_i^{(1)} w_j^{(2)} w_k^{(3)} x(r_i^{(1)} + r_j^{(2)} + r_k^{(3)}). \quad (6)$$

The weighting in equation (6) is a convolution of the weights for each domain, and the array beam pattern is the product of the patterns of each domain.

2.4 Weight Computation

Beamforming weights can be calculated using diagonally-loaded Sample Matrix Inversion. The loaded covariance matrix in domain q is

$$R_l^{(q)} = \frac{1}{m} X^{(q)} X^{(q)H} + \gamma^{(q)} I \quad (7)$$

where H denotes the complex conjugate transpose, $\gamma^{(q)}$ is a loading factor, and I is the identity matrix. The $n_q \times 1$ weight vector is then calculated using [3]

$$w^{(q)} = \frac{R_l^{(q)-1} c^{(q)}}{c^{(q)H} R_l^{(q)-1} c^{(q)}} \quad (8)$$

$c^{(q)}$ is the look-direction vector of the form

$$c^{(q)} = \begin{bmatrix} e^{i k_0 \cdot r_1^{(q)}} & e^{i k_0 \cdot r_2^{(q)}} & \dots & e^{i k_0 \cdot r_{n_q}^{(q)}} \end{bmatrix}^T \quad (9)$$

where $k_0 = k n_0$ and n_0 is a unit vector in the look direction, and $k = 2\pi/\lambda$, where λ is the wavelength. Diagonal loading reduces weight jitter in each domain, desensitises the weights to insignificant signals and reduces the influence of signals incident near to the look-direction.

In the HPRF results presented in section 3, $\gamma^{(q)}$ is chosen to be three times the magnitude of the median eigenvalue of the covariance matrix at the q^{th} stage of domain factorisation. This value is typically higher than might be used purely for weight jitter control. We have made no attempt to optimise this, merely choosing a value which works well in a wide range of simulated conditions.

Main beam clutter can cause severe distortion of the adapted beams, if it is allowed to influence the weight calculation. However, it is easily dealt with by temporal pre-filtering of the data used for weight calculation at each domain level. The weights are then applied to the unfiltered data.

Remembering that the main beam of the first and second domains may be very broad, it is important to ensure that jamming entering these beams is not cancelled. A variety of simple modifications are possible, to ensure this. This issue is discussed in reference [4].

2.5 Preventing cancellation of strong targets

It is possible for an adaptive beamformer to cancel or suppress a strong target echo in the same way as for a main-beam jammer. Maintaining adaption to jamming, whilst inhibiting suppression of target-like signals could be approached in a variety of ways. For example, (a) range averaging the covariance to dilute the effect of a target in one range bin relative to jamming and clutter that appears in many range bins; (b) range exclusion - a variant of range-averaging, in which adaption for a given range bin is based on data from adjacent bins; (c) spatial filtering, to attempt to remove the target signal; (d) Doppler filtered adaption, in which the intent is to remove contributions to the signal covariance that are attributable to sources with narrow Doppler spectra (i.e. target-like signals).

Here we have examined the Doppler filtering approach. Two implementations are possible. These are briefly described as follows.

(i) In many cases - particularly in the absence of main beam jamming - the strong target signal will be visible as a line in the Doppler spectrum of the third domain (or even from the second domain). It will be partially cancelled by the adaptive beamformer, whilst weaker signals may be invisible thanks to the loss of overall beamformer gain. Under such conditions, we can modify the Doppler filter that is used to remove main-beam clutter from the data used for adaption. The modified filter would remove the stronger target signal in addition to the clutter, as shown in section 3.

(ii) In the presence of main beam jamming, it may be impossible to estimate the Doppler frequency of the strong target, as described above. In such cases, an indirect solution is possible. The signals output from the penultimate domain can be transformed into Doppler space, and a number of covariance matrices formed, each with selected Doppler lines removed. The Doppler frequency of a strong target-like signal will be indicated by a disproportionate difference between the eigenvalue spectra of the "correct" and "incorrect" covariance matrices. This is because all its energy will be concentrated in a single Doppler bin - in contrast to that of the jammer, which will fall approximately equally into all bins.

3. Simulation results

We have simulated an AI radar in level flight at 300ms^{-1} at an altitude of 1000m. A high PRF (150kHz, providing unambiguous Doppler up to 1100ms^{-1}) means that more clutter enters each range bin, stressing the spatial adaption to a greater degree than might be the case for a lower PRF. There are 256 pulses in the pulse-train (a low number for HPRF). We have simulated a peak transmitter power of 3W per element, with no aperture shading, and a randomly

chosen 10% of elements assumed to have failed (not transmitting). The element failure has the effect of raising transmit sidelobes to around -40dB.

Clutter is simulated using a mixture of 'equal brightness' reflections (e.g. grass) and clutter discretised disposed at random. We include 8 range-ambiguous clutter bands. The first 2 or 3 bands dominate, unless main-beam clutter is strong. Three powerful sidelobe noise jammers and two targets complete the picture. The target ranges and cross-sections are 40km and 1m^2 , respectively. The targets are close to, but not exactly on the look-direction. One is approaching (Doppler outside the clutter spectrum) and the other one is being pursued (Doppler inside the clutter).

Fig. 3 shows the adapted gain pattern for the whole array, in u - v coordinates, for this scenario. Jammer positions are

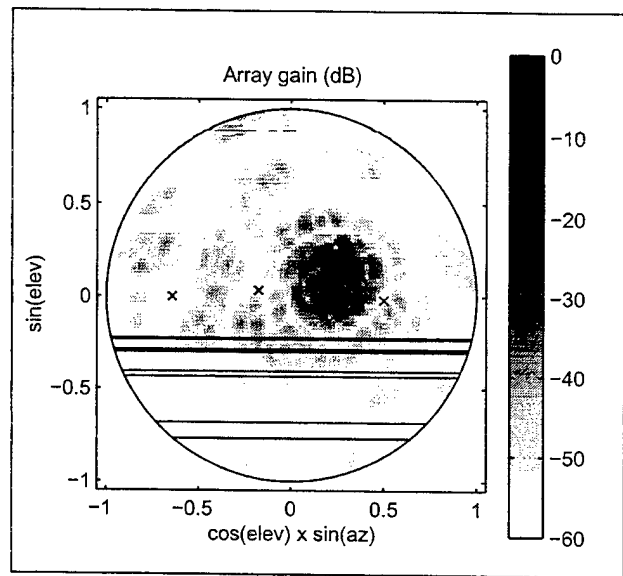


Figure 3. EDAR gain pattern, in u - v coordinates, following adaption to sidelobe clutter and jamming.

marked 'x' and the positions of the first four clutter rings are indicated with pairs of horizontal lines. We can see that very low gain is directed towards both clutter and jamming. The overall array efficiency is -2.5dB relative to a uniformly shaded beamformer. Fig. 4a shows the Doppler spectrum of the data from a single element. The background level is due to the sidelobe jamming, and the clutter Doppler lies approximately between 0 and 20kHz. Fig. 4b shows the Doppler spectrum of the beamformed output, showing the two targets well above the residual clutter, jamming and thermal noise.

In Fig. 5a, we show the effect of increasing the power reflected from the approaching target by 30dB. The strong target has no effect at the lower domain levels, because the process used to prevent premature cancellation of main-beam jamming [4] suppresses any influence of signals

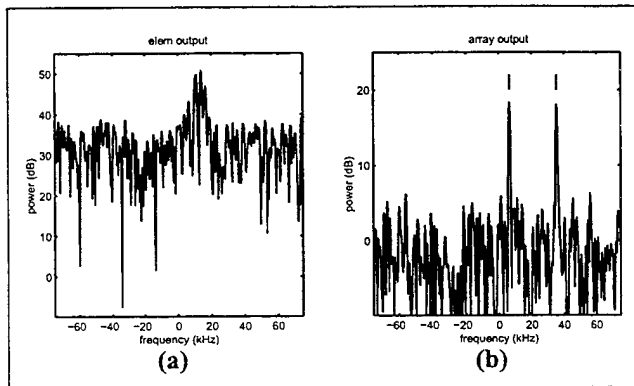


Figure 4. Doppler spectra in the presence of 3 sidelobe jammers and ground clutter (a) at the output of a single array element, (b) at the output of the adaptive EDAR processing. The two vertical ticks above the main peaks in (b) indicate the true target Doppler frequencies. Main beam clutter has been removed using a fixed Doppler filter, following beamforming.

incident near the look-direction. However, at the top domain level, the gain adaption has responded to the strong target and both targets are severely attenuated. The array directivity has degraded to -21dB, though the precise loss will depend on the processing parameters.

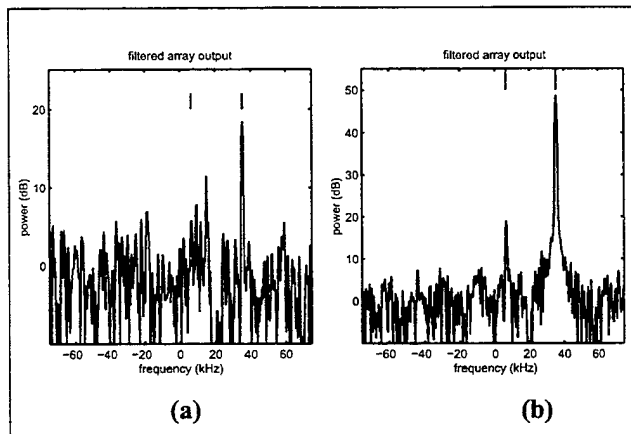


Figure 5. Doppler spectra in the presence of 3 sidelobe jammers and ground clutter, with strength of fast target increased by 30dB. (a) Without extended Doppler filter (b) With extended Doppler filter.

However, the strong target is clearly visible (indeed, it is visible in the output from domain 2) and therefore its Doppler frequency can be estimated. Using a modified Doppler filter (i.e. with a notch at the target Doppler frequency, as shown in Fig. 6) recovers the directivity. Both targets are then visible, as shown in Fig. 5b.

Finally, we have simulated an AI radar in level flight at 300ms^{-1} at an altitude of 2000 feet. A medium PRF waveform is used (14.285kHz, with a bandwidth of 4MHz).

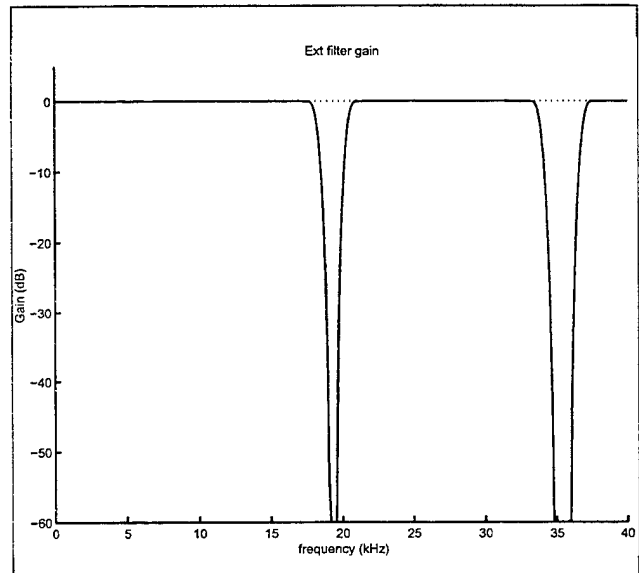


Figure 6. Gain of modified clutter filter. The notch near 19kHz removes main beam clutter. The notch at 36kHz removes the strong target.

There are 128 pulses, and (to represent the effect of pulse compression) groups of 35 adjacent range-gates have been averaged into the covariance matrix. We have simulated a peak transmitter power of 10W per element, with 12.5% duty ratio. There is no aperture shading on transmit, but a randomly chosen 1% of elements do not transmit. (This raises the transmit sidelobes to a realistic level.)

In this simulation the clutter is modelled using

$$\sigma^0 = \gamma \sin \theta + \gamma_{cv} \exp(-(90-\theta)^2 / \psi_0^2) \quad (10)$$

where σ^0 is the clutter cross-section, θ is the grazing angle, $\gamma = 0.2$, $\gamma_{cv} = 10$, and $\psi_0 = 10^0$. The first term in equation (10) is a constant gamma model for the clutter, and the second term simulates the altitude line return.

Fig. 7 shows range-Doppler maps for beamformers pointed at 30 degrees in azimuth. These are (a) a fixed beamformer, (b) 3-tap pre-Doppler STAP processing of data from a 64-sub-arrayed antenna, and (c) EDAR/RDGA processing, as previously described. In each case, we have simulated random amplitude and phase errors (0.2dB and 2.5 degrees RMS, respectively). There are 25 targets at different ranges and Dopplers (most of which are visible, on a regular grid) and sidelobe clutter. Target strengths are equivalent to a 1m^2 object at a range of 50km. The plots are scaled to give constant thermal noise level in each range-Doppler cell, equal to kTB , where k is Boltzmann's constant, $T = 290\text{K}$ and B is the bandwidth.

In the absence of errors [4], EDAR domain-factored RDGA processing removes almost all of the sidelobe clutter. In the

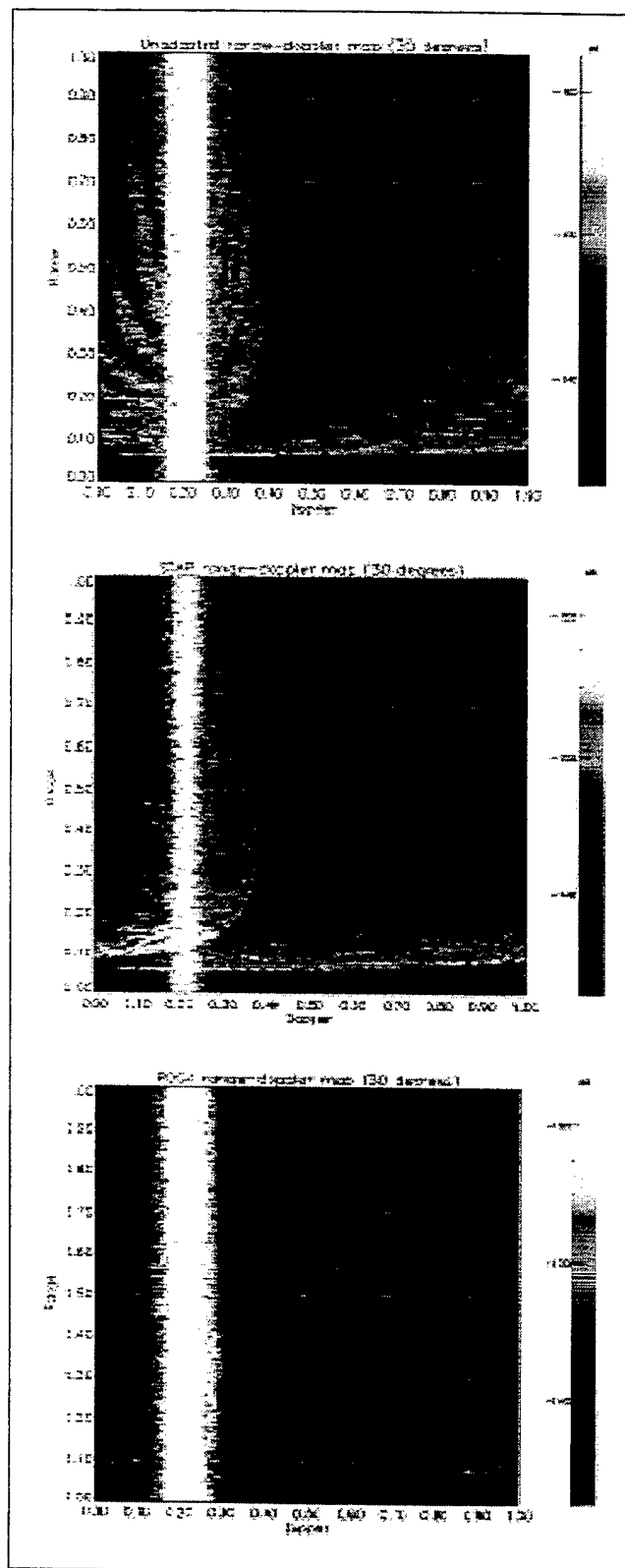


Figure 7. Range-Doppler maps for (a) fixed beamformer, (b) 3-tap pre-Doppler STAP on 64-sub-array antenna, (c) EDAR/RDGA. Calibration errors of 0.2dB and 2.5 degrees rms have been simulated.

presence of errors (Fig. 7c) there is increased breakthrough of the strongest clutter returns (although, in practice, the closest range returns would be eclipsed). It is interesting to note that, in some cases, the recovered signal-to-noise ratios from the fixed beamformer (Fig. 7a) are higher than from the STAP beamformer (Fig. 7b). RDGA on the EDAR beamformer gives the best performance, with a valuable increase in the area of the useable range-Doppler detection space. Performance may be improved still further by (i) a simplified form of STAP processing on output beams formed by EDAR/RDGA, to enhance detection of slow targets; (ii) reducing the number of range-gates over which the covariance matrix is averaged; (iii) increasing the number of elements in domain 3; (iv) potentially more accurate calibration of an element-digitised array.

4. Conclusions

Using domain factorisation, adaptive processing of a large element-digitised phased array can be achieved with realistic sample support. Range-dependent gain adaption enables effective spatial adaption for cancellation of distributed clutter. Strong target returns can be preserved by intelligent Doppler filtering prior to the final level of adaption. Random calibration errors can cause some breakthrough of altitude line clutter, although the method is no more sensitive than other techniques. Future work should examine the potential for reducing errors by element-level calibration.

5. References

- [1] *Element accessed array radar processing*. G.D. Wills, H.D. Rees, I.D. Skidmore, pp 196 - 207, Proc. SPIE Advanced Signal Processing, Algorithms, Architectures and Implementations VIII, 22 - 24 July, 1998, San Diego, CA.
- [2] *Space Time Adaptive Processing*. R. Klemm, IEE Publications, 1999.
- [3] *Adaptive filter theory, 2nd Ed*. S. Haykin, Prentice Hall Inc, 1991.
- [4] *Adaptive clutter and jammer cancellation for element-digitised airborne radar*. J.L. Mather, H.D. Rees, I.D. Skidmore, Proc. Asilomar Conf. Signals Systems and Computers, Pacific Grove, CA, 25-27 October 1999.

This work was carried out as part of Technology Group TG9 of the MoD Corporate Research Programme.

© British Crown Copyright 2000. Published with the permission of the Defence Evaluation and Research Agency on behalf of the Controller HMSO.

ADAPTIVE BEAMFORMER ORTHOGONAL REJECTION TEST (ABORT)

Nicholas B. Pulsone and Charles M. Rader *

Massachusetts Institute of Technology Lincoln Laboratory
244 Wood Street, Lexington, MA 02420
pulsone@ll.mit.edu rader@ll.mit.edu

ABSTRACT

Research in the area of signal detection in the presence of unknown interference has resulted in a number of adaptive detection algorithms. Examples of such algorithms include the Adaptive Matched Filter (AMF), the Generalized Likelihood Ratio Test (GLRT), and the Adaptive Coherence Estimator (ACE). Each of these algorithms results in a tradeoff between detection performance for matched signals and rejection performance for mismatch signals. For example, AMF has better matched signal detection characteristics than ACE, but ACE has better mismatched signal rejection capabilities. This paper introduces a new detection algorithm which we call *Adaptive Beamformer Orthogonal Rejection Test* – ABORT. Our test decides if an observation contains a multidimensional signal belonging to one subspace or if it contains a multidimensional signal belonging to an orthogonal subspace when unknown complex Gaussian noise is present. In our analysis we use a statistical hypothesis framework to develop a generalized likelihood ratio decision rule. We evaluate the performance of this decision rule in both the matched and mismatched signal cases. Our results show that in the matched signal case, ABORT's detection performance exceeds that of ACE and is comparable to AMF and GLRT. In the mismatched signal case, ABORT's discrimination capability is better than AMF and GLRT, but not as good as ACE's.

1. INTRODUCTION

We assume that we have a set of training signals, x_k , $k = 1, \dots, K$ in an N -dimensional complex space, which are characterized by a covariance matrix, \mathbf{R} , unknown to us. Although \mathbf{R} is unknown we can estimate it by computing \mathbf{S}

$$\mathbf{S} = \sum_{k=1}^K x_k x_k^H \quad (1)$$

We are given another signal x which is corrupted by zero-mean complex Gaussian interference n with statistics characterized by \mathbf{R} . x may also contain a signal proportional to the unit vector v , with proportionality constant a . It may alternatively have some other disturbance proportional to v_\perp where v_\perp is any vector orthogonal to v . Or it may have only the interference.

*This work was sponsored by the United States Navy under Air Force Contract F19628-95-C-0002. Opinions, interpretations, conclusions and recommendations are those of the author and are not necessarily endorsed by the United States Air Force or the United States Navy.

Research in the area of signal detection in the presence of unknown interference has resulted in a number of adaptive detection algorithms. None is clearly best (uniformly most powerful). Examples of such algorithms include the following: Adaptive Matched Filter [9], Generalized Likelihood Ratio Test [2], and Adaptive Coherence Estimator [4].

Of these, the AMF has the least computational cost. One computes

$$t_{\text{AMF}} = \frac{|v^H \mathbf{S}^{-1} x|^2}{v^H \mathbf{S}^{-1} v} = |w^H x|^2 \quad (2)$$

and then t_{AMF} is compared to a threshold η_{AMF} . If it exceeds the threshold we say that a signal proportional to v is present, and otherwise we say that it is absent. η_{AMF} is selected as a compromise between missing signals and reporting false alarms. Since $w \equiv (\mathbf{S}^{-1} v) / \sqrt{v^H \mathbf{S}^{-1} v}$ may be computed in advance, the test reduces to computing $w^H x$ for each observation and comparing its energy to a threshold, so it is rather efficient.

For the GLRT or ACE one computes one of the more complicated expressions

$$t_{\text{GLRT}} = \frac{|v^H \mathbf{S}^{-1} x|^2}{(v^H \mathbf{S}^{-1} v)(1 + x^H \mathbf{S}^{-1} x)} \quad (3)$$

$$t_{\text{ACE}} = \frac{|v^H \mathbf{S}^{-1} x|^2}{(v^H \mathbf{S}^{-1} v)(x^H \mathbf{S}^{-1} x)} \quad (4)$$

and compares it with a threshold η_{GLRT} or η_{ACE} .

None of these three algorithms is uniformly most powerful, and indeed no such algorithm is possible [1]. The choice of algorithm must represent a compromise between good probability of detection for weak signals, low probability of reporting false detections due to strong signals perpendicular to v (sidelobe signals), efficient computation, etc.

Recently we have begun to use two-stage algorithms. We use the AMF criterion with a rather weak threshold to select signals worthy of further consideration. Then we apply either ACE [7, 8] or GLRT [5] to make a final decision. AMF decides if a signal is likely to be present and then ACE (or GLRT) decides whether it is likely to be proportional to v .

This paper introduces a new detection algorithm which we call *Adaptive Beamformer Orthogonal Rejection Test* – ABORT. It can also be used in a two-phase test where the first phase is again AMF. In the second phase we ask whether the signal is more likely to lie in the one-dimensional subspace v or in the complementary subspace v_\perp , given that we expect it to be corrupted by an interference with covariance \mathbf{R} , estimated by the sample covariance matrix \mathbf{S} .

We summarize the procedure as follows:

- First we compute the estimated covariance matrix \mathbf{S} using (1).
- Next we compute $w = (\mathbf{S}^{-1}v)/\sqrt{v^H \mathbf{S}^{-1}v}$.
- Then for each observation x we compute t_{AMF} using (2).
- We compare t_{AMF} with a threshold η_{AMF} . If it is smaller, we reject the hypothesis that a signal proportional to v is present.
- But if $t_{\text{AMF}} > \eta_{\text{AMF}}$ we compute

$$\tilde{t} = \frac{1 + t_{\text{AMF}}}{2 + x^H \mathbf{S}^{-1}x}$$

and we compare this with another threshold $\tilde{\eta}$. If it is less than the threshold, we declare that the signal present is not proportional to v . If it is greater than the threshold we declare a detection.

The remainder of this paper provides the derivation and analysis for the ABORT algorithm. In Section 2 we formulate ABORT using a likelihood ratio framework. In Section 3 we illustrate with an example the matched and mismatched performance of ABORT relative to the AMF, GLRT and ACE detectors. Section 3 also provides the analysis which describes the matched and mismatched probability of detection for the ABORT algorithm as well as the probability of false alarm. Finally, in Section 4 we conclude with a brief summary.

2. LIKELIHOOD RATIO TEST

In Section 1 we introduced ABORT as the second phase in a two-phase test (AMF followed by ABORT). In this section we analyze the performance of the ABORT. Although not shown here, it is possible to choose the threshold of the first test (AMF) such that the performance of the two-phase test is identical to ABORT alone. For this case, the analysis below not only characterizes ABORT but also the two-phase test. In an upcoming paper we will describe how to choose thresholds for the two-phase test that satisfy this condition.

ABORT decides if a complex N -component test vector x contains a signal vector v or if x contains a signal v_{\perp} where v_{\perp} is orthogonal to v . This problem is posed as a decision between two possible hypotheses,

$$x = \begin{cases} n + av_{\perp}, & \text{orthogonal signal-in-noise, } H_0 \\ n + av, & \text{signal-in-noise, } H_1 \end{cases} \quad (5)$$

where a is an unknown complex scalar. We formulate ABORT using a generalized likelihood ratio approach. The approach parallels the derivation for the GLRT given in [2]. Where possible we use the same notation used in [2]. Let us begin with an expression for the N -dimensional probability density function (PDF) for one of the training vectors x_k ,

$$f(x_k) = \frac{1}{\pi^N |\mathbf{R}|} \exp[-x_k^H \mathbf{R}^{-1} x_k], \quad (6)$$

where $|\mathbf{R}|$ is the determinant of \mathbf{R} . Since all the training vectors are independent and identically distributed, the joint PDF for the test vector and all the training vectors is,

$$f(x, x_1, \dots, x_K) = \left\{ \frac{1}{\pi^N |\mathbf{R}|} \right\}^{K+1} \exp \left[- \sum_{k=1}^{K+1} x_k^H \mathbf{R}^{-1} x_k \right]. \quad (7)$$

where we define $x_{K+1} \equiv x - ay$ in which y is v for hypothesis H_1 and v_{\perp} for hypothesis H_0 . Noting that $x^H \mathbf{R}^{-1} x = \text{tr}(\mathbf{R}^{-1} x x^H)$, we can express (7) as,

$$f(x, x_1, \dots, x_K) = \left\{ \frac{1}{\pi^N |\mathbf{R}|} \exp[-\text{tr}(\mathbf{R}^{-1} \mathbf{T})] \right\}^{K+1}, \quad (8)$$

where \mathbf{T} is the $N \times N$ matrix,

$$\mathbf{T} = \frac{1}{K+1} \left\{ (x - ay)(x - ay)^H + \sum_{k=1}^K x_k x_k^H \right\}. \quad (9)$$

In the likelihood ratio approach we maximize the PDF given in (8) over the unknown parameters; namely \mathbf{R} and a . First, we maximize over the covariance matrix \mathbf{R} assuming that $K \geq N$ (typically $2N \leq K \leq 5N$). As indicated in [2], the positive definite matrix which maximizes the joint PDF in (8) is simply \mathbf{T} . If we replace \mathbf{R} with \mathbf{T} in (8) we obtain,

$$m = \max_{\mathbf{R}} f(x, x_1, \dots, x_K) = \left\{ \frac{1}{(e\pi)^N |\mathbf{T}|} \right\}^{K+1}. \quad (10)$$

In what follows we separately maximize the expression given in (10) over the remaining unknown parameters for each hypothesis. Using the results in [2] we maximize m over a under hypothesis H_1 as follows,

$$\max_a m | H_1 = \left\{ \frac{(K+1)^N}{(e\pi)^N |\mathbf{S}| (1 + x^H \mathbf{S}^{-1} x - t_{\text{AMF}})} \right\}^{K+1}, \quad (11)$$

where \mathbf{S} is defined in (1) and t_{AMF} is defined in (2). Similarly, we can use the results in [6] to maximize (10) over a and v_{\perp} under hypothesis H_0 to infer,

$$\max_{a, v_{\perp}} m | H_0 = \left\{ \frac{(K+1)^N}{(e\pi)^N |\mathbf{S}| (1 + t_{\text{AMF}})} \right\}^{K+1}. \quad (12)$$

The generalized likelihood ratio test for ABORT is obtained by comparing the ratio of (11) over (12) to a threshold. For convenience we take the $(K+1)^{\text{th}}$ root of the resulting ratio to obtain the following test,

$$t = \frac{1 + t_{\text{AMF}}}{1 + x^H \mathbf{S}^{-1} x - t_{\text{AMF}}} \underset{H_0}{\overset{H_1}{\geq}} \ell. \quad (13)$$

Note that the test given in (13) can also be expressed in an equivalent and more convenient form after some simple algebra as follows,

$$\tilde{t} = \frac{1 + t_{\text{AMF}}}{2 + x^H \mathbf{S}^{-1} x} \underset{H_0}{\overset{H_1}{\geq}} \tilde{\eta}, \quad (14)$$

where $\tilde{t} = t/(t+1)$ and $\tilde{\eta} = \ell/(\ell+1)$. The likelihood ratio given in (13) is convenient for analysis whereas the form given in (14) is more suitable for implementation.

3. PERFORMANCE ANALYSIS

We begin this section with a performance curve for the ABORT algorithm and relate it to the AMF, GLRT and ACE detection algorithms. The curve for ABORT was generated with numerical

integration techniques using expressions derived in the following subsections. We have confirmed these performance curves using extensive Monte Carlo simulations.

The example we consider assumes a system of dimension $N = 5$ with $K = 25$ training vectors and we choose the detection thresholds (η_{AMF} , η_{GLRT} , η_{ACE} and $\bar{\eta}$) for each of the four tests such that the average probability of false alarm in a noise only environment is $P_{\text{FA}} = 10^{-4}$. In the figure we illustrate contours of constant detection probability for the AMF, GLRT, ACE and ABORT algorithms respectively. In these plots we vary the signal to interference plus noise power ($0 \text{ dB} \leq \text{SINR} \leq 25 \text{ dB}$) and mismatch angle ($0.2 \leq \cos^2 \theta \leq 1$). The desirable properties for a candidate algorithm are higher detection probabilities for strong matched signals and lower detection probabilities for weak or mismatched signals. On the contour plots this corresponds to higher detection probabilities in the upper right-hand corner and lower detection probabilities elsewhere. We see that AMF does a poor job discriminating between matched and mismatched signals while we see that ACE appears to be too selective and sacrifices P_{D} performance. GLRT has acceptable performance. However, we see that the proposed ABORT algorithm has similar matched performance as well as improved mismatched performance relative to the GLRT.

We derive analytical expressions for the probability of false alarm as well as expressions for the probability of detection for both matched and mismatched signals. In our analysis we first derive the expression for the mismatched probability of detection, then specialize this expression for the matched probability of detection followed by the expression for the probability of false alarm.

3.1. Mismatched Probability of Detection

In this context mismatch refers to the angle in N -dimensional space between the steering vector v used in the detector and the received signal v_m contained in the test vector (we introduce the notation v_m for the test vector to distinguish it from the steering vector v). Note that v_m is aligned with v under hypothesis H_1 and orthogonal to v under hypothesis H_0 . In general, v_m can be divided into a v component and a v_{\perp} component and so here we assume the signal vector v_m arrives from a general direction possibly different from the steering vector v . To aide in our analysis we define the cosine of the mismatched angle θ between v_m and v in the whitened space as follows,

$$\cos^2 \theta \equiv \frac{|v^H \mathbf{R}^{-1} v_m|^2}{(v^H \mathbf{R}^{-1} v)(v_m^H \mathbf{R}^{-1} v_m)}. \quad (15)$$

Consider the likelihood ratio test given in (13). If we introduce the quantity

$$\beta_{\theta} \equiv \frac{1}{1 + x^H \mathbf{S}^{-1} x - t_{\text{AMF}}}, \quad (16)$$

referred to as the loss factor in [2] and [9], then we can express the test given in (13) as follows,

$$t = \bar{t}_{\text{GLRT}} + \beta_{\theta} \underset{H_0}{\overset{H_1}{\geq}} \eta, \quad (17)$$

where $\bar{t}_{\text{GLRT}} = t_{\text{GLRT}}/(1 - t_{\text{GLRT}})$ and t_{GLRT} is given in (3). The distribution of the test statistic t depends on two random and related quantities – a complex non-central F -distributed random variable

$F_{1,L}(\delta_{\beta_{\theta}})$ (due to \bar{t}_{GLRT}) and a complex non-central beta-distributed random variable β_{θ} (due to the loss factor) – as follows:

$$t \stackrel{d}{=} F_{1,L}(\delta_{\beta_{\theta}}) + \beta_{\theta}. \quad (18)$$

In (18) the non-centrality parameter $\delta_{\beta_{\theta}}$ is related to the SINR $c_{\theta} \equiv |a|^2 \cdot v_m^H \mathbf{R}^{-1} v_m \cdot \cos^2(\theta)$ as $\delta_{\beta_{\theta}}^2 \equiv c_{\theta} \cdot \beta_{\theta}$ and the integer $L \equiv K - N + 1$. We assume that v_m has unit norm, i.e. $v_m^H v_m = 1$. Note that the two random quantities used to describe the test statistics are related by β_{θ} . The probability density function for the random variable β_{θ} has been derived in [3] and is expressible in terms of the following finite sum,

$$f(\beta_{\theta}) = e^{-s_{\theta} \beta_{\theta}} \sum_{\ell=0}^{L+1} \binom{L+1}{\ell} \frac{K!}{(K+\ell)!} s_{\theta}^{\ell} f_{L+1, N-1+\ell}(\beta_{\theta}), \quad (19)$$

where $s_{\theta} = |a|^2 \cdot v_m^H \mathbf{R}^{-1} v_m \cdot \sin^2(\theta)$ and $f_{n,m}(\beta)$ is the central beta density defined as follows

$$f_{n,m}(\beta) \equiv \frac{(n+m-1)!}{(n-1)!(m-1)!} \beta^{n-1} (1-\beta)^{m-1}, 0 \leq \beta \leq 1. \quad (20)$$

We define the mismatch probability of detection for ABORT as the probability of choosing hypothesis H_1 , i.e. using the relation in (18) we say,

$$P_{\text{D}}(\theta) = \Pr[F_{1,L}(\delta_{\beta_{\theta}}) > \eta - \beta_{\theta}]. \quad (21)$$

Using the finite sum expression for the cumulative distribution function of a complex non-central F -distribution given in [2] together with the expression in (21), the mismatched probability of detection for ABORT is as follows

$$P_{\text{D}}(\theta) = \int_0^1 P_{\text{D}}(\theta) | \beta_{\theta} \cdot f(\beta_{\theta}) d\beta_{\theta}, \quad (22)$$

where $P_{\text{D}}(\theta) | \beta_{\theta}$ is the mismatched probability of detection for ABORT conditioned on β_{θ} as follows,

$$P_{\text{D}}(\theta) | \beta_{\theta} = 1 - \frac{1}{\tau_{\theta}} \sum_{m=1}^L \binom{L}{m} (\tau_{\theta} - 1)^m G_m \left(\frac{\delta_{\beta_{\theta}}^2}{\tau_{\theta}} \right), \quad (23)$$

in which $\tau_{\theta} = 1 + \eta - \beta_{\theta}$ and the function $G_m(x)$ is defined in terms of the incomplete Gamma function $\Gamma(m, x)$ as follows

$$G_m(x) = \frac{\Gamma(m, x)}{(m-1)!} = e^{-x} \sum_{n=0}^{m-1} \frac{x^n}{n!}. \quad (24)$$

3.2. Matched Probability of Detection

The analytical expression for the probability of detection for a matched signal is obtained by substituting $\theta = 0$ into (22) as shown,

$$P_{\text{D}} = P_{\text{D}}(\theta = 0) = \int_0^1 P_{\text{D}} | \beta_0 \cdot f(\beta_0) d\beta_0, \quad (25)$$

where the conditional probability of detection for a matched signal is defined as follows,

$$P_{\text{D}} | \beta_0 = 1 - \frac{1}{\tau_0} \sum_{m=1}^L \binom{L}{m} (\tau_0 - 1)^m G_m \left(\frac{\delta_{\beta_0}^2}{\tau_0} \right). \quad (26)$$

Note that for the matched case with $\theta = 0$, the distribution of the loss factor given in (16) reduces to the central beta density whose PDF is given in (20).

3.3. Probability of False Alarm

The probability of false alarm for ABORT is defined in this context as the probability of selecting the signal in noise hypothesis (H_1) when the SINR = 0 (i.e., $a = 0$). We obtained the analytical expression for the probability of false alarm from (25) by setting $a = 0$. Hence, the P_{FA} is as follows

$$P_{FA} = \int_0^1 P_{FA}|\beta_0 \cdot f(\beta_0) d\beta_0, \quad (27)$$

where $P_{FA}|\beta_0$ is the probability of false alarm conditioned on the loss factor. After substituting $a = 0$ in (26) and using the Binomial Theorem we obtain the following,

$$P_{FA}|\beta_0 = \tau_0^{-L}. \quad (28)$$

4. SUMMARY

We have developed and analyzed the ABORT algorithm that can be efficiently implemented as part of a two-step detector. We have demonstrated that the ABORT algorithm has matched signal detection performance commensurate with the AMF and GLRT detection algorithms which is generally an improvement over ACE performance. Furthermore, we have demonstrated that the ABORT algorithm has better mismatch discrimination capabilities than both AMF and GLRT but not ACE. ABORT provides an alternative detection strategy in the unknown multichannel noise environment. When faced with the tradeoff between matched signal detection versus mismatched signal rejection, ABORT offers commensurate matched signal detection performance as well as improved sidelobe rejection performance relative to the benchmark GLRT detector.

5. ACKNOWLEDGEMENTS

The authors would like to thank Ed Baranoski for his comments and suggestions and also Christ Richmond and Ram Raghavan for insightful discussions.

6. REFERENCES

- [1] S. Bose and A. O. Steinhardt. A maximal invariant framework for adaptive detection with structured and unstructured covariance matrices. *IEEE Trans. on Signal Processing*, 43(9):2164–2175, September 1995.
- [2] E. J. Kelly. An adaptive detection algorithm. *IEEE Transactions on AES*, 22(1):115–127, March 1986.
- [3] E. J. Kelly. Adaptive detection in non-stationary interference, Part III. Technical Report 761, MIT Lincoln Laboratory, Lexington, MA, 1987.
- [4] L. T. McWholter L. L. Scharf. Adaptive matched subspace detectors and adaptive coherence. In *Proceedings of the 30th Asilomar Conference on Signals and Systems*, volume 2, pages 1114–1117, Los Alamitos, CA, November 1996.
- [5] N. B. Pulsone and M. A. Zatman. A computationally-efficient two-step implementation of the GLRT. In *Proceedings of the Adaptive Sensor Array Processing Workshop*, Lexington, MA, March 1999.
- [6] R. S. Raghavan, N. B. Pulsone, and D. J. McLaughlin. Performance of the GLRT for adaptive subspace detection. *IEEE Transactions on AES*, 32(4):1473–1487, October 1996.
- [7] C. D. Richmond. Statistical performance analysis of the adaptive sidelobe blanker algorithm. In *Proceedings of the 31st Asilomar Conference on Signals and Systems*, volume 1, pages 872–876, Los Alamitos, CA, November 1997.
- [8] C. D. Richmond. An analysis of an adaptive detection algorithm for non-homogeneous environments. In *ICASSP Proceedings*, volume 4, pages 2005–2008, Seattle, Washington, May 1998.
- [9] F. C. Robey, D. R. Fuhrmann, E. J. Kelly, and R. A. Nitzberg. A CFAR adaptive matched filter detector. *IEEE Transactions on AES*, 28(1):208–216, January 1992.

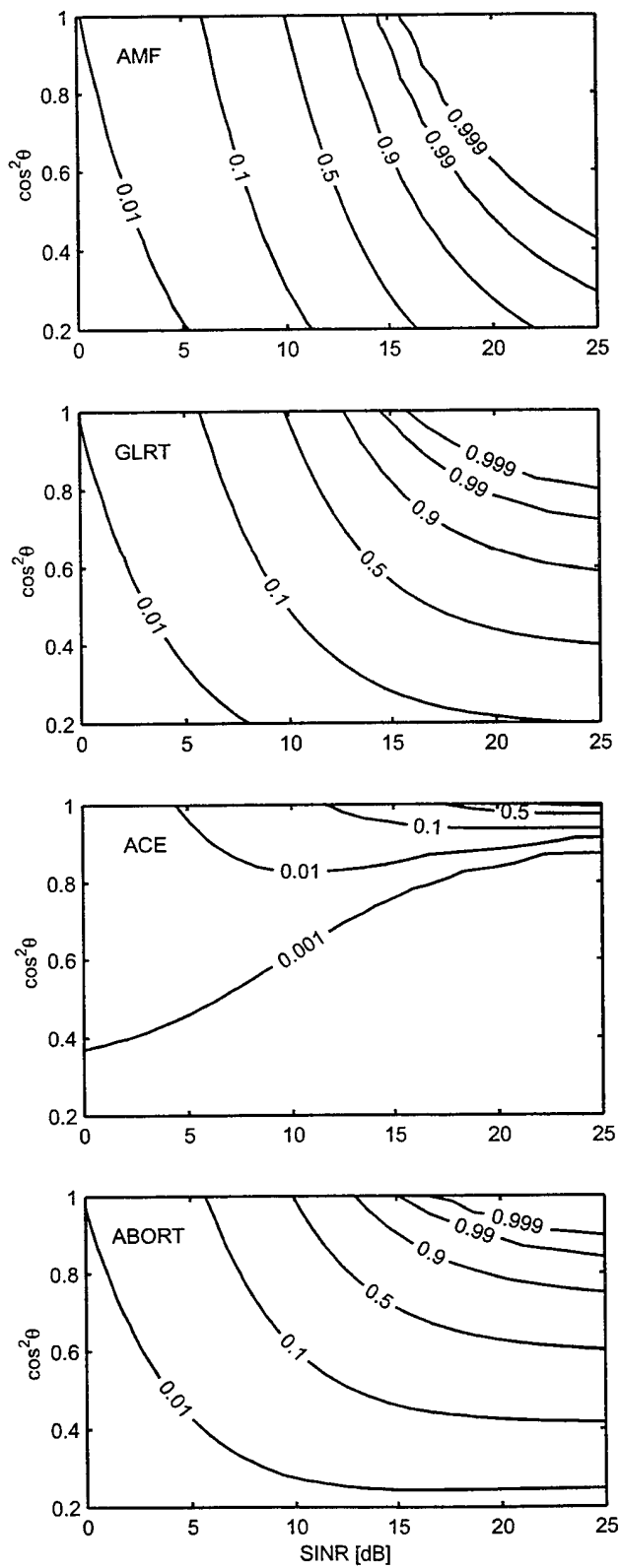


Figure 1: Contours of constant P_D for the AMF, GLRT, ACE and ABORT. System Parameters: $N = 5$, $K = 25$, $P_{FA} = 10^{-4}$.

CRAMÉR-RAO BOUNDS: THE ADAPTIVE ARRAY STORY

Christ D. Richmond *

Massachusetts Institute of Technology
Lincoln Laboratory
244 Wood Street, Rm J-150C
Lexington, MA 02420, USA
christ@ll.mit.edu

ABSTRACT

Cramér-Rao bounds (CRBs) are often used in practice to ascertain the effectiveness of a proposed parameter estimation algorithm. Extensive research on CRBs exists in the literature. CRBs on target parameter estimates for the classical adaptive detection/estimation problem posed by Reed et. al. and Kelly for the constant (Swerling 0) target case are deducible from existing results (Zeira 1990 and Francos 1995). Colored noise-only training losses are not reflected in the CRBs for Swerling 0 target parameters. We briefly outline the argument for this and likewise extend analysis to include targets with Swerling II fluctuations. For Swerling II targets the colored noise parameters are coupled to those of the signal in the Fisher Information Matrix (FIM). Thus, adaptive training losses are reflected in the CRBs; however, the Maximum Likelihood (ML) estimates of the signal parameters are biased in general. The CRBs are therefore only accountable in the asymptotic regimes.

1. INTRODUCTION

Signal parameter estimation is an important part of many adaptive sensor array systems. The Cramér-Rao (lower) bound (CRB) provides a useful metric from which one can often ascertain the effectiveness of a proposed parameter estimation algorithm. The CRB has been used extensively in the communications, radar, and sonar communities. Existing results on signal parameter estimation typically assume that several signal bearing data snapshots are available for estimation [1]–[9]. In this analysis we address parameter accuracy within the context of adaptive estimation. Specifically, we assume that several signal bearing and several signal free (training) snapshots are available for estimation. The goal is to determine whether CRBs based on this totality of data will quantify the observed loss in parameter accuracy due to colored noise (noise + interference) only training. It is of interest to consider CRBs for both constant (conditional/nonrandom) and Swerling II fluctuating (unconditional/random) signal models.

The notational convention used throughout this paper is as follows. Boldfaced capitals represent matrices, e.g. \mathbf{A} , and boldfaced lower case represent column vectors, e.g. \mathbf{a} . Real and complex scalars will be denoted by italics, e.g. a . The scalar elements

of a matrix (or vector) will be denoted with the same symbol indexed, e.g. the element of \mathbf{A} in the i -th row and j -th column is given by $A_{i,k}$. It is sometimes convenient to denote this also by $[\mathbf{A}]_{i,k} \triangleq A_{i,k}$. The gradient of a multivariate function $f(\mathbf{A})$ is denoted by $\nabla_{\mathbf{A}} f$ and sometimes by $\frac{\partial f}{\partial \mathbf{A}}$ where the resulting gradient has the same dimensions as the matrix (or vector) \mathbf{A} . Note that $[\nabla_{\mathbf{A}} f]_{i,k} = \frac{\partial f}{\partial A_{i,k}}$. Differentiating a matrix of multivariate functions is necessary on occasion. Hence, the notation $\frac{\partial \mathbf{A}}{\partial \alpha}$ represents a matrix of derivatives where the i -th row and j -th column of this matrix is given by $\frac{\partial A_{i,k}}{\partial \alpha}$.

2. THE CRAMÉR-RAO BOUND INEQUALITY

The Cramér-Rao bound (CRB) is typically defined for and involves differentiation with respect to real-valued parameters [10]. Many problems in array processing involve complex data (in phase and quadrature components) and therefore complex-valued parameters. Considering the real and imaginary parts of each complex parameter is one viable approach to keeping all parameters real so that the classical formulations of the CRB can be applied to problems with complex parameters [6]. In this presentation, however, CRB computations involving both real and complex parameters simultaneously is considered. Two truths make this a rather painless process: (i) converting real parameters (the real and imaginary parts) to complex parameters can be considered a simple (linear) change of coordinates, and (ii) the CRB is independent of the coordinate system in which calculations are made.

Let the set of complex-valued and real-valued parameters be denoted collectively by the vector $\mathbf{a} = [a_1, a_2, \dots, a_A]^T$. Define the differential operator

$$\frac{\partial}{\partial \mathbf{a}} \triangleq \begin{cases} \frac{\partial}{\partial a} \left(\begin{array}{c} \text{the usual partial} \\ \text{derivative wrt.} \\ \text{a real variable} \end{array} \right) & , \quad a \in \mathcal{R} \\ \frac{1}{2} \left[\frac{\partial}{\partial \text{Re}(a)} - j \frac{\partial}{\partial \text{Im}(a)} \right] & , \quad a \in \mathcal{C} \end{cases} \quad (1)$$

If $a \in \mathcal{C}$, then $\frac{\partial}{\partial a^*}$ is defined by changing the $-j$ in eq(1) to $+j$. Note that the complex differential operator is the usual one arising from what is commonly referred to as Wirtinger calculus [13] from which conjugate gradient based methods originate. This calculus treats a and a^* as independent variables and allows computation of CRBs involving complex parameters.

* This work was sponsored by DARPA under Air Force contract F19628-95-C-0002. Opinions, interpretations, conclusions, and recommendations are those of the author and are not necessarily endorsed by the USAF.

The parameters in \mathbf{a} can be subdivided into two groups: (i) parameters of interest, and (ii) nuisance parameters. It will be assumed throughout that *all parameters of interest are real*. Let the likelihood function of the data from which the parameters \mathbf{a} will be estimated be denoted by p . Define the elements of the Fisher Information Matrix (FIM) by

$$J_{i,k} \triangleq -E \left\{ \frac{\partial^2 \ln p}{\partial a_i \partial a_k} \right\}, \quad \text{FIM} \triangleq \mathbf{J} = [J_{i,k}]. \quad (2)$$

Let $\mathbf{J}^{-1} = [J^{i,i}]$ and an unbiased estimate of a parameter of interest be given by \hat{a}_i . The CRB inequality says that for any unbiased estimate of \hat{a}_i with variance $\sigma_{a_i}^2$:

$$\sigma_{a_i}^2 \geq J^{i,i}. \quad (3)$$

3. ADAPTIVE DETECTION AND ESTIMATION

In adaptive detection signal presence is sought in a complex $N \times 1$ vector observation (or *snapshot*) \mathbf{x}_T often called the *primary* data vector or *test cell*. The goal is to classify the test cell into one of two categories:

$$H_0 : \mathbf{x} = \mathbf{n}, \quad \text{or} \quad H_1 : \mathbf{x} = S\mathbf{v} + \mathbf{n}; \quad (4)$$

noise only (null hypothesis H_0), or target signal plus noise (hypothesis H_1). The noise is complex zero mean circular Gaussian with covariance \mathbf{R} . The covariance \mathbf{R} is assumed to be an unknown parameter. The target array response vector is denoted by \mathbf{v} and assumed to be a known quantity in the detection phase, but post-detection is refined in the estimation phase. The symbol S represents the complex target amplitude. It is assumed deterministic under the constant target model (Swerling 0), and assumed complex Gaussian under the Swerling II assumption, i.e. $S \sim CN(0, \sigma_S^2)$.

A *secondary* data set (or training set) consisting of L_n data samples¹ $\mathbf{X} = [\mathbf{x}_1 | \dots | \mathbf{x}_{L_n}]$ is typically acquired, to estimate the unknown \mathbf{R} . It is assumed that each training snapshot \mathbf{x}_i is signal free, zero mean, and shares the same covariance, i.e. $\text{cov}(\mathbf{x}_i) = \mathbf{R}$ for $i = 1, \dots, L_n$.

3.1. Relevant System Losses in Detection

Researchers have quantified very useful measures which capture the penalty for signal free training in the detection area. Two very well-known metrics include: (i) the signal-to-interference plus noise ratio (SINR) loss (related to probability of detection (PD)), and (ii) the constant false alarm rate (CFAR) loss (related to the probability of false alarm (PFA)).

The SINR loss is the additional SINR required in the adaptive case (with signal free training) in order to obtain the same PD as one would in the clairvoyant (\mathbf{R} known) case. The CFAR loss is manifested by a higher threshold required in the adaptive case versus the clairvoyant case to attain the same PFA. Figure 1 illustrates these losses. It plots PD versus SINR for three cases: (i) the matched filter (MF), which is the optimal detector when \mathbf{R} is known, with constant signals, (ii) the adaptive matched filter

(AMF), which is the sample matrix inversion (SMI) [11] counterpart of the MF for \mathbf{R} unknown, with constant signals, and (iii) the MF with Swerling II signals. The PFA was chosen to be 10^{-6} . Note that for a PD of 0.9 the AMF requires an addition 6dB or so more SINR than the MF. This difference in required SINR is due exclusively to the need to train over the signal free data set, and is referred to as the SINR loss. Similarly, the threshold for the MF is 11.4dB and for the AMF it is 20.4dB. The difference in threshold values is again due to the signal free training and is referred to as the CFAR loss.

Both of these measures have proven to be very useful in the detection area. Can we quantify similar losses on bounds for achievable parameter accuracy?

3.2. Losses in Parameter Accuracy

Once a signal is detected, signal parameters are estimated (refined). These estimates are likewise based on the totality of data available; namely, the test cell as well as the signal free training set. In this analysis we shall assume that there are L_s data vectors containing the signal of interest, and L_n signal free data vectors. *This is to be contrasted with all of the literature on CRBs, which typically assume that several signal bearing data vectors are available only.*

When $L_s = 1$ and \mathbf{R} is assumed known the CRB inequality for the signal complex amplitude S is known to be

$$\sigma_S^2 \geq \frac{1}{\mathbf{v}^H \mathbf{R}^{-1} \mathbf{v}}. \quad (5)$$

The the Maximum Likelihood (ML) estimate of S when both \mathbf{R} and S are unknown is known to be unbiased with a variance which is proportional to this CRB

$$\sigma_{S_{ML}}^2 = \frac{1}{\mathbf{v}^H \mathbf{R}^{-1} \mathbf{v}} \cdot \left[\frac{L_n}{L_n - N + 1} \right]. \quad (6)$$

The proportionality constant provides a direct measure of estimation loss due to signal free training. Indeed, it gives a direct measure of the efficiency of the ML estimate. Will the CRBs on all signal parameters quantify this observed loss due to signal free training? Answering this question is the goal of this analysis.

4. PARAMETER ACCURACY FOR CONSTANT TARGETS

The likelihood function for the complete data set consisting of L_s signal bearing snapshots and L_n signal free snapshots is given by

$$p_0 = \pi^{-N(L_s + L_n)} \cdot |\mathbf{R}|^{-(L_s + L_n)} \times \exp \left[- \sum_{k=1}^{L_s} (\mathbf{x}_k - \mathbf{v} S_k)^H \mathbf{R}^{-1} (\mathbf{x}_k - \mathbf{v} S_k) - \text{tr} \mathbf{R}^{-1} \mathbf{X} \mathbf{X}^H \right] \quad (7)$$

where it is assumed that the signal array response is parameterized by the signal parameters of interest, i.e. $\mathbf{v} = \mathbf{v}(u_1, u_2, \dots, u_M)$ where $u_m \in \mathbb{R}$. Let the parameter vector \mathbf{a} be given by

$$\mathbf{a} = [u_1, u_2, \dots, u_M, S_1, S_2, \dots, S_{L_s}, S_1^*, S_2^*, \dots, S_{L_s}^*, \text{vec}(\mathbf{R})]^T \quad (8)$$

¹Under both hypotheses, it is assumed that $L_n \geq N$.

where the S_k 's and \mathbf{R} are considered nuisance parameters and CRBs are sought for the parameters of interest $\mathbf{u} \triangleq [u_1, \dots, u_M]^T$. Define

$$\|\mathbf{s}\|^2 \triangleq \sum_{k=1}^{L_s} |S_k|^2, \quad \mathbf{v}_{u_n} \triangleq \frac{\partial \mathbf{v}}{\partial u_n}. \quad (9)$$

It can be shown that the elements of the FIM are given by

$$-E \left\{ \frac{\partial^2 \ln p_0}{\partial S_l^* \partial S_k} \right\} = \begin{cases} 0, & l \neq k \\ \mathbf{v}^H \mathbf{R}^{-1} \mathbf{v}, & l = k \end{cases} \quad (10)$$

$$-E \left\{ \frac{\partial^2 \ln p_0}{\partial u_n \partial u_m} \right\} = \|\mathbf{s}\|^2 \cdot (\mathbf{v}_{u_m}^H \mathbf{R}^{-1} \mathbf{v}_{u_n} + \mathbf{v}_{u_n}^H \mathbf{R}^{-1} \mathbf{v}_{u_m}) \quad (11)$$

$$-E \left\{ \frac{\partial^2 \ln p_0}{\partial u_m \partial S_k} \right\} = \left[E \left\{ \frac{\partial^2 \ln p_0}{\partial u_m \partial S_k^*} \right\} \right]^* = S_k^* \mathbf{v}_{u_m}^H \mathbf{R}^{-1} \mathbf{v} \quad (12)$$

$$-E \left\{ \frac{\partial \nabla_{\mathbf{R}^*} \ln p_0}{\partial R_{i,k}} \right\} = (L_s + L_n) \cdot \mathbf{R}^{-1} \mathbf{e}_i \mathbf{e}_k^H \mathbf{R}^{-1} \quad (13)$$

where \mathbf{e}_k is the standard Euclidean basis vector. The cross terms of the FIM between the elements of \mathbf{R} (the colored noise parameters) and those of u_m and S (the signal parameters) in theory should capture the relevant losses in achievable accuracy of parameters u_m due to the need to train on signal free data. It can be shown, however, that these cross terms are in fact zero, *i.e.*

$$E \left\{ \frac{\partial^2 \ln p_0}{\partial R_{i,k} \partial u_n} \right\} = E \left\{ \frac{\partial^2 \ln p_0}{\partial R_{i,k}^* \partial u_n} \right\} = 0, \quad (14)$$

$$E \left\{ \frac{\partial^2 \ln p_0}{\partial R_{i,k} \partial S_l} \right\} = E \left\{ \frac{\partial^2 \ln p_0}{\partial R_{i,k}^* \partial S_l} \right\} = 0, \quad (15)$$

$$E \left\{ \frac{\partial^2 \ln p_0}{\partial R_{i,k} \partial S_l^*} \right\} = E \left\{ \frac{\partial^2 \ln p_0}{\partial R_{i,k}^* \partial S_l^*} \right\} = 0. \quad (16)$$

Zeira et al [1] and Francos et al [2] demonstrated this decoupling for a single signal bearing snapshot via the Slepian-Bang formula. Having multiple signal bearing snapshots and additional signal free snapshots does not change this. Hence, inverting the FIM to obtain the CRBs on the parameters \mathbf{u} leads to the same results as already appear in the literature. A somewhat unanticipated result.

5. PARAMETER ACCURACY FOR SWERLING II TARGETS

If we now allow the target amplitudes S_k to fluctuate with Swerling II statistics, then each signal bearing snapshot becomes zero mean with a covariance matrix having both a signal component and a noise component. The likelihood function for the full data set is given by

$$p_{II} = \pi^{-N(L_s + L_n)} \cdot \left[\prod_{k=1}^{L_s} |\mathbf{R}_{S_k}|^{-1} \right] \cdot |\mathbf{R}|^{-L_n} \times \exp \left[-\text{tr} \left(\mathbf{R}^{-1} \mathbf{X} \mathbf{X}^H + \sum_{k=1}^{L_s} \mathbf{R}_{S_k}^{-1} \mathbf{x}_{S_k} \mathbf{x}_{S_k}^H \right) \right] \quad (17)$$

where $\mathbf{R}_{S_k} = \mathbf{R} + \sigma_{S_k}^2 \mathbf{v} \mathbf{v}^H$. Let the parameter set be given by

$$\mathbf{a} = [u_1, u_2, \dots, u_M, \sigma_{S_1}^2, \dots, \sigma_{S_{L_s}}^2, \text{vec}(\mathbf{R})]^T \quad (18)$$

where the elements of \mathbf{u} remain the parameters of interest. The elements of the FIM can in general be written as

$$-E \left\{ \frac{\partial^2 \ln p_{II}}{\partial \alpha \partial \beta} \right\} = L_n \cdot \text{tr} \left(\mathbf{R}^{-1} \frac{\partial \mathbf{R}}{\partial \alpha} \mathbf{R}^{-1} \frac{\partial \mathbf{R}}{\partial \beta} \right) + \sum_{k=1}^{L_s} \text{tr} \left(\mathbf{R}_{S_k}^{-1} \frac{\partial \mathbf{R}_{S_k}}{\partial \alpha} \mathbf{R}_{S_k}^{-1} \frac{\partial \mathbf{R}_{S_k}}{\partial \beta} \right). \quad (19)$$

The needed partials are given by

$$\frac{\partial \mathbf{R}}{\partial u_i} = \mathbf{0}, \quad \frac{\partial \mathbf{R}}{\partial \sigma_{S_l}^2} = \mathbf{0}, \quad (20)$$

$$\frac{\partial \mathbf{R}_{S_l}}{\partial u_i} = \sigma_{S_l}^2 (\mathbf{v}_{u_i} \mathbf{v}^H + \mathbf{v} \mathbf{v}_{u_i}^H), \quad (21)$$

$$\frac{\partial \mathbf{R}_{S_l}}{\partial \sigma_{S_n}^2} = \begin{cases} 0, & n \neq l \\ \mathbf{v} \mathbf{v}^H, & n = l \end{cases} \quad (22)$$

$$\frac{\partial \mathbf{R}_s}{\partial R_{i,k}} = \frac{\partial \mathbf{R}}{\partial R_{i,k}} = \mathbf{e}_i \mathbf{e}_k^H, \quad \frac{\partial \mathbf{R}_s}{\partial R_{i,k}^*} = \frac{\partial \mathbf{R}}{\partial R_{i,k}^*} = \mathbf{e}_k \mathbf{e}_i^H. \quad (23)$$

Clearly, the cross terms of the FIM capturing the loss for estimating \mathbf{R} are nonzero in this case. In the next section we consider some numerical examples which explore the resulting CRBs on angle accuracy and compare the root mean square (RMS) error of ML estimates to the predicted CRB limits.

6. NUMERICAL EXAMPLES

Consider an angle of arrival estimation example consisting of an $N = 18$ element uniform linear array (ULA) with $\lambda/2$ element spacing in an environment consisting of a 30dB (element JNR) jammer located at array broadside in a background of spatially white noise. Assume that $L_s = 1$ signal bearing snapshot and $L = N$ signal free training samples are available for estimation. The CRB on angle accuracy is plotted as a function of the true signal angle for a 0dB SNR signal in figure 2.

The noise floor limit predicts that a near 10 to 1 beamsplitting ratio is possible. For constant targets note that as the signal approaches the broadside interference the achievable accuracy declines and then returns to the noise floor limit when the signal is coincident in angle with the jammer. For Swerling II targets and \mathbf{R} known, however, the fluctuation loss degrades this predicted accuracy at this coincidence. When training is considered the bounds for the Swerling II target only change slightly near interference. If $L \geq 2N$, then this difference is even smaller. This small deviation from the \mathbf{R} known case is an indication that although the cross terms of the FIM capturing the signal training losses are nonzero for the Swerling II case, they're relatively small compared to the other elements of the FIM.

Practically speaking the CRB is simply a bound on achievable performance. There exist no instructions on how one can achieve this bound. We do know, however, that if an efficient unbiased estimate of a parameter exists, then it is the ML estimate [10]. In the next section we consider the RMS performance of ML estimates and examine their closeness to the CRB.

6.1. Maximum Likelihood Estimation

As in the previous section we restrict attention to $L_s = 1$ signal bearing and L_n signal free snapshots. Recall that $\mathbf{u} = [u_1, \dots, u_M]$, and define the sample covariance matrix (SCM) and the AMF statistic (as a function of the unknown signal parameters of interest) respectively as

$$\hat{\mathbf{R}} \triangleq \frac{1}{L_n} \mathbf{X} \mathbf{X}^H \quad (24)$$

and

$$t_{AMF}(u_1, \dots, u_M) \triangleq \frac{|\mathbf{v}^H(\mathbf{u}) \hat{\mathbf{R}}^{-1} \mathbf{x}|^2}{\mathbf{v}^H(\mathbf{u}) \hat{\mathbf{R}}^{-1} \mathbf{v}(\mathbf{u})}. \quad (25)$$

For constant targets it can be shown that the ML estimates of the unknown parameters of interest are given by

$$\hat{\mathbf{u}}_{ML} = \arg \max_{\mathbf{u}} t_{AMF}(u_1, \dots, u_M), \quad (26)$$

and for Swerling II targets a quasi-ML estimate is given by

$$\hat{\mathbf{u}}_{ML} = \arg \max_{\mathbf{u}} t_{AMF}(\mathbf{u}) - \ln[t_{AMF}(\mathbf{u})]. \quad (27)$$

In both cases these ML estimates involve several nonlinear operations. It is known [10] that the ML estimates will achieve the CRB *non-asymptotically* if and only if its error can be expressed as a linear combination of the gradient of the log likelihood:

$$\hat{\mathbf{a}}_{ML} - \mathbf{a} = \Omega(\mathbf{a}) \cdot \nabla_{\mathbf{a}} \ln p(\mathbf{x}_T, \mathbf{X} | \mathbf{a}). \quad (28)$$

Using this theorem it can be shown for both signal models that for the adaptive array problem an efficient unbiased estimate of the signal parameters does not exist non-asymptotically.

6.1.1. More Numerical Results

Using Monte-Carlo simulations (5000 trials for each point) the RMS error and bias of the ML angle estimators of the previous section are plotted in figures 3 - 7 for exactly the same ULA interference environment.² Note that in the constant signal case when the target is away from the interferer and \mathbf{R} is known exactly the ML estimator does an excellent job obtaining the CRB as it is least biased in this region. As the signal approaches broadside the bias increases and the RMS of the ML estimator deviates significantly from the bound. When the signal is coincident with the interferer the bias returns to zero but the RMS of the ML estimator reaches its maximal deviation from the CRB. This large deviation is due to the inherent nature of the MF and AMF statistics to provide unit variance on noise plus interference. When the signal and jammer are coincident in angle the signal gets nulled along with the jammer and the resulting ML search surface is approximately flat (0dB). See figure 5 which illustrates the average ML search surface for various true target positions. Away from broadside there is a nice clear peak at the true target position as one searches over angle. When the target and jammer are coincident the search surface flattens out. The RMS for the ML estimator, in fact, is less than a beamwidth away from the RMS one would obtain if the ML estimator were uniformly distributed between 0 and 180 degrees.

²The ML searches in angle are performed over all possible angles. In practice, however, the search is likely to be limited to a beamwidth or so around the mainlobe. So the results are somewhat conservative.

Note in figure 3 the apparent loss in angle accuracy due to signal free data training. It is this loss which we sought the CRB to quantify. As one might expect, the bias and the RMS of the ML estimators decrease with increased sample support L_n . Curiously, for $L_n = N$ the bias appears to be approximately linear in signal angle.

In the Swerling II signal case note the apparent bias in figure 7. Even when \mathbf{R} is known perfectly there's a significant bias in the ML estimator. The signal fluctuations causes the RMS error to deviate significantly from the predicted CRB for all signal angles for the given SNR and array configuration. The bias in the ML estimates in these non-asymptotic cases liberates the predicted CRBs from unaccountability in the non-asymptotic (low SNR and threshold) regimes.

7. CONCLUSIONS

In the adaptive estimation problem several signal bearing data snapshots and several signal free snapshots (training set) are assumed available. It appears that all existing results on signal parameter accuracy have only considered CRBs based on having several signal bearing snapshots available. In detection many useful measures have been developed which quantify the loss in performance due to the need to train over the signal free snapshots. In this analysis we sought the CRB to provide analogous measures for bounds on parameter accuracy. The case of constant signals as well as signal with Swerling II fluctuations have been considered. It was shown that for the constant signal case the CRBs do not reflect the observed losses in achievable parameter accuracy due to signal free training. In contrast, the CRBs for the Swerling II case do reflect these losses for unbiased estimates. The predicted loss in accuracy due to signal free training is negligible away from interference in the cases considered.

The ML estimates in both signal model cases are in general biased, but asymptotically unbiased. Therefore the CRBs for unbiased estimators that have been considered here are only accountable in the high SINR superfluous training sample case.

Finally, it should be mentioned that bounds other than the CRB do exist, and may do a better job quantify the training loss in parameter accuracy.

8. REFERENCES

- [1] A. Zeira, A. Nehorai, "Frequency Domain Cramér-Rao Bound for Gaussian Processes," *IEEE Trans. on Sig. Proc.* Vol. 38, No. 6, pp. 1063-1066 (1990).
- [2] J. M. Francos, B. Friedlander, "Bounds for Estimation of Complex Exponentials in Unknown Colored Noise," *IEEE Trans. on Sig. Proc.* Vol. 43, No. 9, pp. 2176-2185 (1995).
- [3] P. Stoica, A. Nehorai, "MUSIC, Maximum-Likelihood, and Cramér-Rao Bound," *IEEE Trans. Acoust., Speech, and Sig. Proc.* Vol. 37, No. 5, 720-741 (1989).
- [4] P. Stoica, A. Nehorai, "Performance Study of Conditional and Unconditional Direction-of-Arrival Estimation," *IEEE Trans. on Acoustics, Speech, and Sig. Proc.* Vol. 38, No. 10, pp. 1783-1795 (1990).
- [5] P. Stoica, J. Li, "Study of the Cramér-Rao Bound as the Numbers of Observations and Unknown Parameters Increase," *IEEE Signal Processing Letters*, Vol. 3, No. 11, pp. 299-300 (1996).

- [6] P. Stoica, R. Moses, *Introduction to Spectral Analysis*, Prentice-Hall, Inc., Upper Saddle River, NJ, 1997, Appendix B.
- [7] E. Bossé, R. Turner, M. Lecours, "Tracking Swerling Fluctuating Targets at Low Altitude Over the Sea," *IEEE Trans. on Aero. Elec. Sys.*, Vol. 27, No. 5, pp. 806-822 (1991).
- [8] J. Ward, "Cramér-Rao Bounds for Target Angle and Doppler Estimation with STAP Radar," *29th Asilomar Conf. on Signals, Sys., and Comp.*, November 1995.
- [9] S. Smith, "Accuracy and Resolution Bounds for Adaptive Sensor Array Processing," *9th IEEE Sig. Proc Workshop on Stat. Sig. & Array Proc.*, September 1998.
- [10] H. L. Van Trees, *Detection, Estimation, and Modulation Theory*, John Wiley & Sons, Inc., 1968.
- [11] I. S. Reed, J. D. Mallett, L. E. Brennan, "Rapid Convergence Rate in Adaptive Arrays," *IEEE Trans. Aerospace and Electronic Systems*, Vol. AES-10, No. 6, 853-863 (1974).
- [12] E. J. Kelly, "An Adaptive Detection Algorithm," *IEEE Trans. Aerosp. Electron. Syst.*, Vol. AES-22, 115 - 127 (1986).
- [13] R. Remmert, *Theory of Complex Functions*, Springer-Verlag, New York, Inc. 1991.

9. FIGURES

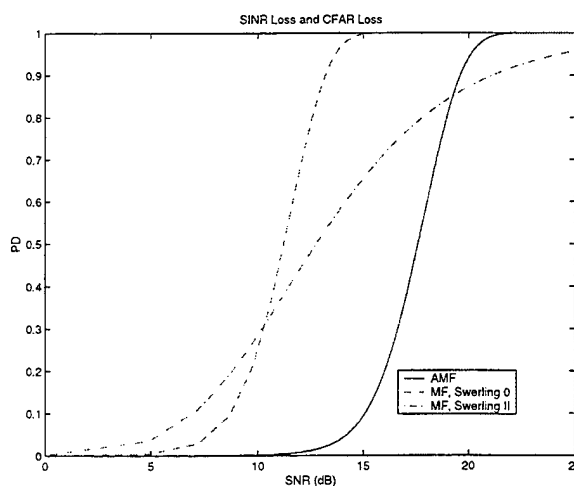


Figure 1: Detection Losses due to Training

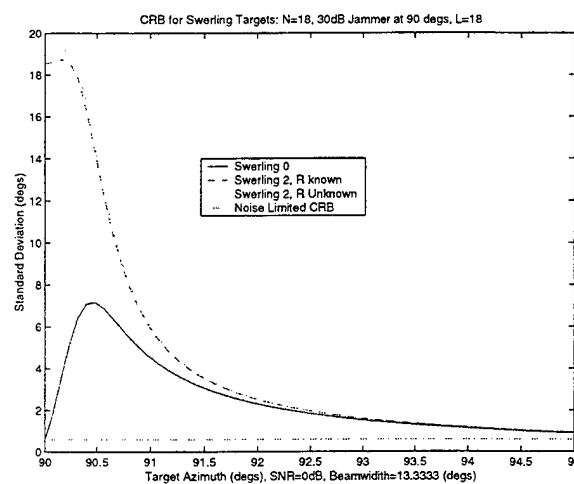


Figure 2: Predicted CRBs on Angle Accuracy

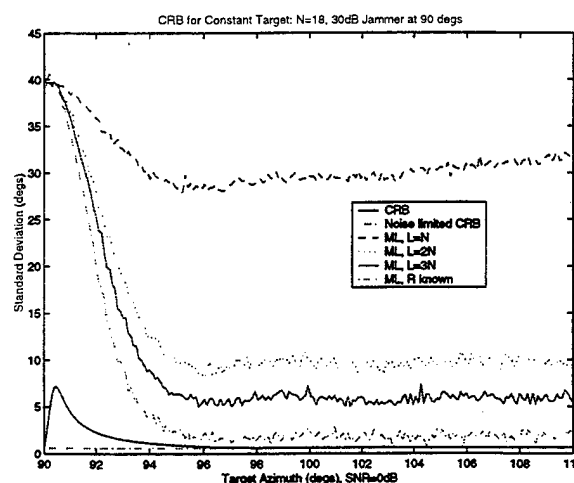


Figure 3: RMS on ML Estimates, Constant Signals

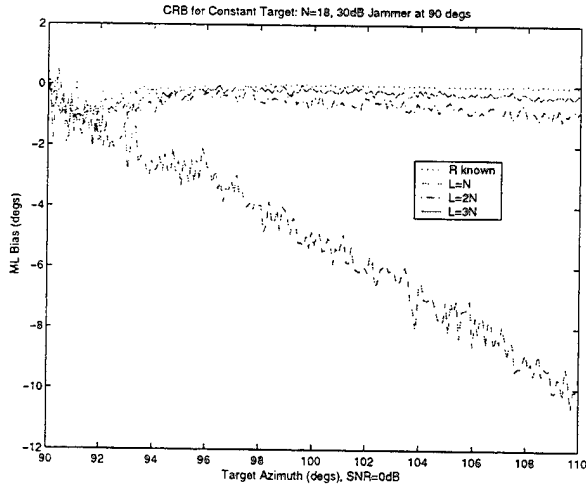


Figure 4: Bias of ML Estimates, Constant Signals

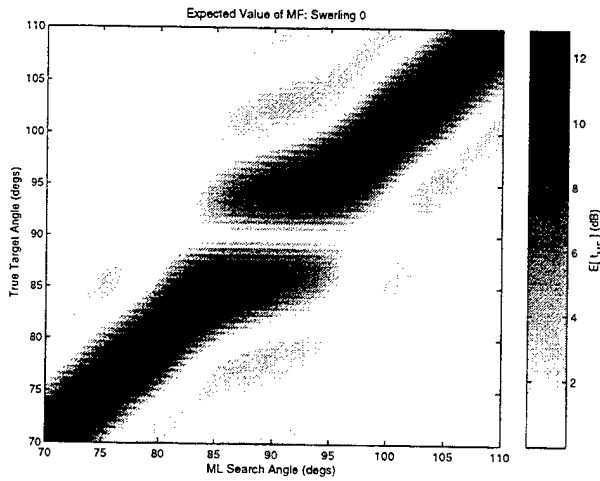


Figure 5: Expected ML Search Surface: $E\{t_{MF}(\theta)\}$

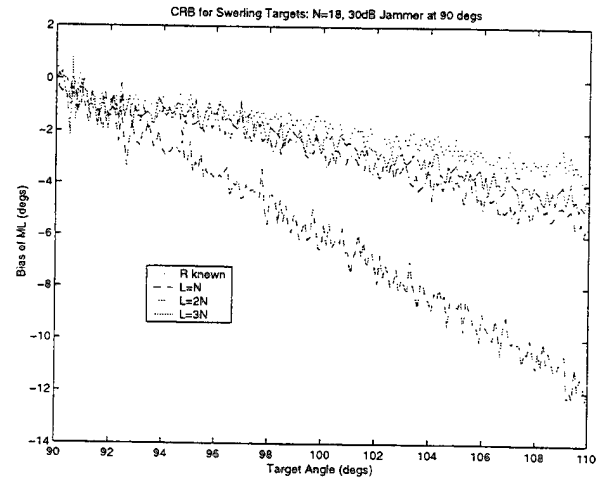


Figure 7: Bias on ML Estimates, Swerling II

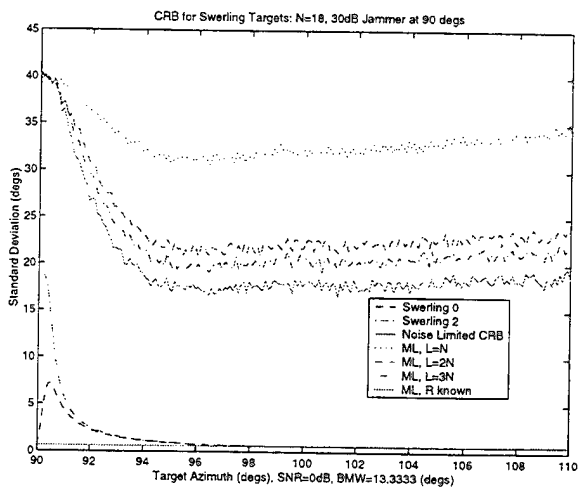


Figure 6: RMS on ML Estimates for Swerling II Targets

SIMULTANEOUS DOA ESTIMATION OF FULLY CORRELATED AND UNCORRELATED GAUSSIAN SOURCES IN NONUNIFORM LINEAR ANTENNA ARRAYS

Yuri I. Abramovich and Nicholas K. Spencer

Cooperative Research Centre for Sensor Signal and Information Processing (CSSIP),
SPRI Building, Technology Park, Mawson Lakes S.A. 5095, Australia

yuri@cssip.edu.au

nspencer@cssip.edu.au

ABSTRACT

We investigate the problem of nonuniform array design and suitable signal processing for the improved DOA estimation of mixed fully correlated and uncorrelated sources. We demonstrate that *partial-array* geometry design together with the *generalised spatial smoothing* technique and covariance fitting are a suitable framework with respect to a trade-off between DOA estimation performance for fully correlated and uncorrelated sources.

1. INTRODUCTION

In many applications, such as passive source location or jammer mapping, the true directions of sources should be discriminated from multipath directions for some relatively small number of multipath sources embedded in a substantial number of single-mode propagated sources [1]. The main problem here is to select a supporting antenna array geometry and corresponding signal processing technique. Indeed, DOA estimation of fully correlated sources advocates significant redundancy in array geometry, ultimately preferring a uniform array and standard spatial smoothing [2]. Conversely, given a particular number of antenna channels M available for digital processing (elements, subarrays, etc.), sparse (minimum redundancy) arrays are preferable for uncorrelated Gaussian sources because larger aperture means better resolution; moreover, sparse arrays allow estimation of a "superior" number of sources ($m \geq M$), impossible with a uniform array.

For a small number of multipath sources, we have introduced [3, 4] a special class of nonuniform geometry with embedded "partial arrays" that permits generalised spatial smoothing (GSS) over some number of such subarrays with identical covariance lag structure. The number of elements in each partial array only marginally exceeds the expected (small) number of multipath sources, reducing the overall redundancy to a level required for the effective resolution of these sources.

Naturally when some additional uncorrelated sources are present, the "partial-array" covariance matrix estimated via spatial averaging becomes "saturated", *ie.* of full rank, that makes multipath resolution impossible. Clearly, we need to differentiate uncorrelated and fully correlated sources in order to avoid this saturation and to enable effective multipath resolution. Such a technique is introduced and analysed in this paper.

2. ALGORITHM DESCRIPTION

Consider an M -element sparse linear array with sensors located at positions $d \equiv [d_1 \equiv 0, d_2, \dots, d_m]$ measured in half-wavelength

units. The DOA estimation problem for m_u uncorrelated and m_c fully correlated multipath-propagated sources can be formulated as the estimation of an unknown azimuthal angle parameter $\theta \equiv [\theta_u, \theta_{c1}, \dots, \theta_{cm_c}]$ in the equation

$$y(t) = S(\theta_u)x(t) + \sum_{j=1}^{m_c} \xi_j(t)S(\theta_{c_j})b_j + \eta(t) \quad (1)$$

for $t = 1, \dots, T$, where $y(t) \in \mathcal{C}^{M \times 1}$ is the column vector of array sensor outputs observed at time t (the "snapshot"); $S(\theta_u) \in \mathcal{C}^{M \times m_u}$ is the array manifold matrix; $x(t) \in \mathcal{C}^{m_u \times 1}$ is the vector of uncorrelated Gaussian signal amplitudes; b_j is the "non-zero" eigenvector of the rank-one covariance matrix B_j of the j^{th} set of ℓ_j multipath signals with DOA's $\theta_j = [\theta_1^{(j)}, \dots, \theta_{\ell_j}^{(j)}]$; $\xi_j(t)$ is the complex amplitude of the j^{th} multipath signal; $\eta(t) \in \mathcal{C}^{M \times 1}$ is additive noise, and $\mathcal{C}^{p \times q}$ is the space of $p \times q$ complex-valued matrices.

For this model

$$\mathcal{E}\{x(t_1)x^H(t_2)\} = \begin{cases} P & \text{for } t_1 = t_2 \\ 0 & \text{for } t_1 \neq t_2 \end{cases} \quad (2)$$

with $P \equiv \text{diag}[p_1, \dots, p_{m_u}]$. We also assume that the additive noise is white and Gaussian:

$$\mathcal{E}\{\eta(t_1)\eta^H(t_2)\} = \begin{cases} \sigma I_M & \text{for } t_1 = t_2 \\ 0 & \text{for } t_1 \neq t_2 \end{cases} \quad (3)$$

with

$$\mathcal{E}\{\xi_j(t_1)\xi_k^*(t_2)\} = \begin{cases} \sigma_j & \text{for } j = k, t_1 = t_2 \\ 0 & \text{otherwise} \end{cases} \quad (4)$$

and so this model is explicitly described by the M -variate Hermitian spatial covariance matrix R given by

$$R = S(\theta_u)PS^H(\theta_u) + \sum_{j=1}^{m_c} \sigma_j S(\theta_{c_j})b_j b_j^H S^H(\theta_{c_j}) + \sigma I_M. \quad (5)$$

In what follows, we restrict our investigation to the class of *identifiable* scenarios. By this assumption we exclude the subset of "manifoldly ambiguous" scenarios that for fully correlated sources are proven to be nonidentifiable (for a Gaussian model). Practically, this means that all synthetic wavefronts of fully correlated wavefronts in (5) are not identical to the plane-wave model, *ie.*

$$S(\theta_j)b_j \neq a s(\theta) \quad \text{for any } \theta. \quad (6)$$

We make the additional assumption (essential for the proposed method) that the overall signal subspace dimension of the covariance matrix is less than its dimension, *ie.*

$$m \equiv m_u + m_c < M. \quad (7)$$

With these assumptions, our approach to identifying the uncorrelated sources given the sample covariance matrix \hat{R}

$$\hat{R} = \frac{1}{T} \sum_{t=1}^T \mathbf{y}(t) \mathbf{y}^H(t) \quad (8)$$

is quite straightforward. Whereas the above mentioned signal-subspace dimension ($m + m_c$) could be established via traditional information criteria, the standard MUSIC technique

$$\hat{\theta}_u = \min_{\theta} s^H(\theta) \hat{G}_{M-\hat{m}} \hat{G}_{M-\hat{m}} s(\theta) \quad (9)$$

could provide the DOA estimates for the uncorrelated sources. Here $\hat{G}_{M-\hat{m}}$ is the $M \times (M - \hat{m})$ matrix of noise-subspace eigenvectors of the matrix R . The only essential difference with respect to standard MUSIC is that only $\hat{m}_u < \hat{m}$ dominant peaks are associated with the DOA's of uncorrelated sources. With respect to the identifiability assumption (6) for large sample support ($T \gg 1$) essential for covariance-matching methods, this option is quite reliable.

The crucial point in our technique is now to get an estimate of fully correlated counterpart \hat{R}_c of the covariance matrix R . Several options could be considered. First of all, with the set $\hat{\theta}_u$ of DOA estimates for uncorrelated sources, one can reject these signals from the input mixture and get a covariance matrix estimate \hat{R}_c as a result of projection:

$$\hat{R}_c^{(1)} = P \hat{R} P \quad (10)$$

$$P = I - S(\hat{\theta}_u) [S^H(\hat{\theta}_u) S(\hat{\theta}_u)]^{-1} S^H(\hat{\theta}_u). \quad (11)$$

Clearly such an approach, if it works, could be effective in the pre-asymptotic domain for comparatively small sample support, provided that the set of DOA estimates $\hat{\theta}_u$ for uncorrelated sources is sufficiently accurate. On the other hand, the plane-wavefront model that is essential for spatial averaging principles is no longer accurate as a result of such a transformation. Effectively, the component

$$\delta S(\theta_j) = -S(\hat{\theta}_u) [S^H(\hat{\theta}_u) S(\hat{\theta}_u)]^{-1} S^H(\hat{\theta}_u) s(\theta_j) \quad (12)$$

could be treated as a specific distortion of the plane wavefront $s(\theta_j)$, that limits the efficiency of spatial smoothing. Obviously, this distortion is scenario-specific, and only for comparatively large separation between correlated and uncorrelated sources, when

$$\frac{|s^H(\theta_{uj}) s(\theta_{cl})|^2}{s^H(\theta_{uj}) s(\theta_{uj}) s^H(\theta_{cl}) s(\theta_{cl})} \ll 1 \quad (13)$$

where θ_{uj} and θ_{cl} are the DOA's of the uncorrelated and correlated sources respectively, one can expect that this distortion could be tolerated. Clearly, the signal-to-noise ratio as well as an increased sample support cannot improve the spatial averaging accuracy that is limited by this distortion.

Another approach that can be proposed for an asymptotically large sample volume T , is to get an estimate $\hat{R}_c^{(2)}$ of the fully

correlated component of the covariance matrix \hat{R} by extracting an estimate of the uncorrelated component:

$$\hat{R}_c^{(2)} = \hat{R} - S(\hat{\theta}_u) \hat{P} S^H(\hat{\theta}_u) \quad (14)$$

where \hat{P} is the m -variate diagonal matrix of power estimates for uncorrelated sources. Obviously, this is a covariance-matching type of technique, similar to COMET [5] or to the augmentation technique of Pillai *et al.* [6]. To ensure the zero-mean cross-terms in the sample covariance matrix are insignificant, the required sample support must be sufficiently large for these techniques. For the specified condition on the overall number of sources (7), the power estimates for uncorrelated sources could be obtained directly by

$$\hat{p}_j = \frac{1}{S^H(\theta_j) \hat{R}^{-1} S(\theta_j)}. \quad (15)$$

Though this is an asymptotically efficient estimate, it does not guarantee that the covariance matrix $\hat{R}_c^{(2)}$ is positive definite. A condition on the power estimates \hat{p}_j ($j = 1, \dots, \hat{m}_u$) that keeps $\hat{R}_c^{(2)}$ positive definite, *ie.*

$$\hat{R}_c^{(2)} = \hat{R} - \sum_{j=1}^{\hat{m}_u} \hat{p}_j s(\hat{\theta}_{ju}) s^H(\hat{\theta}_{ju}) > 0 \quad (16)$$

is given by a standard LMI (linear matrix inequality) problem and the convex programming technique [7] can be used to find an appropriate solution. For example, the standard LMI problem

$$\text{Find } \min - \sum_{j=1}^{\hat{m}_u} \hat{p}_j \text{ subject to } \hat{R}_c^{(2)} > 0 \quad (17)$$

leads to the maximum power estimates \hat{p}_j that keeps $\hat{R}_c^{(2)}$ positive definite. Now, when the "best" estimate for the correlated component of the input covariance matrix is defined ($\hat{R}_c^{(1)}$ or $\hat{R}_c^{(2)}$), we may apply the generalised spatial smoothing (GSS) technique for multipath DOA estimation [4, 8].

Here we consider the DOA estimation problem for some small pre-specified maximum number of coherent signals m (of arbitrary configuration) using the special class of *partial-array* NLA geometries and the corresponding *generalised spatial smoothing* (GSS) algorithm.

Let the *co-sequence* of an array d be its set of $(M-1)$ consecutive intersensor separations (*ie.* differences), while its *co-array* is the sorted set of $M(M-1)/2$ differences. We define a *partial array* to be a group of nonuniform linear noncontiguous sub-arrays of identical co-sequence structure [3]. Associated with each partial array are its *multiplicity* κ (number of occurrences or instances), *order* ℓ (number of co-sequence elements involved), and aperture a . A given NLA will have n embedded partial arrays, with a total of N instances. The GSS technique may be applied to a NLA providing it yields at least one partial array of multiplicity $\kappa \geq m$ and order $\ell \geq m$, where m is the number of fully correlated signals. Examples of partial arrays and their properties are more fully discussed in [9].

The GSS algorithm introduced in [3] consists of an initialisation step followed by local ML refinement. The initialisation step is based on the *PA-MUSIC* approach involving all appropriate partial arrays.

Suppose that an NLA yields a n partial arrays, each of multiplicity κ_i , order ℓ_i and aperture a_i ($i = 1, \dots, n$). Let $A_i^{(k)}$ be a $(\ell_i + 1) \times M$ selection matrix with 1 in each row on the position of the j^{th} element of the k^{th} instance this i^{th} partial array, $j = 1, \dots, (\ell_i + 1)$. Then the covariance matrix for this instance of the partial array is

$$\hat{R}_i^{(k)} = A_i^{(k)} \hat{R}_c^{(1,2)} A_i^{T(k)}. \quad (18)$$

If any instance of a partial array occurs as a mirror image (ie. in reverse order), then the corresponding matrix should be reversed and complexly conjugated:

$$\hat{R}_i^{(k)} = J [A_i^{(k)} \hat{R}_c^{*(1,2)} A_i^{T(k)}] J \quad (19)$$

where

$$J = \begin{bmatrix} & & & 1 \\ & & & \\ & & & \\ 1 & & & \end{bmatrix}. \quad (20)$$

Thus for each partial array we may define the $(\ell_i + 1) \times (\ell_i + 1)$ partial array covariance matrix by spatial smoothing to be

$$\hat{R}_i = \sum_{k=1}^{\kappa_i} \hat{R}_i^{(k)}. \quad (21)$$

Let \hat{G}_i be the noise eigen-subspace of \hat{R}_i , then \hat{G}_i consists of at least one eigenvector (since $m \ll M$). The PA-MUSIC technique is:

$$\text{find } \max_{\theta} f_{PA}(\theta) := \min_{\theta} \sum_{i=1}^n a_i^H(\theta) \hat{G}_i \hat{G}_i^H a_i(\theta) \quad (22)$$

where $a_i(\theta)$ is the $(\ell_i + 1)$ -variate manifold ("steering") vector which corresponds to the given partial array geometry. Evidently this approach eliminates non-coinciding ambiguities. More specifically, the co-array of the synthetic partial array that is constructed by all of the properly averaged covariance lags produced by all of the partial arrays, should have a manifold dimensionality that exceeds the pre-defined number of fully correlated sources. Thus the effectiveness of DOA estimation delivered by GSS is directly related to the number, variety and $\kappa\ell a$ -properties of the available partial arrays. For this reason, the sum $\sum_{j=1}^n a_j^2 = A$ could be treated as a cost function for antenna geometry optimisation. Details of a three-stage optimisation approach appear in [9].

3. SIMULATION RESULTS

The following example illustrates array geometry optimisation results for a 16-element array. The initial choice $M_1 = 10$ gives us the starting-point 10-element non-redundant Sverdlik array [10]

$$d_{55}^{(0)} = [0, 1, 6, 10, 23, 26, 34, 41, 53, 55]. \quad (23)$$

The exhaustive tree search of stage two yields 37 candidate gap-free geometries, each with 14 elements and 36 redundancies. The integer programming maximisation of stage three finds that of these candidates, one in particular is the best (in the search range $\ell = 3$ and $c \in [1, 18]$), since with the addition of two sensors (8,19) it yields the 16-element NLA

$$d_{55} = [0, 1, \underline{5}, 6, \underline{8}, 10, \underline{19}, 23, 26, 34, \underline{37}, 41, \underline{44}, \underline{52}, 53, 55] \quad (24)$$

ℓ	κ	3	4
3		40	9
4		33	3
5		12	0

Table 1: Partial array distribution by multiplicity (κ) and order (ℓ) for d_{55} for $m = 3$ and the search range $\ell \in [3, 5]$ and $c \in [1, 30]$.

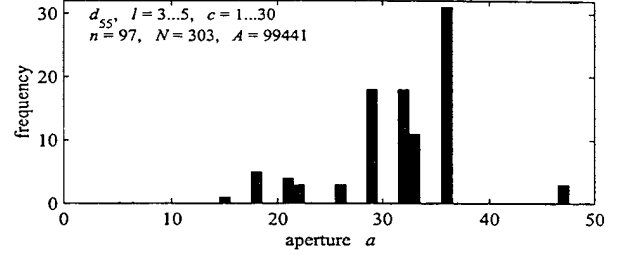


Figure 1: Aperture histogram of partial arrays embedded in d_{55} .

having the maximal cost function $A = 38467$ (and 65 redundancies). Thus we have partitioned our $M = 16$ elements in this example by $\{M_1 = 10, M_2 = 4, M_3 = 2\}$.

Table 1 shows the $\kappa\ell$ -distribution and Fig. 1 illustrates the a -distribution of partial arrays for d_{55} for the expanded search range $\ell \in [3, 5]$ and $c \in [1, 30]$, whence we find $A = 99441$. This array performs better than the 16-element ULA because of the large numbers of embedded partial arrays, each of significant aperture. The minimum-redundancy array of comparable total aperture ($M_a = 58$) has 13 elements, so we could consider d_{55} to be a type of "optimal" solution by the introduction of only three additional elements to the minimum-redundancy structure.

Table 1 makes it clear that uncorrelated signals, if not properly removed from the covariance matrix estimate, "saturate" the partial-array covariance matrix so that the noise subspace disappears.

Thus for the following scenario of d_{55} with $m_u = 3$ uncorrelated and two fully correlated sources, the introduced technique does not seem to have an obvious alternative. The set of DOA's $w_u = [-0.4, -0.2, 0.6]$ for uncorrelated sources and the correlated DOA's $w_c = [0, 0.1]$ were selected to demonstrate the ability to properly resolve multipath in severe super-resolution conditions for a 16-element array. The sample support has been selected large enough to accommodate the covariance-matching technique ($T = 10^4$), with experiments involving SNR of 0, 10 and 20 dB for each signal. Our calculations started from the true (deterministic) M -variate covariance matrix of the input mixture in order to verify the asymptotic ($T \rightarrow \infty$) properties of our technique.

As expected, standard MUSIC unambiguously extracts uncorrelated sources (Fig. 2), so that both projection and power estimation used to create $\hat{R}_c^{(1)}$ and $\hat{R}_c^{(2)}$ respectively, are also accurate. Nevertheless, the partial-array (PA) MUSIC pseudo-spectrum for projection technique ($\hat{R}_c^{(1)}$) illustrated by Fig. 3 exhibits significant distortions that lead to a significant sidelobe level of -2 dB. Clearly, such technique must lead to a significant probability of abnormal estimates, when wrong (sidelobe) directions are selected instead of the true ones.

On the contrary, spatial averaging for $\hat{R}_c^{(2)}$ results in a perfect resolution of the multipath, illustrated by Fig. 4. Obviously, the

	$\hat{R}_c^{(1)}$	$\hat{R}_c^{(2)}$	\hat{R}_c	$\hat{R}_c^{(1)}$	$\hat{R}_c^{(2)}$	\hat{R}_c	$\hat{R}_c^{(1)}$	$\hat{R}_c^{(2)}$	\hat{R}_c
Probability of Outlier(s)	0.356	0.208	0.037	0.385	0.088	0.004	0.430	0.124	0.000
Bias ($\times 10^{-4}$)	18	9	4	19	5	1	19	4	0
Std Dev ($\times 10^{-4}$)	10	11	8	8	7	2	7	7	0

Table 2: Simulation results for $T = 10^4$ with SNR of 0 dB (left), 10 dB (middle) and 20 dB (right).

absence of cross-terms makes this estimation ideal and advocates for a reasonable asymptotic accuracy, while the accuracy given by the projection technique could hardly be improved upon either by larger sample volume T or by larger SNR.

On the other hand, the covariance-matching technique is found to be quite sensitive with respect to the accuracy of uncorrelated-source power estimates. For the same accurate R and θ_u , Fig. 5 illustrates the PA-MUSIC pseudo-spectrum for the set of inaccurate power estimates $\hat{p} = [93.6, 74.8, 111.9]$ produced by a different (linear-programming based [11]) matching technique. Clearly, inaccurate rejection of the uncorrelated sources covariance matrix leads to a significant distortion in PA-MUSIC pseudo-spectrum.

Finally, sample PA-MUSIC pseudo-spectra are given in Figs. 6 and 7 for projection and for covariance matching options respectively. These figures demonstrate that for $T = 10^4$ both methods exhibit asymptotic properties, close enough to the results obtained for the exact covariance matrix R .

The statistical efficiency of the introduced technique has been analysed via 1000 Monte-Carlo trials each, with the results presented at Table 2. For several SNR's, the bias and standard deviation are presented for the least accurate DOA estimate, along with the sample probability of abnormal estimation (when some side-lobe exceeds a correct peak in the MUSIC pseudo-spectrum). For comparison, similar data is presented for the GSS technique when no uncorrelated sources are present.

We see that only for the case when no uncorrelated signals are present, an increase in SNR directly improves the multipath resolution performance. For both techniques, linked with extraction of the correlated sources, performance parameters are practically stable for any SNR that exceeds a comparatively low level (about 0 dB). These results also demonstrate that direct suppression of uncorrelated signals in input data prior to GSS leads to a significant distortion in the plane-wave model and consequently, to an unacceptable estimation accuracy with almost 50% wrong identification. The covariance-matching technique is more appropriate, though the sample support required for proper identification is quite significant.

4. SUMMARY AND CONCLUSIONS

We have demonstrated that specifically designed nonuniform linear antenna arrays supported by an appropriate signal processing technique, can address the problem of DOA estimation for a mixture of uncorrelated and a small number of fully correlated (multipath) signals. It has been shown that direct rejection of identified uncorrelated sources leads to an inappropriate degradation in multipath resolution due to a significant distortion introduced by the plane-wave model. While a covariance-matching technique is more appropriate, the sample support required for reliable performance is asymptotically large. This final requirement is common for most covariance-matching-type techniques, typical for nonuniform antenna array applications [12, 13].

5. REFERENCES

- [1] U. Nickel, "Aspects of implementing super-resolution methods into phased array radar," *International Journal of Electronics and Communications*, submitted 1998.
- [2] T.J. Shan, M. Wax, and T. Kailath, "On spatial smoothing for direction-of-arrival estimation of coherent signals," *IEEE Trans. Acoust. Sp. Sig. Proc.*, vol. 33, pp. 806–811, 1985.
- [3] Y.I. Abramovich and N.K. Spencer, "Generalised spatial smoothing using partial arrays for multiple target bearing estimation," in *Proc. ICASSP-98*, Seattle, 1998, vol. 4, pp. 2061–2064.
- [4] Y.I. Abramovich and N.K. Spencer, "Nonuniform linear antenna array design and signal processing for DOA estimation of Gaussian sources," in *Proc. DASP-99*, LaSalle, IL, 1999, pp. 1–6.
- [5] B. Ottersten, P. Stoica, and R. Roy, "Covariance matching estimation technique for array signal processing applications," *Digital Signal Processing*, vol. 8, pp. 185–210, 1999.
- [6] S. Pillai, Y. Bar-Ness, and F. Haber, "A new approach to array geometry for improved spatial spectrum estimation," *Proc. IEEE*, vol. 73 (10), pp. 1522–1524, 1985.
- [7] S. Boyd, L. El Ghaoui, E. Feron, and V. Balakrishnan, *Linear Matrix Inequalities in System and Control Theory*, Society for Industrial and Applied Mathematics, Philadelphia, 1994, SIAM Studies in Applied Mathematics Vol. 15.
- [8] Y.I. Abramovich and N.K. Spencer, "Design of nonuniform linear antenna array geometry and signal processing algorithm for DOA estimation of Gaussian sources," *Digital Signal Processing*, to appear in 2000.
- [9] N.K. Spencer, "Nonlinear signal processing and nonuniform linear antenna array design for DOA estimation of coherent sources," in *Proc. NSIP-99*, Antalya, 1999, pp. 849–853.
- [10] M.B. Sverdlik, *Optimal Discrete Signals*, Sovetskoe Radio, Moscow, 1975, In Russian.
- [11] Y.I. Abramovich, N.K. Spencer, and A.Y. Gorokhov, "Resolving manifold ambiguities in direction-of-arrival estimation for nonuniform linear antenna arrays," *IEEE Trans. Sig. Proc.*, vol. 47 (10), pp. 2629–2643, 1999.
- [12] Y.I. Abramovich, D.A. Gray, A.Y. Gorokhov, and N.K. Spencer, "Positive-definite Toeplitz completion in DOA estimation for nonuniform linear antenna arrays — Part I: Fully augmentable arrays," *IEEE Trans. Sig. Proc.*, vol. 46 (9), pp. 2458–2471, 1998.
- [13] Y.I. Abramovich, N.K. Spencer, and A.Y. Gorokhov, "Positive-definite Toeplitz completion in DOA estimation for nonuniform linear antenna arrays — Part II: Partially augmentable arrays," *IEEE Trans. Sig. Proc.*, vol. 47 (6), pp. 1502–1521, 1999.

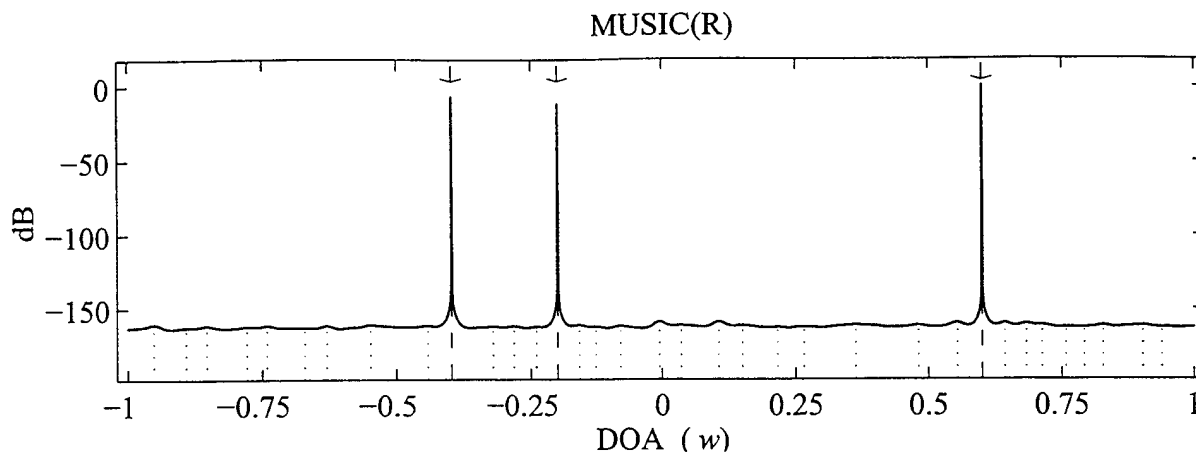


Figure 2: MUSIC pseudo-spectrum of the exact (deterministic) covariance matrix R .

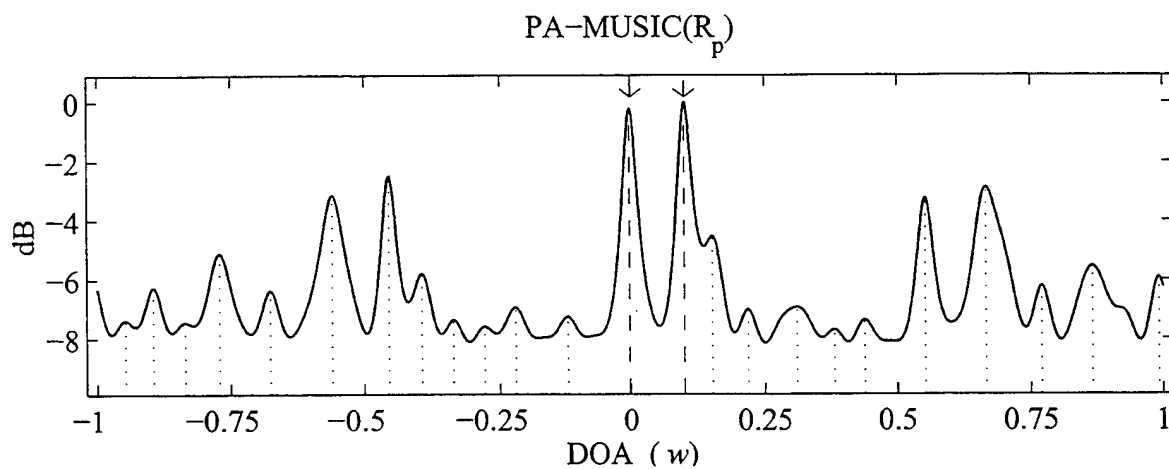


Figure 3: PA-MUSIC pseudo-spectrum of the exact projected covariance matrix $R_c^{(1)}$.

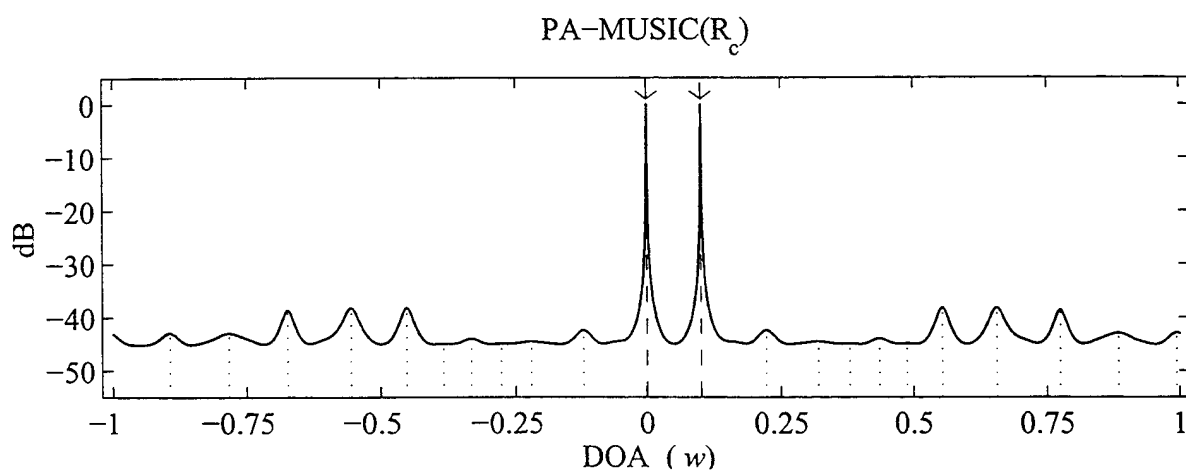


Figure 4: PA-MUSIC pseudo-spectrum of the covariance matrix $\hat{R}_c^{(2)}$.

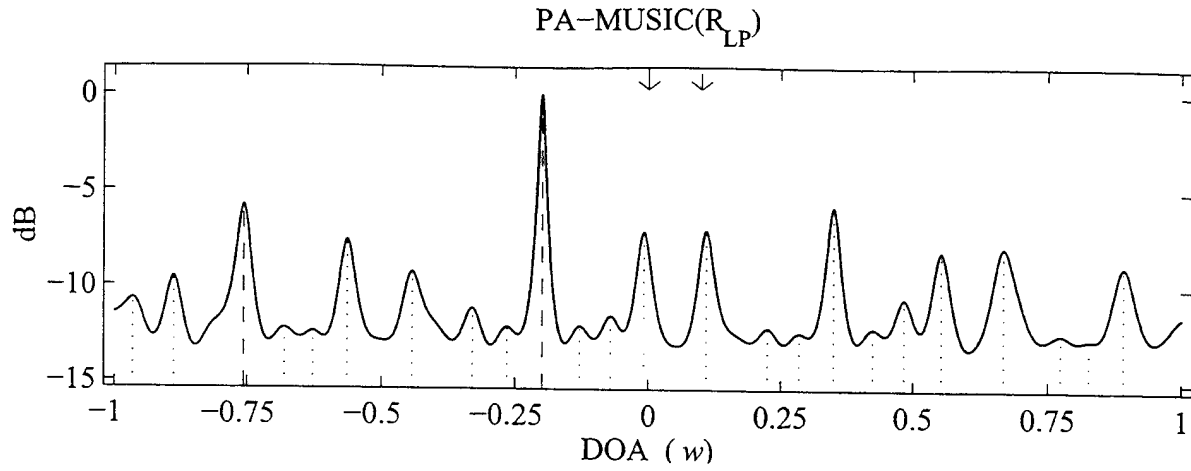


Figure 5: PA-MUSIC pseudo-spectrum of the covariance matrix R_{LP} .

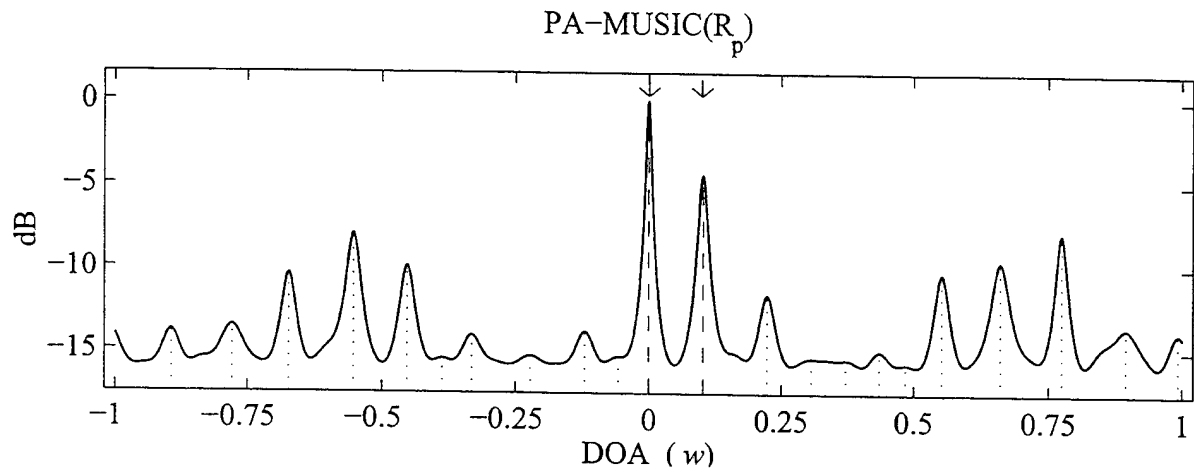


Figure 6: PA-MUSIC pseudo-spectrum of a stochastic projected covariance matrix $\hat{R}_c^{(1)}$.

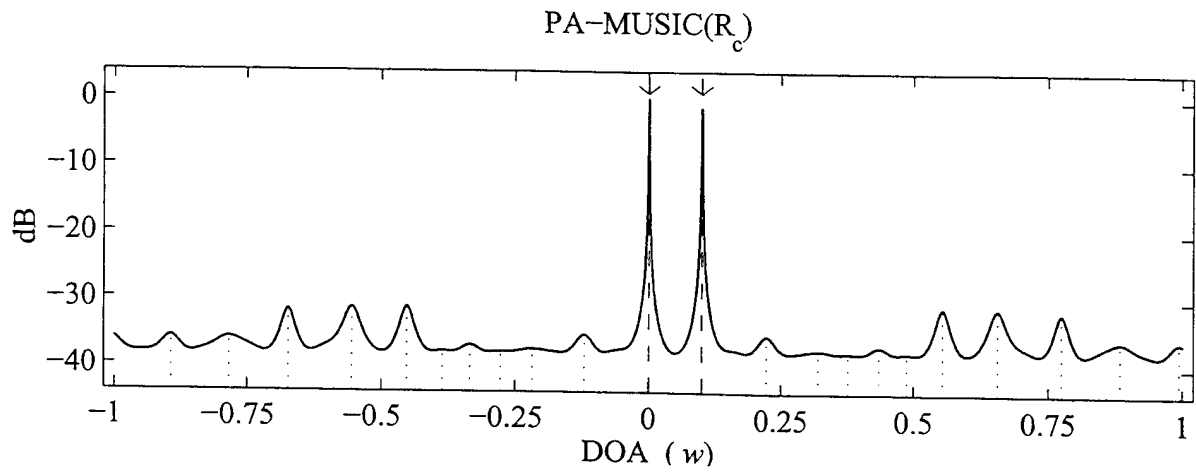


Figure 7: PA-MUSIC pseudo-spectrum of a stochastic covariance matrix $\hat{R}_c^{(2)}$.

ARRAY CALIBRATION FOR CIRCULAR-ARRAY STAP USING CLUTTER SCATTERING AND PROJECTION MATRIX FITTING

Daniel R. Fuhrmann and David W. Rieken

Electronic Systems and Signals Research Laboratory
Department of Electrical Engineering
Washington University
St. Louis, Missouri 63130
danf@essrl.wustl.edu, rieken@essrl.wustl.edu

ABSTRACT

The problem of estimating an array manifold from calibration data, or from a set of response vectors on a fixed grid, is considered. It is argued that points in the array manifold should be viewed as elements of complex projective space, and in this context a technique for estimating smooth functions from azimuth/elevation to complex projective space is proposed. The proposed technique comprises 5 steps: 1) free-space phase compensation, 2) computation of a sequence of rank-one projections, 3) weighted least-squares fitting of the projections using a spherical harmonic basis, 4) principal component analysis at each direction, and 5) restoration of free-space phase. A simulation demonstrating the application of this technique to an airborne circular array, with clutter returns used as calibration data, is presented.

1. INTRODUCTION

Array calibration is an important practical concern in the implementation of high-resolution sensor arrays for surveillance applications. The success or failure of various high-resolution adaptive array processing algorithms depends critically on accurate knowledge of the array response. Methods for determining this array response under realistic conditions, or even when the array is in operation, are highly desirable.

The idea of using clutter returns for airborne array calibration was proposed by Robey and presented in a series of papers by Robey *et al.* [1] and Koerber and Fuhrmann [2,3]. The basic principle is to exploit the redundancy or deterministic relationship between azimuth and Doppler at zero velocity. The technique is this: for each CPI, resolve all radar returns in Doppler but do not carry out any spatial processing. A column from the data cube at Doppler f_m may be considered as a sample of the spatial response at the associated azimuth ϕ_m . Using the collection of such columns over multiple range gates, an

estimate of the spatial response vector $\mathbf{a}(\phi_m)$ can then be determined using principal component analysis.

In the original formulation of the calibration-on-clutter concept, it was assumed that the airborne array was a uniform linear array, and as such there was little if any range dependence in the array response. Thus, the data from multiple range gates at Doppler f_m could be considered as independent samples all supporting an estimate of the response vector at azimuth ϕ_m . However, the next generation of airborne radar arrays will in all probability *not* be uniform linear arrays. For example, in a STAP system under development for the U.S. Navy E-2C surveillance aircraft, the radar includes an electronically-steerable circular ring array of UHF antennas. It has been shown that such an array has a non-negligible range dependence in its response [4].

In the circular array, or in any planar array, it is clear that in the calibration process one should seek a description of the array response as a function of both azimuth and elevation. The data which are available to support such an estimate consist of one vector each from a grid in azimuth/elevation space. What is then needed is a mechanism for filtering or smoothing the data to create a description of the array manifold over the entire continuous azimuth/elevation domain. The difficulty in doing so is that each data vector is not an element of the array manifold; rather it is the response vector multiplied by an unknown complex scalar which accounts for clutter reflectivity, range attenuation, and other factors.

Formally, the problem is this. Let \mathbf{z}_k , $k = 1 \dots K$ be a set of complex vectors in \mathbb{C}^N , where each k represents an index into azimuth/elevation space. Each data vector can be written as

$$\mathbf{z}_k = \mathbf{a}(\theta_k, \phi_k)s_k + \mathbf{n}_k \quad (1.1)$$

where $\mathbf{a}(\theta_k, \phi_k)$ is the array response vector at elevation θ_k and azimuth ϕ_k , s_k is an unknown complex scalar, and \mathbf{n}_k is an additive noise term. For the remainder of this paper

it will be assumed that the power of \mathbf{n}_k is small and can be ignored, hence the problem becomes more one of data-fitting rather than statistical estimation. The problem is to determine the array manifold over all (θ, ϕ) from this finite set of data vectors.

2. WHAT IS THE ARRAY MANIFOLD?

Before tackling the estimation problem posed above, it is appropriate to take up the question of exactly what is meant by the term *array manifold*. In most published definitions, it is simply the set of all response vectors $\mathbf{a}(\theta, \phi)$. In this definition, the array response vector itself must be carefully defined. When we say that

$$\mathbf{z}(t) = \mathbf{a}(\theta, \phi)s(t)$$

two features of the array response are implicitly assumed. First, $s(t)$ must be defined as the field strength at a particular spatial reference point, which may or may not be one of the sensor locations. All free-space phase calculations are made relative to this reference. Second, $\mathbf{a}(\theta, \phi)$ has units associated with it, that being the ratio of the units of the output of the receiver (volts, say), to the units of the incident field strength (volts/meter). [Aside: in some definitions, $s(t)$ is the output of one of the sensors, and the gains and phases of the sensors are all expressed relative to the reference sensor. This definition is problematic when the gain of the reference sensor becomes small in a particular direction.]

Now most adaptive array processing algorithms are invariant to the choice of spatial reference or the units of gain, since 1) phase terms are usually cancelled out in the formation of beamformer weight vectors, sample covariance matrices, and the like, and 2) the choice of gain units does not affect SNR. However, for the purposes of describing the array manifold, the choice of the spatial reference actually makes a difference, since it affects the "shape" of the array manifold considered as a submanifold of C^N . Attempts at interpolating the array manifold or fitting it to a set of basis functions would thus depend strongly on the selection of a parameter which is irrelevant to the signal processing objectives.

For this reason, we argue that the appropriate quantity to use in defining the array manifold is the equivalence class of vectors given by $s\mathbf{a}(\theta, \phi)$ where s ranges over all complex scalars. This equivalence class is exactly the one-dimensional vector space $\text{span}\{\mathbf{a}(\theta, \phi)\}$. The space of all one-dimensional subspaces of C^N is called complex projective space, and is denoted CP^N . With this viewpoint the array manifold may be considered a submanifold of CP^N . The problem of array calibration becomes one of estimating a function $P: S^2 \rightarrow CP^N$. The challenge is that

CP^N is a non-Euclidean space, and thus standard sorts of fitting procedures, such as expansions in terms of orthogonal bases, are not directly applicable.

The work described in the following sections represents an initial attempt at this interesting problem. We take a hybrid approach, in that a coordinate representation of each point in CP^N is used, and these coordinates are in fact filtered using an appropriate set of orthogonal basis functions (the spherical harmonics). After filtering, the resulting set of points no longer lie in CP^N , but are assumed close and can be projected back into that space.

We now formally re-state the problem first given in Section 1. Let \mathbf{z}_k , $k = 1 \dots K$, be a set of vectors in C^N where k is an index into azimuth/elevation space, as in (1.1). Associate with each vector $\mathbf{a}(\theta, \phi)$ the operator $P(\theta, \phi)$, the projection operator onto the space $\text{span}\{\mathbf{a}(\theta, \phi)\}$. The problem is to estimate the function $P: S^2 \rightarrow CP^N$ which best explains the available data.

3. PROPOSED TECHNIQUE

Our proposed technique comprises 5 steps: 1) free-space phase compensation, 2) formation of a set of rank-one projection matrices, 3) weighted least-squares fitting of the matrices using spherical harmonic basis functions, 4) principal component analysis for projecting the results back into CP^N , and 5) restoring the free-space phase. Each of these steps will be explained in the following subsections.

In the following description, we will use the notation P to describe a point in CP^N , and the notation \mathbf{P} to denote a rank-one projection matrix. \mathbf{P} is the matrix description of the projection operator onto a 1-dimensional subspace, and it uniquely identifies that subspace. Although it is not an efficient technique, we will use $\mathbf{P}(\theta, \phi)$ to be a coordinate representation for the point P on the array manifold at direction (θ, ϕ) .

3.1. Free-Space Phase Compensation

The first step in the proposed processing is to remove the effects of phase shifts due to nominal sensor location. These phase shifts are given by $e^{j2\pi \frac{\mathbf{k}^T \mathbf{x}}{\lambda}}$, where \mathbf{x} is the sensor position, \mathbf{k} is a unit vector pointing in the direction (θ, ϕ) , and λ is the wavelength. These phase shifts are usually the most significant factor defining the array response, but since they are known and cause the array response to vary rapidly with direction, it is desirable to remove their effect in array calibration.

The array response vector $\mathbf{a}(\theta, \phi)$ can be written in the form

$$\mathbf{a}(\theta, \phi) = \tilde{\mathbf{a}}(\theta, \phi) \circ \mathbf{b}(\theta, \phi) \quad (3.1)$$

where $\mathbf{b}(\theta, \phi)$ is the vector of free-space phase shifts, and \circ represents pointwise or Hadamard vector multiplication. $\tilde{\mathbf{a}}(\theta, \phi)$ is then a pointwise multiplicative deviation from the nominal response. In an array of omnidirectional sensors, $\tilde{\mathbf{a}}(\theta, \phi)$ is the all-ones vector at all (θ, ϕ) . Our approach to array calibration is to estimate $\tilde{\mathbf{a}}$, which is assumed slowly-varying with respect to direction.

Free-space phase compensation is meaningful as well when we consider the array manifold to be the set of projection operators $P(\theta, \phi)$ as described in Section 2. In this case we have

$$\mathbf{P}(\theta, \phi) = \tilde{\mathbf{P}}(\theta, \phi) \circ [\mathbf{b}(\theta, \phi) \mathbf{b}^H(\theta, \phi)] \quad (3.2)$$

Both \mathbf{P} and $\tilde{\mathbf{P}}$ are rank-one projection matrices. An equivalent representation for \mathbf{P} would be

$$\mathbf{P}(\theta, \phi) = \mathbf{B}(\theta, \phi) \tilde{\mathbf{P}}(\theta, \phi) \mathbf{B}^H(\theta, \phi) \quad (3.3)$$

where $\mathbf{B}(\theta, \phi) = \text{diag}\{\mathbf{b}(\theta, \phi)\}$. Since \mathbf{B} is a diagonal matrix with unit-norm diagonal elements it represents a unitary transformation.

To apply free-space compensation directly to the data, we compute

$$\tilde{\mathbf{z}}_k = \mathbf{z}_k \circ \mathbf{b}^*(\theta_k, \phi_k) \quad (3.4)$$

The $\tilde{\mathbf{z}}_k$ are then used to estimate $\tilde{\mathbf{P}}(\theta, \phi)$.

3.2. Sample Projection Matrix Computation

Every $\tilde{\mathbf{z}}_k$ is assumed to be an estimate of $\tilde{\mathbf{a}}(\theta_k, \phi_k)$, scaled by an unknown complex constant. An estimate of $\mathbf{P}(\theta_k, \phi_k)$ can be formed according to

$$\hat{\mathbf{P}}(\theta_k, \phi_k) = \frac{\tilde{\mathbf{z}}_k \tilde{\mathbf{z}}_k^H}{\tilde{\mathbf{z}}_k^H \tilde{\mathbf{z}}_k} \quad (3.5)$$

In the noiseless case, $\hat{\mathbf{P}}(\theta_k, \phi_k)$ would be exactly equal to $\tilde{\mathbf{P}}(\theta_k, \phi_k)$, but in the presence of noise or model inaccuracies there will be some error. The step described in the next section takes the entire set of $\hat{\mathbf{P}}(\theta_k, \phi_k)$ and in effect filters them by fitting the set to a low-order orthogonal expansion in the space of Hermitian matrices.

3.3. Weighted Least-Squares Fitting with Spherical Harmonics

This subsection describes the key step in the calibration process, that of finding a smooth function to fit to the data points $\hat{\mathbf{P}}_k$. At this point, we consider the matrices $\hat{\mathbf{P}}_k$ not as points in CP^N , but rather as elements of the larger space of $N \times N$ Hermitian matrices. This larger space is a Euclidean vector space, and so techniques for fitting the

data to set of basis functions apply. It is recognized that the result, after fitting, will not be a matrix function which takes values in CP^N .

A simple analogy to the fitting procedure is this. Let $x_1 \cdots x_K$ be a sequence of vectors in \mathbb{R}^2 , all of which have unit norm, i.e., they take values on the unit circle. If a lowpass filter is applied independently to each of the components of the x_k sequence, the resulting set of points $y_1 \cdots y_K$ will not necessarily fall on the unit circle. However, it is a simple matter to project each of the y_k back onto the unit circle to complete the fitting procedure.

For our problem, the domain of the desired smooth function is the sphere S^2 , and the range is CP^N . For a low-order series expansion, we need to identify a set of functions $f: S^2 \rightarrow \mathbb{C}$ which are orthonormal on the sphere and which increase in variability with increasing order. Such a set of functions are the *spherical harmonics*. These are a set of complex-valued functions $Y_{lm}(\theta, \phi)$ which are orthonormal on the sphere and which form a complete basis for the Hilbert space of integrable functions on the sphere. They are analogous to the complex exponentials, which form a basis for integrable functions on the circle, as represented in Fourier series expansions.

The spherical harmonic basis functions have two indices, l and m , such that $l \geq 0$ and $-l \leq m \leq l$. Each $Y_{lm}(\theta, \phi)$ can be factored according to

$$Y_{lm}(\theta, \phi) = A_m(\phi) B_{l|m|}(\theta) \quad (3.6)$$

The functions $A_m(\phi)$ are simply complex exponentials in azimuth:

$$A_m(\phi) = \frac{1}{\sqrt{2\pi}} e^{jm\phi} \quad (3.7)$$

The functions $B_{l|m|}(\theta)$ are real solutions to the differential equation

$$\frac{\sin \theta}{B} \frac{d}{d\theta} \left(\sin \theta \frac{dB}{d\theta} \right) + l(l+1) \sin^2 \theta = -m^2 \quad (3.8)$$

and are all l th-order trigonometric polynomials. Recursive formulas for these functions and explicit expressions for lower-order ones may be found in standard references in quantum mechanics [5].

The simplest fitting procedure involving the data $\hat{\mathbf{P}}_k$ and the basis functions Y_{lm} up to order $l = L$ would be to choose coefficients c_{ijlm} to minimize the squared error in the expression

$$\hat{P}_{ij}(\theta_k, \phi_k) \approx \sum_{l=0}^L \sum_{m=-l}^l Y_{lm}(\theta_k, \phi_k) c_{ijlm} \quad (3.9)$$

This can be set up as a straightforward matrix-vector least-squares problem which can be solved using standard tools

such as those available in MATLAB.

One drawback to the simple least-squares approach is that it gives equal weight to each of the $\hat{\mathbf{P}}_k$. As an alternative, one might wish to give more weight to the larger vectors \mathbf{z}_k , because they should have greater influence. Accordingly, one could solve for the coefficients c_{ijlm} through the minimization problem

$$\min_{c_{ijlm}} \sum_{k=1}^K |\mathbf{z}_k|^2 \left| \hat{p}_{ij}(\theta_k, \phi_k) - \sum_{l=0}^L \sum_{m=-l}^l Y_{lm}(\theta_k, \phi_k) c_{ijlm} \right|^2 \quad (3.10)$$

Again, this is easily solved using standard tools.

The weighted least-squares approach may appear *ad hoc*, but it can be motivated by the following arguments. Suppose one is given a set of vectors $\mathbf{x}_1 \cdots \mathbf{x}_K$ and wishes to compute the sample covariance matrix. This is obviously

$$\mathbf{S} = \frac{1}{K} \sum_{k=1}^K \mathbf{x}_k \mathbf{x}_k^H \quad (3.11)$$

\mathbf{S} is the solution to the minimization problem

$$\min_{\mathbf{S}} \sum_{k=1}^K \|\mathbf{S} - \mathbf{x}_k \mathbf{x}_k^H\|_F^2 \quad (3.12)$$

Clearly the larger \mathbf{x}_k have more influence in determining the structure of \mathbf{S} . Now consider the alternative minimization problem

$$\min_{\mathbf{S}} \sum_{k=1}^K \|\mathbf{S} - \mathbf{P}_k\|_F^2 w_k \quad (3.13)$$

where the \mathbf{P}_k are rank-one projection matrices formed from the data, i.e.,

$$\mathbf{P}_k = \frac{\mathbf{x}_k \mathbf{x}_k^H}{\mathbf{x}_k^H \mathbf{x}_k} \quad (3.14)$$

and the weights are given by the squared magnitudes of the data, i.e.,

$$w_k = \mathbf{x}_k^H \mathbf{x}_k \quad (3.15)$$

The solution to this minimization problem is easily found to be

$$\mathbf{S} = \frac{1}{\sum_{k=1}^K w_k} \sum_{k=1}^K \mathbf{P}_k w_k \quad (3.16)$$

and since

$$\mathbf{P}_k w_k = \mathbf{x}_k \mathbf{x}_k^H \quad (3.17)$$

we see that the solutions to the minimization problems (3.12) and (3.13) are the same to within a scale factor.

Now the process of forming an average of a set of data vectors is equivalent to fitting those data vectors to a single all-ones basis vector. In the averaging that we propose to carry out through the implementation of (3.10), this concept is extended to the case where the fitting is done to a larger number of basis vectors, the low-order spherical harmonics.

The Hermitian matrices which are the output of this fitting procedure, considered as a function of azimuth and elevation, are denoted $\tilde{\mathbf{P}}(\theta, \phi)$.

3.4. Principal Component Analysis

Because the projection matrices in the previous section were treated as elements of the vector space of Hermitian matrices in the filtering operation, the results of the filtering will be lifted off of the manifold CP^N . However, under the assumption that the function $\tilde{\mathbf{P}}(\theta, \phi)$ is already smooth, the estimates $\tilde{\mathbf{P}}(\theta, \phi)$ should be close to CP^N . It remains to project each smoothed matrix back into CP^N . This is accomplished by standard principal component techniques: at each (θ, ϕ) , we determine the nearest rank-one matrix to $\tilde{\mathbf{P}}(\theta, \phi)$. This is $\lambda_1 \mathbf{u}_1 \mathbf{u}_1^H$, where λ_1 is the largest eigenvalue of $\tilde{\mathbf{P}}$ and \mathbf{u}_1 is the corresponding unit-norm eigenvector. The resulting rank-one estimate of $\tilde{\mathbf{P}}(\theta, \phi)$ is denoted $\tilde{\mathbf{P}}_{est}(\theta, \phi)$.

3.5. Restoration of Free-Space Phase

After estimation of the multiplicative deviation $\tilde{\mathbf{P}}(\theta, \phi)$, we restore the effect of the free-space phase according to

$$\mathbf{P}_{est}(\theta, \phi) = \tilde{\mathbf{P}}_{est}(\theta, \phi) \odot [\mathbf{b}(\theta, \phi) \mathbf{b}^H(\theta, \phi)] \quad (3.6)$$

At this point, it is now appropriate to represent the array manifold using a single $N \times 1$ vector to represent each point in CP^N . One such choice would be to set $\mathbf{a}(\theta, \phi)$ equal to the unique vector in the range of $\mathbf{P}_{est}(\theta, \phi)$ which has unit norm and first element real.

4. SIMULATION EXAMPLE

The array calibration procedure described in the section above was implemented on a synthetic data set chosen to simulate a set of clutter returns for an airborne pulsed-Doppler radar system employing an electronically scanned circular array. The array parameters were chosen to mimic the UESA array under development for the E-2C [4]. The radar system used a carrier frequency of 450 MHz, a pulse repetition frequency (PRF) of 300 Hz, and a coherent processing interval (CPI) of 18 pulses. The aircraft was assumed to be flying at an altitude of 9 km at a velocity of

50 m/s. Range gate spacing was set to 5 km, resulting in 78 non-ambiguous range gates out to the horizon being processed for each pulse. The power in the clutter returns was chosen make the clutter-to-noise ratio (CNR) equal to 30 dB at 100 km. In one resulting STAP data cube there are $17 \times 78 = 1326$ vector clutter samples, corresponding to a sampling of azimuth/elevation space covering the region $-60^\circ \leq \phi \leq +60^\circ$ and $0^\circ \leq \theta \leq 60^\circ$. Because of the relationship between elevation and range, the sampling was very dense near $\theta = 0$ (i.e. out toward the horizon) and somewhat sparse for elevations corresponding to close ranges.

The perturbed array was simulated by taking the 20 elements in the 120° arc, and slightly perturbing their locations and orientations in a random way. This is illustrated in Figure 4.1, shown here in black-and-white. The inner product of the nominal and the perturbed array response vectors (each normalized to unit norm) was in the range 0.8-0.9 over most of (θ, ϕ) space.

Using the processing described above, a set of calibrated array response vectors was determined. The inner product of the perturbed and calibrated array response vectors was very close to 1.0 over the entire region of (θ, ϕ) space covered by the sampling grid.

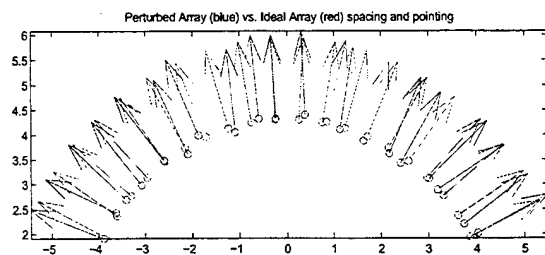


Figure 4.1. Nominal and Perturbed Arrays

The result of the calibration procedure is illustrated for one particular look direction, $\phi = 0^\circ$, $\theta = 2^\circ$, in Figure 4.2. This shows the magnitude and phase of the array response vectors at this look direction. The baseline, or nominal, array response is the response determined from element positions and nominal cosine element patterns. The truth is the array response determined from the perturbed array. Finally, the calibrated array response is that determined from the calibration procedure described here.

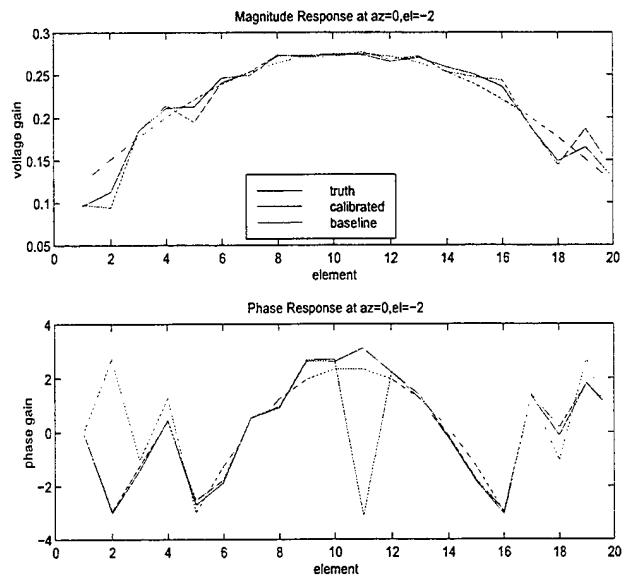


Figure 4.2. Calibrated Array Response

5. CONCLUSION

The problem of estimating an array manifold from calibration data, or from a set of response vectors on a fixed grid, was presented. It was argued that points in the array manifold should be viewed as elements of complex projective space, and in this context a technique for estimating smooth functions from azimuth/elevation to complex projective space was proposed. The proposed technique comprises 5 steps: 1) free-space phase compensation, 2) computation of a sequence of rank-one projections, 3) weighted least-squares fitting of the projections using a spherical harmonic basis, 4) principal component analysis at each direction, and 5) restoration of free-space phase. A simulation demonstrating the application of this technique to an airborne circular array, with clutter returns used as calibration data, was presented.

ACKNOWLEDGEMENT

This work was supported in part by a grant from the Office of Naval Research (DRF) and a research contract from MIT Lincoln Laboratory (DWR).

REFERENCES

- [1] F. Robey, D. Fuhrmann, and S. Krich, "Array Calibration Utilizing Clutter Scattering", *Proc. 7th IEEE SP Workshop on Statistical Signal and Array Processing* (Quebec City, Canada), June 1994.
- [2] M. Koerber and D. Fuhrmann, "Radar Antenna Calibration Using Range-Doppler Data", *Proc. 7th IEEE SP*

Workshop on Statistical Signal and Array Processing
(Quebec City, Canada), June 1994.

[3] M. Koerber and D. Fuhrmann, "Array Calibration by Fourier Series Parameterization: Scaled Principal Components Method", *Proc. ICASSP 93* (Minneapolis, MN), April 1993.

[4] M. Zatman, "Circular Array STAP", in *Proc. IEEE Radar Conference*, 1999.

[5] L. Pauling and E. Wilson, *Introduction to Quantum Mechanics*, Dover, New York, 1985.

THEORY AND APPLICATION OF ADAPTIVE TRANSMITTER RADAR

Joseph R. Guerci

DARPA/SPO
3701 N. Fairfax Drive
Arlington, VA 22203
JGuerci@darpa.mil

S. Unnikrishna Pillai

Polytechnic University
Five Metrotech Center
Brooklyn, NY 11201
Pillai@fire.poly.edu

ABSTRACT

Recent advances in linear amplifier and arbitrary waveform generation technology have spawned interest in adaptive transmitter systems as a means for both optimizing target signal gain and enhancing ID. In this paper, rigorous theoretical performance bounds are constructively established for the joint transmitter-target-channel-receiver optimization problem in the presence of additive colored noise (ACN), (e.g., interference multipath). For the ACN case, an analytical solution is obtained as an eigenvector (with associated maximum eigenvalue) of a homogeneous Fredholm integral equation of the second type. The kernel function is Hermitian and is obtained from the cascade of the target impulse response with the ACN whitening filter.

The theoretical performance gains achievable over conventional transmitter strategies (e.g., chirp) are presented for various simulation scenarios including interference multipath mitigation. Also discussed, is the potential effectiveness of an optimal discriminating pulse solution for the N -target ID problem that arises naturally from the theory.

1. INTRODUCTION

A fundamental and ubiquitous design problem encountered in radar, is that of jointly optimizing the transmitter and receiver, given some knowledge of the target and channel characteristics. At its most basic level, one is concerned with judiciously selecting the operating band, transmit waveform modulations, and receiver processing strategy, in order to maximize the probability of detecting the presence of a "target" while maintaining a prescribed rate of false alarms [1] (or maximizing correct classification for target ID applications).

In real-world applications, issues of cost, complexity and reliability can often weigh heavily on the design process. However, they are not static constraints. As technology progresses, new design-space domains can be explored, and previous assumptions revisited. For example, recent advances in low-noise, high-power linear amplifiers and high-speed, digitally programmable arbitrary waveform generators, has allowed radar designers to consider the use of sophisticated "pulse

shaping" techniques [2]-[6] heretofore considered impractical.

A first generation of so-called "matched illumination-reception" radars has been proposed based on relaxing the "point target" assumption common to most surveillance radars [2]-[5]. A point target, by definition, has a flat response (and linear phase) across the instantaneous operating band of the radar. Thus, under this assumption, no attempt is made to "shape" (pre-emphasize) the transmit pulse. However, given *a priori* knowledge (deterministic or statistical) concerning the range extended (non-point) target scattering characteristics, an optimal pulse shape can be designed which maximizes the energy reflected off of a target [2]-[5]. Specifically, for the finite pulse duration and receiver integration case, it is obtained as the solution of a homogeneous Fredholm integral equation of the second kind whose kernel is formed from the impulse response of the target [2], [8]-[9]. In the case of an interference channel consisting only of additive white noise, this transmit waveform, coupled with a linear filter receiver "matched" to the shape of the "echo," has been shown to maximize the output SNR [2], [8]-[9]. A constrained optimization procedure, in which deterministic waveform constraints are specified, such as "pulse compression" modulation, is contained in [7].

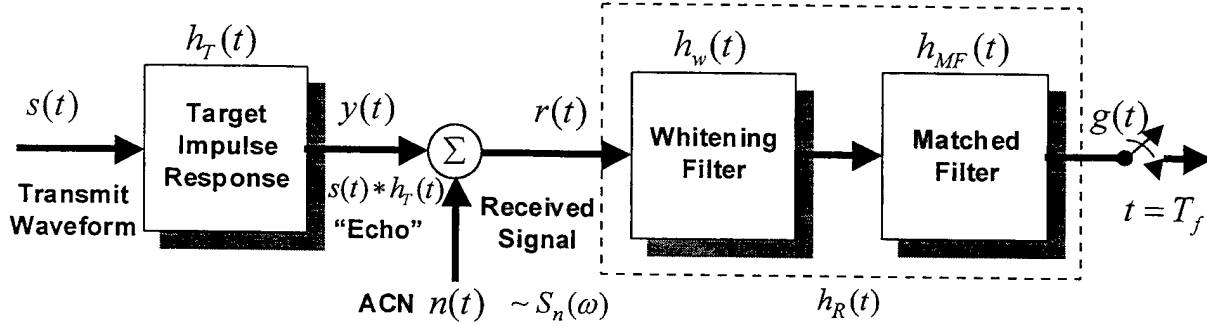
In this paper, rigorous theoretical performance bounds are constructively established for the joint transmitter-target-channel-receiver optimization problem in the presence of additive colored noise (ACN), (e.g., interference multipath). For the ACN case, an analytical solution is obtained as an eigenvector (with associated maximum eigenvalue) of a homogeneous Fredholm integral equation of the second type (i.e., an eigensystem). The kernel function is Hermitian and is obtained from the cascade of the target impulse response with the ACN whitening filter. The theory is illustrated via its application to both the interference multipath (colored noise) and the N -target ID problems. In the later application, a strategy for determining an optimal discriminating pulse is derived and illustrated via a three-target ID example.

Although generally nonlinear, an effective iterative procedure has recently been obtained for the signal dependent noise case (e.g., clutter reverberation channel)

Opinions, interpretations, conclusions, and recommendations are those of the authors and are not necessarily endorsed by DARPA or the Department of Defense.

[8]-[9]. Also in [10], the theory has been extended to the multichannel case, which allows for the inclusion of polarization and other physical degrees-of-freedom (DOFs) in the transmit-receive chain.

$$SINR_{opt} = \frac{E_{y_W}}{\sigma_W^2} = \frac{1}{\sigma_W^2} \int_{T_i}^{T_f} |y_W(t)|^2 dt \quad (1)$$



2. BASIC PROBLEM FORMULATION

Consider the basic elements of a radar design problem (see Fig. 1). A transmitter produces a waveform $s(t)$ that interacts with a target whose impulse response is given by $h_T(t)$. The resulting “echo” $y(t)$ is then corrupted by additive, wide sense stationary (w.s.s.) colored noise (ACN) $n(t)$ with associated power spectrum $S_n(\omega)$, to form the received signal $r(t)$. A “receiver” characterized by an impulse response $h_R(t)$ then processes $r(t)$. Note that linearity has been assumed in both the target interaction and receiver. We will also defer to the final section a discussion on how to address the case when the target impulse response is not known exactly.

Our objective is to jointly optimize the choice of transmit waveform $s(t)$ and receiver response $h_R(t)$ to maximize the output SINR at some prespecified sampling instant $t = T_f$, subject to finite pulse duration and observation constraints. It is the explicit inclusion of these constraints that has lead to a different solution than those obtained in other investigations [3]-[5].

2.1 Solution

We proceed by first considering the structure of the optimum receiver. It is a well-established fact that the optimum receiver for a known signal embedded in w.s.s. ACN, is a whitening filter $h_W(t)$ followed by a matched filter $h_{MF}(t)$ that is matched to the “whitened” target echo $y_W(t) = y(t) * h_W(t)$, where $*$ denotes the usual linear convolution operator [1].

The corresponding optimum SINR is given by

where E_{y_W} is the energy contained in the whitened target echo $y_W(t)$ over the interval $[T_i, T_f]$, and σ_W^2 is the expected energy (variance) of the whitened ACN process.

Thus, to maximize the output SINR, it suffices to maximize the energy in the whitened echo response $y_W(t)$, subject to a finite duration constraint on $s(t)$, i.e.,

$$\max_{s(t)} \int_{T_i}^{T_f} |y_W(t)|^2 dt. \quad (2)$$

The solution to (2) can be obtained by expressing $y_W(t)$ in terms of $s(t)$, rearranging terms, and then applying Schwarz’s inequality. Specifically, we have

$$E_y = \int_{T_i}^{T_f} |y_W(t)|^2 dt = \int_{T_i}^{T_f} |s(t) * h(t)|^2 dt \quad (3)$$

where

$$h(t) = h_T(t) * h_W(t), \quad (4)$$

i.e., $h(t)$ is the impulse response of the cascade of the target impulse response with that of the whitening filter. (3) can further be expressed as

$$\begin{aligned} E_y &= \int_{T_i}^{T_f} \left(\int_0^T s(\tau_1) h(t - \tau_1) d\tau_1 \right) \left(\int_0^T s^*(\tau_2) h^*(t - \tau_2) d\tau_2 \right) dt \\ &= \int_0^T \int_0^T s(\tau_1) s^*(\tau_2) K^*(\tau_1, \tau_2) d\tau_2 d\tau_1 \end{aligned} \quad (5)$$

where the superscript $*$ denotes complex conjugation. Note that we have required that the transmit pulse be of finite duration (i.e., $s(t) \in [0, T]$). $K^*(\tau_1, \tau_2)$ is the conjugate of the generally positive definite Hermitian kernel function $K(\tau_1, \tau_2)$ given by

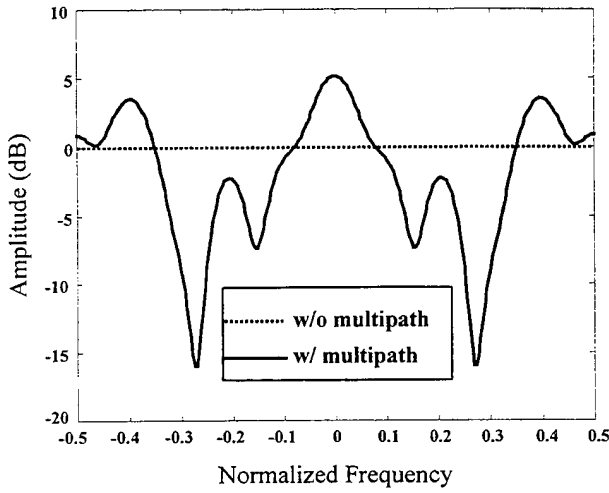


Fig. 2 Normalized interference power spectrum with and without multipath.

$$K(\tau_1, \tau_2) = \int_{T_i}^{T_f} h^*(t - \tau_1) h(t - \tau_2) dt \quad (6)$$

Applying Schwarz's inequality to (5) yields the optimum choice $s_{\text{opt}}(t)$ for transmit waveform, namely,

$$\lambda_{\text{max}} s_{\text{opt}}(\tau_1) = \int_0^T s_{\text{opt}}(\tau_2) K(\tau_1, \tau_2) d\tau_2, \quad (7)$$

i.e., $s(t)$ must be an eigenfunction (with maximum associated eigenvalue) of a homogeneous Fredholm integral equation of the second kind [11] with kernel given by (6). The corresponding optimum receive filter is thus given by

$$h_R(t) = h_T(t) * h_W(t) * s_{\text{opt}}(t) \quad (8)$$

Note that the existence of a causal whitening filter $h_W(t)$ is guaranteed due to the w.s.s. assumption of the ACN [1]. Also, substitution of the solution to (7) into (1), yields the optimum SINR (and thus the upper bound for any similarly constrained pulse).

2.2 Application to Interference Multipath

An interesting and potentially useful application of the present formulation is the so-called colored noise problem, which in a tactical radar setting may take the form of in-band RFI [6] or interference multipath [12]. In these situations, it is possible to "tailor" a transmit waveform to "anti-match" to the interference power spectrum. Thus

achieving an SINR gain over conventional waveforms (e.g., chirp).

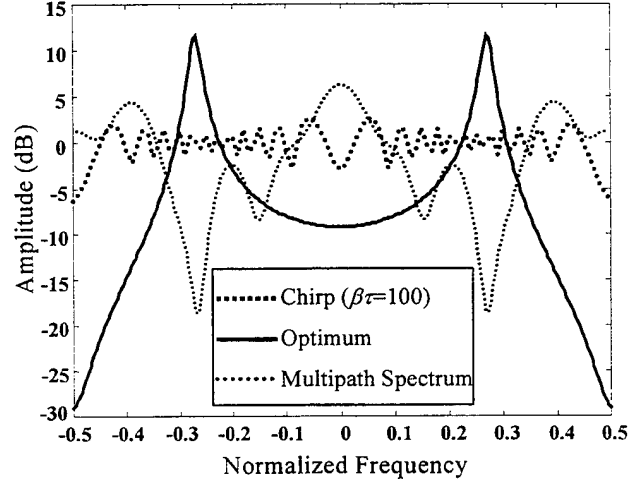


Fig. 3 Waveform spectra for the optimum pulse and chirp with multipath spectrum superimposed.

For simplicity, the usual "point target" assumption will be employed for the target since our objective is to illustrate interference rejection. Of course if available, target information is easily included via (4) and (8).

Consider the colored noise interference power spectrum of Fig. 2, which results from passing a broadband (white noise) source through a multipath channel with impulse response

$$h_{MP}(t) = \delta(t) + .9\delta(t-2) + .5\delta(t-5) + .2\delta(t-10), \quad (9)$$

which consists of a direct path, and three discrete multipath delays at 2, 5, and 10 range resolution cells.

Fig. 3 displays the spectra of a chirp waveform with a time-bandwidth product (" $\beta\tau$ ") of 100 along with that of the optimum transmit waveform $s_{\text{opt}}(t)$ obtained from (7). The resulting SINR gain over a conventional chirp is 9.6 dB, which is due to both the increase in SINR at the input to the receiver (8.6 dB), as well as the mismatch loss of the chirp receiver (1.0 dB).

It is important to note that the above attenuation of the interference is for *all* look directions. It is not based on spatial nulling. This can be a significant advantage for small antenna arrays (relative to the operating wavelength), since it has the effect of "tightening" up the interference notch and reducing channel match requirements.

Although the above example was based on the availability of ideal power spectra, one can envision a practical application in which the radar passively "sniffs" the operating band (receive-only) to estimate the interference spectrum.

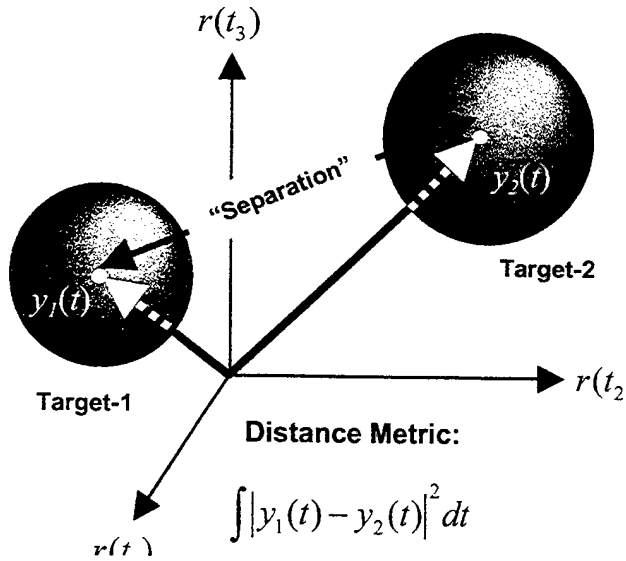


Fig. 4 Function space for received signal under two different target hypotheses.

thereby reducing SINR. An example of such a constrained solution methodology is contained in [6]-[7].

2.3 Application to Target ID

A perhaps more far reaching application of the optimized transmit-receive optimization theory, is to the target ID problem. Formulated as a classical hypothesis testing problem in the presence of additive Gaussian noise, our objective will be to choose a transmit strategy that will maximize the L_2 norm distance between signals corresponding to different targets. The corresponding optimal receive strategy follows from the classical theory [1]. Some earlier work in this area for the two target case can be found in [13]-[14].

Consider the two-target ID problem framed as a classical binary hypothesis-testing problem, i.e.,

$$\begin{aligned} H_1 : r(t) &= y_1(t) + n(t) = h_1(t) * s(t) + n(t) \\ H_2 : r(t) &= y_2(t) + n(t) = h_2(t) * s(t) + n(t) \end{aligned} \quad (10)$$

where $h_1(t)$ and $h_2(t)$ denote the impulse responses of the two targets, respectively.

For the additive (signal independent) noise case, with a unimodal and symmetric probability density function (pdf) and equally likely prior probabilities, the received signal under the two hypotheses can be viewed as two "points" in a function space surrounded by equiprobable "spheres of uncertainty" (see Fig. 4).

From Fig. 4, it is immediately apparent that our objective in designing an optimal transmit waveform is to maximize the separation (in function space) between the two hypotheses. This will insure that for the stated pdf assumptions, the "overlap" will be minimized [16]. Formally, we have

$$\max_{s(t)} \int_{T_i}^{T_f} |y_1(t) - y_2(t)|^2 dt = \max_{s(t)} \int_{T_i}^{T_f} |y(t)|^2 dt, \quad (11)$$

where $y(t) = y_1(t) - y_2(t)$. Interestingly, the solution to (11) is the same as that for (2) with $h(t)$ in (4) replaced with $h_1(t) - h_2(t)$.

The extension of the above to the N -target ID problem is relatively straightforward [16]. The objective is to maximize the average (weighted average in general) separation between hypotheses. The solution has the form [16]

$$\lambda_{\max} s_{\text{opt}}(\tau_1) = \int_0^T s_{\text{opt}}(\tau_2) K(\tau_1, \tau_2) d\tau_2 \quad (12)$$

where

$$K(\tau_1, \tau_2) = \sum_{m,n} \binom{N}{2} w_{m,n} \int_{T_i}^{T_f} h_{m,n}^*(t - \tau_1) h_{m,n}(t - \tau_2) dt \quad (13)$$

and

$$h_{m,n}(t) = h_m(t) - h_n(t). \quad (14)$$

In (14), $h_m(t)$ and $h_n(t)$ denote the impulse responses between m -th and n -th target pairs. $\{w_{m,n}\}$ are weighting factors that allow for (amongst other things) the assignment of relative "importance" in separating different pairs (e.g., military versus civilian). Note that the self-pairings ($m=n$) naturally drop out of (14).

To illustrate the impact that optimally "tailored" waveforms can have on the target discrimination problem, consider the three impulse responses of Fig. 5. The chirp waveform of Fig. 6 (a) was compared with an optimal waveform obtained from (12) subject to the same finite pulse duration/integration and transmit energy constraints (see Fig 6(b)). The optimum receive structure consisted of a bank of three matched filters, each matched to a different target assumption.

A Monte Carlo simulation, consisting of a thousand independent trials, was conducted in which additive Gaussian white noise (AGWN) was introduced to produce a 0 dB SNR before matched filtering. The sample probability for correct classification for the optimum pulse was 99.99% (one error per thousand), compared to a relatively low 58.40% for the chirp.

probability for correct classification for the optimum pulse was 99.99% (one error per thousand), compared to a relatively low 58.40% for the chirp.

constrained optimizations that lead to, for example, phase-only modulation schemes.

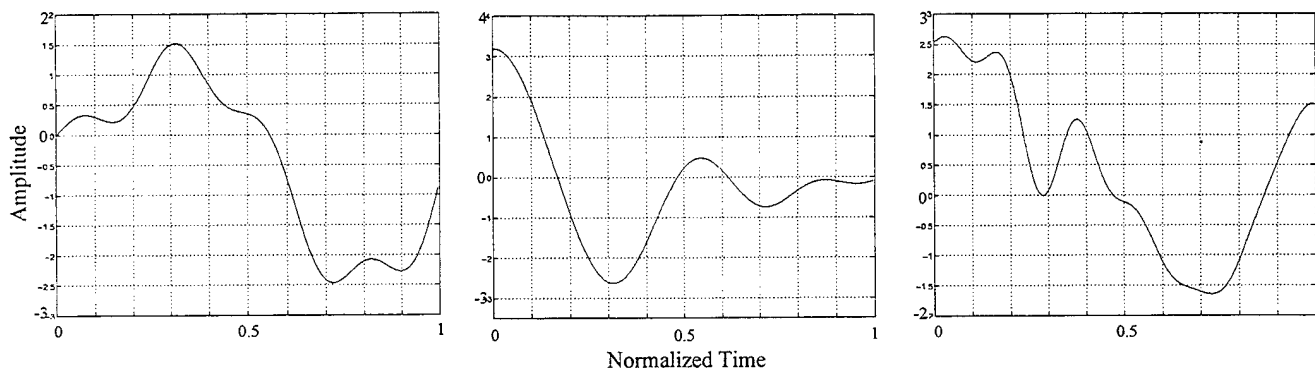


Fig. 5 Three target signatures employed in simulation.

The above N -target ID problem also inherently provides an approach for addressing the problem of specifying the target signatures (used in the optimization) as well. For example, if the aspect angle of the target is not precisely known, and this degree of uncertainty can lead to non-negligible mismatch errors, then several different aspects can be hypothesized and a structure identical to the above ID example can be employed. Other hypotheses could also be included relating to different target configurations (e.g., extra payloads) or deployments (e.g., camouflage).

3. CONCLUSIONS AND AREAS FOR FUTURE INVESTIGATION

A formal theory for jointly optimizing the transmit waveform and receiver filter was presented for the additive colored noise case. The methodology was applied to colored noise problems arising from, for example, interference multipath. When applied to a simple multipath channel example, a gain of 9.6dB was realized over a conventional chirp.

A theory for N -target ID was introduced and illustrated with a three "target" ID problem. The resulting probability of correct classification was dramatically better than that achieved by a conventional chirp.

The extension to the generally nonlinear clutter (signal dependent noise) case can be found in [8]-[9]. In [16], a more complete derivation of the N -target ID problem can be found. An extension to the multichannel case (e.g., polarization) can be found in [10].

Some important areas for future investigation include applications to more realistic targets and noise environments, and extensions of the theory such as

4. REFERENCES

- [1] H. L. Van Trees, *Detection, Estimation, and Modulation Theory*, Part I, John Wiley & Sons, New York
- [2] J. R. Guerci, et al., US Patents 5121125, 5146229, 5381154, 5392050.
- [3] D. T. Gjessing, *Target Adaptive Matched Illumination Radar Principles and Applications*, IEE Electromagnetic Waves Series (22), Peter Peregrinus Ltd., 1986.
- [4] A. Farina and F. A. Studer, "Detection with High Resolution Radar: Great Promise, Big Challenge," *Microwave Journal*, pp. 263-273, May 1991.
- [5] I. J. LaHaie, R. O. Harger, S. R. Robinson, J. K. Miller, "An Evaluation of Nonsinusoidal Radar Techniques," Final Report, AD-A171-484, Erim, Ann Arbor, MI, June 1985.
- [6] H. H. Schrieber and M. G. O'Connor, "Adaptive Waveform Radar," US Patent 4,901,082, February 1990.
- [7] J. R. Guerci, R. Schutz, and J. Hulsmann, "Constrained Optimum Matched Illumination-Reception Waveform Design Process," US Patent 5,146,229, September 1992.
- [8] S. U. Pillai, D. C. Youla, S. Oh, and J. R. Guerci, "Optimum Transmit-Receiver Design in the Presence of Signal-Dependent Interference and Channel Noise," *Proceedings of the 33rd Asilomar Conference on Signals, Systems, and Computers*, October 24-27, Pacific Grove, CA 1999.
- [9] S. U. Pillai, D. C. Youla, H. S. Oh, and J. R. Guerci, "Matched Transmit-Receiver Design in the Presence of Signal Dependent Noise," *IEEE Transactions on Information Theory*, Vol. 46, No. 2, March 2000.

- [10] S. U. Pillai, H. S. Oh and J. R. Guerci, "Multichannel Matched Transmit-Receiver Design in Presence of Signal Dependent Interference and Noise," *Proceedings of the First IEEE Sensor Array and Multichannel Signal Processing Workshop*, 16-17 March 2000, Cambridge, MA.

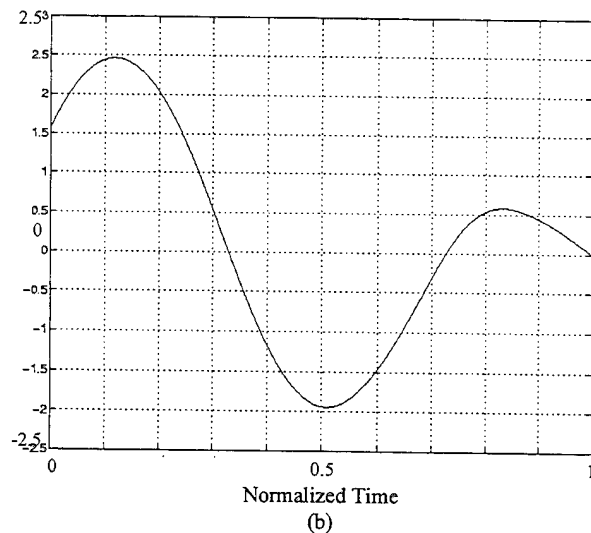
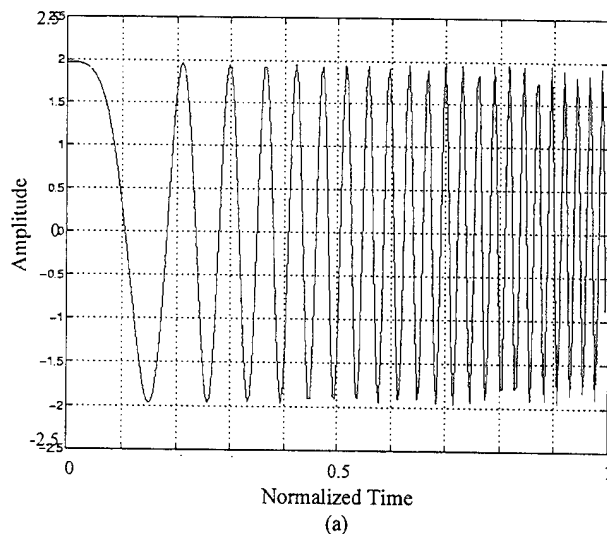


Fig. 6 (a) Conventional chirp waveform (correct classification = 58.40%). (b) Optimum pulse (correct classification = 99.99%).

- [11] D. Porter and D. S. G. Stirling, *Integral Equations: A Practical Treatment from Spectral Theory to Applications*, Cambridge University Press, 1990.
- [12] R. L. Fante and J. A. Torres, "Cancellation of Diffuse Jammer Multipath by an Airborne Adaptive Radar," *IEEE Transactions on Aerospace and Electronic Systems*, Vol. 31, April 1995.
- [13] E. T. Jaynes and C. R. Smith, "Theory of Radar Target Discrimination," Technical Report RD-AS-91-6, February 1991.
- [14] L. S. Riggs, M. A. Richards, T. H. Shumpert and C. R. Smith, "On Waveform Design for Optimal Target Discrimination," *International Journal of Imaging Systems and Technology*, Vol. 4, pp. 327-335, 1992.
- [15] J. R. Guerci, "Optimum Matched Illumination-Reception Radar for Target Classification", US Patent 5,381,154, January 1995.
- [16] J. R. Guerci, S. U. Pillai and J. S. Goldstein, "Optimum Transmit-Receiver Design for Target Identification," (in preparation).

DISTRIBUTED PROCESSING FOR 3-D LOCALIZATION USING ACOUSTIC VECTOR SENSORS ON THE SEABED OR BATTLEFIELD

Malcolm Hawkes and Arye Nehorai

EECS Department
University of Illinois
851. S. Morgan St
Chicago, IL 60607

hawkes@eecs.uic.edu, nehorai@eecs.uic.edu
www.eecs.uic.edu/~hawkes, www.eecs.uic.edu/~nehorai

ABSTRACT

We derive fast wideband algorithms for determining the bearing and 3-D position of a target using a distributed array of acoustic vector sensors (AVS's) situated on a reflecting boundary. Each AVS locally estimates the bearing from its location to the target using a rapid wideband estimator we develop based on the acoustic intensity vector; adaptations of beamforming-based bearing estimators are also discussed. The local bearing estimates are then transmitted to a central processor where they are combined to determine the 3-D position. Closed-form weighted least-squares (WLS) and reweighted least-squares algorithms are proposed to achieve this. We also present a bound on the mean-square angular error of the local bearing estimates and use it along with the data to adaptively determine the weights for the WLS routine. The results are relevant to the localization of underwater and battlefield sources using seabed sensors and ground sensors respectively. Numerical simulations are presented for both scenarios.

1. INTRODUCTION

Acoustic emissions from battlefield or underwater sources can provide an invaluable signature by which to detect, locate, and track hostile units. The passivity of an acoustic surveillance system allows it to monitor the battlefield or ocean without giving away its own presence. Passive acoustic surveillance has long been used underwater but its battlefield application [1] is more recent. The feasibility of acoustic localization and tracking on the battlefield [2]-[5] has been demonstrated.

We propose using *acoustic vector sensors* (AVS's) located on the ground or the seabed, to perform the surveillance function. These sensors measure the (scalar) acoustic pressure and all three components of the acoustic particle velocity vector at a given point, and possess a number of advantages over arrays of pressure sensors [6]-[9]. The ability of a single AVS to rapidly determine the bearing of a wideband makes them especially attractive for the present problem. Vector sensors for underwater applications have already been constructed [10], [11], and sea-tested [12], [13]. Recently, a new aero-acoustic velocity sensor called the Microflown [17], [18]

has become commercially available, from Microflown Technologies, B.V. [16] in the Netherlands, that would be appropriate for the battlefield context. As the probe is micro-machined a lightweight portable AVS could be constructed. The use of vector sensors near a boundary has been analyzed in [9], and they have been tested on a mock vessel hull [14] and at the seabed [15].

In this paper we develop fast wideband algorithms for finding the bearing of an acoustic source using a single AVS on the ground or seabed, and for combining bearing estimates from several arbitrary locations to determine its 3-D position. The bearing estimate is based on the measured acoustic intensity vector. We derive an optimal bound on its mean-square angular error (MSAE) [20], [21], and use it to obtain a data-based measure of the bearing estimator's accuracy. Each AVS transmits its bearing estimate, the estimate of its variability, and its current location, to a central processor (CP), which uses them to determine 3-D position. We propose a weighted least-squares (WLS) method to estimate position using the variability measures supplied by the sensors as weights. We also develop a re-weighted least-squares (RWLS) algorithm, to account for the different ranges of the sensors from the target. Note that these 3-D position estimation algorithms are independent of how the bearing estimates are obtained; they could come from subarrays of pressure sensors or other direction finders (passive or active).

As each AVS transmits only a bearing estimate rather than all measurements to the CP, this is a decentralized processing scheme [19]. The resulting 3-D position estimator is suboptimal because it does not make use of correlations between different locations, but it has numerous advantages: sensor placement is arbitrary and need not be fixed so sensors can be dropped (from the air or sea surface) and may be used in a dynamic context, carried by battlefield units for example; each sensor provides local target bearing information (especially valuable in the dynamic context), without the need to communicate with the CP. Even when communication is made, minimal data is sent, so minimizing the risk of detection and telemetry requirements; lastly, the algorithms are wideband and very computationally efficient as they require no numerical optimization.

In Section 2 we present the mathematical model for the sensor measurements. Section 3 develops the bearing estimation algo-

This work was supported by the Air Force Office of Scientific Research under Grants F49620-99-1-0067 and F49620-00-1-0083, and the National Science Foundation under Grant MIP-9615590.

gorithms, derives the performance bound and presents the procedure to adaptively estimate the variability. The WLS and RWLS 3-D position estimates are constructed in Section 4 and Section 5 provides numerical examples. Section 6 concludes.

2. MEASUREMENT MODEL

Assume there is a single source, located above a flat planar boundary, radiating spherical waves and that has bearing \mathbf{u} relative to an AVS located on the surface, which defines the x, y -plane. As long as the source is not too close to the boundary, the acoustic field may be obtained using a ray acoustics approximation, i.e. using an image source with bearing \mathbf{u}_{im} obtained by negating the z -component of \mathbf{u} . Let $\tilde{p}(t)$ be the source signal's complex envelope referenced to the sensor's location. The image source's signal is then $\mathcal{R}\tilde{p}(t)$, where the complex-valued \mathcal{R} is to be determined. As long as the sensor is more than a few wavelengths from the source, the velocity in a spherical wave is proportional to pressure (see e.g. [23]) and in the radial direction. Summing the original and image source contributions, the pressure and velocity fields at the sensor are

$$p(t) = (1 + \mathcal{R})\tilde{p}(t) \quad (2.1)$$

$$\mathbf{v}(t) = -\frac{1}{\rho_0 c}(\mathbf{u} + \mathcal{R}\mathbf{u}_{im})\tilde{p}(t), \quad (2.2)$$

where ρ_0 is the density and c is the speed of sound. The presence of the boundary imposes the condition $-p(t)/v_z(t) = Z_{in}$ at $z = 0$ [23], where $v_z(t)$ is the z -component of $\mathbf{v}(t)$, and Z_{in} is the specific acoustic impedance of the surface. Therefore

$$Z_{in} = -\frac{(1 + \mathcal{R})\rho_0 c}{(1 - \mathcal{R})\sin \psi}, \quad (2.3)$$

where ψ is the source's elevation with respect to the sensor, and

$$\mathcal{R} = \frac{Z_{in} - \rho_0 c / \sin \psi}{Z_{in} + \rho_0 c / \sin \psi}. \quad (2.4)$$

The quantity \mathcal{R} is known as the reflection coefficient. In general Z_{in} , and hence \mathcal{R} , depend on frequency as well as ψ , however, this model assumes they are approximately constant over the bandwidth.

The AVS's measurement vector may therefore be written

$$\mathbf{y}(t) \triangleq \begin{bmatrix} y_p(t) \\ \mathbf{y}_v(t) \end{bmatrix} = \mathbf{h}\tilde{p}(t) + \mathbf{e}(t) \quad t = 1, 2, \dots, \quad (2.5)$$

where $y_p(t)$ is the pressure measurement, $\mathbf{y}_v(t)$ contains the three orthogonal velocity measurements normalized by $-1/\rho_0 c$, $\mathbf{e}(t)$ represents noise, and the steering vector \mathbf{h} is given by

$$\mathbf{h} = \begin{bmatrix} 1 + \mathcal{R} \\ (1 + \mathcal{R})\cos \phi \cos \psi \\ (1 + \mathcal{R})\sin \phi \cos \psi \\ (1 - \mathcal{R})\sin \psi \end{bmatrix}, \quad (2.6)$$

where ϕ is the source's azimuth relative to the sensor. Expression (2.6) assumes the three velocity components are aligned with the coordinate axes, or that the data have been rotated to achieve this.

2.1. Statistical Assumptions

We assume that the signal and noise processes $\tilde{p}(t)$ and $\mathbf{e}(t)$ are zero-mean uncorrelated processes with finite second order moments and that

$$E\{\tilde{p}(t)\overline{\tilde{p}(\tau)}\} = \sigma_s^2 \delta_{t,\tau} \quad (2.7)$$

$$E\{\mathbf{e}(t)\mathbf{e}(\tau)^H\} = \sigma^2 I \delta_{t,\tau}, \quad (2.8)$$

where $\delta_{t,\tau}$ is the Kronecker delta function, I is the identity matrix, overbar indicates conjugation, and superscript H represents conjugate transposition.

2.2. Multiple Sensors

Now suppose there are m sensors located at $\mathbf{r}_1, \dots, \mathbf{r}_m$, and denote the 3-D source position vector by $\boldsymbol{\theta}$. Letting $\tilde{p}(t)$ be the source signal reference to the origin, the measurements from the array are

$$\mathbf{y}_i(t) = \mathbf{h}(\mathbf{u}_i) \frac{\|\boldsymbol{\theta}\|}{\|\boldsymbol{\theta} - \mathbf{r}_i\|} \tilde{p}((t - \tau_i)/\alpha_i) + \mathbf{e}_i(t), \quad (2.9)$$

for $i = 1, \dots, m$, $t = 1, 2, \dots, N$, where the \mathbf{u}_i are the sensor to source bearing vectors, τ_i is the differential time delay with respect to the origin, and α_i accounts for the effect of Doppler. The estimation schemes presented make no use of correlations between sensors at different locations, so expressions for the Doppler and time delay in terms of source position and velocity are not important (except for the purposes of simulation). For the same reason, we do not need to make any assumptions regarding noise correlation between sensors at different locations. Note that for a moving source, \mathbf{u}_i , $\boldsymbol{\theta}$, τ_i , and α_i , will generally vary with time, however, we assume that the observation interval is short enough such that they are approximately constant.

3. LOCAL BEARING ESTIMATION

In this section we derive fast wideband algorithms to estimate \mathbf{u} with a single AVS. Acoustic intensity is a vector quantity defined as the product of pressure and velocity. Since the x and y components of the intensity vector are the same for both real and image sources, the horizontal component of acoustic intensity is parallel to the projection of \mathbf{u} onto the x, y -plane. Therefore we can use an estimate of the horizontal acoustic intensity to determine azimuth. Note that [6] used this technique to derive an estimator for the full bearing vector using an AVS in free space, however, it cannot be used to find the elevation when the boundary is present.

The measured horizontal component of acoustic intensity is

$$\mathbf{I}_h(t) \triangleq y_p(t) \begin{bmatrix} \tilde{y}_{v_x}(t) \\ \tilde{y}_{v_y}(t) \end{bmatrix}. \quad (3.10)$$

Thus, under the noise model of equation (2.8),

$$E\{\mathbf{I}_h(t)\} = \sigma_s^2 |1 + \mathcal{R}|^2 \cos \psi \begin{bmatrix} \cos \phi \\ \sin \phi \end{bmatrix}. \quad (3.11)$$

Since this is purely real we let $\hat{\mathbf{s}} = N^{-1} \sum_{t=1}^N \text{Re}\{\mathbf{I}_h(t)\}$, and by the strong law of large numbers $\hat{\mathbf{s}} \rightarrow E\{\mathbf{I}_h(t)\}$. Thus we can estimate azimuth from

$$\hat{\mathbf{u}}_h \triangleq \begin{bmatrix} \cos \hat{\phi} \\ \sin \hat{\phi} \end{bmatrix} = \frac{\hat{\mathbf{s}}}{\|\hat{\mathbf{s}}\|} \rightarrow \mathbf{u}_h \triangleq \begin{bmatrix} \cos \phi \\ \sin \phi \end{bmatrix}. \quad (3.12)$$

Equation (3.12) is independent of \mathcal{R} , so this estimator can determine the azimuth without knowledge of the ground or seabed's reflective characteristics. Since the magnitude of the horizontal component of acoustic intensity depends strongly on the elevation, so will the accuracy of this azimuthal estimator. By adapting the analysis of [6] to the present scenario, we can show that its asymptotic MSAE is

$$\text{MSAE}(\hat{\mathbf{u}}_h) \triangleq \lim_{N \rightarrow \infty} N E(\hat{\phi} - \phi)^2 = \frac{1 + |1 + \mathcal{R}|^2 \rho}{2\rho^2 |1 + \mathcal{R}|^4 \cos^2 \psi}, \quad (3.13)$$

where $\rho = \sigma_s^2 / \sigma^2$ is the signal-to-noise ratio (SNR).

Obtaining an estimator of the elevation requires that the functional form of \mathcal{R} be known. The vertical component of acoustic intensity $I_v(t) \triangleq y_p(t) \bar{y}_{v_z}(t)$ has expected value

$$E\{I_v(t)\} = \sigma_s^2 (1 + \mathcal{R})(1 - \bar{\mathcal{R}}) \sin \psi. \quad (3.14)$$

Using equation (3.11) we see that

$$\chi \triangleq \frac{E\{I_v(t)\}}{\|E\{I_h(t)\}\|} = \frac{1 - \bar{\mathcal{R}}}{1 + \bar{\mathcal{R}}} \tan \psi, \quad (3.15)$$

is a function of ψ alone, which we estimate from the statistic

$$\hat{\chi} = \frac{\sum_{t=1}^N I_v(t)}{\|\sum_{t=1}^N \text{Re}\{I_h(t)\}\|}. \quad (3.16)$$

The elevation estimate $\hat{\psi}$ is then the solution to

$$\hat{\chi} = \frac{1 - \bar{\mathcal{R}}(\hat{\psi})}{1 + \bar{\mathcal{R}}(\hat{\psi})} \tan \hat{\psi}. \quad (3.17)$$

3.1. Battlefield Scenario

For this scenario, the boundary is modeled as a locally reacting surface, i.e. Z_{in} is independent of ψ . This model is been shown to be a good approximation to various ground surfaces [26]. Substituting (2.4) into (3.15) we obtain $\chi = \rho_0 c / (Z_{in} \cos \psi)$. Hence, the elevation can be estimated from

$$\hat{\psi} = \text{Re} \left\{ \cos^{-1} \left| \frac{\rho_0 c}{\hat{\chi} Z_{in}} \right| \right\}. \quad (3.18)$$

3.2. Seabed Scenario

Here we model the seabed as the interface between two liquid layers, one of which is absorptive; this corresponds approximately to a water-packed sandy bottom [24, pp. 11]. The model is

$$\mathcal{R}(\psi) = \frac{\eta \sin \psi - j(\cos^2 \psi - n^2)^{1/2}}{\eta \sin \psi + j(\cos^2 \psi - n^2)^{1/2}}, \quad (3.19)$$

where η is the ratio of sand density to water density and n is the index of refraction. Absorption is accounted for by assuming the index of refraction is complex, i.e. $n = n_0(1 + i\alpha)$, with $\alpha > 0$. For the sandy ocean bottom typical values are $n_0 = 0.83$, $\eta = 2.7$, $\alpha = 0.1$ [24, pp. 11]. Substituting (3.19) into (3.15) gives

$$\chi = \frac{-j\sqrt{\cos^2 \psi - n^2}}{\eta \cos \psi}, \quad (3.20)$$

and so we estimate ψ using

$$\hat{\psi} = \text{Re} \left\{ \cos^{-1} \left| \frac{n}{\sqrt{\hat{\chi}^2 \eta^2 + 1}} \right| \right\}. \quad (3.21)$$

3.3. Beamforming Estimators

The intensity based estimators outlined above are only effective when there is one dominant source, however, an AVS can identify up to 2 sources [25]. To deal with multiple source situations and to obtain more accurate bearing estimators, we consider the following adaptations of conventional and minimum variance beamforming-based estimators:

$$\hat{\mathbf{u}}_c = \underset{\mathbf{u}}{\text{argmax}} \left\{ \mathbf{h}^H \hat{\mathbf{R}} \mathbf{h} / \|\mathbf{h}\|^2 \right\} \quad (3.22)$$

$$\hat{\mathbf{u}}_{mv} = \underset{\mathbf{u}}{\text{argmax}} \left\{ \|\mathbf{h}\|^2 / (\mathbf{h}^H \hat{\mathbf{R}}^{-1} \mathbf{h}) \right\}, \quad (3.23)$$

where $\hat{\mathbf{R}}$ is the sample covariance matrix. The vector \mathbf{h} is independent of frequency because all four AVS components are co-located, so unlike traditional pressure-array beamforming estimators, these are wideband estimators. However, its magnitude depends on the angle, thus the presence of the normalizing factor $\|\mathbf{h}\|^2$ to partially compensate for this. Nevertheless, these estimators will not have the same statistical properties as their usual counterparts. Of course a 2-D numerical search is required so they are not as fast as the intensity algorithms, which could be used to initialize the search.

3.4. Estimator Performance

In general, there is no simple expression for the MSAE of the intensity-based estimator of the complete bearing \mathbf{u} . Instead we use a bound on the MSAE [20], [21], given by

$$\text{MSAE}_b(\mathbf{u}) = N \{ \cos^2 \psi \text{CRB}(\phi) + \text{CRB}(\psi) \}, \quad (3.24)$$

where $\text{CRB}(\cdot)$ indicates the Cramér-Rao bound (CRB), that holds for a large class of estimators [21]. If the signals and noise are Gaussian it is given by [27]

$$\text{MSAE}_b = \frac{1}{2\rho} \left(1 + \frac{1}{\rho \|\mathbf{h}\|^2} \right) \left(\frac{\cos^2 \psi}{\|\partial \mathbf{h} / \partial \phi\|^2} + \frac{1}{\|\partial \mathbf{h} / \partial \psi\|^2 - |(\partial \mathbf{h}^H / \partial \psi) \mathbf{h}|^2 / \|\mathbf{h}\|^2} \right). \quad (3.25)$$

where

$$\|\mathbf{h}\|^2 = |1 + \mathcal{R}|^2 (1 + \cos^2 \psi) + |1 - \mathcal{R}|^2 \sin^2 \psi \quad (3.26)$$

$$\left\| \frac{\partial \mathbf{h}}{\partial \phi} \right\|^2 = |1 + \mathcal{R}|^2 \cos^2 \psi \quad (3.27)$$

$$\left\| \frac{\partial \mathbf{h}}{\partial \psi} \right\|^2 = |1 + \mathcal{R}|^2 \sin^2 \psi + |1 - \mathcal{R}|^2 \cos^2 \psi + 2|\mathcal{R}'|^2 - 4 \text{Re}\{\mathcal{R}'\} \cos \psi \sin \psi \quad (3.28)$$

$$\left| \frac{\partial \mathbf{h}^H}{\partial \psi} \mathbf{h} \right|^2 = |\bar{\mathcal{R}}' \{ (1 + \mathcal{R})(1 + \cos^2 \psi) - (1 - \mathcal{R}) \sin^2 \psi \} + (|1 - \mathcal{R}|^2 - |1 + \mathcal{R}|^2) \cos \psi \sin \psi|^2, \quad (3.29)$$

and \mathcal{R}' is the derivative \mathcal{R} with respect to ψ .

It may be seen that MSAE_b is a function of the SNR ρ and the elevation ψ , but not the azimuth. Therefore we must estimate MSAE_b by plugging in estimates ρ and ψ . The bearing estimator itself already provides us with an estimate of ψ so it remains to estimate ρ . If we knew the maximum-likelihood (ML) estimate of \mathbf{u} , say

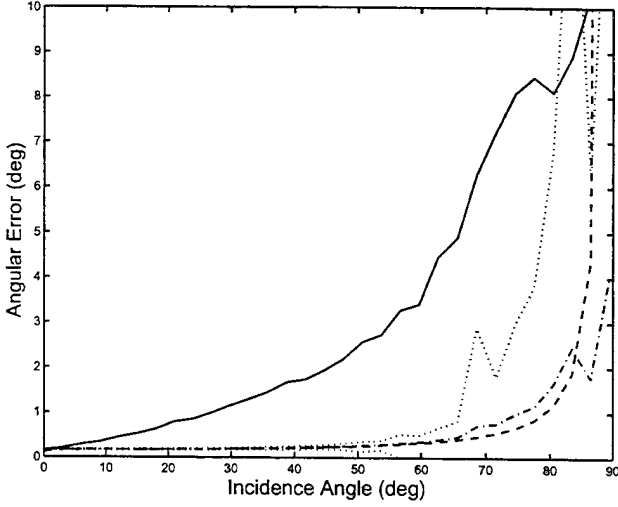


Figure 1: Battlefield scenario: Performance, $\text{MSAE}^{1/2}$, of fast bearing estimator (solid), and bound $\text{MSAE}_b^{1/2}$ (dashed), for 20dB source with 350 snapshots. Also shown is mean estimated bound $\widehat{\text{MSAE}}_b^{1/2}$ (dash-dotted) plus and minus three empirical standard deviations (dotted). 500 realizations were used.

$\hat{\mathbf{u}}_{\text{ML}}$, then we could use closed form expressions, see e.g. [22], to find the ML estimates of $\hat{\sigma}^2$ and $\hat{\sigma}_s^2$ (assuming Gaussian signals and noise). Since we don't know $\hat{\mathbf{u}}_{\text{ML}}$, we shall use our actual estimate of $\hat{\mathbf{u}}$. Therefore we have

$$\hat{\sigma}^2 = \frac{1}{3} \text{Re} \left\{ \text{tr} \left[\left(I - \frac{\hat{\mathbf{h}}\hat{\mathbf{h}}^H}{\|\hat{\mathbf{h}}\|^2} \right) \hat{\mathbf{R}} \right] \right\} \quad (3.30)$$

$$\hat{\sigma}_s^2 = \frac{1}{\|\hat{\mathbf{h}}\|^4} \hat{\mathbf{h}}^H [\hat{\mathbf{R}} - \hat{\sigma}^2 I] \hat{\mathbf{h}}, \quad (3.31)$$

where $\hat{\mathbf{h}} = \mathbf{h}(\hat{\mathbf{u}})$ and $\hat{\mathbf{R}}$ is the sample covariance matrix. So our estimate of the SNR is $\hat{\rho} = \hat{\sigma}_s^2 / \hat{\sigma}^2$. This scheme avoids a singular value decomposition of the sample covariance so keeping processing requirements to a minimum. Finally, we plug $\hat{\rho}$ and the elevation estimate $\hat{\psi}$ into (3.25) to obtain $\widehat{\text{MSAE}}_b$. Note that this means of assessing variability is appropriate for any bearing estimator not just those discussed above.

4. CENTRALIZED POSITION ESTIMATION

If all the $\hat{\mathbf{u}}_i$ were without error the collection of m lines passing through each \mathbf{r}_i with direction $\hat{\mathbf{u}}_i$ would intersect at the true source position. Therefore, we shall choose $\hat{\boldsymbol{\theta}}$ to be the point that minimizes a weighted sum of the minimum squared distances to each line. The result is a closed-form estimator. Any point along the line defined by the i th sensor's location and bearing estimate is described by $\mathbf{r}_i + \mu_i \hat{\mathbf{u}}_i$ for some μ_i . For fixed $\boldsymbol{\theta}$ the point of closest approach occurs when $\mu_i = \hat{\mathbf{u}}_i^T (\boldsymbol{\theta} - \mathbf{r}_i)$, i.e. μ_i is the projection of the vector from \mathbf{r}_i to $\boldsymbol{\theta}$ onto the direction $\hat{\mathbf{u}}_i$. Thus, the weighted least squares (WLS) estimate of $\hat{\boldsymbol{\theta}}$ is

$$\hat{\boldsymbol{\theta}} = \underset{\boldsymbol{\theta}}{\text{argmin}} \sum_{i=1}^m \|\mathbf{r}_i + \hat{\mathbf{u}}_i^T (\boldsymbol{\theta} - \mathbf{r}_i) \hat{\mathbf{u}}_i - \boldsymbol{\theta}\|^2 w_i, \quad (4.32)$$

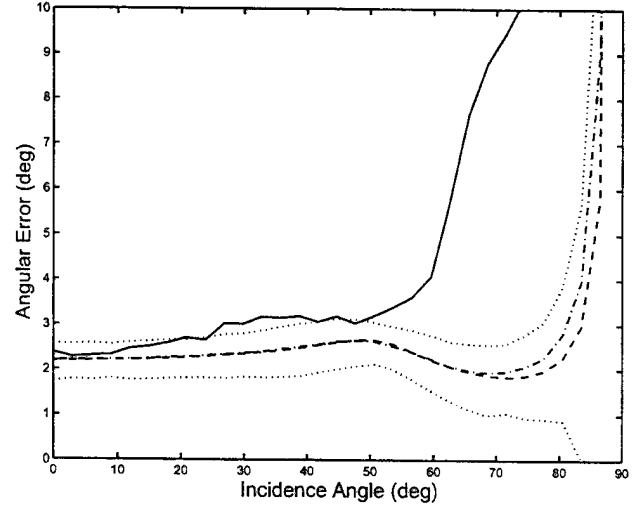


Figure 2: Underwater scenario: Performance, $\text{MSAE}^{1/2}$, of fast bearing estimator (solid), and bound $\text{MSAE}_b^{1/2}$ (dashed), for 3dB source with 175 snapshots. Also shown is mean estimated bound $\widehat{\text{MSAE}}_b^{1/2}$ (dash-dotted) plus and minus three empirical standard deviations (dotted). 500 realizations were used.

where the w_i is the weight corresponding to $\hat{\mathbf{u}}_i$. Equation (4.32) has the closed-form solution

$$\hat{\boldsymbol{\theta}} = \left[\left(\sum_{i=1}^m w_i \right) I - \hat{\mathbf{U}} \mathbf{W} \hat{\mathbf{U}}^T \right]^{-1} \mathbf{A} \mathbf{w}, \quad (4.33)$$

where $\mathbf{w} = [w_1, \dots, w_m]^T$, $\mathbf{W} = \text{diag}\{\mathbf{w}\}$, $\hat{\mathbf{U}} = [\hat{\mathbf{u}}_1, \dots, \hat{\mathbf{u}}_m]$, and

$$\mathbf{A} = [(I - \hat{\mathbf{u}}_1 \hat{\mathbf{u}}_1^T) \mathbf{r}_1, \dots, (I - \hat{\mathbf{u}}_m \hat{\mathbf{u}}_m^T) \mathbf{r}_m]. \quad (4.34)$$

Weights should reflect the accuracy of each individual bearing estimate. Therefore it is natural to use $1/\widehat{\text{MSAE}}_b$, where $\widehat{\text{MSAE}}_b$ is the variability estimated by the procedure in Section 3.4. Note that it does not matter how the bearing estimates are obtained. For example each AVS could be replaced by a small subarray of hydrophones.

4.1. Reweighting

Errors in the bearing estimates from sensors far from the source have a much greater effect upon $\hat{\boldsymbol{\theta}}$ than those from sensors nearby. The contribution of the i th bearing estimate to the squared error criterion is approximately $l_i^2 \delta_i^2$, where l_i is the distance of the source from the i th sensor and δ_i is the angular error of $\hat{\mathbf{u}}_i$. Although we do not know the l_i , we do have an estimate of them after we have estimated $\boldsymbol{\theta}$ using the above WLS procedure. Therefore we propose a re-weighted least-squares (RWLS) estimator constructed as follows: Find $\hat{\boldsymbol{\theta}}$ using the weights $w_i = 1/\widehat{\text{MSAE}}_b(\mathbf{u}_i)$. Using this $\hat{\boldsymbol{\theta}}$, estimate the distances from each sensor to the source as $\hat{l}_i = \|\hat{\boldsymbol{\theta}} - \mathbf{r}_i\|$, then construct a re-weighted estimate $\hat{\boldsymbol{\theta}}_R$, again using WLS but now with weights $w_i = 1/(\hat{l}_i^2 \cdot \widehat{\text{MSAE}}_b(\mathbf{u}_i))$.

5. NUMERICAL EXAMPLES

5.1. Local Bearing Estimation

For the purposes of simulation we use a Gaussian distributed signal and noise. For the battlefield problem we take $Z_{in}/(\rho_0 c) = 11 + 13i$, which was measured by [26] for grass-covered flat ground at 215Hz, and use a 20dB source with 350 snapshots. For the underwater case we use the parameters given in Section 3.2, a 3dB, source and 175 snapshots. Figures 1 and 2 summarize the results, which are independent of azimuth, as a function of incidence angle γ , say (i.e. $\gamma = \pi/2 - \psi$). In both cases $\hat{\mathbf{u}}$ is close to the bound at normal incidence (source directly above sensor). As incidence increases the performance, though not the bound, worsens steadily for the battlefield scenario. For the underwater case performance stays approximately constant and close to the bound before worsening rapidly around 55° , at the same time as the bound actually decreases. In both cases, performance and bound tend to ∞ as the incidence reaches grazing, because $|\mathbf{h}| \rightarrow 0$, and therefore so does the SNR. Of course, the underwater estimator is generally rather more accurate than the battlefield estimator across the board (we are using a higher SNR and more snapshots for the latter). Examination of the standard deviation of the elevation and azimuthal estimates separately (not shown), reveals that the majority of the angular error, especially in the battlefield scenario, is due to errors in the elevation rather than the azimuth. Thus, the 3-D location system can determine the x, y -coordinates (ground track) of a target can be rather more accurately than its 3-D position or height

Except at large incidence, the quantity $\widehat{\text{MSAE}}_b(\mathbf{u})$ is seen to estimate $\text{MSAE}_b(\mathbf{u})$ well. This is especially true for the battlefield problem, and is probably due to the higher SNR in the simulation. It is possible that on any run $\hat{\psi} = 0$, with finite probability if the argument of the inverse cosine in (3.18) is greater than one. In this case our technique fails to yield an estimate of MSAE_b , because it is theoretically infinite if ψ really is zero as $|\mathbf{h}| = 0$. In our simulation, this never occurred below 66° incidence, and the chances of it occurring rose to about 50% within a few degrees of grazing incidence. However, we do not expect that such large incidences will need to be measured in this application and so this should not be a problem in practice. If it does occur at one sensor in the array, a solution would be to use the average of the $\widehat{\text{MSAE}}_b$ obtained from the other sensors as its weight in the WLS location procedure.

5.2. Centralized Position Estimation

In these examples there are six sensors located on the boundary at (0, 0), (20, 26.6), (40, 38.1), (60, -21.3), (-100, -32.0), and (70, 40.4), and a wideband source at (15, 13.4, 100) (in units of meters). These locations are chosen such that if the sampling frequency is equal to the speed of sound (330m/s for air, 1500 m/s for water) all differential delays are multiples of the sampling period. We use a Gaussian signal and noise and assume they are independent and identically distributed (i.i.d) after sampling. This will be the case if the bandwidth prior to demodulation is equal to the sampling frequency and the spectral density is symmetric about the center frequency, e.g. bandlimited white noise. For example, in air, a 50-380Hz signal downsampled around 215Hz and sampled at 330Hz, and in water, a 100-1600Hz signal downsampled around 850Hz and sampled at 1500Hz would give rise to these statistics.

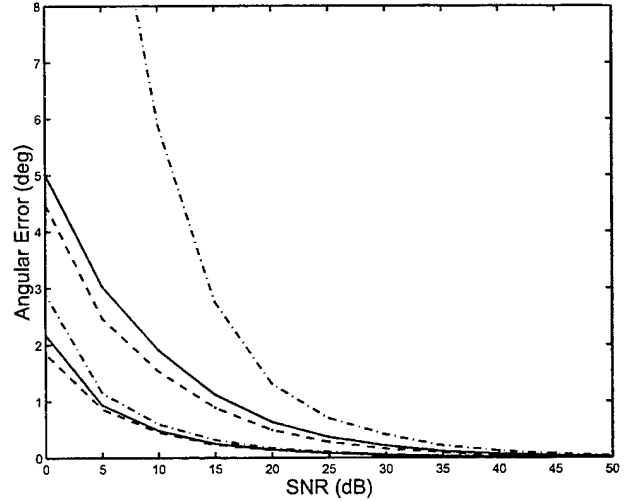


Figure 3: Angular estimation performance in terms of $\text{MSAE}^{1/2}$ for the WLS (solid), RWLS (dashed), and unweighted LS (dash dotted) 3-D position estimators. Upper 3 curves are for battlefield scenario, lower 3 for underwater. The scenario is described in the text.

Signal level at each sensor is determined by spherical spreading but Doppler not included; noise power and reflection properties are the same at each sensor.

Figures 3 and 4 show the MSAE and mean-square range error (MSRE), defined by $E(\|\hat{\theta}\| - \|\theta\|)^2$, of the position estimated for both the basic WLS estimator and the reweighted estimator, versus SNR (defined as the ratio of signal power on the ground directly below the source when the boundary is not present to the noise power at each sensor). A total of 350 snapshots were used with 500 realizations. Unsurprisingly, both MSAE and MSRE decrease as SNR increases, however, the estimated bearing is rather more accurate than the estimated range. It is known that the CRB on range for a passive sensor array increases as the fourth power of the range [28], so this observation seems quite consistent. The underwater problem results in the more accurate source position estimate. The WLS method improves considerably on unweighted least-squares, showing the value of transmitting the variability measure to the CP. The re-weighting scheme is seen to provide a small but noticeable improvement over WLS.

6. CONCLUSION

We developed a fast, wideband decentralized processing scheme for local bearing estimation and global 3-D source localization of a target using a distributed array of acoustic vector sensors on the battlefield or the seabed. The algorithm requires minimal communication between each sensor and the base so reducing the likelihood of detection in a hostile environment.

7. REFERENCES

- [1] D. Lake, "Battlefield acoustic signal processing and target identification," <http://www.galaxy.gmu.edu/stats/colloquia/colljan3098.html>, George Mason Univ. CSI/Stat. Colloq., Jan 1998.

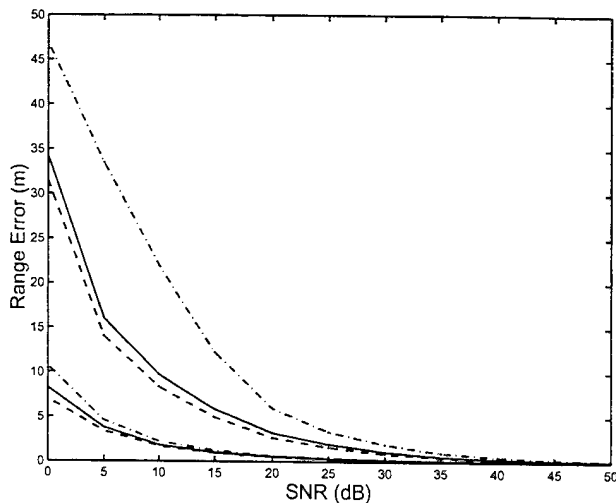


Figure 4: Range estimation performance $MSRE^{1/2}$ for the WLS (solid), RWLS (dashed), and unweighted LS (dash dotted) 3-D position estimators. Upper 3 curves are for battlefield scenario, lower 3 for underwater. The scenario is described in the text.

- [2] D. Lake and D. Keenan, "Maximum likelihood estimation of geodesic subspace trajectories using approximate methods and stochastic optimization," *Proc. 9th IEEE SP Workshop on Stat. Sig. & Array Proc. (SSAP)*, Portland, OR, Sept. 1998, pp. 148–151.
- [3] T. Pham and B. Sadler, "Adaptive wideband aeroacoustic array processing," *Proc. 8th IEEE SP Workshop on Stat. Sig. & Array Proc. (SSAP)*, Corfu, Greece, June 1996, pp. 295–298.
- [4] B.G. Ferguson, "Time-delay estimation techniques applied to the acoustic detection of jet aircraft transits," *J. Acoust. Soc. Am.*, vol. 106, pp. 255–264, July 1999.
- [5] B.G. Ferguson and B.G. Quinn, "Application of the short-time Fourier transform and the Wigner-Ville distribution to the acoustic localization of aircraft," *J. Acoust. Soc. Am.*, vol. 96, pp. 821–827, 1994.
- [6] A. Nehorai and E. Paldi, "Acoustic vector-sensor array processing," *IEEE Trans. on Sig. Proc.*, vol. 42, no. 9, pp. 2481–2491, Sept. 1994. A short version appeared in *Proc. 26th Asilomar Conf. Sig., Syst. & Comput.*, Pacific Grove, CA, Oct. 1992, pp. 192–198.
- [7] M. Hawkes and A. Nehorai, "Acoustic vector-sensor beamforming and Capon direction estimation," *IEEE Trans. Sig. Proc.*, vol. 46, pp. 2291–2304, Sept. 1998.
- [8] M. Hawkes and A. Nehorai, "Effects of sensor placement on acoustic vector-sensor array performance," *IEEE J. Oceanic Eng.*, vol. 24, pp. 33–40, Jan. 1999.
- [9] M. Hawkes and A. Nehorai, "Acoustic vector-sensor processing in the presence of a reflecting boundary," accepted (subject to minor revision) by *IEEE Trans. Sig. Proc.* Preliminary results appeared in "Surface-mounted acoustic vector-sensor array processing," *Proc. Intl Conf. Acoust., Speech & Sig. Proc. (ICASSP96)*, pp. 3170–3173, Atlanta, GA, May 1996.
- [10] G.L. D'Spain and W. S. Hodgkiss, "The simultaneous measurement of infrasonic acoustic particle velocity and acoustic pressure in the ocean by freely drifting swallow floats," *IEEE J. Oceanic Eng.*, vol. 16, pp. 195–207, Apr. 1991.
- [11] J.C. Nickles et al, "A vertical array of directional acoustic sensors," *Proc. Mast. Oceans thru Tech. (Oceans 92)*, Newport, RI, Oct. 1992, pp. 340–345.
- [12] G.L. D'Spain, W. S. Hodgkiss, and G. L. Edmonds, "Energetics of the deep ocean's infrasonic sound field" *J. Acoust. Soc. Am.*, vol. 89, pp. 1134–1158, Mar. 1991.
- [13] G.L. D'Spain et al, "Initial analysis of the data from the vertical DIFAR array," *Proc. Mast. Oceans thru Tech. (Oceans 92)*, Newport, RI, Oct. 1992, pp. 346–351.
- [14] B.A. Cray and R.A. Christman, "Acoustic and vibration performance evaluations of a velocity sensing hull array," in *Acoustic Particle Velocity Sensors: Design, Performance and Applications*, (M. J. Berliner and J. F. Lindberg, Eds.), Woodbury, NY: AIP, 1996, pp. 177–188.
- [15] R.J. Brind and N.J. Goddard, "Beamforming of a V-shaped array of sea-bed geophone sensors," *J. Acoust. Soc. Am.*, vol. 105, no. 2, pt. 2, pp. 1106, Feb. 1999.
- [16] Microflown Technologies, B.V., Netherlands <http://www.microflown.com>.
- [17] H.-E. de Bree, P. Leussink, T. Korthorst, H. Jansen, T. Lamerink, and M. Elwenspoek, "The μ -flown: a novel device for measuring acoustic flows," *Sensors and Actuators A*, vol. 54, pp. 552–557, June 1996.
- [18] F. van der Eerden, H.-E. de Bree, and H. Tijdeman, "Experiments with a new particle velocity sensor in an impedance tube," *Sensors and Actuators A*, vol. 69, pp. 126–133, Aug. 1998.
- [19] P. Stoica, A. Nehorai, and T. Söderström, "Decentralized array processing using the MODE algorithm," *Circ., Syst., & Sig. Proc.*, vol. 14, pp. 17–38, 1995.
- [20] A. Nehorai and E. Paldi, "Vector-sensor array processing for electromagnetic source localization," *IEEE Trans. Sig. Proc.*, vol. 42, pp. 376–398, Feb. 1994.
- [21] A. Nehorai and M. Hawkes, "Performance bounds for estimating vector systems," to appear in *IEEE Trans. Sig. Proc.*, June 2000.
- [22] B. Ottersten, M. Viberg, P. Stoica, and A. Nehorai, "Exact and large sample maximum likelihood techniques for parameter estimation and detection in array processing," in *Radar Array Processing*, (Ed.: S. Haykin, J. Litva, and T.J. Shepherd), Springer-Verlag: Berlin, 1993, pp. 99–151.
- [23] A.D. Pierce, *Acoustics—An Introduction to its Physical Principles and Applications*. New York: McGraw-Hill, 1981.
- [24] L.M. Brekhovskikh, *Waves in Layered Media*, 2nd Ed. New York, NY: Academic Press, 1980.
- [25] B. Hochwald and A. Nehorai, "Identifiability in array processing models with vector-sensor applications," *IEEE Trans. Sig. Proc.*, vol. 44, pp. 83–95, Jan. 1996.
- [26] T.F.W. Embleton, J.E. Piercy, and N. Olsen, "Outdoor sound propagation over ground of finite impedance," *J. Acoust. Soc. Am.*, vol. 59, pp. 267–277, Feb. 1976.
- [27] M. Hawkes and A. Nehorai, "Battlefield target localization using acoustic vector sensors and distributed processing," *Proc. 1999 Meeting of the IRIS Specialty Group on Battlefield Acoustics and Seismics (Invited)*, pp. 111–128, Laurel, MD, Sept. 1999.
- [28] Y. Rokah, "Array processing in the presence of uncertainty," Ph.D. dissertation, Yale University, New Haven, CT, 1986.

SPACE-TIME MATCHED-FIELD DEPTH ESTIMATION WITH ACTIVE SONAR

Granger Hickman and Jeffrey Krolik

Department of Electrical and Computer Engineering
Duke University
Box 90291
Durham, NC 27708
gwh@ee.duke.edu, jk@ee.duke.edu

ABSTRACT

This paper concerns the use of complex multipath propagation for discriminating target depth with a low-frequency active sonar. Although matched-field processing techniques, which exploit full-wave modeling of multipath propagation, have been demonstrated in passive sonar applications, their practical application has been precluded by uncertainty in modeling the complex amplitudes of rays or modes, which is exacerbated in active sonar by the unknown complex back-scattering characteristics of the target. In this paper, a space-time matched-field technique is proposed which avoids the need to model complex ray/mode amplitudes and instead exploits changes in the complex target return seen between consecutive sonar pings at a horizontal array to discriminate target depth. Results with simulated and real data indicate target depth determination to within 10 percent of the ocean bathymetry can be achieved even in a highly range-dependent environment.

1. INTRODUCTION

Despite many experimental demonstrations of range-depth matched-field processing (MFP) for passive sonar, its practical application has largely been precluded by the difficulty of accurately modeling the relative complex amplitudes of modes or rays from a set of hypothesized source locations. In active sonar, uncertainty of the complex target scattering function also contributes to this problem. In this paper, in an extension of an approach to matched-field altitude estimation for OTH radar, a multi-ping method is developed for matched-field depth estimation (MFDE) which avoids the need to model complex ray/mode amplitudes on individual pings and instead models the changes in the coherent, but unresolved, multipath target returns from ping-to-ping [1]. In particular, the pattern of rapid shape changes due to

target motion, which is seen in figure (1) as fading of the complex space-time active return, is strongly dependent on target depth. Using a ray trace multipath propagation model to predict rapid fading, and first-order Markov modeling to handle slow fluctuations due to target aspect changes and medium fluctuations, a maximum likelihood (ML) estimate of target depth is developed here. The ML estimator involves a generalized correlation of space-time data vectors from consecutive sonar pings, where the multipath propagation model is used to compensate for target depth-dependent changes of the return between pings.

2. MODELING MULTIPATH ACTIVE SONAR RETURNS

Consider a horizontal linear hydrophone array receiving returns scattered off a target and surface boundaries in the presence of additive noise. For the k^{th} ping the signal returned to the receiver array may be decomposed into its component bistatic eigenray paths. The l^{th} such component of the sonar return will have a time delay $\tau_{l,k}$ and a Doppler shift $\omega_{l,k}$. Both of these quantities are also functions of target depth, z , and target range, r_k . Given a frequency index n , and Doppler index m , denote the filtered temporal spectrum waveform for the l^{th} component by $f_k(\omega_n - \omega_{l,k})$ and the beamformed complex spatial spectrum waveform by $g_k(\kappa_m - \kappa_{l,k})$. The model for the complex frequency-wavenumber return (in the absence of reverberation) is then

$$\begin{aligned} x[n, m, k] &= e^{j\theta_k} \sum_{m=1}^M s_{l,k} f_k(\omega_n - \omega_{l,k}) g_k(\kappa_m - \kappa_{l,k}) \\ &\quad + \eta[n, m, k] \end{aligned} \quad (1)$$

where $s_{l,k}$ is the complex amplitude weighting of the l^{th} multipath ray, θ_k is the unknown phase path, and $\eta[n, m, k]$ is additive white noise.

Since the target return is concentrated within a small neighborhood in the frequency-wavenumber domain, only

Supported by ONR 321US under Contract N00014-99-1-0080. The authors would like to thank Jim Alsup of SPAWAR-SSC San Diego for his helpful suggestions and for providing the transponder data.

the data in the vicinity of the transmitted signal center frequency and arrival wavenumber is essential. Therefore, the $NM \times 1$ vector \mathbf{x}_k can be used to represent an $N \times M$ block of the complex frequency-wavenumber return in this neighborhood. The data model given by equation (1) can then be written as

$$\mathbf{x}_k = e^{j\theta_k} \mathbf{H}_k \mathbf{s}_k + \mathbf{n}_k \quad (2)$$

where

$$(\mathbf{H}_k)_{nN+m,l} = f_k(\omega_n - \omega_{l,k}) g_k(\kappa_m - \kappa_{l,k}) \quad (3)$$

Equations (1) and (2) neglect reverberation, but reverberation may be included by assuming that the transmitted signal is also scattered to the receiver by uncorrelated patches on the ocean floor with the same time delay as the target. Thus, including reverberation terms yields the data model

$$\mathbf{x}_k = e^{j\theta_k} \mathbf{H}_k \mathbf{s}_k + \sum_{p=1}^P e^{j\theta_{p,k}} \mathbf{H}_{p,k} \mathbf{g}_{p,k} + \mathbf{n}_k \quad (4)$$

The complex multipath ray amplitudes are assumed to be zero mean Gaussian random vectors with diagonal covariance matrices

$$\Lambda_s = E[\mathbf{s}_k \mathbf{s}_k^H] \quad (5)$$

and

$$\Lambda_{gp} = E[\mathbf{g}_{p,k} \mathbf{g}_{p,k}^H] \quad (6)$$

The additive noise is also assumed to be zero mean Gaussian with $NM \times NM$ covariance matrix $\sigma^2 \mathbf{I}_n$. The pdf $p(\mathbf{x}_k|z)$ then describes a zero mean Gaussian random vector with covariance matrix

$$\mathbf{R}_k = \mathbf{H}_k \Lambda_s \mathbf{H}_k^H + \sum_{p=1}^P \mathbf{H}_{p,k} \Lambda_{gp} \mathbf{H}_{p,k}^H + \sigma^2 \mathbf{I}_n \quad (7)$$

The objective is to estimate (from a sequence of pings, \mathbf{x}_k) the depth, z , which appears in equation (4) via \mathbf{H}_k .

3. MAXIMUM LIKELIHOOD DEPTH ESTIMATION WITH MULTIPLE PINGS

To achieve a ML estimate of target depth that uses multiple pings, it is necessary to calculate the joint distribution of the data snapshots conditioned on the target depth. Denote the data snapshots for $K+1$ pings ($k = 0, \dots, K$) by the composite vector \mathbf{X}_K , and likewise denote the collected phase path differences by the vector $\Delta\Theta_K = (\Delta\theta_1, \dots, \Delta\theta_K)$, where $\Delta\theta_k = \theta_k - \theta_{k-1}$. Neglecting aspect dependent target backscatter characteristics, assume the complex multipath ray amplitudes are correlated from one ping to the next, so that $E[\mathbf{s}_k \mathbf{s}_{k-1}^H] = \Lambda_s$. Slow random fluctuations

are handled here by modeling \mathbf{s}_k as a first-order Markov process, in which case the joint pdf can be rewritten as

$$p(\mathbf{X}_K|z, \Delta\Theta_K) = p(\mathbf{x}_0|z) \prod_{k=1}^K p(\mathbf{x}_k|\mathbf{x}_{k-1}, \Delta\theta_k, z). \quad (8)$$

Thus, the joint pdf on \mathbf{X}_K (conditioned by z and $\Delta\Theta_K$) can be expressed as a product of terms, each of which describes the change in the received signal from the $k-1^{st}$ ping to the k^{th} .

An ML estimate of the target depth can now be calculated by maximizing $p(\mathbf{X}_K|z, \Delta\Theta_K)$ over $\Delta\Theta_K$ and z . Since consecutive multipath amplitudes \mathbf{s}_{k-1} and \mathbf{s}_k are both zero-mean Gaussian and jointly Gaussian, it then follows that $p(\mathbf{x}_k|\mathbf{x}_{k-1}, \Delta\theta_k, z)$ is also Gaussian with mean and covariance defined as

$$\begin{aligned} \mathbf{m}_k &= \mathbf{T}_k \mathbf{R}_{k-1}^{-1} \mathbf{x}_{k-1} \\ \mathbf{Q}_k &= \mathbf{R}_k - \mathbf{T}_k \mathbf{R}_{k-1}^{-1} \mathbf{T}_k^H \end{aligned} \quad (9)$$

where $\mathbf{T}_k = \mathbf{H}_k \Lambda_s \mathbf{H}_{k-1}^H e^{j\Delta\theta_k}$ [2]. Maximization of the log-likelihood in equation (8) over $\Delta\Theta_K$ yields

$$L(z) = \log p(\mathbf{x}_0|z) + \sum_{k=1}^K L_k(z) \quad (10)$$

where $L_k(z) = \max_{\Delta\theta_k} \log p(\mathbf{x}_k|\mathbf{x}_{k-1}, z, \Delta\theta_k)$, which, from equation (9), can be written

$$\begin{aligned} L_k(z) &= -\log \pi^N |\mathbf{Q}_k| - \mathbf{x}_k^H \mathbf{Q}_k^{-1} \mathbf{x}_k \\ &\quad + 2 \max_{\Delta\theta_k} (e^{j\Delta\theta_k} \mathbf{x}_k^H \mathbf{Q}_k^{-1} \mathbf{P}_k \mathbf{x}_{k-1}) \\ &\quad - \mathbf{x}_{k-1}^H \mathbf{P}_k^H \mathbf{Q}_k^{-1} \mathbf{P}_k \mathbf{x}_{k-1} \end{aligned}$$

where $\mathbf{P}_k = \mathbf{T}_k \mathbf{R}_{k-1}^{-1}$. The maximization in this expression can be performed explicitly by requiring the phasor $e^{j\Delta\theta_k}$ to rotate the complex quantity $\mathbf{x}_k^H \mathbf{Q}_k^{-1} \mathbf{P}_k \mathbf{x}_{k-1}$ into a positive, real quantity. Therefore, log-likelihood term can be written as

$$\begin{aligned} L_k(z) &= -\log \pi^N |\mathbf{Q}_k| - \mathbf{x}_k^H \mathbf{Q}_k^{-1} \mathbf{x}_k \\ &\quad + 2|\mathbf{x}_k^H \mathbf{Q}_k^{-1} \mathbf{P}_k \mathbf{x}_{k-1}| - \mathbf{x}_{k-1}^H \mathbf{P}_k^H \mathbf{Q}_k^{-1} \mathbf{P}_k \mathbf{x}_{k-1} \end{aligned} \quad (11)$$

The ML estimate of target depth can be calculated by a one-dimensional numerical maximization of the cumulative sum in equation (10) with respect to the depth, z .

One final adjustment to the estimator is necessary: for each hypothesized depth, each matrix \mathbf{H}_k must be normalized by $\sum_{k=1}^K \mathbf{H}_k \Lambda_s \mathbf{H}_k^H$ to insure that the hypothesized total energy scattered to the receiver from the target is a constant function of depth.

4. SIMULATION AND REAL DATA RESULTS

In order to evaluate the performance of the ML depth estimation approach presented here, histograms of the depth estimates are computed over 100 Monte Carlo runs as a function of SNR and target depth. The environment, summarized in figure (2), was from the Bravo run of the Shallow Water Active Classification sea trial number 3 (SWAC-3), a NATO event conducted in November 1995 near the Mediterranean coast of Spain. The received signal was from a transponder on a moving underwater platform, and the receiver array had 144 phones. The signal waveform was a linear FM pulse sweeping from 395 Hz to 400 Hz with a rectangular envelope of duration 0.5 s. The repetition rate of the pings was 60 s. The underwater platform moved at a depth of 50 m.

Figure (3) shows histograms for a simulated platform moving at a depth of 50 m. Three different SNR were used (10, 15, and 20 dB). At all SNR shown, the depth estimate is within 10 meters of the true depth, with a modest bias which decreases as the SNR increases. Figure (4) shows histograms for a target at a depth of 20 m (for SNR 20, 25, and 30 dB). For this depth, the distribution of the estimates shows two peaks — one peak at the correct depth of 20 meters, and a second peak at 26 meters. As the SNR increases, the peak at 20 meters increases in height and the peak at 26 meters decreases in height. There is a clear depth-dependence shown in the histograms of figures (3) and (4). In particular, the ML depth estimator seems to perform worse at shallower depths, requiring higher SNR to get commensurate performance. Reference to figure (2) indicates a possible reason for the observed difference in performance. A target at a depth of 20 meters traps energy in the surface duct, while a target at a depth of 50 meters does not. Since the receiver array is below the surface duct (at a depth of 70 meters), much deeper fading is witnessed when the target is in the surface duct. Furthermore, the overall SNR is defined to be numerically equal to the SNR of the strongest ping obtained in the sequence of pings observed. Therefore, the overall target strength (seen at the receiver) for a fixed SNR is not constant with depth, leading to a change in estimator performance as the depth is changed.

Figure (5) illustrates a simulation of the log-likelihood surface described by equation (10) evolving over sixteen pings for a depth of 50 m. Clearly, a single ping is not sufficient to estimate the depth, but after five pings the ML depth estimate converges to within two meters of the correct depth. Furthermore, as the log-likelihood surface accumulates in time, the ambiguity of the peak in the depth dimension decreases, which is indicative of improvement in the estimate.

Figure (6) shows the time evolving log-likelihood surface for real transponder data from the SWAC-3 experiment.

The transponder moved monotonically from 14 km to 17 km in range relative to the receiver in 16 minutes, and moved from about 18 degrees to 15 degrees (relative to the receiver array's broad side) in the same time. The transponder depth was 50 m, and additional uncorrelated noise was added to the real data to achieve an SNR of 30 dB. Notice that the ML depth estimate requires six pings to converge to within one meter of the true depth. The ambiguities persist longer than in the simulation, even though the SNR is higher. This may be due to unresolved mismatch issues in the current model, but this real-data result serves as validation of the ML estimation technique described in this paper.

5. CONCLUSIONS

In this paper, a space-time matched-field maximum log-likelihood estimate of target depth for active sonar was developed for multiple sonar pings. Through simulation it was shown that, for the SWAC-3 environmental parameters and a SNR of 20 dB, a depth estimate within 10 meters could be achieved after relatively few sonar pings. Furthermore, the ML depth estimator was successfully applied to real transponder data gathered in the SWAC3 experiment, which is a positive indication for the validity of the approach.

6. REFERENCES

- [1] M. Papazoglou and J. Krolik, "Matched-field estimation of aircraft altitude from multiple over-the-horizon radar revisits," *IEEE Trans. on Signal Processing*, vol. 47, no. 4, Apr. 1999, pp 966-976.
- [2] C. W. Therrien, *Discrete Random Signals and Statistical Signal Processing*, Prentice-Hall, Englewood Cliffs, NJ, 1992, pp 43-44.
- [3] J. P. Hermand and W. I. Roderick, "Acoustic mode-based matched-filter processing for fading time-dispersive ocean channels: Theory and experiment," *J. Acoustical Soc. of Amer.*, vol. 94, no. 4, Oct. 1993, pp 445-64.
- [4] T. C. Yang and T. W. Yates, "Scattering from an object in a stratified medium II: Extraction of scattering signature," *J. Acoustical Soc. of Amer.*, vol. 96, no. 2, pt. 1, Aug. 1994, pp 1020-31.
- [5] H. Bucker, "Active matched-field tracking," *J. Acoustical Soc. of Amer.*, vol. 99, no. 3, Mar. 1996, pp 1783-4.

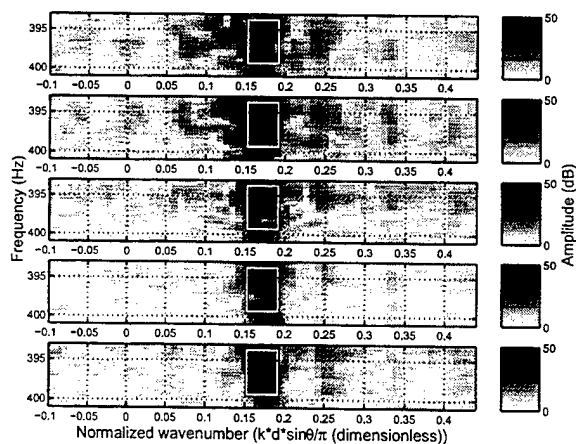


Figure 1: Frequency-wavenumber log-amplitude plots for five transponder pings from the SWAC-3 data set. Notice the rapid changes in the shape of the complex envelope as the transponder moves about 800 m in 200 m steps.

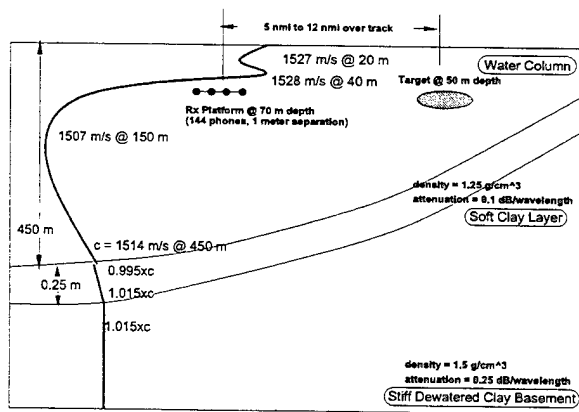


Figure 2: SWAC-3 Run Bravo Scenario and Environment

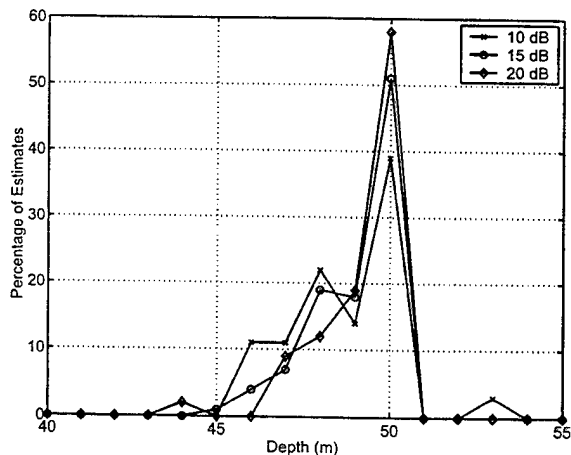


Figure 3: Histogram approximation of the depth estimate for SNR of 10, 15, and 20 dB. 100 random realizations were used in each case. The true depth of the target was 50 m.

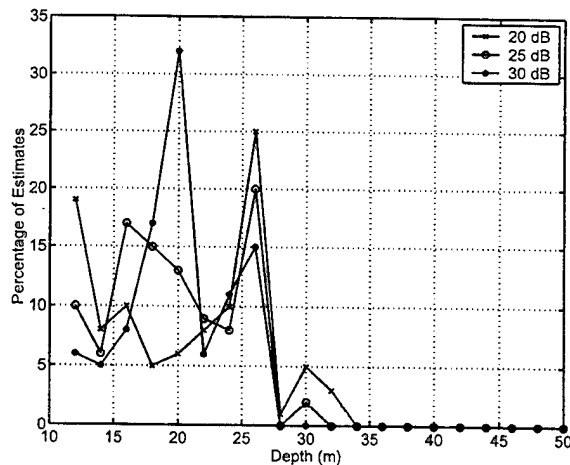


Figure 4: Histogram approximation of the depth estimate for SNR of 20, 25, and 30 dB. 100 random realizations were used in each case. The true depth of the target was 20 m.

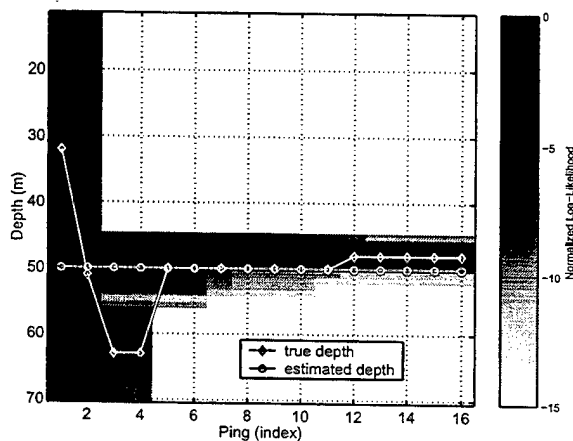


Figure 5: Simulated log-likelihood surface evolving over 16 pings. The true depth is 50 m, and the estimated depth is 48 m after 16 pings. The SNR is 20 dB.

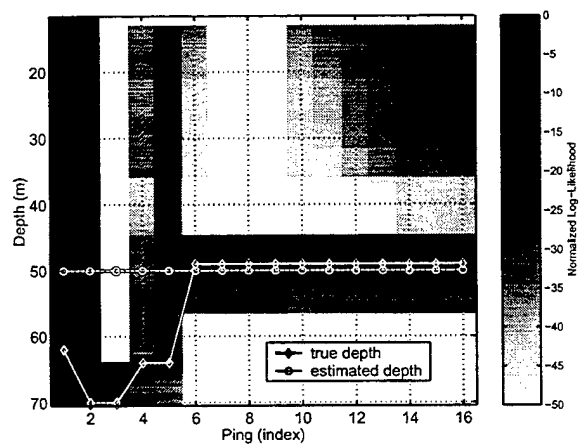


Figure 6: Real data log-likelihood surface evolving over 16 ping. The true depth of the transponder is 50 m, and the estimated depth is 49 m after 16 pings. The SNR is 30 dB.

Adaptive Matched Field Processing for a Moving Target in a Noisy Shallow Water Channel

Lisa M Zurk, Nigel Lee, James Ward, and Andrew Gronosky*

MIT Lincoln Laboratory

244 Wood St.

Lexington, MA, 02420 USA

ABSTRACT

In this paper we apply Adaptive Matched Field Processing (AMFP) algorithms to passively detect and localize a submerged source in a shallow water environment in the presence of loud surface ship interference. To achieve this goal, the capability of AMFP is extended by applying a source motion compensation algorithm and a time-varying spatial filter that is used to remove the signature of a moving surface ship. Construction of the spatial filter is achieved using three alternate methods that utilize either prior knowledge of the ship's position or a data estimation, or both. We present results from the data obtained during the Santa Barbara Channel Experiment (SBCX) that show the increase in SINR that is achieved for a towed submerged source in the presence of shipping noise with the application of these techniques.

1. INTRODUCTION

Passive detection and localization of acoustic sources in shallow water channels is complicated by channel-specific multipath propagation. One method of addressing this situation is to incorporate knowledge of the propagation physics into the signal processing. Adaptive Matched Field Processing (AMFP) utilizes the output of a propagation model to form the steering vectors and applies adaptivity to mitigate the high sidelobes present in a conventional processor and to reject interference [1]. One limitation to this approach is the degradation due to the motion of the target and interferers, which violates the assumption of stationarity present in the covariance estimation. The presence of target motion during the observation period leads to smearing of the AMFP peak and loss of signal energy. Movement of the interferer during the observation period will spread the signature of the interferer across the eigenvector spectrum of the covariance matrix, and will consume adaptive degrees of freedom (DOF) potentially preventing adequate nulling of surface interference. Finally, large arrays typically require increased observation intervals, and during these intervals appreciable motion can occur. In addition, the motion is greater relative to the fine localization peaks supplied by large apertures, and this results in the most severe motion effects.

In this paper we present techniques which can limit the losses from both target and interference motion. We begin by describing an AMFP architecture and the SBCX data set. We then review a motion compensation algorithm [2] that mitigates the degradation due to target motion. In Section 3, we describe a time-varying spatial filter that is applied to remove moving interferers.

2. ADAPTIVE MATCHED FIELD PROCESSING (AMFP)

Adaptive Matched Field Processing (AMFP) incorporates knowledge of the propagation physics directly into the signal processing by employing a propagation model to construct the steering vectors (also called replica vectors) [1]. With appropriate environmental knowledge and a sufficiently rigorous propagation model, one can achieve extremely fine localization accuracy by exploiting the richness of the multipath. For the results in this paper, we use the KRAKEN normal mode program [3] with an adiabatic assumption to derive range dependent replica vectors. Defining $\Theta = (r, \phi, z)$ to denote the three-dimensional spatial position in range, azimuth and depth, the beamformer output steered to the direction Θ can be

written as $P(\Theta) = w(\Theta)^H \hat{K} w(\Theta)$ where $w(\Theta)$ is the $N \times 1$ weight vector, \hat{K} is the $N \times N$ sample covariance matrix formed from averaging L snapshots of data

$$\hat{K} = \frac{1}{L} \sum_l x_l x_l^H$$

and x_l is the pressure field observed across an N hydrophone array at time t_l .

For a conventional processor, the weights are normalized replica vectors. Adaptive processing computes the weight vector that is dependent on the sample covariance matrix as well as the replica vector. For the AMFP results in this paper we will use the Minimum Variance Distortionless Response with diagonal loading (MVDR-DL) [4].

* This work was sponsored by DARPA under Air Force Contract F19628-95-C0002. Opinions, interpretations, conclusions and recommendations are those of the author and are not necessarily endorsed by the United States Air Force.

3. SANTA BARBARA CHANNEL EXPERIMENT (SBCX)

The SBCX experiment was conducted in April 1998 in the 200-m deep littoral waters of the Santa Barbara Channel. One of the passive acoustic sensors deployed during the experiment was a 150-hydrophone volumetric array called the FFP array. For the results in this paper, we will use one of the five 30-phone VLAs that comprised the FFP array. The VLAs were instrumented for element localization.

One of the acoustic sources deployed during SBCX was a J15-3 transducer that was towed by a research vessel, the Acoustic Explorer (AX). It was used to generate a comb sequence of 12 tones at approximately 159 dB re 1 μ Pa source level. All the results shown in this paper are from the comb sequence recorded on the FFP array during the X2 exercise on April 11. The AX had an on-board GPS receiver for position information and a radar station was utilized to produce track information for surface vessels in the SBCX area.

4. TARGET MOTION COMPENSATION

The adaptive algorithm makes an implicit assumption that the environment is stationary during the observation period, and hence, assumes that neither the target (submarine) nor the interference (surface ships) are moving. In this section we consider the effect of the first assumption and briefly discuss a method of source motion compensation to address it. In the next section we examine the effects of interference motion and present a method to address it.

The change in target position over the observation time results in a spread of the AMFP peak and a corresponding loss of signal energy. This spread can be prevented by adjusting the amplitude and phase across each data snapshot so that the target appears stationary. The adjustment is determined by applying a propagation model to a velocity hypothesis for the target. The resulting covariance matrix contains the signature of a target that has been "focused" to a stationary position at a chosen point; in this paper we use the position of the target at the middle of the observation period as the focus point. A by-product of the motion compensation is that sources moving along other tracks are de-focused. Details of the motion compensation algorithm are given in [2].

5. TIME-VARYING SPATIAL INTERFERENCE FILTER

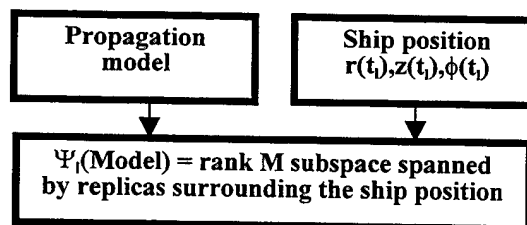
The primary source of low frequency noise (interference) is from loud merchant ships that are prevalent in the coastal regions. The strong signals from these ships can leak through the sidelobes of the adaptive processor and obscure the target peak. Typically, these ships have appreciable movement during the observation interval, and this spreads their signatures across the eigenvector spectrum. The result is that the moving interferer consumes adaptive DOF and thus the ability to null strong interferers is limited. The number of adaptive DOF

consumed by a moving interferer is roughly equivalent to the number of resolution cells the interferer transits during the observation time. Spatial resolution for MFP is determined by the mode spread of the underwater channel, and is about 10λ in range for SBCX.

One method of removing the interference is to explicitly filter the data by projecting to a sub-space that is orthogonal to the interference subspace. However, because the interference is moving, the rank of its subspace over the entire observation interval can be quite large and the corresponding signal space will be limited. We propose to increase the signal subspace by applying a time-varying spatial filter for each data snapshot that only removes the subspace for the interferer position at that time. The spatial filter is constructed from the null space of the interference subspace Ψ . In [5] we proposed a model-based method of interference removal. In this paper, we extend the investigation by considering three methods of estimating Ψ : model-based, data-based, and a hybrid method. For each data snapshot, the spatial interference filter is applied first, followed by the target motion compensation. The resulting filtered and compensated snapshot is then used as in (1) to estimate the data covariance matrix.

In the following subsections we describe the three methods of estimating the interference subspace.

5.1 Model-based filter



The model-based method constructs a filter assuming some prior knowledge of the ship's position is available. An example might be the tracking of a merchant ship by an airborne asset in the region. In order to estimate the interference subspace, we utilize a propagation model to determine the acoustic signature from an interference source at the given position. To protect against inaccuracies in the ship position, we compute the interference subspace spanning a region in space centered at the instantaneous position of the ship with some range and depth padding. The amount of padding necessary is determined by the accuracy of the prior knowledge. The padding will also increase the size of the interference subspace.

Even with this protection in place, the model-based method is sensitive to inaccuracies in both the ship position information and the propagation model

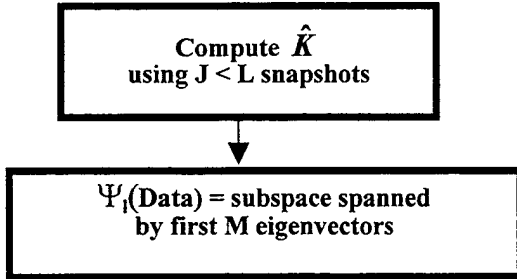
5.2 Data-based Filter

The data-based method constructs a filter by exploiting the fact that the interference is strong and can thus be estimated with a small number of snapshots J , which is less than the total number of snapshots L . At each time t_i ,

the interference subspace is computed by calculating a covariance matrix with J snapshots centered on the l th snapshot

$$\hat{K} = \sum_{j=l-\frac{J}{2}}^{l+\frac{J}{2}} x_j x_j^H$$

The M dominant eigenvectors of this covariance matrix are then used as an estimate for Ψ .



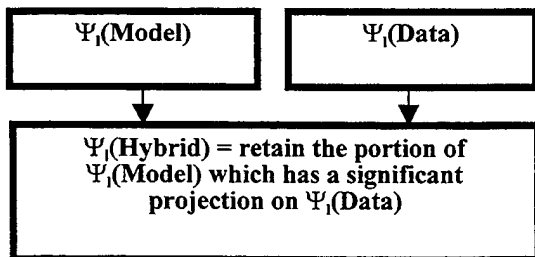
The data-based method has the advantage that it does not depend on the accuracy of spatial knowledge or a propagation model. However, surface ships that are moving rapidly can still occupy several eigenvectors over even a few snapshots. Furthermore, the target signature, particularly if it is strong, can be erroneously included in the interference subspace and filtered out.

5.3 Hybrid Filter

The hybrid method attempts to combine the robustness of the data-based approach with the use of prior knowledge so that the eigenvectors pertaining to the interference and the target can be distinguished. To accomplish this, the replica vectors v_m , $m=1,2,\dots,M$ that span the ship position (section 5.1) are projected onto the subspace obtained by data estimation (section 5.2). The interference subspace is then made up of those replica vectors with significant projection onto the data:

$$v_m^H \Psi_l(\text{Data}) \geq \gamma$$

where γ as an adjustable parameter representing the minimum acceptable projection.



6. RESULTS

In this section we present results from the SBCX showing the improvement obtained from applying interference rejection and target motion compensation. Our results are derived from a 200 sec section of data in which the Acoustics Explorer (AX) was approximately 5.5 kilometers from the FFP array while a merchant ship was operating in the Eastbound shipping lane, as shown in Fig. 1. At the hydrophone level, there is a significant amount of noise from the surface ship in the lower frequencies (up to ~125 Hz) which masks the presence of the tones from the AX comb sequence.

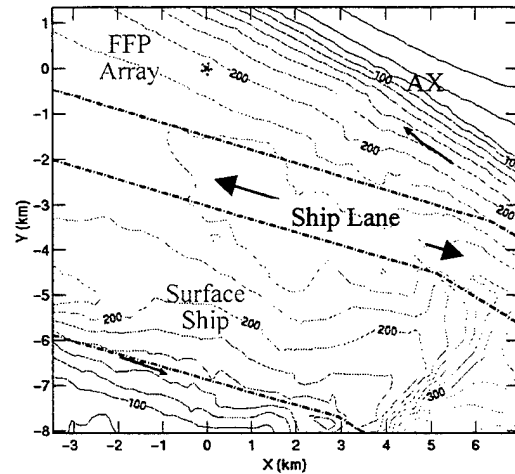


Fig. 1: Site plot showing the bathymetry contours in the region of the FFP array along with the track of the Acoustic Explorer and the track of the merchant ship.

As discussed in Section 5, the temporally varying position of the ship will cause a spread of the ship's energy across the eigenvector spectrum and a portion of this energy can bleed through the sidelobes of the adaptive processor and obscure target detection. This is the case in the top-right ambiguity surface in Fig. 2, which has been calculated for the 94 Hz tone in the region of the range and at the azimuth of the Acoustic Explorer (AX). There is poor azimuthal discrimination for a single VLA (half power beamwidths are about 65 degrees) because the horizontal aperture is solely due to the 14-degree tilt of the VLA. This allows a large amount of energy from the interference to bleed through the sidelobes of the AMFP obscuring the peak of the AX. As seen in the plot, the towed source is not visible.

The plot in Fig. 2b shows the same data but with the addition of target motion compensation. The motion compensation serves to accumulate the source energy at the focus position (5.4 km) while simultaneously de-focusing any other sources moving with a different track, such as the surface ship. However, this "de-focused" ship

energy appears as a higher background noise level and in turn decreases the SINR.

The interference filtering described in Section 5 explicitly removes the energy from the moving interferer and thus prevents its effect on the sidelobes of the adaptive processor. The results of applying a time-varying spatial filter are shown in Fig. 2c-e. The plot in 2c shows the result when a model-based filter (rank 7) is applied. For the SBCX data set, the merchant ship position was accurately determined by measurements from a radar station, and the shallow water channel was well characterized. Because of the accurate prior knowledge, the model-based filtering successfully removed the energy from the surface ship with a resultant SINR of 11.2 dB

The plots in Fig. 2d-e show the result when a data-based filter is applied. Fig 2d was obtained by removing only the largest eigenvector (rank 1 subspace) estimated from $J=7$ snapshots. In Fig 2e the top two eigenvectors (rank 2) are removed. In neither case is the interference energy completely removed, as seen from the high background noise levels. This is because the rank of the estimated interference subspace is not large enough. However, as the size of the subspace is increased, the filtering begins to remove the target energy, as seen in Fig. 2e. The data-based filtering only gives information on the strength of the sources, so if the target is fairly strong it can be misinterpreted as a interferer and removed.

The final plot in Fig. 2f is the result of hybrid filtering. The result is very similar to that in Fig 2c, indicating most of the replica vectors in the model were a good representation of the observed data.

7. CONCLUSIONS

In this paper we have addressed the effects of target and interference motion on the performance of an Adaptive Matched Field Processor (AMFP). We have presented a technique for explicitly removing the energy from a moving interference source by applying a time-varying spatial filter derived from prior knowledge. We have presented results from the SBCX that show the increased SINR obtained when the interference filter is applied in conjunction with a motion compensation algorithm [2].

We have presented three types of filtering which rely upon both model- and data-based estimation. The results shown here are indicative of the scenario where the ship track and channel are well-known, in which case the model-based filtering is successful. Conversely, for the strong signal case the data-based technique can remove target energy. We should note that we have processed data where the target energy was significantly weaker. In this case, a rank 2 data-based rejection performed very well. Further investigation is needed to ascertain the sensitivity of these techniques to errors in the propagation model, environmental knowledge, or spatial resolution of the prior knowledge.

8. REFERENCES

- [1] A.B. Baggeroer, W.A. Kuperman, and P.N. Mikhalevsky, An Overview of Matched Field Methods in Ocean Acoustics, *IEEE J. of Oceanic Engineering*, vol. 18, pp 401-424, 1993
- [2] L.M. Zurk, N. Lee, and J. Ward, 3D Adaptive Matched Field Processing for a Moving Source in a Shallow Water Channel, *IEEE Oceans '99*, Seattle, WA, Sept. 1999
- [3] M.B. Porter, The KRAKEN normal mode program, *Rep. SM-245* (SACLANT Undersea Research Center, La Spezia, Italy, 1991)
- [4] J. Capon, High resolution frequency wavenumber spectrum analysis, *Proc. of the IEEE*, vol. 57, pp1408-1418, 1969
- [5] A. B. Baggeroer and H. Cox, Passive Sonar Limits Upon Nulling Multiple Moving Ships with Large Aperture Arrays, *33rd Asilomar Conference on Signals, Systems & Computers*, Pacific Grove, CA, Nov. 1999
- [5] L. M. Zurk N. Lee, and J. Ward, Interference Rejection for Passive Sonar using Prior Information with Adaptive Matched Field Processing, *5th European Conference on Underwater Acoustics*, Lyon, France, July 2000

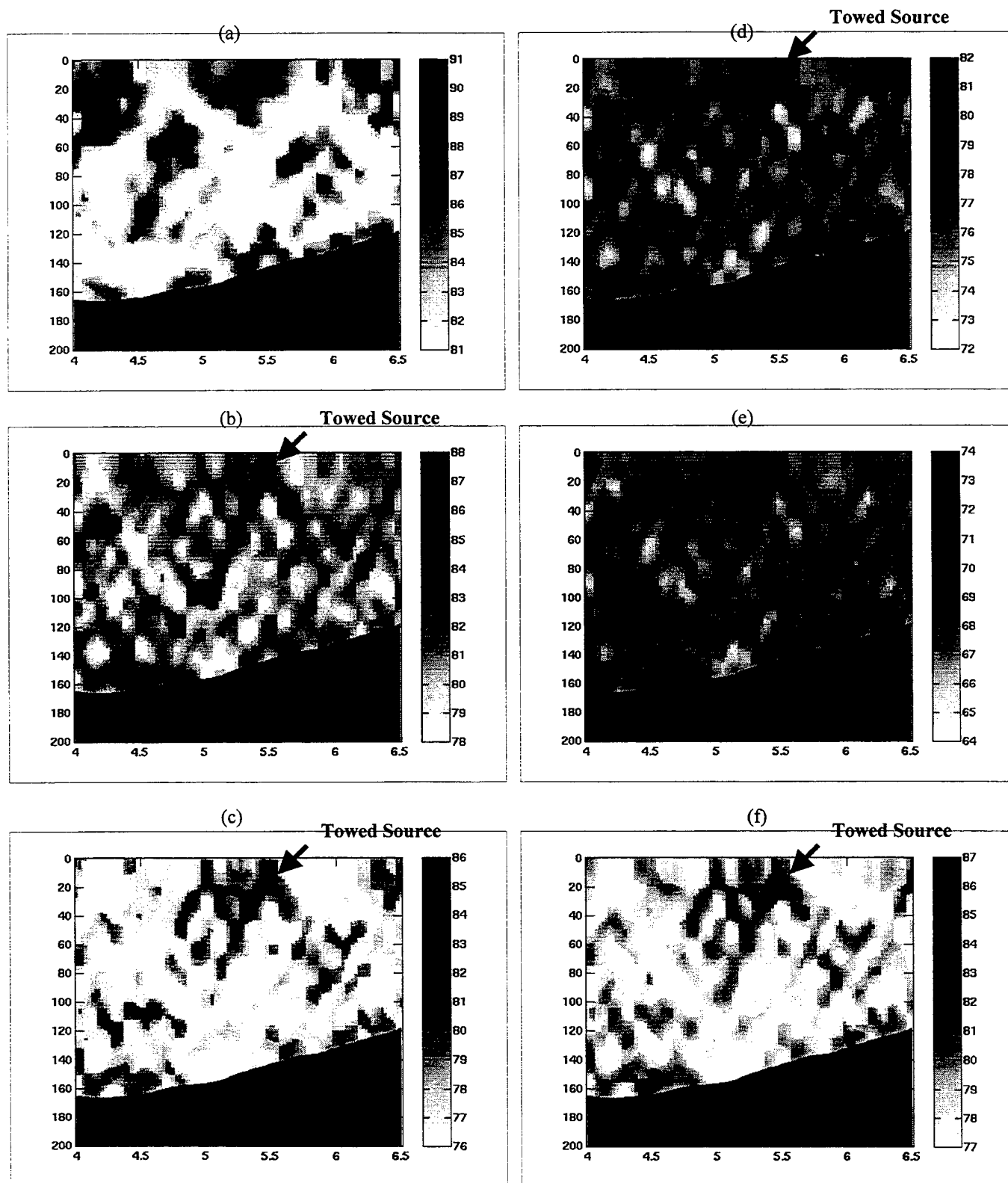


Fig. 2. Ambiguity surfaces calculated for the 94 Hz tone (SL=159 dB) at the bearing angle of the Acoustic Explorer (109 deg). Position of towed source is 5.0-5.75 km in range and 30 m in depth. All surfaces are output of MVDR with diagonal loading. Panels are as follows. a) AMFP surface with no target motion compensation or ship filtering. b) AMFP with target motion compensation; SNR=7.5 dB. c) AMFP with model-based ship filtering (rank 7) and target motion compensation; SNR=11.2 dB. d) AMFP with data-based ship filtering (rank 1) and target motion compensation; SNR=6.3 dB. e) AMFP with data-based ship filtering (rank 2) and motion compensation; SNR=5.4 dB. f) AMFP with hybrid ship filtering ($\gamma=0.6$) and target motion compensation; SNR=10.8 dB.

ADAPTIVE SELF-NOISE SUPPRESSION FOR PASSIVE SONAR TOWED ARRAYS

Vincent E. Premus*

MIT Lincoln Laboratory
244 Wood Street, Lexington, MA 02420
vpremus@ll.mit.edu

ABSTRACT

Non-acoustic self-noise observed on passive sonar towed arrays can impose serious limitations on the detection and discrimination of acoustic signatures in the very low frequency (VLF) acoustic band. Non-acoustic self-noise consists of mechanically induced vibrations, or cable strum, associated with vortex shedding in hydrodynamic flow. This interference tends to dominate the dynamic range of the lofargram display used by the sonar analyst to classify signatures. A beamspace adaptive sidelobe canceller architecture for the coherent cancellation of non-acoustic self-noise is presented. The approach is based on the recognition that most vibrational modes of the array propagate at a phase speed substantially less than that of acoustic signals in the water column. This permits the formation of an adaptive interference reference beam steered to non-acoustic wavenumber space. The phenomenology underlying the self-noise is discussed and characterized using k - ω analysis. Adaptive cancellation results will be presented for several hours of passive sonar towed array data.

1. INTRODUCTION

Towed array self-noise can impose severe limitations on passive sonar target detection at very low frequencies. Self-noise is generally associated with mechanical vibrations induced by hydrodynamic flow over the array elements, or hydrophones, as the array is towed through the medium [1]. The vibrations propagate as transverse and longitudinal modes in the array body, much like a vibrating string with fixed boundary conditions. The vibrations produce local accelerations at each hydrophone pressure head. The acoustic response induced by this phenomenon can be several orders of magnitude stronger than that of acoustic signals propagating through the water column, dominating the

lofargram displays used by sonar analysts to identify contacts.

Mechanical self-noise suppression techniques such as vibration isolation and cable fairing are capable of attenuating the propagation of vibrations in the array body. Signal processing techniques such as noise spectrum equalization are also employed to provide some dynamic range compression at the display level. However, this approach is an incoherent technique, i.e. ignores phase, and thus comes at some cost to signal of interest (SOI) detectability. In this paper, a technique is presented which exploits phase and the propagation physics underlying array-borne mechanical vibrations to spatially reject this form of broadband interference.

2. CHARACTERIZATION OF TOWED ARRAY SELF-NOISE

2.1 Self-noise mechanisms

There are three principal mechanisms responsible for the generation of non-acoustic self-noise in towed arrays: flow noise, own-ship machinery, and vortex shedding. Flow noise is spatially isotropic with a spatial correlation length that is very small compared with sensor spacing. Linear beamforming is very effective at rejecting noise of this type. Vibrations associated with own-ship machinery represent a source of non-acoustic noise that couples directly to the tow cable and the hydrophone array. Most towed arrays are designed with vibration isolation that attenuates such vibrations before they propagate to the hydrophones. The third mechanism, vortex shedding, results from the shedding of vortices induced by hydrodynamic flow normal to the array axis. Hydrophone outputs can be dominated by the local accelerations resulting from transverse vibrations excited by vortex shedding. Such vibrations propagate within the array body at phase speeds substantially lower than that of acoustic signals in the water column, generally in the range 15 m/s to 1500 m/s. This physical property forms

Sponsored in part by PEO-USW ASTO, under Air Force Contract F19628-95-C-0002. Opinions, interpretations, conclusions, and recommendations are those of the author and are not necessarily endorsed by the U.S. Air Force.

the basis for the adaptive self-noise cancellation architecture described in this work.

2.2 Vortex shedding

When an array is subject to hydrodynamic flow with a component normal to its axis, a wake is formed. When the velocity of the flow increases beyond a certain threshold, eddies, or vortices, begin to form and separate from the wake. Eventually these vortices shed from the wake in an asymmetric fashion. This asymmetric shedding imparts an oscillatory lift force locally on the array which, depending on the properties of the array such as tension and density, can excite transverse vibrations which propagate along the array axis. The frequency of vortex shedding in hydrodynamic flow is related to properties of the flow and the array via the empirically determined Strouhal relation [2]:

$$f_s = \frac{Sv}{d},$$

where S is the Strouhal number, equal to 0.21 in the laminar flow regime characteristic of most towed array environments, v is the velocity of flow normal to the array axis, and d is the cable diameter. Note that the normal component of velocity of flow can vary with time in response to platform motion and local inhomogeneities in the turbulent medium.

The transfer function to which the Strouhal excitation is applied is governed by the wave equation subject to the boundary conditions of the array under tow. For example, assuming fixed boundary conditions for the array, the preferred frequencies of vibration or modes of the array corresponding to the solution of the wave equation is given by:

$$f_n = \frac{n}{2L} \sqrt{\frac{T}{m_c}},$$

where T is cable tension, m_c is mass per unit length of the cable, and L is the cable length. Figure 1 depicts notionally the interaction of the Strouhal excitation with the structural modes of the array. Cable strum due to vortex shedding is strongly excited when the Strouhal excitation frequency is closely aligned with a resonant mode of the cable transfer function.

2.3 Wavenumber-frequency analysis

The decomposition of an array snapshot into its constituent acoustic and non-acoustic components is

accomplished using a wavenumber-frequency, or k - ω , transform. The k - ω transform is a 2-d FFT in space and time. Maximum unambiguous wavenumber resolvable is equal to π/d , where d is the sensor spacing. Resolution in wavenumber is governed by the aperture length, L . For non-dispersive propagation, frequency and wavenumber are linearly related via

$$k(f) = \frac{2\pi f}{c_p},$$

where c_p equals the phase speed of the wavefront.

Figures 2 and 3 depict k - ω plots for the two towed arrays that form the basis for this study. The arrays differ in a number of ways including aperture length, number of hydrophones, spatial sampling interval, cross-section, and the degree of mechanical vibration isolation employed. The k - ω plot associated with the first array exhibits much superior resolution relative to that of the second, due to its greater length and number and density of hydrophones. In each figure, the water-borne acoustic cone is delineated by the innermost pair of black lines. These lines intersect at coordinates (k, ω) equal to $(0, 0)$. For non-dispersive propagation, wavenumber and frequency are linearly related via the phase speed of the wavefront. Thus, signals propagating in the water column at or near 1478 m/s, the nominal speed of sound in water, are constrained to lie along lines within the water-borne acoustic cone. Higher wavenumber modes associated with vibrations, or non-acoustic signals, propagating at lower phase speeds fall outside the acoustic cone.

Figure 2 clearly depicts two discrete vibrational modes with phase speeds of 15 m/s and 700 m/s, respectively, occurring in the long aperture array at the onset of a turn. Observe that there is good separation between these modes and the acoustic cone. There is some sidelobe penetration into the acoustic cone of energy from these modes, but it is relatively weak. Figure 3, on the other hand, depicts a much different situation for the short aperture array. A vibrational mode is observed to reside just outside the acoustic cone, at a phase speed of approximately 1000 m/s. The poor separation means significant mainlobe leakage of the non-acoustic interference into forward endfire, in addition to the usual sidelobe leakage which typically penetrates all of bearing space. Mainlobe and sidelobe leakage of mechanical vibrations into the water-borne acoustic cone is the principal mechanism whereby non-acoustic noise impacts noise levels in beamformed towed array data.

3. ADAPTIVE CANCELLATION ARCHITECTURE

3.1 Reference isolation

The adaptive approach adopted in this work is based on a time-domain adaptive sidelobe canceller, first proposed in the mid-1960's by Widrow [3]. A block diagram of the algorithm is shown in Figure 4. The key to this approach presented herein lies in the formation of the interference reference. Recognizing from the k - ω analysis that the mechanical vibrations propagate at sub-acoustic phase speeds, it is clear that a signal-free interference reference is available by steering a beam into non-acoustic k - ω space. The k - ω plot in the block diagram of Figure 4 illustrates the placement of a candidate reference beam for the short aperture array.

3.2 LMS Tapped Delay Line Filter

The adaptive filter implementation consists of a tapped delay line with filter weights updated via least-mean-square (LMS) algorithm. The number of delay line taps is a function of the interference bandwidth and the sample rate of the time series. The adaptivity coefficient, μ , is inversely related to the sum of the power in the filter taps. For this problem, these parameters were empirically tuned to yield a misadjustment level, or ratio of excess mean-squared-error to minimum mean-squared-error, of 0.05, and a convergence time of approximately 2 minutes.

3.3 Robustness to signal self-cancellation

In the formation of an interference reference, the potential for signal of interest to contaminate the reference channel is clearly of concern. In the case of a reference beam steered to non-acoustic space, this potential can be quantified by considering the phase speed dependence of the array beampattern. Figure 5 depicts a plot of the beampattern versus phase speed for a frequency within the bandwidth of the cable strum interference. At this frequency, acoustic signals propagating at 1478 m/s in the water column will contribute to the non-acoustic reference via the first sidelobe at -13 dB. This level of rejection is generally sufficient to prevent SOI cancellation of most quiet targets.

4. TOWED ARRAY DATA RESULTS

Figure 6(a) shows a plot of the coherence between primary and reference channels for an 8 minute snapshot of data from the short aperture array. The coherence is defined as the normalized cross-spectrum, or

$$C_{xy}(f) = \frac{P_{xy}(f)}{|P_{xx}(f)|^{1/2} |P_{yy}(f)|^{1/2}}.$$

For interference cancellation to be supported, there must be significant coherence between the interference as sampled by the reference channel and the manifestation of the interference in the primary, in this case the forward endfire acoustic beam. From Figure 6(a) it is seen that coherence is nearly perfect over the bandwidth of the cable strum, 0 to $f_s/4$. An additional measure of expected cancellation performance is represented by the cancellation ratio, CR, which is a function of the coherence spectrum given by,

$$CR(f) = \frac{1}{1 - |C_{xy}(f)|^2}.$$

The cancellation ratio supported by the coherence spectrum shown in Figure 6(a) ranges from 15 to 30 dB over the bandwidth of the cable strum interference.

Figure 6(b) depicts a time slice of the power spectrum for the short aperture array data corresponding to Figure 6(a). The power spectrum density (PSD) of the forward endfire acoustic beam is plotted both before and after the adaptive strum cancellation algorithm. It is seen that over the portion of the spectrum where the cancellation ratio predicted a 15-30 dB reduction in the cable strum noise floor, the PSD noise floor after strum cancellation is in fact decreased by a corresponding magnitude. Observe that a narrowband signal at frequency $3f_s/64$, detectable in the post-cancellation PSD, was completely buried in the self-noise floor prior to applying the adaptive sidelobe canceller algorithm.

5. CONCLUSIONS

An approach has been presented for cable strum self-noise suppression based on an adaptive sidelobe canceller architecture. The key feature of this approach lies in the formation of the interference reference by steering a beam to non-acoustic k - ω space. Towed array data examples show that the approach is capable of coherently rejecting cable strum in towed array data by as much as 15 to 30 dB.

6. REFERENCES

- [1] J. W. Bedenbender, R. C. Johnston, and E. B. Neitzel, "Electroacoustic characteristics of marine seismic streamers," *Geophysics*, vol. 35, no. 6, Dec. 1970, pp. 1054-1072.
- [2] L. Prandtl, "The generation of vortices in fluids of small viscosity," *J. Royal Aeronautical Society*, vol. 31, Dec. 1927, pp. 720-741.
- [3] B. Widrow and S. Stearns, *Adaptive Signal Processing*, Prentice-Hall, 1985.

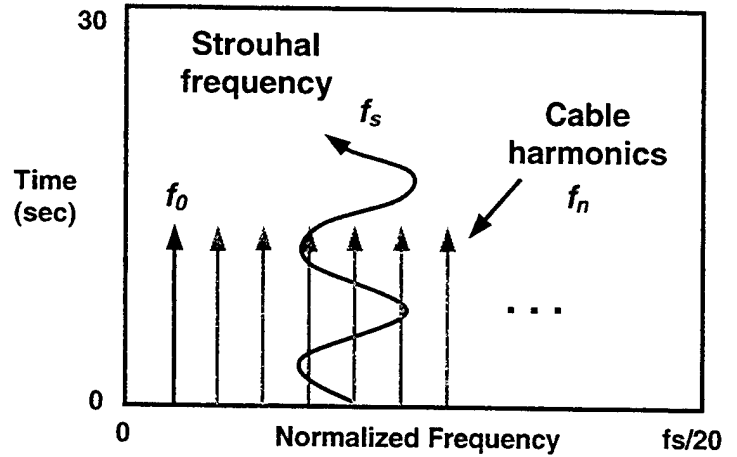


Figure 1 Notional depiction of time varying Strouhal excitation and array vibrational modes.

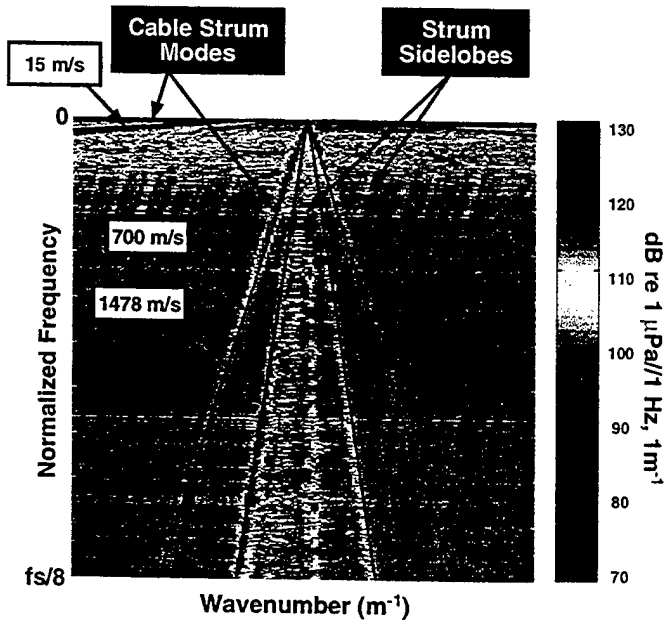


Figure 2 Frequency-wavenumber plot for long-aperture array during onset of own-ship turn. Discrete array structural modes are clearly observed at 15 m/s and 700 m/s phase speed. Some sidelobe leakage into acoustic cone is apparent.

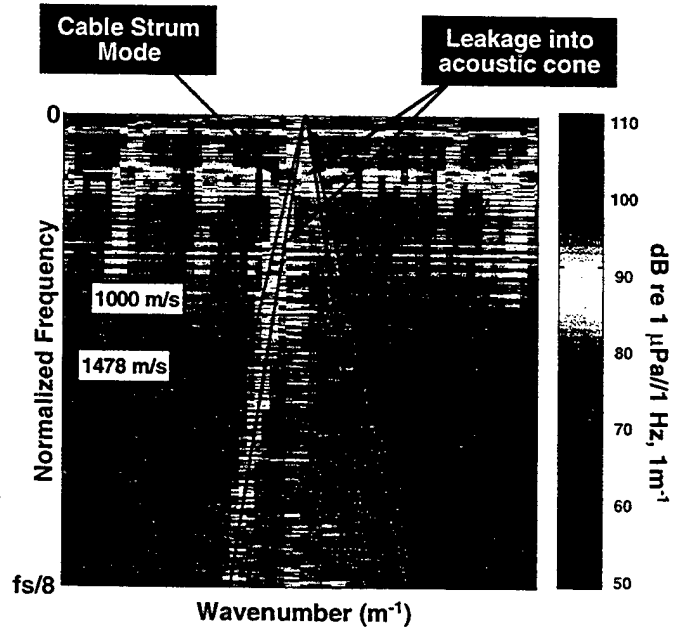


Figure 3 Frequency-wavenumber plot for short-aperture array during straight tow. A cable mode exists just outside the acoustic cone at 1000 m/s. Significant mainlobe and sidelobe leakage into the acoustic cone at forward endfire is observed.

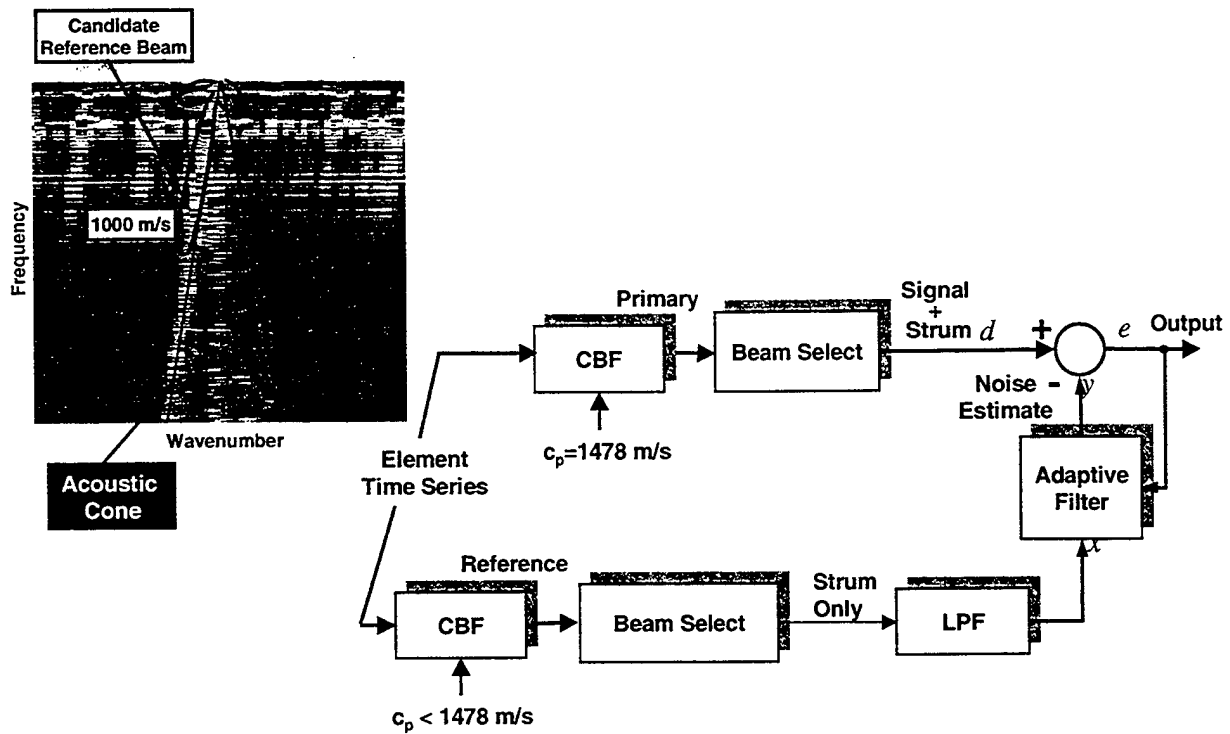


Figure 4 Adaptive sidelobe canceller block diagram. Inset depicts k - ω plot for short aperture array with candidate reference beam steered to non-acoustic space.

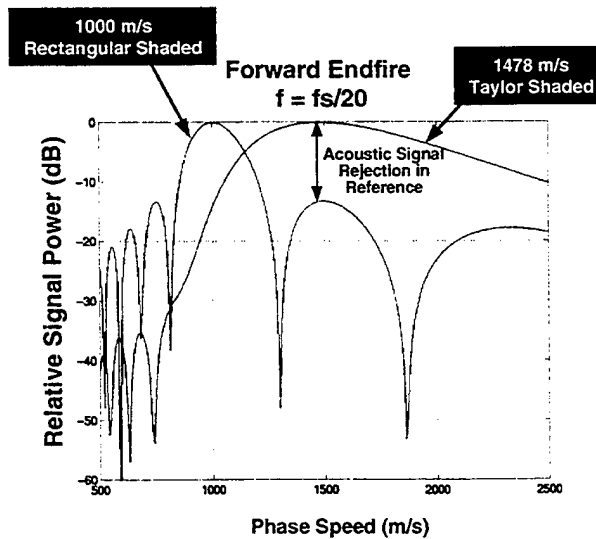


Figure 5 Phase speed dependent beam pattern illustrates potential for signal contamination of reference beam.

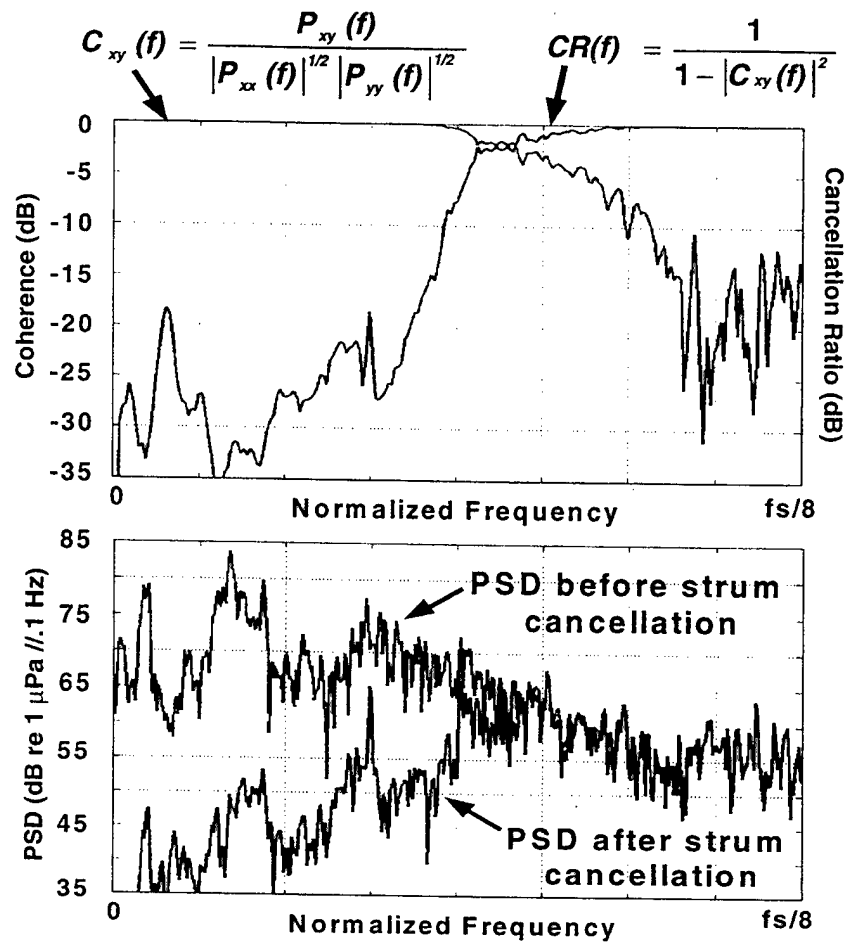


Figure 6 (a) Coherence between primary and reference channel, (b) PSD before and after strum cancellation. Adaptive strum canceller decreases cable strum-induced noise floor by as much as 15 to 30 dB. Note narrowband signal at $3f_s/64$, buried in noise floor in the original PSD, is detectable in post-cancellation PSD.

A UNIFIED METHOD FOR PASSIVE MEASUREMENT AND TRACKING OF CONTACTS FROM AN ARRAY OF SENSORS

Robert E. Zarnich, Kristine L. Bell, and Harry L. Van Trees

George Mason University, School of IT & Engineering, Fairfax, VA 22030-444 USA
rzarnich@gmu.edu, kbell@gmu.edu, hlv@gmu.edu

ABSTRACT

A multiple target track estimation method which operates directly from array data is presented. The Maximum A-Posteriori (MAP) estimator for contact states is derived for temporally uncorrelated signals and uncorrelated contact tracks. This batch estimator is an iterative algorithm employing a nested pair of Expectation Maximization (EM) based algorithms. The hidden data are intermediate direction finding estimates of synthetic signal estimates, each conditioned on prior track distributions. This method eliminates the data association step of traditional multitarget tracking approaches by conditioning the measurement process on individual target state distributions. This approach results in a process similar to the EM algorithm for direction finding by Miller and Fuhrmann, with an additional penalty term imposed by the track distributions. Simulation results for two relevant submarine towed array scenarios are presented and discussed.

1. INTRODUCTION

An important and pervasive problem in the engineering of sensor systems is the detection and tracking of multiple contacts through observations made from an array of sensors. An optimal approach would estimate the tracks of objects directly from the array snapshot data, however the solution to this estimation problem is quite difficult.

Traditional solutions partition the track estimation operation into two isolated processes: direction-of-arrival (DOA) estimation from array snapshot data, followed by track estimation from the DOA estimates. This partitioning results in procedures which are suboptimal and which require data association to match DOA estimates to contacts. Many approaches have been offered to solve the data association problem [1], however it continues to be a significant area of research and can be a major contributor to poor system performance.

In [2], a Maximum A-Posteriori (MAP) solution for estimating the target states directly from the array data was

The authors would like to thank the Department of the Navy's Program Executive Office for Undersea Warfare, Advanced Systems and Technology Office (PEO(USW) ASTO) for the support provided for this effort.

proposed. This approach discretizes the target state space and employs a Viterbi algorithm for determining the optimal state sequences. It provides an elegant but computationally expensive solution.

In this paper we will develop an efficient MAP estimation technique for determining the tracks of multiple objects without a discrete state space approach. We take the approach of introducing 'hidden data' as in the Expectation-Maximization (EM) [3] and Space Alternating Generalized EM (SAGE) [4] algorithms. This allows us to develop an iterative procedure for estimating the target states and provides a mechanism to control the trade-off between convergence rate and estimation error.

The paper is organized as follows. In Section 2, the signal and motion model is formulated and the joint pdf for the multitarget tracking problem is specified. In Section 3.1, a solution for the single target case is developed, and in Section 3.2 the concept is extended to multiple targets. Simulation results are presented in Section 4, and a summary is given in Section 5.

2. STATISTICAL MODEL AND ASSUMPTIONS

We consider the multitarget tracking problem where there are M contacts radiating signals received by an array of sensors. The number of objects M is assumed known and the trajectories of the objects are uncorrelated with the trajectories of other objects. We assume for simplicity the targets and the array lie in the $x - y$ plane, and that the array is linear, although we can easily extend the results to other geometries. This is illustrated in Figure 1. The 2-dimensional state is defined as its bearing $u = \cos(\theta)$ and bearing rate \dot{u} . Thus the state of the m th contact at snapshot k is $\mathbf{x}_{k,m} = [u_{k,m}, \dot{u}_{k,m}]^T$. We assume the motion of the objects is described by a first order Gauss-Markov process, i.e. for the m th contact,

$$\mathbf{x}_{k,m} = \mathbf{F}\mathbf{x}_{k-1,m} + \mathbf{w}_{k,m} \quad (1)$$

where $\mathbf{F} = \begin{bmatrix} 1 & t_k \\ 0 & 1 \end{bmatrix}$, t_k is the time interval from k to $k+1$, and $\mathbf{w}_{k,m}$ is a zero mean white Gaussian noise process with covariance \mathbf{Q} which is assumed known and fixed over the

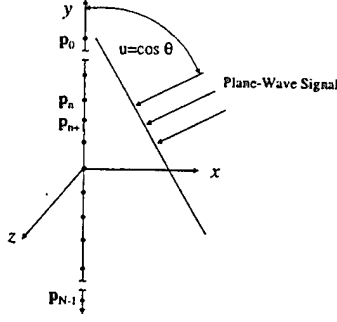


Figure 1: Array Observation Geometry

observation period and equal for all objects. Under these assumptions, the pdf of $\mathbf{x}_{k,m}$ given $\mathbf{x}_{k-1,m}$ is

$$\varphi(\mathbf{x}_{k,m}|\mathbf{x}_{k-1,m}) = \frac{1}{2\pi \det[\mathbf{Q}]^{\frac{1}{2}}} \cdot \exp\left(-\frac{1}{2}(\mathbf{x}_{k,m} - \mathbf{F}\mathbf{x}_{k-1,m})^T \mathbf{Q}^{-1}(\mathbf{x}_{k,m} - \mathbf{F}\mathbf{x}_{k-1,m})\right). \quad (2)$$

At the array, the observations have the form

$$\mathbf{y}_k = \sum_{m=1}^M s_{k,m} \mathbf{v}(u_{k,m}) + \mathbf{n}_k \quad (3)$$

where $s_{k,m}$ is the frequency domain signal from the m th object at the k th snapshot with $E[s_{k,m} s_{k,m}^*] = \alpha_{k,m}$. The vector $\mathbf{v}(u_{k,m})$ is the array response vector for the DOA $u_{k,m}$, and \mathbf{n}_k is a vector of uncorrelated sensor noise samples. The source signals and noise are sample functions of independent zero-mean Gaussian random processes. The signal powers, $\alpha_{k,m}$, are time varying and the noise covariance matrix is constant with $E[\mathbf{n}_k \mathbf{n}_k^H] = \sigma_n^2 \mathbf{I}$. Let $\mathbf{X}_k = [\mathbf{x}_{k,1}, \mathbf{x}_{k,2}, \dots, \mathbf{x}_{k,M}]^T$ and $\alpha_k = [\alpha_{k,1}, \alpha_{k,2}, \dots, \alpha_{k,M}]^T$. The array data \mathbf{y}_k is then jointly complex Gaussian with zero mean and covariance

$$\mathbf{K}_{\mathbf{y}_k}(\mathbf{X}_k, \alpha_k) = \sum_{m=1}^M \alpha_{k,m} \mathbf{v}(u_{k,m}) \mathbf{v}^H(u_{k,m}) + \sigma_n^2 \mathbf{I}. \quad (4)$$

The pdf of the array data conditioned on the target states is

$$p(\mathbf{y}_k|\mathbf{X}_k : \alpha_k) = \frac{\exp(-\mathbf{y}_k^H \mathbf{K}_{\mathbf{y}_k}^{-1}(\mathbf{X}_k, \alpha_k) \mathbf{y}_k)}{\pi^N \det[\mathbf{K}_{\mathbf{y}_k}(\mathbf{X}_k, \alpha_k)]}. \quad (5)$$

Note that the array data depends on the target state $\mathbf{x}_{k,m}$ only through the bearing $u_{k,m}$ and not the bearing rate $\dot{u}_{k,m}$. We will use both $\mathbf{x}_{k,m}$ and $u_{k,m}$ to denote bearing as necessary in the subsequent derivation in order to reduce notational complexity.

The single scan joint pdf conditioned on the previous contact state is

$$\Upsilon(\mathbf{y}_k, \mathbf{X}_k|\mathbf{X}_{k-1} : \alpha_k) = p(\mathbf{y}_k|\mathbf{X}_k : \alpha_k) \prod_{m=1}^M \varphi(\mathbf{x}_{k,m}|\mathbf{x}_{k-1,m}). \quad (6)$$

There are \mathcal{K} snapshots in an observation batch. No data is available at $k = 0$ so we assume a Gaussian prior distribution on object states with mean $\bar{\mathbf{x}}_{0,m}$ and covariance $\bar{\mathbf{P}}_{0,m}$. The joint pdf over the batch is

$$\Upsilon(\mathbf{Y}, \mathbf{X} : \alpha) = \prod_{\nu=1}^M \varphi(\mathbf{x}_{0,\nu}) \cdot \left\{ \prod_{k=1}^{\mathcal{K}} p(\mathbf{y}_k|\mathbf{X}_k : \alpha_k) \prod_{m=1}^M \varphi(\mathbf{x}_{k,m}|\mathbf{x}_{k-1,m}) \right\} \quad (7)$$

where $\mathbf{Y} = \{\mathbf{y}_1, \dots, \mathbf{y}_{\mathcal{K}}\}$, $\mathbf{X} = [\mathbf{X}_1, \dots, \mathbf{X}_{\mathcal{K}}]$, and $\alpha = [\alpha_1, \dots, \alpha_{\mathcal{K}}]$.

3. MAP ESTIMATOR DEVELOPMENT

Traditional calculus based optimization is not a tractable approach and a brute force Newton type algorithm for the maximization of Eq. (7) has difficulties from both an analytic and an implementation perspective as discussed in [5]. An exact solution under a discrete state space model is provided by [2], however it is computationally very expensive. What is desired is a solution which provides a tractable and efficient algorithm.

Nonlinear programming methods [6] such as relaxation and auxiliary penalty functions solve optimization problems iteratively by finding the solution to an approximated problem and successively force the approximation and the original problem to converge with each iteration. We use a similar approach. Assume we have an 'observation error' at the array. We can model the 'observed' DOA as

$$\mu_{k,m} = u_{k,m} + e_{k,m} \quad (8)$$

where $p(e_{k,m}) = \mathcal{N}(0, \sigma_{e_{k,m}}^2)$, therefore

$$p(\mu_{k,m}|\mathbf{x}_{k,m}) = \mathcal{N}(u_{k,m}, \sigma_{e_{k,m}}^2). \quad (9)$$

Accounting for this error term, the observed array data is then given by (3) with $u_{k,m}$ replaced $\mu_{k,m}$ and the pdf of the array data conditioned on the corrupted observation of target states is

$$p(\mathbf{y}_k|\mu_k : \alpha_k) = \frac{\exp(-\mathbf{y}_k^H \mathbf{K}_{\mathbf{y}_k}^{-1}(\mu_k, \alpha_k) \mathbf{y}_k)}{\pi^N \det[\mathbf{K}_{\mathbf{y}_k}(\mu_k, \alpha_k)]}, \quad (10)$$

where $\mu_k = [\mu_{k,1}, \dots, \mu_{k,M}]^T$. The modified single scan joint pdf is

$$\begin{aligned} \Upsilon(y_k, \mu_k, \mathbf{X}_k | \mathbf{X}_{k-1} : \alpha_k) \\ = p(y_k | \mu_k, \mathbf{X}_k, \mathbf{X}_{k-1}, : \alpha_k) p(\mu_k, \mathbf{X}_k | \mathbf{X}_{k-1}) \quad (11) \\ = p(y_k | \mu_k : \alpha_k) \prod_{m=1}^M p(\mu_{k,m} | \mathbf{x}_{k,m}) \varphi(\mathbf{x}_{k,m} | \mathbf{x}_{k-1,m}). \end{aligned}$$

and the modified joint batch pdf is

$$\begin{aligned} \Upsilon(\mathbf{Y}, \mathbf{M}, \mathbf{X} : \alpha) = \prod_{\nu=1}^M \varphi(\mathbf{x}_{0,\nu}) \cdot \\ \left\{ \prod_{k=1}^K p(y_k | \mu_k : \alpha_k) \prod_{m=1}^M p(\mu_{k,m} | \mathbf{x}_{k,m}) \varphi(\mathbf{x}_{k,m} | \mathbf{x}_{k-1,m}) \right\}, \quad (12) \end{aligned}$$

where $\mathbf{M} = [\mu_1, \dots, \mu_K]$. While on the surface it appears we have complicated the problem, this formulation will allow us to develop an iterative procedure for estimating \mathbf{M} and \mathbf{X} .

In the limit as the 'observation error' variance goes to zero we have $p(\mu_k | \mathbf{x}_k)$ taking on the behavior of a Test Sequence. By initially assuming a large error variance and successively reducing it with every iteration cycle, we recover the original problem. This provides a mechanism to control the trade off between convergence rate and estimation error.

This auxiliary 'observation error' has a real physical counterpart. In all real systems we employ physical devices which are subject to error as well as observe energy through a propagation channel with random fluctuation. In these systems, particularly towed hydro-acoustic arrays, this error manifests itself as minor propagation fluctuation and random array orientation error. By treating this error term up front, we get the same structure as in Eq. (12).

3.1. Single Signal MAP Estimator

Considering only a single signal we drop the notation on m and Eq. (12) becomes

$$\begin{aligned} p(\mathbf{Y}, \mu, \mathbf{X} : \alpha) = \\ \varphi(\mathbf{x}_0) \prod_{k=1}^K p(y_k | \mu_k : \alpha_k) p(\mu_k | \mathbf{x}_k) \varphi(\mathbf{x}_k | \mathbf{x}_{k-1}). \quad (13) \end{aligned}$$

For a fixed μ and α , the MAP estimator of \mathbf{X} is now the fixed interval Kalman smoother. On the other hand, for a fixed \mathbf{X} , we can solve for both μ and α using Maximum Likelihood Estimation (MLE) techniques from array process where an additional 'penalty' term is imposed due to $p(\mu_k | \mathbf{x}_k)$.

Eq. (13) is of an identical form used by the SAGE algorithm [4]. It is shown in [4] that if the observed data (y), the

hidden data (μ), and the non-random parameters of interest (θ) are related as follows,

$$f(y, \mu; \theta) = f(y | \mu) f(\mu; \theta), \quad (14)$$

then (y, μ) is an *Admissible Complete-Data Space* for the estimation of θ . Since we are interested in MAP estimation, θ is a random parameter. The requirement for MAP estimation can be restated as

$$f(y, \mu, \theta) = f(y | \mu) f(\mu | \theta) f(\theta). \quad (15)$$

Eq. (13) is of the form of (15) for an admissible hidden data space, with the noisy bearing vector μ behaving as the hidden data. Since our form and the required SAGE form are equivalent, we will borrow from the SAGE theory for its convergence proof as well as the optimization technique to construct a MAP estimation algorithm.

A detailed development of the algorithm is presented in [5] and the results are summarized here. The algorithm is initialized by defining an initial track and signal power in the vicinity of their true values. The observation error variance is initially set to the Cramér-Rao Bound [8] and reduced at every iteration. This ensures that the estimation error introduced by the 'observation error' is significantly less than the inherent resolution of the array. The Algorithm consists of the Expectation (E) Step and the Maximization (M) step as follows:

- E-Step: Estimate μ_k^p for each $k = 1, \dots, K$ by finding

$$\begin{aligned} \mu_k^p = \underset{\mu}{\operatorname{argmax}} \quad - \ln \left[\frac{\mathbf{v}^H(\mu) \mathbf{C}_{y_k} \mathbf{v}(\mu)}{N} \right] \\ + \frac{\mathbf{v}^H(\mu) \mathbf{C}_{y_k} \mathbf{v}(\mu)}{N \sigma_n^2} - \frac{(\mu - u_k^{p-1})^2}{2 \sigma_{e_{k,m}}^2}, \quad (16) \end{aligned}$$

where $\mathbf{C}_{y_k} = \mathbf{y}_k \mathbf{y}_k^H$. The error variance is set to $\sigma_{e_{k,m}}^2 = \epsilon^p \cdot \sigma_{CRB_k}^2$, where ϵ^p is a scaling parameter chosen for convergence properties and $\sigma_{CRB_k}^2$ is the Cramér-Rao Bound evaluated at the estimated bearing u_k^{p-1} and power α_k^{p-1} from the previous iteration. The E-Step is in fact a Penalized Maximum Likelihood Estimate (PMLE) of the noisy bearing μ_k , where the penalty term is based on the relationship of μ_k to the true bearing u_k through the 'observation error'.

- M-Step:

– Part I: Compute α_k by

$$\alpha_k^p = \max \left[\frac{1}{N} \left(\frac{\mathbf{v}^H(\mu_k^p) \mathbf{C}_{y_k} \mathbf{v}(\mu_k^p)}{N} - \sigma_n^2 \right), 0 \right]. \quad (17)$$

- Part II: Compute \mathbf{X}^p using the μ_k^p as the ‘state measurements’ and $\epsilon^p \cdot \sigma_{CRB}^2$ as their variances in a fixed interval Kalman smoother.

The M-Step produces PMLEs of α_k and a MAP estimate of the states \mathbf{x}_k via the Kalman smoother.

- Increment $p = p + 1$ and iterate.

We carry out these steps for a prescribed number of iterations and accept the final value as the MAP estimate.

3.2. Multiple Signal MAP Estimator

To extend this idea we need only to consider the idea of nesting an EM Algorithm within the single signal MAP estimator algorithm. If we could separate the mixed observed signals in \mathbf{Y} into M distinct signals \mathbf{Z}_m where $\mathbf{Y} = \sum_{m=1}^M \mathbf{Z}_m$, we would have all we need to solve the multiple contact problem. Since we have assumed contacts with uncorrelated signals we can employ the technique of Miller and Fuhrmann in [7] to synthesize M single signals from the mixed data in \mathbf{Y} . At each scan we then have the standard EM Algorithm for direction finding, modified with the quadratic penalty term. There are then $M \times \mathcal{K}$ estimates to form and M fixed interval Kalman smoothers in parallel for every iteration. The extension of the single signal algorithm to multiple signals results in the following algorithm.

- E-Steps:

$$\mathbf{K}_{\mathbf{z}_k, m}^{p, q} = \alpha_{k, m}^{p, q-1} \mathbf{v}(\mu_{k, m}^{p, q-1}) \mathbf{v}^H(\mu_{k, m}^{p, q-1}) + \frac{\sigma_n^2}{M} \mathbf{I} \quad (18)$$

$$\mathbf{K}_{\mathbf{y}_k}^{p, q} = \sum_{m=1}^M \mathbf{K}_{\mathbf{z}_k, m}^{p, q} \quad (19)$$

$$\begin{aligned} \mathbf{R}_{\mathbf{z}_k, m}^{p, q} &\equiv E[\mathbf{R}_{\mathbf{z}_k, m} | \mathbf{C}_{\mathbf{y}_k}, \mathbf{K}_{\mathbf{y}_k}^{p, q}] \\ &= \mathbf{K}_{\mathbf{z}_k, m}^{p, q} (\mathbf{K}_{\mathbf{y}_k}^{p, q})^{-1} \mathbf{C}_{\mathbf{y}_k} (\mathbf{K}_{\mathbf{y}_k}^{p, q})^{-1} \mathbf{K}_{\mathbf{z}_k, m}^{p, q} \\ &\quad + \mathbf{K}_{\mathbf{z}_k, m}^{p, q} - \mathbf{K}_{\mathbf{z}_k, m}^{p, q} (\mathbf{K}_{\mathbf{y}_k}^{p, q})^{-1} \mathbf{K}_{\mathbf{z}_k, m}^{p, q} \end{aligned} \quad (20)$$

$$\begin{aligned} \mu_{k, m}^{p, q} &= \underset{\mu}{\operatorname{argmax}} - \ln \left[\frac{\mathbf{v}^H(\mu) \mathbf{R}_{\mathbf{z}_k, m}^{p, q} \mathbf{v}(\mu)}{N} \right] \\ &\quad + \frac{M \mathbf{v}^H(\mu) \mathbf{R}_{\mathbf{z}_k, m}^{p, q} \mathbf{v}(\mu)}{N \sigma_n^2} - \frac{(\mu - u_{k, m}^{p-1})^2}{2 \sigma_{e_k, m}^2} \end{aligned} \quad (21)$$

where again $\sigma_{e_k, m}^2 = \epsilon^p \cdot \sigma_{CRB, k, m}^2$.

- M-Step, Part I:

$$\begin{aligned} \alpha_{k, m}^{p, q} &= \\ \max &\left[\frac{1}{N} \left(\frac{\mathbf{v}^H(\mu_{k, m}^{p, q}) \mathbf{R}_{\mathbf{z}_k, m}^{p, q} \mathbf{v}(\mu_{k, m}^{p, q})}{N} - \frac{\sigma_n^2}{M} \right), 0 \right]. \end{aligned} \quad (22)$$

Increment $q = q + 1$ and iterate.

- M-Step, Part II: Compute \mathbf{X}^p with M independent fixed interval Kalman smoothers using M and the associated variances. Increment $p = p + 1$ and iterate.

The iterations may be performed for fixed number of cycles or until some convergence criterion is reached. The trade-off is algorithm complexity vs. estimation accuracy. Similarly, the choice of the reduction schedule for ϵ^p represents a tradeoff between convergence speed and estimation accuracy. One possibility is to set $\epsilon^p = \eta \epsilon^{p-1}$ where $0 < \eta < 1$. In explicit pseudo-code form, the algorithm is:

Initialize $\alpha_{k, m}^0, \mathbf{x}_{k, m}^0 \quad \forall k, m$

for $p = 1, \dots, p_{max}$

$\epsilon^p = \eta^{(p-1)}$

for $k = 1, \dots, \mathcal{K}$

Update/Reduce ‘Observation Error’ Variance

$\Sigma_k = CRB(\mathbf{X}_k^{p-1}, \alpha_k^{p-1}) [8]$

$\sigma_{e_k, m}^2 = \epsilon^p \cdot \Sigma_k(m, m) \quad \forall m$

Update Bearing and Power Estimates

Initialize $\mu_{k, m}^{p, 0} = u_{k, m}^{p-1} \quad \forall m$

Initialize $\alpha_{k, m}^{p, 0} = \alpha_{k, m}^{p-1, q_{max}} \quad \forall m$

for $q = 1, \dots, q_{max}$

Compute $\mathbf{K}_{\mathbf{z}_k, m}^{p, q} \quad \forall m$ {Eq. (18)}

Compute $\mathbf{K}_{\mathbf{y}_k}^{p, q}$ {Eq. (19)}

for $m = 1, \dots, M$

Compute $\mathbf{R}_{\mathbf{z}_k, m}^{p, q}$ {Eq. (20)}

Find $\mu_{k, m}^{p, q}$ {Eq. (21)}

Compute $\alpha_{k, m}^{p, q}$ {Eq. (22)}

end $\{m\}$

end $\{q\}$

end $\{k\}$

Update State Estimates ($\mathbf{H} = [1 \ 0]$)

for $m = 1, \dots, M$

Initialize $\mathbf{b}_{0|m} \equiv \bar{\mathbf{x}}_{0, m}, \mathbf{P}_{0|m} \equiv \bar{\mathbf{P}}_{0, m}$

Forward Kalman Filter

for $k = 1, \dots, \mathcal{K}$

$\mathbf{P}_{k|k-1} = \mathbf{F} \mathbf{P}_{k-1|k-1} \mathbf{F}^T + \mathbf{Q}$

$\mathbf{W}_k = \mathbf{P}_{k|k-1} \mathbf{H}^T \left\{ \mathbf{H} \mathbf{P}_{k|k-1} \mathbf{H}^T + \sigma_{e_k, m}^2 \right\}^{-1}$

$\mathbf{P}_{k|k} = \mathbf{P}_{k|k-1} - \mathbf{W}_k \mathbf{H} \mathbf{P}_{k|k-1}$

$\mathbf{b}_{k|k} = \mathbf{F} \mathbf{b}_{k-1|k-1} + \mathbf{W}_k \left\{ \mu_{k, m}^{p, q} - \mathbf{H} \mathbf{F} \mathbf{b}_{k-1|k-1} \right\}$

end $\{k\}$

Backward Kalman Smoother

Set $\mathbf{x}_{\mathcal{K}, m}^p = \mathbf{b}_{\mathcal{K}| \mathcal{K}}$

for $k = \mathcal{K} - 1, \dots, 1$

$\mathbf{G} = \mathbf{P}_{k|k} \mathbf{F}^T \mathbf{P}_{k+1|k}^{-1}$

$\mathbf{x}_{k, m}^p = \mathbf{b}_{k|k} + \mathbf{G} [\mathbf{x}_{k+1, m}^p - \mathbf{F} \mathbf{b}_{k|k}]$

end $\{k\}$

end $\{m\}$

end $\{p\}$.

The algorithm must be initialized in the vicinity of the true tracks. An initialization process is developed in [5] which estimates the number of targets and their initial tracks. The algorithm has a great intuitive appeal in that given an assumed track for each contact, we decompose the array data into the M synthetic signal covariances for each snapshot, find their directions constrained to the neighborhood of the current track, and then adjust the current track estimate to satisfy a weighted least squares criterion (the fixed interval Kalman smoother). We repeat the process and at every iteration we enforce a stricter relationship between the 'observed' DOA and the estimated track.

The outstanding feature of this approach is that the association of the measurements to tracks is implicit since each measurement is conditioned, via the Gaussian penalty term, on its track. This provides a near optimal measurement for each track.

4. RESULTS

Two simulated scenarios were used to develop and test the algorithm. An array of 10 elements is used. Contact parameters are summarized for both scenarios in Tables 1 and 2. In scenario 1, the 'Target' starts as the left-most trace in Figure 2(a), Interferer 3 is the next trace to the right, then Interferer 2 and then Interferer 1. In scenario 2, Interferer 3 starts as the left most trace in Figure 3(a), then the Target is the next trace to the right, then Interferer 2 and then Interferer 1. In the simulations, a fixed number of iterations was

Table 1: Parameters for Scenario 1

Contact	SNR	RMSE
Target	-7dB	$2.56 \cdot 10^{-2}$
Interferer 1	0dB	$6.10 \cdot 10^{-3}$
Interferer 2	-7dB	$8.99 \cdot 10^{-3}$
Interferer 3	0dB	$4.85 \cdot 10^{-3}$

Table 2: Parameters for Scenario 2

Contact	SNR	RMSE
Target	-10dB	$2.45 \cdot 10^{-2}$
Interferer 1	0dB	$5.62 \cdot 10^{-3}$
Interferer 2	-10dB	$2.94 \cdot 10^{-2}$
Interferer 3	0dB	$3.76 \cdot 10^{-3}$

used with $p_{max} = 10$ and $q_{max} = 5$. The error reduction parameter was set to $\eta = 0.1$. Figures 2(a) and 3(a) show the true paths of the contacts summarized in Tables 1 and 2 as they move through the observation space. Figures 2(b) and 3(b) show the true tracks (marked with the tick marks) and the estimated tracks (lines) after 10 iterations overlaid on the data.

The results were compared to the discrete state space (DSS) technique proposed in [2]. This required developing a straightforward extension of their algorithm to the stochastic signal model used here. Table 3 shows the estimation accuracy performance of the two algorithms. Both algorithms were initialized with the same information and great care was taken to tune the algorithm of [2] to the data and to make it as computationally efficient as possible. Our

Table 3: Continuous State Space (CSS) vs. Frenkel and Feder Discrete State Space (DSS) Algorithm for Scenario 1

Cntct	RMSE DSS	RMSE CSS	$\frac{RMSE_{DSS}}{RMSE_{CSS}}$
Target	$5.32 \cdot 10^{-2}$	$2.56 \cdot 10^{-2}$	2.09
Intf 1	$11.2 \cdot 10^{-3}$	$6.10 \cdot 10^{-3}$	1.84
Intf 2	$1.03 \cdot 10^{-2}$	$8.99 \cdot 10^{-3}$	1.15
Intf 3	$6.90 \cdot 10^{-3}$	$4.85 \cdot 10^{-3}$	1.42

continuous state space (CSS) technique out-performed the discrete state space algorithm of [2] from both an RMS Error perspective and in computational complexity. The execution time for the CSS algorithm was about 4 minutes, while the execution time for the DSS algorithm was approximately 20 hours. These times were on a 550MHz Dell PC using MATLAB® v5.3.

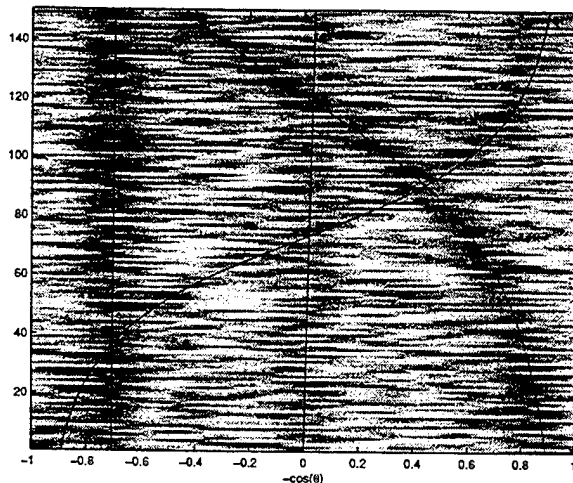
5. CONCLUSIONS

We have developed an efficient algorithm for the MAP estimation of multiple contact tracks. To construct this algorithm we introduced an observation error to decouple the Gauss-Markov motion model and the array data model. Convergence of the artificial problem to the original problem was enforced through the reduction of the 'observation error' variance with each iteration. The single target solution was extended to multiple targets by using the decomposition capabilities of the EM algorithm developed in [7] to break the problem into M single target problems.

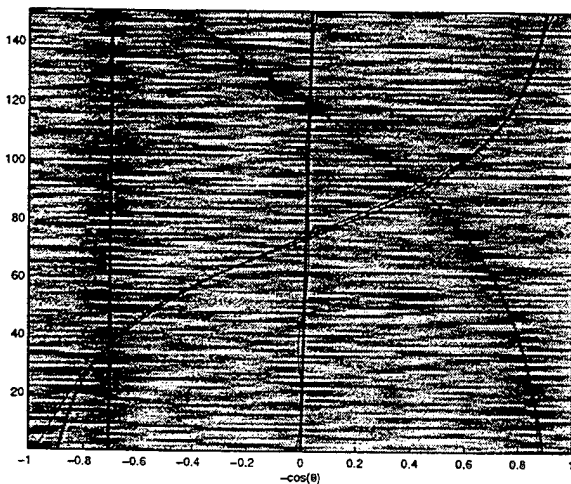
The algorithm performed very well. In addition to accuracy, the convergence rate was quite good. The algorithm provides a substantial reduction in computation to a discrete state space solution while also decreasing the RMS error. A sequential version for real-time estimates, and a beamspace formulation for computational considerations, are developed and discussed in [5]. The sequential version is presented in [9].

6. REFERENCES

- [1] *Multitarget-Multisensor Tracking Applications and Advances, Volumes I & II*, Y. Bar-Shalom Editor, YBS Publishing, Storrs, CT, 1998.

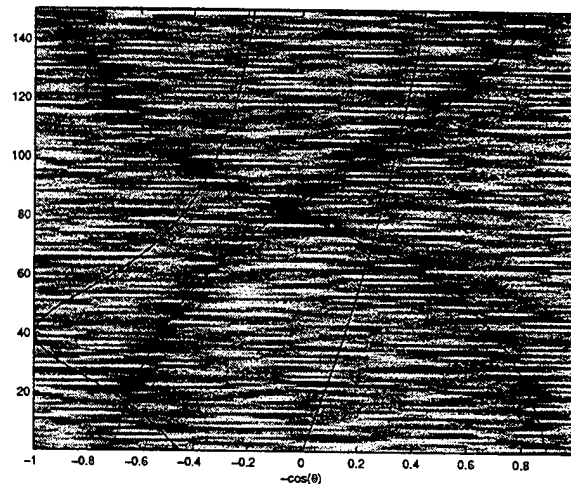


(a) Truth Overlay for Scenario

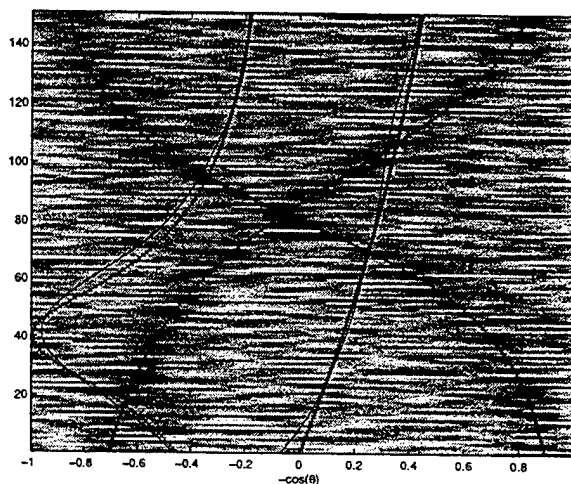


(b) Truth and Track Overlay

Figure 2: Results for First Scenario



(a) Truth Overlay for Scenario



(b) Truth and Track Overlay for Scenario

Figure 3: Results for Second Scenario

- [2] L. Frenkel and M. Feder, "Recursive Expectation-Maximization (EM) Algorithms for Time-Varying Parameters with Applications to Multiple Target Tracking," *IEEE Transactions on Signal Processing*, vol. 47, no. 2, pp. 306-320, February 1999.
- [3] A. P. Dempster, N. M. Laird, and D. B. Rubin, "Maximum Likelihood from Incomplete Data via the EM Algorithm," *Journal of the Royal Statistical Society, Series B*, vol. 39, no. 1, pp. 1-38, 1977.
- [4] J. A. Fessler and A. O. Hero, "Space-Alternating Generalized Expectation-Maximization Algorithm," *IEEE Transactions on Signal Processing*, vol. 42, no. 10, pp. 4664-4677, October 1994.
- [5] R. E. Zarnich, "A Unified Method for the Measurement and Tracking of Narrowband Contacts from an Array of Sensors," PhD Thesis, George Mason University, Fairfax, Virginia, March 2000.
- [6] S. G. Nash and A. Sofer, *Linear and Nonlinear Programming*, McGraw-Hill, 1996.
- [7] M. I. Miller and D. R. Fuhrmann, "Maximum-Likelihood Narrow-Band Direction Finding and the EM Algorithm," *IEEE Transactions on Acoustics, Speech, and Signal Processing*, vol. 38, no. 9, pp. 1560-1577, September 1990.
- [8] A. J. Weiss and B. Friedlander, "On The Cramér Rao Bound for Direction Finding of Correlated Signals," *IEEE Transactions on Signal Processing*, vol. 41, no. 1, pages 495-499, January 1993.
- [9] R. E. Zarnich, K. L. Bell, and H. L. Van Trees, "A Sequential Extension of the Unified MAP Track Estimation Method," *Proceedings of 1st IEEE Sensor Array and Multichannel Signal Processing Workshop*, March 2000.

REPORT DOCUMENTATION PAGE			Form Approved OMB No. 0704-0188	
Public reporting burden for this collection of information is estimated to average 1 hour per response, including the time for reviewing instructions, searching existing data sources, gathering and maintaining the data needed, and completing and reviewing the collection of information. Send comments regarding this burden estimate or any other aspect of this collection of information, including suggestions for reducing this burden, to Washington Headquarters Services, Directorate for Information Operations and Reports, 1215 Jefferson Davis Highway, Suite 1204, Arlington, VA 22202-4302, and to the Office of Management and Budget, Paperwork Reduction Project (0704-0188), Washington, DC 20503.				
1. AGENCY USE ONLY (Leave blank)	2. REPORT DATE 5 September 2000	3. REPORT TYPE AND DATES COVERED Project Report		
4. TITLE AND SUBTITLE Proceedings of the Adaptive Sensor Array Processing (ASAP) Workshop, 14-15 March 2000		5. FUNDING NUMBERS C — F19628-00-C-0002		
6. AUTHOR(S) Joan O'Brien, Editor				
7. PERFORMING ORGANIZATION NAME(S) AND ADDRESS(ES) Lincoln Laboratory, MIT 244 Wood Street Lexington, MA 02420-9108		8. PERFORMING ORGANIZATION REPORT NUMBER ASAP-8, Volume 1		
9. SPONSORING/MONITORING AGENCY NAME(S) AND ADDRESS(ES) DARPA/ISO 3701 N. Fairfax Drive Arlington, VA 22203-1714		10. SPONSORING/MONITORING AGENCY REPORT NUMBER ESC-TR-99-074		
11. SUPPLEMENTARY NOTES None				
12a. DISTRIBUTION/AVAILABILITY STATEMENT Approved for public release; distribution is unlimited.			12b. DISTRIBUTION CODE	
13. ABSTRACT (Maximum 200 words) This year marks the eighth annual ASAP workshop, which is sponsored jointly by the DARPA Advanced and Tactical Technology Offices, the Navy AEGIS and E2C Program Offices, the Office of Naval Research and the NAVSEA Advanced Systems and Technology Office. This year, the first IEEE Sensor Array and Multichannel (SAM) Signal Processing Workshop in nearby Cambridge, Massachusetts will follow the ASAP workshop on 16-17 March 2000. This unique pairing of ASAP with SAM will provide an unparalleled opportunity for the adaptive sensor array processing community, combining ASAP's focus on state-of-the-art signal processing advances for military systems with the broader international scope and strong academic participation of the IEEE SAM workshop. As this workshop has evolved over its eight-year history, a common theme has been to highlight the similarity of adaptive sensor processing techniques for various disciplines. The ASAP forum has provided researchers from academia, government, and industry the opportunity to discuss common problems and develop ideas and solutions related to how these diverse technologies can be applied to national defense interests. This year's workshop will continue to stress the strong coupling between government, industry, and academia. A key theme will be the cross-fertilization of ideas between the ASAP and SAM participants to provide new areas of exploration and accelerate technological advances.				
14. SUBJECT TERMS			15. NUMBER OF PAGES 126	
			16. PRICE CODE	
17. SECURITY CLASSIFICATION OF REPORT Unclassified	18. SECURITY CLASSIFICATION OF THIS PAGE Same as Report	19. SECURITY CLASSIFICATION OF ABSTRACT Same as Report	20. LIMITATION OF ABSTRACT Same as Report	